University of Genoa

Ph. D. in Systems Engineering

XXX cycle

Multivariate data assimilation in snow modelling at Alpine sites

Supervisors: Prof Dr Eng Luca Ferraris
Dr Simone Gabellani

Tutor: Dr Lorenzo Campo

Candidate: Gaia Piazzi

A Viola Berthe, sii sempre curiosa

#theimportanceofbeingpignola

Acknowledgments

Finally reached the finish line, I want to express my gratitude to all the people who have accompanied me along the way.

I would like to sincerely thank Prof. Luca Ferraris for assigning me this interesting research project and for giving me the opportunity to have lots of interesting experiences, even abroad.

I warmly thank Simone Gabellani for his constant and precious guidance always pointing me to the right path to take, still giving me (quite) full freedom in my research. I am grateful for his encouragement, the teachings in hydrology and beyond, which improved me greatly as a researcher and as a person.

The title page of this dissertation lists Lorenzo Campo as a tutor, but that doesn't do him justice. I am deeply grateful to Lollo, who has always supported me by acting as first rescue in the countless struggling moments during these last years. He has been overly generous with his time and his genius but, more importantly, he has patiently turned me from a naive PhD student into a proudly perfect nerd.

My heartiest thanks to Guillaume Thirel for deeply inspiring and motivating me. From our many fruitful discussions and his advices, I have learned to think critically, while becoming more and more enthusiastic in doing research. He has strongly encouraged me to undertake new challenges by always offering his mentoring support and I cannot thank him enough for that.

I want to thank all my colleagues at CIMA Research Foundation, who have made the everyday life in the office really enjoyable: Flavio, Silvia, Mirko, Valerio, Luca, Elisabetta, Martina. But allow me to address a special thanks to Laura e Daniele, who are something more than colleagues. Our special friendship makes me feel as if everything could be faced with a smile, since I can always rely on you.

Je tiens à remercier Charles Perrin de m'avoir accueillie dans la super équipe HYDRO d'IRSTEA. Au cours de ces mois passés avec vous j'ai vivement compris la valeur et l'importance de la recherche. Il faut bien le dire, vous n'êtes pas seulement des excellents chercheurs, mais aussi des personnes merveilleuses (bon, sauf quand on joue au frisbee…). Un très grand merci à Laure, Helena, Olivier, Vazken, José, Manon, Léonard, Julie, Alban, Philippe,

Cédric, Pierre, Morgane, Daniela, Andrea, Carine, Arnaud, et à Carina de m’avoir prêté son bureau.

I would like to address special thanks to Prof. Gabrielle De Lannoy and Prof. Albrecht Weerts for their relevant suggestions, which have allowed me to significantly improve my dissertation.

Un affettuoso grazie lo rivolgo alla mia famiglia che, anche se un po’ sparpagliata oltralpe, è da sempre la mia più grande fonte di forza. Grazie per continuare a sostenermi e spronarmi ad affrontare nuove sfide. Un grazie speciale a Christian che, con incondizionato affetto e tanta, tantissima pazienza, si è preso cura di me ogni giorno.

Mando un grazie di cuore fino a Londra, alla mia più grande supporter, Giulia: distanza non significa lontananza.

Abstract

The knowledge of snowpack dynamics is of critical importance to several real-time applications such as agricultural production, water resource management, flood prevention, hydropower generation, especially in mountain basins. Snowpack state can be estimated by models or from observations, even though both these sources of information are affected by several errors. With the aim of reducing the simulations uncertainty, an increasing interest focuses on the combined use of data by assimilating snow-related observations within models.

This study aims at investigating the potential of multivariate Data Assimilation (DA) in the framework of snow modelling for hydrological purposes in the Alpine environment. A snow multilayer mass- and energy-balance model has been developed and coupled with different DA schemes. The model has been calibrated and validated at 3 Alpine sites: Torgnon (Italy), Col de Porte (France) and Weissfluhjoch (Switzerland). Two sequential ensemble-based DA methods, namely the Ensemble Kalman Filter (EnKF) and the Particle Filter (PF) have been developed and tested by assimilating several in-situ snow-related measurements.

The development of a multivariate EnKF-based DA scheme has required to address several critical issues, mainly due to the constraining assumptions of this technique, which make more challenging the handling of the strong nonlinearities of the snow modelling system. Several experiments have been performed to assess the EnKF sensitivity to different DA settings, namely the assimilation frequency, the ensemble size, and the impact of assimilating different observations.

A multivariate PF scheme has been implemented by testing different strategies aiming at guaranteeing a sufficiently large ensemble spread, whose poor variance can hinder the effectiveness of the updating procedure. After assessing the impact of the uncertainty of the meteorological forcing data, the perturbation of model parameters has been investigated. Furthermore, with the aim of reducing the system sensitivity to the generally low frequency of in-situ snow observations, an empirical snow density model has been introduced to assess the potential of using additional proxy information on snow mass-related variables within the resampling procedure.

A comparative study between the simulations provided by the two selected ensemble-based DA techniques has allowed to better identify their main weaknesses and strengths. Generally, both the techniques have proved to be suited to multivariate applications, since they allow to take into account different sources of uncertainty.

Contents

CHAPTER 1
Introduction

1.1 Research context

The seasonal presence of snow in mountain regions strongly impacts both energy and water resource balances, not only locally, but also at larger scale. Snow dynamics strongly affect hydrological processes, mainly through the release of the significant water volume stored in winter season, which considerably contributes to the total discharge during the melting period (Barnett et al., 2005; Zappa et al., 2003; Clark and Hay, 2004). Melt water supplies a significant component of the annual water budget, both in terms of soil moisture and runoff, which play a critical role in floods generation in snow-dominated basins. Therefore, the knowledge of snowpack dynamics is of critical importance to several real-time applications especially in mountain areas, such as agricultural production, water resource management, flood prevention, hydropower generation. Thus, when modelling hydrological processes in snow-dominated catchments the reliability of predictions deeply depends on how the model succeeds in catching snow dynamics (Wood et al., 2016).

A growing effort is aimed at enhancing the physical representation of the snowpack in hydrological models. Many different snowpack models have been developed with highly variable degree of complexity, mainly depending on their target application, such as hydrological forecasting, avalanche prediction, climate modelling, and the availability of computational resources and data. Snow models range from the so-called force-restore systems of composite snow-soil layer(s) (Douville et al., 1995; Yang et al., 1997) and explicit snow layer(s) schemes (Verseghy, 1991; Slater et al., 1998) up to detailed internal-snow-process schemes with physical parameterizations (Anderson, 1976; Jordan, 1991; Bartelt and Lehning, 2002; Lehning et al., 2002; Brun et al., 1989; Vionnet et al., 2012; Endrizzi et al., 2014). Intermediate-complexity systems result from simplified versions of the physical parameterization schemes with a reduced snowpack layering (Dutra et al., 2010, 2011; Boone and Etchevers, 2001). One of the main issues is the trade-off between model complexity, input data requirements and the computational demand. Despite progressive improvements, several flaws endure mainly due to uncertainty in parameterizations, errors affecting both meteorological forcing data and initial conditions and approximations in boundary conditions (Liston and Sturm, 1998; Pan et al., 2003). Moreover, there are several physical factors that make an exhaustive reconstruction of snow dynamics challenging: snow intermittence in space and time, stratification and slow phenomena like metamorphism processes, uncertainty in snowfall evaluation, wind transportation (Winstral and Marks, 2014).

Fortunately, in addition to model simulations, other independent snow-related data sources are available, such as ground-based measurements and remotely-sensed observations (Barrett, 2003), both of which suffer from several limitations, however. Ground-based snow measurements only provide point values, affected by an instrumental bias and subject to distortions due to wind action, local topographic features and vegetation interactions. Although remotely-sensed observations cover extended areas, they supply indirect measurements affected by a usually coarse spatial resolution (passive microwave sensors) and the uncertainty in retrieval algorithms.

Data Assimilation (DA) is an objective methodology to combine these different sources of information to obtain the most likely estimate of snowpack state. Several DA techniques have been developed, which allow to update model simulations as observations become available. These DA schemes are currently used with different degree of complexity: direct insertion (Liston et al., 1999; Rodell and Houser, 2004; Malik et al., 2012), optimal interpolation scheme (Brasnett, 1999; Liston and Hiemstra, 2008), Cressman scheme (Cressman, 1959; Dee et al., 2011; Drusch et al., 2004; Balsamo et al. 2015), nudging method (Stauffer and Seaman, 1990; Boni et al., 2010), Kalman filtering techniques (Kalman, 1960; Gelb, 1974; Miller et al., 1994; Evensen, 1994, 2003), and the Particle Filter scheme (De Freitas et al., 2001; Arulampalam et al., 2002; Moradkhani et al., 2005b; Weerts and El Serafy, 2006). Several studies aimed at investigating the feasibility of implementing DA techniques to consistently update snow model simulations. Generally, the assimilation of snow-related observations proves to succeed in improving the analysis snowpack dynamics, with different performances also depending on the main features of the implemented DA method.

1.2 Motivation and goals

In the framework of snow modelling, most publications dealt with univariate assimilation, namely the assimilation of a single observed variable, and relatively few studies aimed at investigating the simultaneous assimilation of observations for multiple model state variables. However, current research results agree on the superior performance of the multivariate assimilation with respect to the univariate one (Charrois et al. 2016). Furthermore, unlike the atmospheric sciences, where the multivariate DA is well established, most DA applications to terrestrial systems present synthetic case studies, especially when dealing with satellite data (Montzka et al. 2012; Liu et al., 2012).

In light of the promising potential of multivariate DA schemes and the lack of their application using real-world data and/or several types of data in snow modelling, this research intends to investigate the feasibility of a multivariate DA scheme through two of the most widely used sequential ensemble-based DA techniques, the Ensemble Kalman Filter (EnKF) and the Particle Filter (PF). Thus, the following questions are addressed:

1) What are the most constraining limitations in implementing multivariate EnKF- and PF-based schemes in the framework of snow modelling and how to overcome them?
2) How do these sequential ensemble-based DA techniques succeed in consistently updating the snowpack system state in a multivariate application?
3) What are the differences in the effectiveness of the two selected DA techniques and the main features of the resulting snow-related analysis simulations?

This thesis aims to answer and discuss these scientific questions through the study of a system consisting of a newly developed multilayer energy- and mass-balance snowpack model coupled with a multivariate DA scheme allowing to test both EnKF- and PF techniques.

The system is evaluated at three Alpine experimental sites in both DA configurations to assess its performances in assimilating snow ground-based measurements under changing local conditions. More generally, this research is intended to investigate the feasibility of a multivariate DA scheme for snow modelling, with the aim of supporting the development of a robust and reliable snow module suited to be implemented within an operational chain for hydrological forecasting in mountain regions.

1.3 Thesis outline

After introducing the context of this research, its motivation and main purposes, this thesis consists of eight main chapters.

Chapter 2 extensively introduces the snow hydrology, with a focus on the spatial and temporal variability of snow-related variables and the impact of the main ruling meteorological forcings on snowpack dynamics. The snow modelling is addressed through an overview on the parameterization laws of the main physical snowpack processes and a critical review of the state of the art up to the more recent studies. A comprehensive survey of in-situ measurements and remotely-sensed observations of snow-related variables is also presented.

Chapter 3 presents the Alpine case studies and describes the snow and meteorological datasets supplied by the analysed measurement stations. After the meteorological characterization of the experimental sites, the pre-processing and quality check of the observational data are explained.

In Chapter 4 the multilayer snowpack model is described into the details of the physical representation of snowpack and the calibration procedure. Snow energy- and mass-related simulations are widely analysed and discussed by assessing their accuracy against the available observational data.

With the Chapter 5 starts the hub of this research, namely the discussion on the DA techniques. A preliminary critical review of the state of art on current applications in the framework of snow modelling precedes the detailed description of the theoretical formulations of Kalman and Particle filtering techniques. Lastly, the experimental setup of this study is introduced by discussing the observational uncertainty and defining the evaluation metrics used to assess the system performances.

By referring to Piazzi et al. 2018a, Chapter 6 extensively describes the multivariate EnKF-based DA scheme by explaining in detail its development, which aimed at meeting the main assumptions of this technique and limiting the impact of the strong system nonlinearities on the updating procedure. Firstly, the approach adopted for the generation of the ensemble of model realizations is defined by describing a newly proposed approach. After testing this methodology, the implementation of the multivariate EnKF scheme is then discussed and the resulting analysis predictions are deeply evaluated. Finally, several experiments are shown with the aim of investigating the system sensitivity to the assimilation frequency, the ensemble size and the impact of assimilating different observations.

The implementation of the multivariate PF scheme is discussed in Chapter 7, following Piazzi et al. (2018b). The main issue of the impoverishment of the particles sample is widely discussed, which turns out to be of even more critical importance in such a multivariate application. The impact of perturbing the meteorological forcing data, as well as the benefit of resampling key model parameters are assessed in terms of filter effectiveness in updating the model state variables. With the aim of mitigating the system sensitivity to the frequency of the assimilated observations, the potential of introducing an additional snow density model is evaluated by assimilating its snow mass-related estimates.

Chapter 8 deals with the comparative study between the performances of the two analysed DA techniques. After assessing the filters effectiveness in reducing the model error affecting the snowpack simulations, the impact of the filters updates on the system physical consistency is investigated by evaluating the scale of the discontinuities characterizing the trend of the analysis predictions. Lastly, the temporal persistence of the filters updates between two following assimilation time steps is assessed.

The last Chapter 9 provides a global synthesis of this research, highlighting the main contributions and the implications of the results. In the end, some ideas for future perspectives and studies are suggested.

CHAPTER 2
Snow hydrology

==

2.1 The hydrological role of snow

Snow-dominated areas play a distinctive role in water supply (Vivoroli et al., 2007). Snowpack dynamics strongly impact seasonal water resources through a temporal redistribution of winter precipitation to spring and summer runoff (Viviroli et al., 2003; Viviroli and Weingartner, 2004).

During winter months, when most precipitation occurs, sizeable volume of water is stored within the snowpack (Lòpez-Moreno et al., 2013a). Nevertheless, the precipitation phase strongly depends on the local elevation and air temperature (Lòpez-Moreno and Nogués-Bravo, 2005). The highest elevation areas mostly receive solid precipitation, whereas the mid-elevation ones have a mixed precipitation regime (Surfleet and Tullos, 2013; Guan et al. 2016). In spring and summer, when precipitation is otherwise scarce, the snowmelt significantly contributes to the total discharge (Verbunt et al., 2003; Zappa et al. 2003; Clark and Hay, 2004).

Glaciers runoff provides a smoothing effect of the interannual variability of summer flows, when the more variable precipitation regime results in irregular runoff (Hock et al., 2005; Zappa and

Kan, 2007; Koboltschnig and Schöner, 2010). Indeed, during the dry period, characterized by high air temperatures, they release the water volume stored in winter months (Casassa et al., 2009). However, a quantitative distinction between snow and glacier meltwater is challenging, even though snow contribution from lower elevations generally precedes the glacial one from higher altitudes (Weingartner and Aschwanden, 1992; Viviroli et al., 2011).

Since meltwater is a massive source of surface water and groundwater recharge (Dettinger, 2014), the water management in mountainous regions is seasonally planned according to the accumulation and melt dynamics of snowpack (Viviroli et al., 2011). Because about one-sixth of the world's population lives in snow-dominated areas (Barnett et al., 2005), a reliable knowledge of the location, extent and quality of the snow water resource is ruling for several real-time services and applications, such as irrigation, agricultural production, water supply, flood prevention, hydropower production.

Furthermore, the seasonal presence of snow strongly impacts the surface energy balance, not only locally, but also at larger scale. Because of its low thermal conductivity, a snowpack produces an insulating effect over the underlying soil, whose temperature variability is severely reduced towards a stable condition (Zhang 2005). Moreover, the high snow albedo entails a remarkable reduction of shortwave radiation absorption, with a resulting lowering of near surface air temperature.

From a hydrological point of view, the most interesting snow variable is the Snow Water Equivalent (SWE), which is an important hydrologic measure as it indicates the actual amount of water stored in a snowpack (DeWalle and Rango, 2008). SWE predictions are a useful tool for hydrological forecasting, since they allow to reliably predict the meltwater that the complete melting of the snowpack would release and the resulting impact on the total discharge.

2.2 Spatial and temporal variability of snow-related variables

Snow cover variability is mainly driven by the meteorological forcing (Bormann et al., 2013; Luce et al., 2014). The precipitation regime, the average air temperature and the shortwave radiation are the most ruling climate forcings (Lòpez-Moreno and Nogués-Bravo, 2005). Jointly, the topography strongly affects the snow spatial distribution (Rice et al., 2011; Molotch and Meromy, 2014; Revuelto et al., 2014). Local elevation, slope and aspect are the most explanatory variables controlling the snow cover persistence. However, the definition of a proper set of predictors well explaining the snow distribution is hindered by the local processes occurring at the small scale (Molotch et al., 2005; Zheng et al., 2016). The definition of the topographic control is made even more difficult by the presence of vegetation impacting the intensities of the meteorological forcings (e.g. wind and incoming solar radiation) (Harpold et al., 2014). Where most of snow accumulation occurs above the tree line, the canopy interception is of secondary importance in the spatial distribution of snowpack (Zheng et al., 2016; Fayad et al., 2017). Nevertheless, in forested areas snow depth can be significantly reduced due to the sublimation or melting of the intercepted snow (Szczypta et al., 2015). Wind-induced erosion and deposition phenomena (e.g. snow drifting) play a primary role in snow redistribution (Gascoin et al., 2013; Vionnet et al., 2014). However, the modelling of the wind-induced snow transport is still challenging due to limiting issues. Firstly, the generation of reliable wind fields over complex topography is taxing. Moreover, snow models are generally unable to well represent the wind snow redistribution, since this is a sub-pixel scale process (Quéno et al., 2016).

An important snow-related variable is the snowpack density, whose state strongly impacts the thermal, mechanical and optical properties of snow layers (Bormann et al., 2013; Sturm et al., 2010). The spatial variability of snow density is mainly driven by the meteorological forcings, including the mean snowfall density, which contributes to the evolution of snowpack density (Svoma, 2011). Seasonal densification of snowpack is ruled by snow metamorphisms, compaction, and melt-refreeze events (Bormann et al., 2013). Furthermore, other local factors impact the snow density, such as slope, vegetation cover and wind exposure, whose intensity has prominent effects on snow densification (e.g. growth of surface hoard) (Stössel et al., 2010). Even though snow density has a lower spatial variability with respect to snow depth (Lòpez-Moreno et al. 2013b), the regional spatial and temporal variability in snow densification rate can be sizeable (Sturm et al., 2010), whereas the interannual variability is generally considered negligible. The snowpack stratification entails a high point vertical variability of snow density (Bormann et al., 2013). Indeed, snow layering can result in sharp density changes along the snowpack thickness according to the occurred snowfall events and previous climate conditions.

2.2.1 Climate forcing to the snowpack

Meteorological forcings are one of the main control factors affecting spatial and temporal variability of snow cover. Snowpack dynamics are mostly ruled by the precipitation regime and the average air temperature during the accumulation period (Lòpez-Moreno and Nogués-Bravo, 2005), which define snowfalls frequency and intensity. The melting period is forced by the incoming radiation and heat fluxes exchanged with both atmosphere and the underlying soil (Herrero et al., 2009). The impact of wind-induced phenomena is generally prominent throughout the whole snow season (Gascoin et al., 2013).

In Mediterranean mountain regions, more than 80% of the annual precipitation occurs during winter months (November to March) (Fayad et al., 2017), and they generally receive more precipitation than surrounding lowlands due to their orographic elevation (Derin et al., 2016). However, both the complexity of atmospheric processes at large scale (Lunquist et al., 2015) and the effect of local topography at finer scale (Lòpez-Moreno et al., 2015) hinder a reliable assessment of the temporal distribution of precipitation and its phase (Derin et al., 2016). Moreover, the widespread lack of observational data, especially at high elevations, and the tendency of gauges to underestimate the precipitation are further limiting factors. A poor knowledge of wind patterns does not allow to properly correct the precipitation-gauge undercatch (Sevruk et al., 1991).

Since rain-on-snow events strongly impact the snowpack energy balance and the snowmelt rate, due to the supply of very high advection heat flux (Molotch and Meromy, 2014), a reliable knowledge of the precipitation phase is of crucial importance (Surfleet and Tullos, 2013). The air temperature is the most ruling factor determining the precipitation phase, together with the relative air humidity (Froidurot et al., 2014). Similarly to the other meteorological forcing variables, the lack of automatic weather stations (AWS) in remote and high-elevation areas entails a certain uncertainty affecting the air temperature monitoring (Raleigh et el., 2016).

Nevertheless, in-situ measurements of air temperature are generally the most widely available data and much less biased with respect to precipitation data.

Most of the snowmelt energy is supplied by the net radiative flux (Lòpez-Moreno et al., 2013b), whose impact significantly varies over time and in space. In the absence of in-situ sensors, the incoming radiative term can be estimated through empirical relationships based on the surface air temperature and relative humidity (Lundquist et al., 2013). However, since the incoming radiation varies with elevation, local topography (e.g. mean aspect, slope orientation) and forest cover, its indirect retrieval can lead to a sizeable overestimation of snowmelt rates (Hinkelman et al., 2015).

The assessment of the heat transfers occurring within the snowpack allows to better evaluate the timing of snowmelt. Sensible and latent heat exchanges are mainly driven by surface air temperature, relative humidity and wind speed. Because most of these meteorological variables have a high spatial variability over complex topography and measurements of wind speed and humidity are often lacking, a reliable estimate of their contribution to snowmelt is challenging. The net turbulent flux strongly impacts the snowmelt throughout the whole snow season with a tendency to increase late in the winter. Whenever rain-on-snow events occur, the contribution of the turbulent fluxes to melt energy is even more prominent due to the advection heat flux. (Mazurkiewicz et al., 2008).

2.3 Snow modelling

When modelling hydrological processes in snow-dominated catchments the quality of predictions deeply depends on how the model succeeds in catching snow dynamics (Wood et al., 2016). Thus, a growing effort is aimed at enhancing the physical representation of snowpack in hydrologic models. Despite progressive improvements, several flaws endure mainly due the uncertainty in parameterizations, errors affecting both meteorological forcing data and initial conditions and approximations in boundary conditions (Liston and Sturm 1998; Pan et al. 2003). Moreover, there are several physical factors that hinder an exhaustive reconstruction of snow dynamics: snow intermittence in space and time, stratification and slow phenomena like metamorphism processes, uncertainty in snowfall evaluation, wind transportation (Winstral and Marks, 2014).

2.3.1 Parameterization of snow physics

The quality of model simulations strongly depends on the representativeness of the parameterization of the main physical processes occurring within the snowpack. Several parameterizations are commonly used to describe each process, ranging from empirical relations to physically-based laws. At a lower level of complexity, some processes can be represented by a constant or simply neglected.

Essery et al. (2013) developed a snow multi-scheme model which combines a range of existing parameterizations of different complexity for the representation of each dominant process. The analysis of the large ensemble of predictions resulting from different model configurations revealed that the simulations using prognostic equations for snow density and albedo generally allow the most consistent performance.

More recently, Layafasse et al. (2017) investigated the uncertainty affecting physically-based multilayer snow models through a multiphysical ensemble system allowing to implement different representation of the main processes.

Commonly, to solve the mass and energy balance equations, models require parameterizations of processes defining surface albedo, thermal conductivity, liquid water content, density of fresh and compacted snow, and turbulent fluxes. Some of the most important processes parameterizations are explained below.

__Fresh snow density__

The density of newly deposited snow mainly depends on the size, shape and packing of the falling crystals, which are defined by the air temperature and humidity during their growth and the wind conditions during their deposition (Essery et al., 2013). Several empirical laws can be used to estimate the density of falling snow (ρ_n), which can rely on only air temperature data (Eq. 2.1; Anderson, 1976; Oleson et al., 2004) or on simultaneous measurements of wind speed $(V, [ms^{-1}])$ and air temperature $(T_a, [°C])$ (Eq. 2.2, Vionnet et al., 2012; Eq. 2.3 Schmucki et al., 2014).

$$\rho_n = \rho_{min} + max\left[a_\rho\left(T_a + b_\rho\right)^{3/2}, 0\right] \qquad [2.1]$$

$$\rho_n = max\left[c_\rho + d_\rho T_a + e_\rho V^{1/2},\ \rho_{min}\right] \qquad [2.2]$$

$$\begin{cases} \log_{10}\rho_n = f_\rho + g_\rho T_a + h_\rho + i_\rho \sin^{-1}\left(\sqrt{j_\rho}\right) + k_\rho \log_{10}(max[V,2]) \ \ if\ T \geq 14°C \\ \log_{10}\rho_n = f_\rho + g_\rho T_a + i_\rho \sin^{-1}\left(\sqrt{j_\rho}\right) + k_\rho \log_{10}(max[V,2]) \ \ if\ T < 14°C \end{cases} \qquad [2.3]$$

The parameters of the three laws are given in Table 2.1. Some models assume a fixed density for fresh snow, generally set equal to 100 kg m^3 (lower densities of 50 or 80 kg m^3 are also used) (Douville et al., 1995).

Equation	**Parameters**
[2.1]	$a_\rho = 1.7\ \mathrm{K}^{-1}$; $b_\rho = 15\ \mathrm{K}$; $\rho_{min} = 50\ \mathrm{kgm}^{-3}$
[2.2]	$c_\rho = 109\ \mathrm{kgm}^{-3}$; $d_\rho = 6\ \mathrm{kgm}^{-3}\mathrm{K}^{-1}$; $e_\rho = 26\ \mathrm{kgm}^{-7/2}\mathrm{s}^{1/2}$; $\rho_{min} = 50\ \mathrm{kgm}^{-3}$
[2.3]	$f_\rho = 3.28$; $g_\rho = 0.03\ \mathrm{K}^{-1}$; $h_\rho = -0.36$; $i_\rho = -0.75$; $j_\rho = 0.8$; $k_\rho = 0.3$

Table 2.1: *Parameter values for fresh snow density parameterizations.*

Whenever a snowfall event occurs, the density of a snow layer having initial density ρ_0 and mass M_s is updated in order to take into account the amount of snowfall (S_f):

$$\rho_s = \frac{M_s + S_f}{M_s/\rho_0 + S_f/\rho_n} \qquad [2.4]$$

Snow compaction

When modelling snowpack dynamics, the snow density is a control variable allowing to estimate the snow mass, which is generally a model prognostic variable, from the snow depth, which is instead one of the most widely measured variable, and vice versa.

Snow compaction entails an increase in snowpack density over time due to the settling of grains, which gradually turn into more rounded forms due to both the weight of the overlying snow and the refreezing of meltwater.

Some models neglect the compaction process by considering a constant value of snowpack density (e.g. equal to 250 kg m^3; Cox et al., 1999). An empirical parameterization of snow compaction generally relies on the assumption that the snow density increases at a rate proportional to the difference between the current density and a maximum density value (ρ_{max}), according to an empirically defined compaction time scale (τ_ρ) (Eq. 2.5; Verseghy, 1991).

The parameterization proposed by Anderson (1976) allows to consider both the two main processes ruling the changes in snowpack density, namely the compaction due to the weight of the overlying snow and metamorphic effects acting on the snow microstructure (Kojima, 1967).

According to this physically-based parameterization, the fresh low density is subject to a rapid settling process, while a slower densification occurs under the load resisted by the compactive viscosity (η) (Eq. 2.6; Boone, 2002; Kojima, 1967).

$$\frac{d\rho_s}{dt} = \tau_\rho{}^{-1}(\rho_{max} - \rho_s) \qquad [2.5]$$

$$\frac{1}{\rho_s}\frac{d\rho_s}{dt} = \frac{M_s}{\eta} + c_1 exp[-c_2(T_{melt} - T_s) - c_3 \max(0, \rho_s - \rho_0)]$$

$$\begin{cases} \dfrac{1}{\rho_s}\dfrac{d\rho_s}{dt} = \dfrac{M_s}{\eta} + c_1 exp[-c_2(T_{melt} - T_s) - c_3 \max(0, \rho_s - \rho_0)] \\ \eta = \eta_0 \exp[c_4(T_{melt} - T_s) + c_5\rho_s] \end{cases} \qquad [2.6]$$

The parameters values are shown in the Table 2.2.

Equation	Parameters
[2.5]	$\rho_{max} = 300\ \text{kgm}^{-3}$; $\tau_\rho = 3.6 \cdot 10^5\ \text{s}$
[2.6]	$c_1 = 2.8 \cdot 10^{-6}\text{s}^{-1}$; $c_2 = 0.042\ \text{K}^{-1}$; $c_3 = 0.046\ \text{m}^3\text{kg}^{-1}$; $c_4 = 0.081\ \text{K}^{-1}$; $c_5 = 0.018\ \text{m}^3\text{kg}^{-1}$; $\rho_0 = 150\ \text{kg m}^{-3}$; $\eta_0 = 3.7 \cdot 10^7\ \text{kg m}^{-1}\ \text{s}^{-1}$

Table 2.2: *Parameter values for snow compaction parameterizations.*

A simplified version of the Eq. 2.6 can be derived by neglecting the c_1 term. Moreover, different values for the viscosity coefficient η_0 can be used, generally approximately ranging from $3.6 \cdot 10^6$ up to $3.7 \cdot 10^7$ (Essery et al., 2013). Nevertheless, it is noteworthy that the complex dependence of the compaction velocity on the snow microstructure hinders its parameterization (Lehning et al., 2002).

Snow albedo

The high fraction of solar radiation reflected from snow surface mainly depends on the grain structure and snow depth. Other local factors contribute to the reflection of shortwave radiation, namely the wavelength and the incidence angle (Lafaysse et al., 2017). An accurate estimate of the surface albedo is of critical importance since this variable strongly affects the snowpack energy balance with a resulting significant impact on the timing of snowmelt. Snow albedo can be simply diagnosed as a function of the snowpack surface temperature. According to this approach, the albedo is typically made to linearly decrease from a maximum value below a critical temperature ($\mathrm{T_c}$) to a minimum at the melting point ($\mathrm{T_{melt}}$) (Eq. 2.7; Cox et al., 1999). At a higher level of complexity, the surface albedo is predicted as prognostic variable, whose temporal evolution can be simulated according different parameterizations.

An empirical parameterization relies on a linear decay of the albedo over time under cold snow conditions and an exponential decay in the presence of melting snow, with a consistent albedo update whenever a snowfall event occurs, (Eq. 2.8; Douville et al., 1995; Boone, 2002; Dutra et al., 2010). The physical parameterization of the surface albedo introduced by Wiscombe and Warren (1980) (Eq., 2.9) allows to estimate both albedos for direct-beam and diffuse radiations in visible and near-infrared wavebands (Marshall and Warren, 1987; Marks et al., 1992; Marshall and Oglesby, 1994; Oleson et al., 2010).

$$\alpha_s = \alpha_{max} + (\alpha_{min} - \alpha_{max}) \max\left(\frac{\mathrm{T_s} - \mathrm{T_c}}{\mathrm{T_{melt}} - \mathrm{T_c}}, 0\right) \tag*{[2.7]}$$

$$\left\{\begin{array}{c}
\underline{\text{ALBEDO FOR COLD SNOW}} \\
\alpha_s(t+\delta t) = \alpha_s(t) - {\tau_\alpha}^{-1}\delta t \\
\underline{\text{ALBEDO FOR MELTING SNOW}} \\
\alpha_s(t+\delta t) = [\alpha_s(t) - \alpha_{min}]\exp(-{\tau_{melt}}^{-1}\delta t) + \alpha_{min} \\
\underline{\text{ALBEDO UPDATE AFTER SNOWFALL EVENT}} \\
\delta\alpha_s = (\alpha_{max} - \alpha_s)\dfrac{S_f\,\delta t}{S_0}
\end{array}\right. \tag*{[2.8]}$$

$$\left\{\begin{array}{c}
\underline{\text{ALBEDOS FOR DIRECT RADIATION}} \\
\alpha_{dir,VIS|NIR=}\,\alpha_{dif,VIS|NIR} + a_\Psi f(\Psi)\big(1 - \alpha_{dif,VIS|NIR}\big) \\
\underline{\text{ALBEDOS FOR DIFFUSIVE RADIATION}} \\
\alpha_{dif,VIS|NIR} = \big(1 - C_{VIS|NIR}\,F_{age}\big)\,\alpha_{0,VIS|NIR} \\
\underline{\text{SNOW AGE FACTOR}} \\
F_{age} = \dfrac{\tau_s}{1+\tau_s} \\
\underline{\text{SNOW AGE}} \\
\tau_s(t+\delta t) = [\tau_s(t) + (r_1 + r_2 + r_3)\,{\tau_0}^{-1}\,\delta t]\left(1 - \dfrac{S_f\,\delta t}{S_0}\right) \\
r_1 = exp\left[T_\alpha\left(\dfrac{1}{T_{melt}} - \dfrac{1}{T_s}\right)\right] \\
f(\Psi) = max\left[\dfrac{1-2\Psi}{1+b_\Psi}, 0\right]
\end{array}\right. \tag*{[2.9]}$$

The parameterizations coefficients are listed in the Table 2.3. As show in Eq. 2.8 and 2.9, both the empirical and physical parameterizations require snowfall and snow temperature as inputs.

More recently, Flanner and Zender (2006) developed a physically-based model applying the main principles of microphysics to predict the evolution of surface albedo.

Equation	Parameters
[2.7]	$\alpha_{max} = 0.8$; $\alpha_{min} = 0.62$; $T_c = (\mathrm{T_{melt}} - 2\mathrm{K})$
[2.8]	$\alpha_{max} = 0.85$; $\alpha_{min} = 0.5$; $S_0 = 10\ kg\,\mathrm{m}^{-2}$; $\tau_\alpha = 10^7\mathrm{s}$; $\tau_m = 3.6 \cdot 10^5\mathrm{s}$
[2.9]	$\alpha_{0,VIS} = 0.95$; $\alpha_{0,NIR} = 0.65$; $a_\Psi = 0.4$; $b_\Psi = 2$; $C_{VIS} = 0.2$; $C_{NIR} = 0.5$; $r_2 = r_1^{10}$; $r_3 = 0.3$; $S_0 = 10\ kg\,\mathrm{m}^{-2}$; $T_\alpha = 5000\ K$; $\tau_0 = 10^6$ s

Table 2.3: *Parameter values for snow albedo parameterizations.*

Snowpack thermal conductivity

Snow thermal conductivity (λ_s) mostly depends on snowpack density (ρ_s) (Calonne et al., 2012). The heat flux (Q_T) within snowpack having a vertical temperature gradient can be evaluated as a function of the snow thermal conductivity (Eq. 2.10).

$$Q_T = \lambda_s \frac{dT_s}{dz} \qquad [2.10]$$

While more complex physically-based models link the snow conductivity to the microstructural properties (Bartelt and Lehning, 2002), generally this thermal quantity is parameterized as a quadratic or power function of snow density (Eq. 2.11; Oleson et al., 2010) (Eq. 2.12; Yen, 1981; Douville et al., 1995; Vionnet et al., 2012).

$$\lambda_s = \lambda_a + \left(a_\lambda \rho_s + b_\lambda {\rho_s}^2\right)(\lambda_i - \lambda_a) \qquad [2.11]$$

$$\lambda_s = c_\lambda \left(\frac{\rho_s}{\rho_{water}}\right)^{n_\lambda} \qquad [2.12]$$

Equation	Parameters
[2.11]	$a_\lambda = 7.75 \cdot 10^{-5}\mathrm{m^3 kg^{-1}}$; $b_\lambda = 1.105 \cdot 10^{-6}\ \mathrm{m^6\ kg^{-2}}$
[2.12]	$c_\lambda = 2.22\ W\ \mathrm{m^{-1}\ K^{-1}}$; $n_\lambda = 1.88$

Table 2.4: *Parameter values for snow thermal conductivity parameterizations.*

Fixed snow thermal conductivity is also used (Cox et al., 1999; Smirnova et al., 2000) with a value ranging around 0.265 W $\mathrm{m^{-1}\ K^{-1}}$.

Turbulent fluxes

Turbulent heat fluxes, namely latent heat flux (LE) and sensible heat flux (H), are commonly approximated through a first-order closure:

$$H = c_a \rho_a C_H V \left(T_{sup} - T_a\right) \qquad [2.13]$$

$$LE = L_H \rho_a C_H V (q_{sup} - q_a) \qquad [2.14]$$

where c_a and ρ_a are specific heat capacity and density of air, respectively, L_H is the latent heat, and C_H is the exchange coefficient. This latter coefficient depends on atmospheric stratification, the surface roughness length for momentum (z_0) and a scalar surface roughness length (z_{0h}). Even though values of z_0 and z_{0h} are flow-dependent, they are generally assumed as constant parameters. The exchange coefficient can be estimated through the Monin-Obukhov similarity theory. However, the implementation of this approach is challenging mainly due to the computational cost required to iteratively solve unstable conditions and the surface decoupling in stable conditions (Louis, 1979). An effective alternative relies on the parameterization of the exchange coefficient as a function of the Richardson number (Ri_B) and the exchange coefficient for neutral stratification (C_{HN}) :

$$C_H = f(Ri_B)\, C_{HN} \qquad [2.15]$$

$$Ri_B = \frac{g z_V \left(T_a - T_{sup}\right)}{T_a\, V^2} \qquad [2.16]$$

$$C_{HN} = k^2 \left[\ln\left(\frac{z_V}{z_0}\right)\right]^{-1} \left[\ln\left(\frac{z_T}{z_{0h}}\right)\right]^{-1} \qquad [2.17]$$

where z_V and z_T are the measurement elevations of wind speed (generally 10 m) and air temperature and humidity (usually 2 m), respectively.

The iterative solution can be approximated through an analytical function:

$$\begin{cases} \underline{\text{UNSTABLE CASE } (\text{Ri}_\text{B} < 0)} \\ f(Ri_B) = 1 - \dfrac{3\, c\, Ri_B}{1 + 3\, c^2\, C_{HN}(-Ri_B z_V / z_0)^{1/2}} \\ \underline{\text{STABLE CASE } (\text{Ri}_\text{B} > 0)} \\ f(Ri_B) = \left[1 + \dfrac{2\, c\, Ri_B}{(1 + Ri_B)^{1/2}}\right]^{-1} \end{cases} \qquad [2.18]$$

where c is set equal to 5 (Louis, 1979).

Snowpack liquid water content

The liquid water content within the snowpack plays an important role, since it strongly impacts the snow metamorphism, the heat exchanges, the compaction dynamics and the mechanical stability. Nevertheless, its high horizontal variability makes this variable hard to model and measure. Even though the rapid gravitational drainage of liquid water from highly permeable snow benefits from the presence of preferential paths (Albert et al., 1999), the capillary tension retains some water volume and hinders the flow among snow layers with different texture (Hirashima et al., 2010). The liquid content can be expressed as a volumetric water content or a water saturation depending on the snow porosity (Essery et al., 2013).

Generally, the common formulation for the liquid water percolation within the snowpack calls for a conceptual bucket approach considering the snow layers as stacked water reservoirs with a homogenous volumetric water content (Lafaysse et al., 2017). When the stored water exceeds the maximum liquid water-holding capacity, the excess water drains towards the underlying layer. Several approaches allow to define the volumetric capacity of each layer (Boone and Etchevers, 2001; Oleson et al., 2004). Many models neglect the storage of liquid water within the snowpack (Douville et al., 1995; Cox et al., 1999).

2.3.2 A critical review of the state of the art

Several snowpack models have been developed with highly variable degree of complexity, mainly depending on their target application, such as hydrological forecasting, avalanche prediction, climate modelling, and the availability of computational resources and data.

Boone and Etchevers (2001) identified three main categories of snow modelling schemes. The first class consists of simple force-restore schemes of composite snow-soil systems (Douville et al. 1995; Yang et al. 1997) and single explicit snow layer schemes (Verseghy 1991; Slater et al. 1998). At a higher level of complexity are the detailed internal-snow-process schemes (Anderson 1976; Brun et al. 1989; Jordan 1991), which simulate the evolution of snow microstructure and snowpack stratification and require a large computational cost. An intermediate category gathers systems resulting from simplified versions of the physical parameterization schemes with a reduced snowpack layering (Lynch-Stieglitz 1994; Sun et al. 1999).

HTESSEL (Hydrology Tiled ECMWF Scheme of Surface Exchanges over Land) (Viterbo and Beljaars 1995; Van Den Hurk et al. 2000; Balsamo et al. 2009; Dutra et al., 2010) is a monolayer snowpack model based on energy and mass balances with a diagnostic representation of snow liquid water. Dutra et al. (2011) performed a multi-layer version of HTESSEL snow scheme through the introduction of a prognostic approach for the modelling of snow liquid content.

The multilayer snow module implemented in the physically-based distributed hydrological model GEOtop (Zanotti et al., 2004; Rigon et al., 2006; Endrizzi et al., 2014) allows to consider the effect of the local topography thanks to a discretization of the landscape based on digital elevation data. This approach enables to accurately evaluate the radiative balance and thus the surface temperature.

Boone and Etchevers (2001) performed an intercomparison analysis among three snow models of increasing complexity. ISBA-FR single snow layer scheme of the composite Interactions between Soil, Biosphere, and Atmosphere (ISBA) force–restore model (Douville et al. 1995).

The highly detailed CROCUS multilayer snow model (Brun et al. 1989, 1992; Vionnet et al. 2012) simulates the physical and microstructural evolution of snowpack and its stratification (up to 50 layers) through a dynamic layering scheme. The coupled ISBA–CROCUS model (ISBA-ES) consists of a three-layers explicit snow-scheme relying on detailed physical parameterizations, internal-snow-process schemes (Anderson, 1976), and a relatively fine vertical resolution.

Among the most sophisticated models, the snow multilayer model SNOWPACK (Bartelt and Lehning, 2002; Lehning et al., 2002) allows a complete depiction of snow microstructure and metamorphism. The model supplies an accurate physical description of snowpack, where each layer is defined through its macro- and microscopic properties (arbitrary number of snow layers). By employing a deforming material Lagrangian coordinate system, a dynamic snowpack mesh enables considering wind erosion and snowdrift, transport and refreezing of meltwater, runoff, water vapor sublimation and snowfalls by adding of removing finite elements in the existing grid.

Many studies aimed at assessing performance of models with different levels of detail and parameterizations with the main purpose of relating differences in model behaviour to differences in model structure (Essery et al., 1999; Boone and Etchevers, 2001; Feng et al., 2008).

Recently, several intercomparison project contrasted different snow models with the purpose of analysing the impact of schemes complexity on the resulting simulations: SnowMIP (Essery and Etchevers, 2004; Etchevers et al., 2004), SnowMIP2 (Rutter et al., 2009), PILPS2d (Schlosser et al., 2000; Slater et al., 2001), PILPS2e (Bowling et al., 2003; Nijssen et al., 2003), Rhône-AGG (Boone et al., 2004). Generally, the comparison results confirmed that models greatly differ in predicting snow accumulation and ablation dynamics. The uncertainty affecting the simulations turns out to be higher whenever snow melt occurs, during spring season, and in case of mid-winter melt events. Almost all the studies agree on stating that no overall optimal modelling scheme can be identified, since the quality of the predictions strictly depends on their application, and the topographic, meteorological and vegetation features of the modelling domain (Rutter et al., 2009). Furthermore, it is noteworthy that an increasing model complexity does not ensure an improvement of simulations.

Fortunately, in addition to model simulations, other independent snow-related data sources are available, namely ground-based measurements and remotely-sensed observations (Barrett, 2003), which are discussed in the following Sections.

2.4 Snowpack in-situ observations

In-situ snow observational data can be supplied by AWS or through manual measurements. However, since ground-based observations only provide point values, they are site-dependent and they do not manage to well catch the spatial variability of the snowpack due to the heterogeneity of both climate and terrain with respect to the network density (Raleigh et al., 2016). In addition to the uncertainty about their spatial representativeness (Lòpez-Moreno et al., 2013a), field measurements are generally affected by an instrumental error (Lundquist et al., 2015) and subjected to distortions due to wind action, local topographic features and vegetation interactions. Nevertheless, the main strength of the AWS is the supply of continuous observations allowing to retrieve the temporal evolution of the snowpack.

The snow height is the most widely available observed variable, which is typically measured with a calibrated snow probe. Under the same local conditions, snowpack depth is generally easier to estimate with respect to the snow density, requiring an elaborate field-work (Sturm et al., 2010; Lòpez-Moreno et al., 2011). As previously explained, because snow density has a lower variability than snow depth (Lòpez-Moreno et al., 2013b), generally fewer measurements are needed.

However, collecting in-situ measures at large scales is challenging, since the variability and heterogeneity of processes in snow-dominated areas are faced with a lack of instrumental records, especially for steeps slopes and high-elevation areas, which are usually not easily accessible. Viviroli et al. (2011) state that generally the gauging network is representative for intermediate altitudes, but its representativeness gradually decreases with the increasing altitude. A general lack of observational data is even getting worse since existing monitoring networks face a tendency for reduction in numbers due to the high operating cost of measuring stations in remote mountain areas with harsh environmental conditions (Viviroli et al., 2011).

At regional scale, airborne and terrestrial Lidar now enable snow depths measurements with a centimetric accuracy. Nevertheless, these techniques are costly and have a low temporal resolution (seasonal scale). A terrestrial time-lapse camera is a cost-effective device to monitor the snow cover variability in space and time, even though its use is restricted to limited spatial scales (less than 1 km^2) (Revuelto et al., 2014; Arslan et al., 2017).

Snow density observations are somewhat limited even in well studied regions (Jonas et al., 2009), and often completely absent in less monitored locations. Ground-based SWE point sample (e.g. from snow pillows for SWE measurements) provides a reliable measure of this hydrological quantity. However, because direct SWE observations are not widely available, a good proxy can be retrieved by multiplying the snow height by the density. Molotch (2009) highlighted the need and high value of more detailed and extensive field monitoring of SWE. Likewise, Viviroli et al. (2011) stressed the important and necessary task of overcoming the lack of observational data, especially at high altitudes, in order to better understand the processes occurring in mountainous areas.

2.5 Snow remote sensing

Because of the difficulties in obtaining ground measurements over mountain regions, remote sensing represents an important tool for monitoring snow properties at larger scales and dealing with the lack of in-situ observational data over high elevation areas. The interactions between snow cover and electromagnetic radiation of different frequencies allow to discern snow cover from other terrestrial surfaces using satellite observations based on different active and passive techniques (Nolin, 2010). Snow cover can be detected through two types of sensors relying on (1) a combination of the visible and infrared, or (2) microwave, portions of the electromagnetic spectrum (Hall et al., 2005; Scherer et al., 2005; Schmugge et al., 2002). These methods are limited by several factors, such as clouds, forest cover fraction, terrain heterogeneity and precipitation (Frei et al., 2012).

2.5.1 Visible and near-infrared

Under specific conditions (e.g. absence of cloudiness), the snow cover detection (i.e. presence or absence of snow) is relatively straightforward through visible observations because of the high albedo of snow (up to 80% or more in the visible part of the electromagnetic spectrum) with respect to most land surfaces. Since the visible imagery captures the sunlight scattered back to the satellite, one of the main issues of the visible imagery is the lack of sufficient illumination (e.g. night-time). The presence of cloud cover hinders the detection of snow cover, as well. Indeed, because a sizeable portion of visible radiation is reflected by clouds, any visible radiative information about the surface is prevented from reaching the sensor. Thus, a cloud removal algorithm is needed to generate meaningful snow products (Gascoin et al. 2015). Moreover, because the albedo of clouds and snow is often similar, the discrimination between cloud- and snow-covered surfaces can be challenging. However, near-infrared bands enable to distinguish between snow and most clouds because the near-infrared reflectance of most clouds is high while the snow one is lower (Frei et al., 2012). Also the vegetation can obstruct visible and infrared information about snow. Indeed, forest canopies protruding above the snowpack reduce the surface albedo (Robinson and Kukla, 1985) and partially or completely obscure the underlying surface, making it difficult to the snow detection (Nolin, 2004; Derksen, 2008). Lastly, surface heterogeneity can affect the interpretation of visible and infrared imagery. For instance, the presence of glaciers may contribute to the overestimation of snow covered area.

Several satellite sensors are currently used to detect snow cover from multispectral imagery.

The NASA Moderate Resolution Imaging Spectroradiometer (MODIS) was launched in 1999 and it flies on NASA's Earth Observing System (EOS) Terra satellite to provide observations of several geophysical variables, including snow. A near-twin MODIS instrument is also flying on board the Aqua platform, which was launched in 2002. Aqua also hosted the Advanced Microwave Scanning Radiometer – Earth Observing System (AMSR-E) until its failure in October 2011. The MODIS instrument measures radiation in 36 spectral bands, including the visible, near infrared, and infrared parts of the electromagnetic spectrum. A fully-automated algorithm provides a hierarchy of snow products based on MODIS observations, including maps of snow-covered areas (SCA, binary snow/no-snow maps), fractional snow cover area (FSC) (Salomonson and Appel, 2004), and daily snow albedo (Klein and Stroeve, 2002) at a good spatial resolution (500 m), and frequent coverage (daily at mid to high latitudes) (Hall and Riggs, 2007; Riggs et al., 2006). In addition, an 8-day composite using observations from prior days allows to detect snow cover wherever persistent cloudiness limits the number of days available for surface observations. The SCA product allows the evaluation of the snow cover duration (SCD), snow cover start (SCS), and snow cover melt-out dates (SCM), and the snow coverage in a watershed. The MODIS snow-mapping algorithm uses a normalized difference between MODIS band 4 (5.45–5.65 mm) and 6 (1.628–1.652 lm) and many additional spectral and threshold tests. Indeed, snow covered land typically has a very high reflectance in visible bands and very low reflectance in the shortwave infrared. The Normalized Difference Snow Index (NDSI) reveals the magnitude of this difference, with values greater than 0 typically indicating the presence of at least some snow. It is noteworthy that since some water bodies may also have a high NDSI value, a further criterion on the red reflectance is generally added to remove their detection. A thermal mask is also included to remove erroneous snow detection over locations where the presence of snow is unlikely.

The Visible Infrared Imaging Radiometer Suite (VIIRS) of the National Snow and Ice Data Center (NSIDC) was designed to improve upon the capabilities of the operational Advanced Very High Resolution Radiometer (AVHRR) and provide observation continuity with MODIS. It is a scanning radiometer, which acquires visible and infrared imagery and global radiometric measurements of the land, atmosphere, cryosphere, and oceans. VIIRS currently flies on the

National Oceanic and Atmospheric Administration (NOAA) Suomi National Polar-orbiting Partnership (NPP) spacecraft, a joint mission implemented by NASA and NOAA. VIIRS snow and ice products include Ice Surface Temperature (IST), Sea Ice Characterization and Snow Cover data record, which encompass two products, namely binary and fractional snow cover products. Information on snow cover distribution is retrieved from the radiance data acquired by VIIRS sensor through the NDSI (bands I1 and I3) and a series of quality control screens designed to alleviate likely errors and flag uncertain snow detections (Key et al., 2013). Binary snow cover is derived at 375 m spatial resolution, whereas the spatial resolution of the fractional snow cover product is 750 m. Both products apply to the land surface only under clear-sky conditions. VIIRS scans the entire globe every one to two days. As such, most locations on Earth are imaged at least per day and more frequently where swaths overlap, for example near the poles. The repeat cycle is 16 days (quasi 8-day).

Sentinel-2 (S2) constellation of the European Earth observation program Copernicus is a polar-orbiting, multispectral high-resolution imaging mission for land, ocean and atmospheric monitoring. In order to fulfil revisit and coverage requirements and provide robust datasets for Copernicus Services, the constellation consists of two satellites, Sentinel-2A and Sentinel-2B, which were launched on 23 June 2015 (operational in early 2016) and 7 March 2017, respectively. Multi-Spectral Imager (MSI) instruments provide fine spatial resolution images having 13 bands in total, in which four bands (blue, green, red and NIR) with a spatial resolution of 10 m and six bands (including SWIR band) with a spatial resolution of 20 m. Two S2 data products are currently available. The product types are the Level-1C Top-Of-Atmosphere (TOA) reflectances and Level-2A Bottom-Of-Atmosphere (BOA) reflectences. Snow detection can be straightforwardly retrieved from both the product type through an NDSI-based approach.

A visible- and infrared-based product widely used for large-scale application is the US National Ice Center (NIC) Interactive Multisensor Snow and Ice Mapping System (IMS). IMS mapping of snow extent (SE) basically relies on visible and near infrared imagery, but includes data from different sources. This product continuously undergoes improvements and refinements (Helfrich et al., 2007). Since the late 1990s, daily IMS maps are provided with a spatial resolution of 4 km (previously weekly maps with a spatial resolution of 24 km). The key feature distinguishing IMS from other products is its processing by trained analysts who combine several technological capabilities as well as sources of information. This data processing allows to supply daily estimates of the SE across the globe, regardless of the presence of clouds. The primary purpose of this satellite product is to provide input to atmospheric forecast models. For this purpose, continued product improvements are advantageous. As a record for evaluating long term environmental change, however, the methodological changes result in temporal inconsistencies in the data set that might be difficult to distinguish from actual variations in SE. To maintain product continuity and a viable long-term record, IMS continues to produce a coarse (24 km) resolution version of the data set.

2.5.2 Passive microwave

Since snow grain dimensions are of the same order of magnitude of microwave wavelengths, snow well succeeds in scattering the microwave radiation naturally emitted from the Earth’s surface (Matzler, 1994). The presence of snow can be straightforwardly detected since the microwave emission from a snow-covered surface is lower with respect to a snow-free surface (Hall et al., 2005; Tedesco and Kim, 2006; Grody, 2008). Furthermore, since the amount of scattering is theoretically proportional to the amount of snow grains, microwave sensors allow to estimate the SWE within the snowpack. Unlike visible and infrared, since passive microwave does not depend on the presence of sunlight, snow cover is detected under many (non-precipitating) cloudy conditions.

Nevertheless, snow monitoring through passive microwave sensors is limited by several factors. One of the major limitations is the snowpack status (i.e. dry or wet snow). In the presence of wet snow, microwave emission of liquid water can mask the snow signal and prevent microwave sensors from detecting snow (Frei et al., 2012). Furthermore, because of the relatively weak microwave signal emitted by terrestrial surfaces, microwave sensor footprints are necessarily large (about 25 km) (Dietz et al., 2012; Frei et al., 2012; Dozier et al., 2016). Uncertainties in snow depth and SWE estimates deeply depends on the physical structure of snowpack which significantly varies in space (Chang et al., 1976; Sturm et al., 1995) and time (Langham, 1981) and can alter the snow backscattering and emission. Therefore, a signal change measured by the satellite sensor due to snow metamorphism can be misinterpreted as a signal change due to a change in SWE. Microwave sensors have a limited capability in detecting the SWE in regions with ephemeral or patchy snow cover (Vuyovich et al., 2014), and they are affected by an overall tendency to underestimate SWE during snowfall and melt seasons (Dozier et al., 2016), mainly ascribable to the high scattering in mountain regions due to relief (Li et al., 2012). Also the vegetation, which emits microwave radiation, can hinder the snow detection (Tedesco et al., 2005). Furthermore, when snowpack reaches a certain critical depth the relationship between snow-amount and microwave brightness temperature reverses (Markus et al., 2006; Derksen, 2008). When SWE exceeds around 150 mm the emission by the snowpack of microwave band radiation is greater than scattering, resulting in a positive relationship between SWE and brightness temperature. This is an additional source of uncertainty in SWE retrievals for deep snowpack.

Some of the difficulties in interpreting the remotely-sensed images are even more limiting in regions with complex terrain (Dozier, 1989; Dietz et al., 2012), due to the variability of slope, aspect, and land cover. Despite of their limitations, several studies demonstrated that microwave sensors generally well succeed in catching the overall seasonal variations of snow accumulation, melt timing, and season length at the macro scale.

Historical passive microwave measurements are available from the Scanning Multichannel Microwave Radiometer (SMMR) instrument (1978–1987), and the Special Sensor Microwave/Imager (SSM/I) instrument (1987 through present), with some slight differences in the frequency bands measured, overpass time, swath width, native footprint resolution, and coverage (Derksen and Walker, 2003; Brodzik et al., 2007). AMSR-E provided a suite of measurements to make it spectrally compatible with both SMMR and SSM/I at higher spatial resolution (Kelly et al., 2004; Derksen et al., 2005). The global AMSR-E SWE products consist of daily, five-day maximum and monthly average SWE estimates.

A promising research currently aims at combining satellite, ground-based observations and models (Frei et al., 2012). An example is the GlobSnow product provided by the European Space Agency (ESA). This is a long-term snow cover data set including global gridded information on SE and SWE with sufficient homogeneity to be suitable for climate change analysis (Pulliainen, 2010). The combination of station observations and snowpack modelling into passive microwave retrieval algorithms provides an accurate product useful for analyses at many different spatial scales, and for near-real time as well as climatological studies (Pulliainen, 2006). From 1995 until 2012 the SE product was based on satellite visible and infrared observations from Envisat

Advanced Along-Track Scanning Radiometer (AATSR) and European Remote Sensing-2 Along Track Scanning Radiometer-2 (ERS-2 ATSR-2) sensors (GlobSnow-1 project). Because of the failure of Envisat satellite (April 2012), the following GlobSnow-2 project has further improved the retrieval methodologies for SE and SWE and has introduced VIIRS to replace the previous sensor, as gap fillers before the launch of the Sentinel-3 sensor. Four sub-products are available: daily, weekly and monthly snow coverage in % of snow cover and daily 4-classes product.

2.5.3 Active microwave

Imaging in the microwave region has the main advantage over passive optical imaging of being independent of clouds and of solar irradiance. However, due to the low spatial resolution of passive microwave remote sensing (several to tens of kilometres), these sensors are excellent tools for snow monitoring at large scales and over uniform surfaces, but they are not useful for mountainous terrain (e.g. Alpine regions). Over complex orography, active microwave remote sensing with higher spatial resolution is needed for snow mapping. Unlike passive microwave sensors, which passively detect emissions coming from earth's surface, active sensors (radar) can emit microwaves that reflect off the target and return to the sensors. As with passive microwave energy, the physical properties of the surface determine the amount and features of the microwave radiation bounced back to the sensor. Different types of active microwave sensors are used for snow detection, namely imaging radar (i.e. Real Aperture Radar and Synthetic Aperture Radar), non-imaging radar (also called scatterometer) and radar altimeter.

Synthetic Aperture Radar (SAR) is an active microwave imaging device with high spatial resolution. This feature, along with the sensitivity of radar wavelengths to surface roughness and moisture content of snow, make SAR a powerful tool for detecting rapidly changing situations on the earth's surface occurring at any weather situation or time of the day. Usually C-band SAR is used for wet snow mapping, and active remote sensing with higher frequency is used for snow water equivalent estimation (Shi et al., 2016).

Sentinel-1 (S1) is a polar-orbiting, all-weather, day-and-night radar imaging mission for land and ocean services. As with S2 mission, S1 constellation consists of two satellites, Sentinel-1A and Sentinel-1B, which were launched on 3 April 2014 and 25 April 2016, respectively. The satellites of the S1 constellation are equipped with a C-band SAR (centre frequency of 5.4 GHz), which is one of the main tools for mapping and monitoring the extent of wet snow areas. Recently, Nagler et al. (2016) developed and validated an algorithm for retrieving snowmelt areas from S1 data. The Sentinel-1 mission, with its systematic and long-term acquisition strategy enables high resolution operational snow cover monitoring over large areas at short revisit intervals. Previously, C-band SAR data of the European Remote Sensing (ERS) satellites ERS-1, ERS-2 and Envisat, and of the Canadian RADARSAT missions have been applied for mapping and monitoring snowmelt area for applications at regional scale (Baghdadi et al., 1997; Nagler et al., 2000). The S1 spacecraft, operating in near polar sun-synchronous orbit at 693 km height, provides highly accurate pointing knowledge and real-time orbit determination, resulting in very high geolocation accuracy of the SAR products (Torres et al., 2012). The orbit repeat cycle is 12 days. Sentinel-1B has the same reference orbit as Sentinel-1A with a 180-degree orbital phasing difference to ensure a revisiting time of 6 days with the two-satellite constellation. In order to meet the observation requirements for a wide range of applications, the S1 SAR instrument supports four operational imaging modes providing different spatial resolution and coverage: Interferometric Wide swath (IW) mode, Extra Wide swath (EW) mode, Strip-Map (SM) mode, and Wave (WV) mode (Torres et al., 2012). Level-1 data (swath-based SAR images) are available in two main categories: Single Look Complex imagery (SLC) and Ground Range Detected imagery (GRD). Snow cover can be detected by exploiting the original backscatter statistics for speckle filtering and classification (Nagler et al., 2016).

CHAPTER 3
Case studies and datasets

==

With the aim of developing and testing the snow modelling system at point-scale, the selection of the case studies has been restricted among experimental sites, where automated weather stations supply meteorological and snow-related measurements of unusually high quality and completeness, since they are extensively verified (Morin et al., 2012; Essery et al., 2013). This constraint is intended to allow to reliably investigate the simulations goodness regardless of inconsistent and spurious in-situ measures. Indeed, the strategic requirements conditioning the placement of pilot sites generally entail that local features are slightly impacting (e.g. wind-induced phenomena, slope, exposure) (Wever et al., 2015), according to the WMO standards.

Another requirement has led to search for measurement sites located at different elevations, with the purpose of investigating the snow model sensitivity to varying meteorological conditions. Furthermore, the selection has been limited over the domain of interest, namely the Alpine region (Hüsler et al., 2014) (Figure 3.1).

3.1 Experimental sites

In order to fulfil all the conditions, three experimental sites have been selected:

1. Col de Porte (France);
2. Weissfluhjoch (Switzerland);
3. Torgnon (Italy).

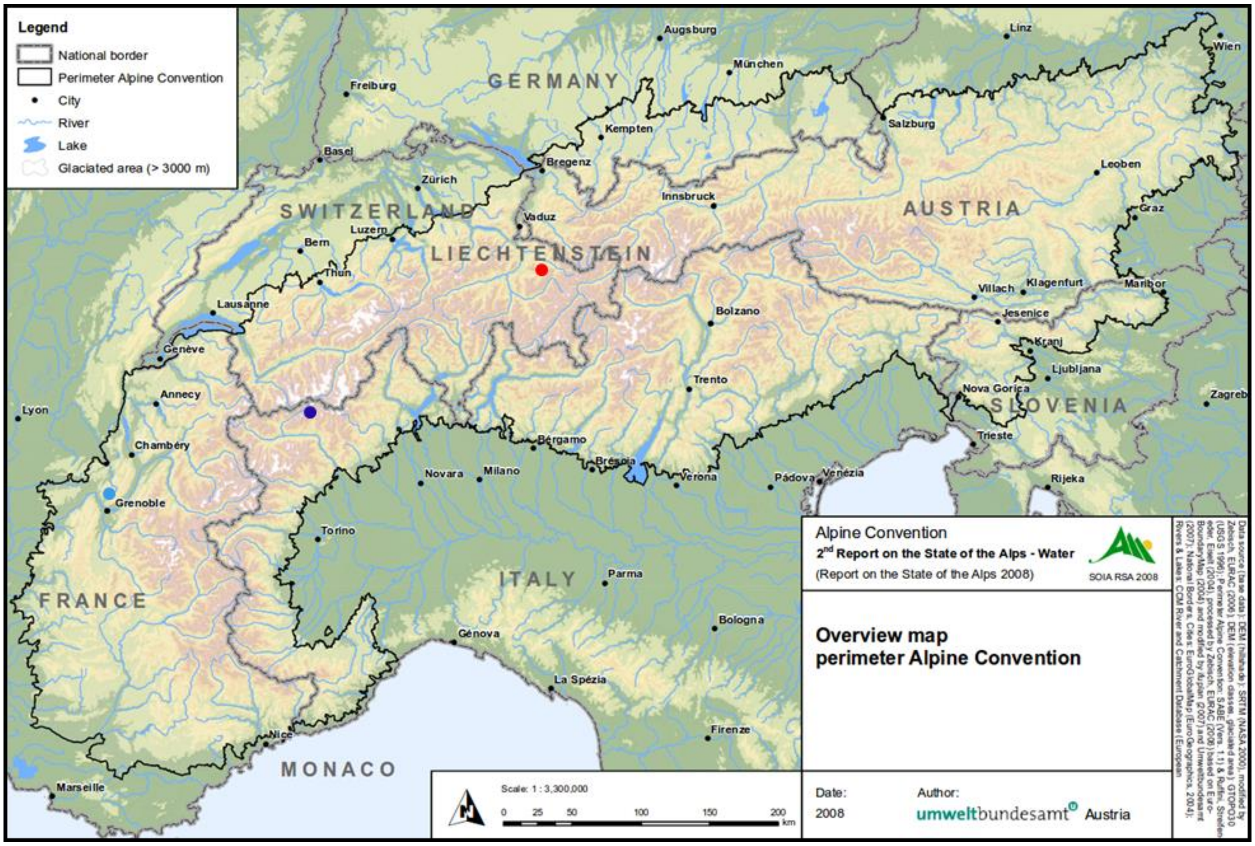

Figure 3.1: *Overview map of Alpine perimeter (Alpine Convention, Report on the State of the Alps 2008). Col de Porte (France), Torgnon (Italy), and Weissfluhjoch (Switzerland) sites are highlighted in light blue, blue, and red, respectively.*

Hereinafter the test sites are briefly described and characterized from a meteorological point of view.

3.1.1 Col de Porte site

The Col de Porte observatory (CDP) is located near Grenoble, in the Chartreuse massif (45°30' N, 5°77' E) at an elevation of 1325 m a.s.l. This pilot site is placed in a grassy meadow surrounded by a coniferous forest on the eastern side. A prominent change in the site environmental setting occurred during the summer 1999, when a natural barrier of trees on the northern side was cut, with a resulting low impact on local wind patterns. However, since generally very low winds are recorded, snowdrift slightly affects the spatial snow distribution at the site (Morin et al., 2012; Lafaysse et al., 2017). Snow cover is usually present from December to April, on average (Lafaysse et al., 2017). Nevertheless, during the winter season surface melt and rainfall events can recursively occur at the relatively low altitude of the experimental site.

All the recorded meteorological and snow observations undergo a careful (mostly manual) quality control and data gaps are filled using backup sensors, or data from neighbouring days (depending on weather conditions). In-situ meteorological data, at the hourly resolution include measurements of 2 m air temperature and relative humidity, 10 m wind speed (by both heated and non-heated anemometers), incoming short- and longwave radiations and precipitation rates, whose measures are corrected for wind speed (above 1 ms^{-1}) and temperature (Forland et al., 1996). Precipitation phase is manually assessed using all possible ancillary information (Lafaysse et al., 2017).

Snow-related observations are provided both at daily scale, and hourly time resolution. Weekly manual snow pits enable to collect internal snowpack information about its major stratigraphic properties, namely the penetration resistance, snow temperature and type, density profiles and the liquid water content. Furthermore, hourly records of temperature and height of vertically free settling disk are available. Snow depth data are manually revised to remove outliers mostly occurring during snowfall. An ultra-sound and a laser (since the winter season 2010-2011) rangers are jointly used to provide the best possible estimate. In addition, manual snow depth measurements are available from weekly snowpit observations. Since the season 2001-2002 SWE has been automatically measured on a daily basis by a ground-based cosmic rays counter. Weekly manual SWE measurements are also available. Hourly snow albedo data are estimated through the radiation sensors, as the ratio between incoming and reflected shortwave radiation (Morin et al., 2012). In addition to threshold-based controls, albedo measurements are discarded whenever snowfall occurs, or when the measured fluxes are too low. Moreover, measurements of snow surface and soil temperatures are hourly available. Snowmelt runoff is hourly estimated through two lysimeters (1 and 5 m^2 surface area), as well.

3.1.2 Weissfluhjoch site

The Weissfluhjoch site (WFJ) (46.82°N, 9.80°E) is located at an altitude of 2540 m a.s.l. in the Swiss Alp, near Davos, Switzerland (WSL Institute for Snow and Avalanche Research SLF, 2015b). This pilot site is placed in an almost flat area of a south-easterly oriented slope. At WFJ the snow season generally starts in October/November and lasts until June/July (Wever et al., 2015). An automated weather station provides meteorological and snowpack measurements. The comprehensive multiyear dataset includes measurements of air temperature and relative humidity, wind speed and direction, incoming and outgoing longwave and shortwave radiation, snow/ice surface temperature, temperature of soil at its interface with the snowpack, snow depth and precipitation from a heated rain gauge. Snow temperatures are measured at 50, 100 and 150 cm above the ground surface, using vertical rods placed approximately 30 cm apart. From September 2013 onwards, soil temperatures are measured at 50, 30 and 10 cm depth. Additionally, snowpack runoff data are supplied by a snow lysimeter with a surface area of 5 m^2 (Wever et al., 2014). The rain gauge and snow lysimeter measure at an interval of 10 min, whereas most other measurements are done at 30 min intervals. An undercatch correction is applied for the measured precipitation (Wever et al., 2014). Furthermore, where possible, data is quality checked and missing data are replaced from backup sensors from the measurement site itself, or (in only a few cases) from the MeteoSwiss weather station at 470m distance and 150m above the measurement site (WSL Institute for Snow and Avalanche Research SLF, 2015b). Lastly, an upward-looking ground-penetrating radar (upGPR) is located at about 20 m from the AWS and it provides 30-min data on liquid water percolation allowing to monitor the progress of the meltwater front (Mitterer et al., 2011; Schmid et al., 2014).

Every 2 weeks, generally in early and in the middle of each month depending on weather conditions, a manual full depth snow profile is performed (WSL Institute for Snow and Avalanche Research SLF, 2015a), according to the guidelines from Fierz et al. (2009). The detailed snow profiling, carried out in the morning hours, provides measurements of snow temperature and snow density with a sampling resolution of 10 cm and 30 cm along the snowpack vertical profile, respectively. Snow density and SWE are evaluated through snow cores using a 60-cm high aluminium cylinder with a cross-sectional area of 70 cm^2 inserted vertically into the snowpack. The snow core is then weighted using a calibrated spring. In order to remove possible effects of the spatial variability, SWE values are adjusted by taking into account differences in snow height at the snow pit and the AWS. Both grain size and shape are evaluated by the observer using a magnifying glass. Also snow wetness is reported in five wetness classes as well as hand hardness in six classes (Fierz et al., 2009).

3.1.3 Torgnon site

Torgnon site (Tellinod, 45°50′ N, 7°34′ E) is located in Aosta Valley, a mountain region in northwestern Italian Alps. The experimental site is subalpine grassland, at an elevation of 2160 m a.s.l. (Filippa et al., 2015). The area slopes lightly (4°) and it is characterized by a typical intra-alpine semi-continental climate, with an average annual temperature of around 3°C and a mean annual precipitation of 880 mm (Galvagno et al., 2013). On average, the snow season lasts from the end of October to late May, when the test site is covered by a thick snow cover (90-120 cm). Since 2008, an automatic weather station provides 30-min averaged records of different meteorological parameters, including air and surface temperatures (HMP45, Vaisala, SI-111 and therm107, Campbell Scientific), soil temperature at 2-, 10-, 35-cm depths, air pressure and relative humidity, incoming and outgoing short- and longwave radiations, and surface albedo (CNR4, Kipp & Zonen), precipitation (OTT Pluvio2, Weighing Rain Gauge), soil water content (CS-616, Campbell Scientific), snow depth (SR50A-L, Campbell Scientific), wind speed and direction (WINDSONIC1-L, Campbell Scientific), ground and turbulent (i.e. latent and sensible) heat fluxes (Galvagno et al., 2017).

During the snow seasons 2013/2014 and 2015/2016, SWE in-situ measurements are available with a sampling resolution of 6 hours (CS725, Campbell & Scientific). The sensor provides comprehensive SWE measures over a sizeable area of 50-100 m^2, with a resulting less impact of several local factors (e.g. snow drifting, vegetation). Bi-weekly manual measures of snow density (snow pits) are available throughout all the winter seasons (3-4 measurements per month, on average).

3.2 Meteorological datasets

The uninterrupted and consistent datasets of meteorological observations supplied by the AWS at the experimental sites are especially suitable for driving snowpack models.

The snowpack thermal state strongly depends on the energy exchanges with the surrounding environment. Radiative fluxes and turbulent transfer of latent and sensible heats play a prominent role in driving snowpack dynamics (e.g. snow settling and ablation) (DeWalle and Rango, 2008). The main control climate forcings ruling both the surface and internal energy balance are the air temperature and the net incoming radiation (Lòpez-Moreno and Nogués-Bravo, 2005). The intensity of convective heat fluxes strongly depends on wind speed and air humidity.

Precipitation rates supply the main input to the snowpack mass balance. When dealing with snow modelling an important issue is the definition of the precipitation phase. Indeed, unlike a snowfall event adding further snow mass, a rain-on-snow event mainly impacts the snowpack thermal state through the supply of advection heat (Würzer et al., 2016). Nevertheless, the precipitation rate is generally provided in terms of total precipitation without any partitioning between rain- and snowfall. At CDP site, the precipitation rate is manually partitioned, according to possible ancillary information, namely air temperature, relative humidity, snow depth and albedo observations (Morin et al., 2012). Conversely, both the Italian and the Swiss stations provide the total precipitation rate. Thus, at these two sites the precipitation phase has been defined a posteriori. According to Froidurot et al. (2014), the precipitation phase is considered as a binary variable, taking the value 0 for snow and 1 for rain. A logistic regression function is used to represent the probability *p(rain)* of occurrence of liquid precipitation as a function of one or more predictor variables X1, X2, ..., Xn (Eq. 3.1). Then, the corresponding probability *p(snow)* of occurrence of solid precipitation is accordingly derived (Eq. 3.2). Following this approach, the air temperature and humidity are assumed as predictor variables contributing to the evaluation of the probability of the precipitation phase.

$$p(rain) = \frac{1}{1 + e^{\alpha_0 + \alpha_1 X_1 + \alpha_2 X_2 + \cdots + \alpha_n X_n}} \qquad [3.1]$$

$$p(snow) = 1 - p(rain) \qquad [3.2]$$

Unlike the snowfall rate, whose estimate is affected by a higher uncertainty (Froidurot et al., 2014), the measurements of the other meteorological forcings are generally extensively controlled and revised at the pilot sites (Morin et al., 2012; Wever et al., 2014). However, a preliminary quality check of the meteorological data has allowed to identify some temporal gaps in the observational time series recorded at WFJ and TGN sites. The lacking observational data have been filled up through a specific approach for each variable.

At TGN site, the time series of air temperature has been reconstructed through the observations of the neighbouring station of Valtournenche (2497 m a.s.l.), whose measurements have been adjusted through a temperature-elevation regression (Figure 3.2) in order to guarantee the overall consistency of the dataset. Since no sizeable temporal gap of the observed air temperature has been detected at WFJ, the lacking values here have been filled through a linear interpolation of the available observations.

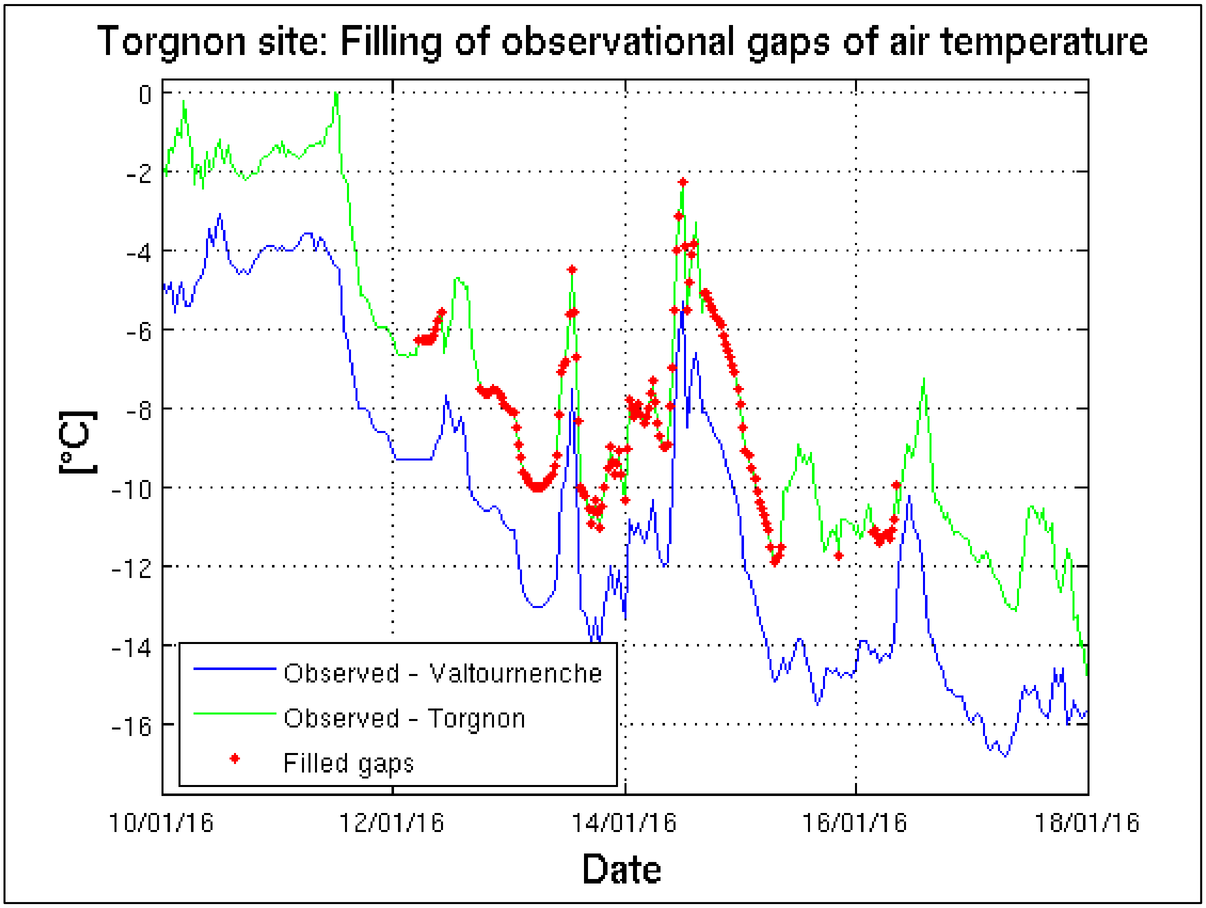

Figure 3.2: *Example of observational gaps filling of the air temperature time series through the measurements of the neighbouring station of Valtournenche – TGN site.*

The missing values of shortwave radiation at WFJ have been replaced through the corresponding observed mean value estimated by averaging the measured solar radiation at that hour of the day throughout the overall snow season. In order to not introduce any inconsistency, the mean values of shortwave radiation have been separately estimated for cloudy and not cloudy conditions (Figure 3.3). The same approach has been implemented to obtain a continuous time series of both wind speed and air temperature, since an interpolation of their observations can lead to spurious measurements.

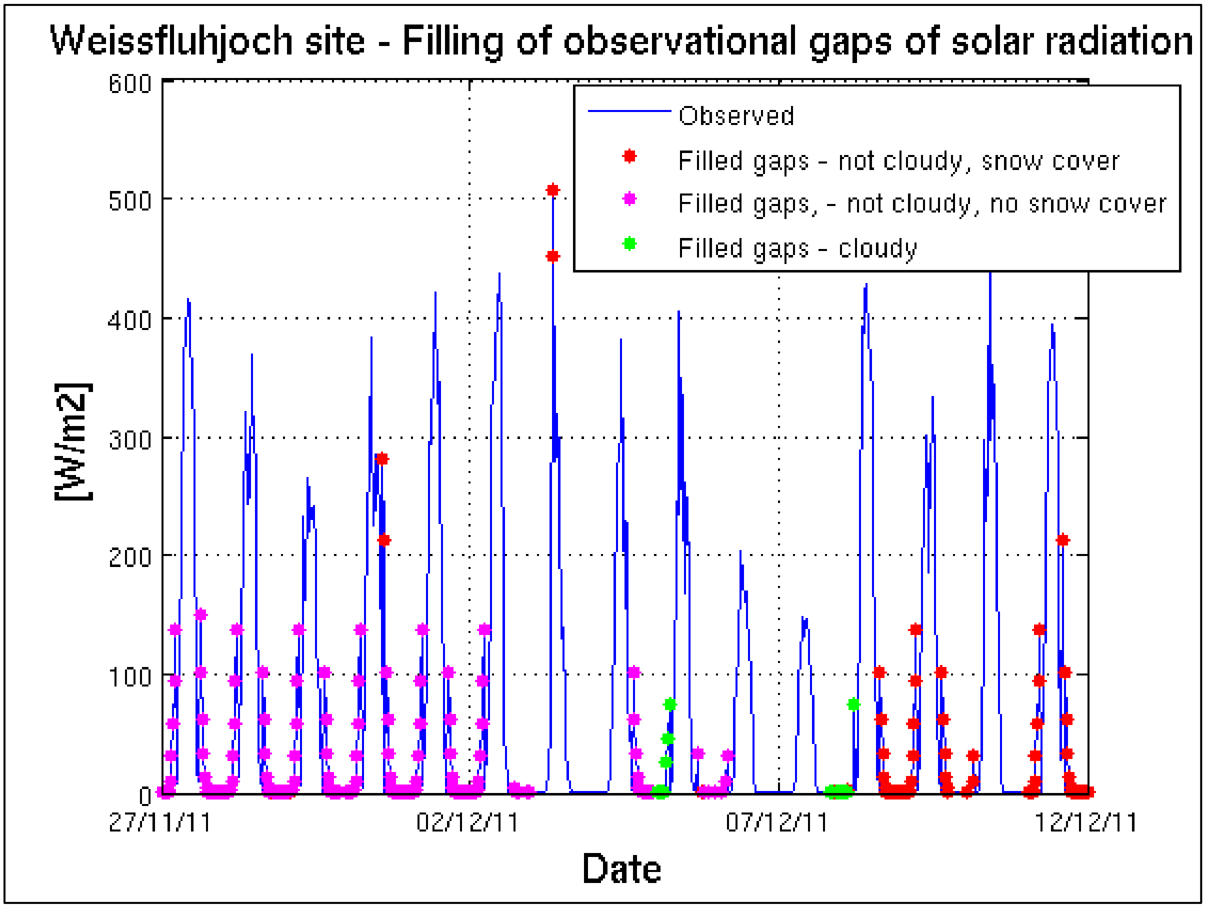

Figure 3.3: *Example of observational gaps filling of the solar radiation time series – WFJ site.*

Because of the intermittence of precipitation events, the retrieval of useful information on the precipitation is generally unfeasible. Thus, the precipitation rate has been set equal to null value when the observational data was missing. Conversely, whenever the conditions for a solid precipitation phase occurred at a lacking observational time step, snowfall rates have been otherwise estimated according to the SWE measures, when available.

3.2.1 Meteorological characterization of test sites

According to the in-situ meteorological observations, a preliminary characterization of the selected experimental sites has been carried out. The most ruling climate forcings, namely air temperature, shortwave radiation, and snowfall rate (Lòpez-Moreno and Nogués-Bravo, 2005) have been analysed together with the snow depth trends.

For each pilot site, the observational data are shown over an average snow season, obtained by averaging all the dataset periods starting in early October until the end of July. The sizeable datasets of the French and Swiss stations have ensured well-representative statistics, based on 18 and 19 full snow seasons, respectively (Table 3.1). The characterization of the TGN site has relied otherwise on a 4-years dataset of observational data.

Site	Dataset size	Snow seasons
CDP	18-years	1993/94, … , 2010/11
WFJ	19-years	1996/97, … , 2014/15
TGN	4-years	2012/13, … , 2015/16

Table 3.1: *Available datasets of the three selected experimental sites.*

The difference in the elevations of the three experimental sites entails prominent differences in the seasonal trends of the meteorological forcing variables. During the Swiss average snow season, the air temperature remains below zero degrees, with several peaks strongly negative (Figure 3.5). Much warmer is the average snow season at the CDP site, where the air temperature hovers around zero degrees, on average (Figure 3.4). Despite of the elevation of the TGN station, here the winter season is less cold than the Swiss one. Furthermore, a higher variability of air temperature affects its seasonal trend with sharp changes above and below zero degrees (Figure 3.6). This trend is likely to be mainly due to the limited size of the observational dataset, which makes the statistics more sensitive to possible peculiar features of some specific snow seasons. As expected, different amounts of incoming solar radiation are recorded as a function of each site elevation. Indeed, the Swiss station, located at the highest altitude, receives more shortwave radiation with respect the other two downstream stations, especially the French one.

Differences in the snowfall regime are prominent both in terms of snowfall intensity and seasonal cumulative snowfall. CDP and WFJ sites show roughly equivalent mean snowfall intensities and frequencies, except for the early and late winter, when only sparse events are recorded at the French station. On the other hand, at the Italian site several heavier events are observed, but snowfalls occur with lower frequency. Because of differences in both the average duration of snow seasons and the snowfall regimes, the resulting cumulative estimates are strongly diversified. Thanks to the high snowfall frequency and a long snow season, cumulative snowfall at WFJ reaches about 1100 mm, on average. The shorter winter season at the French site entails lower cumulative estimate of about 600 mm. Even though the winter season lasts over approximately the same months at the French and the Italian sites, the lower snowfall frequency at TGN leads to a much lower cumulative value (around 500 mm), despite several heavy snowfall events. However, it is important to stress the uncertainty affecting the snowfall observational data, which are empirically derived.

The differences in meteorological forcings result in different snow depth trends. At the Swiss station, the snowpack reaches the highest depth, up to 2 m at the late accumulation period, on average. At the French and Italian sites, the snow depth achieves an average maximum of around 1 m. At CDP snow depths show the highest variability, mainly because at this low altitude the climatological conditions can strongly vary from year to year (i.e. average air temperature and snowfall rates). Conversely, snow depths at TGN reveal a higher variability during the early accumulation period with respect to the late snow season.

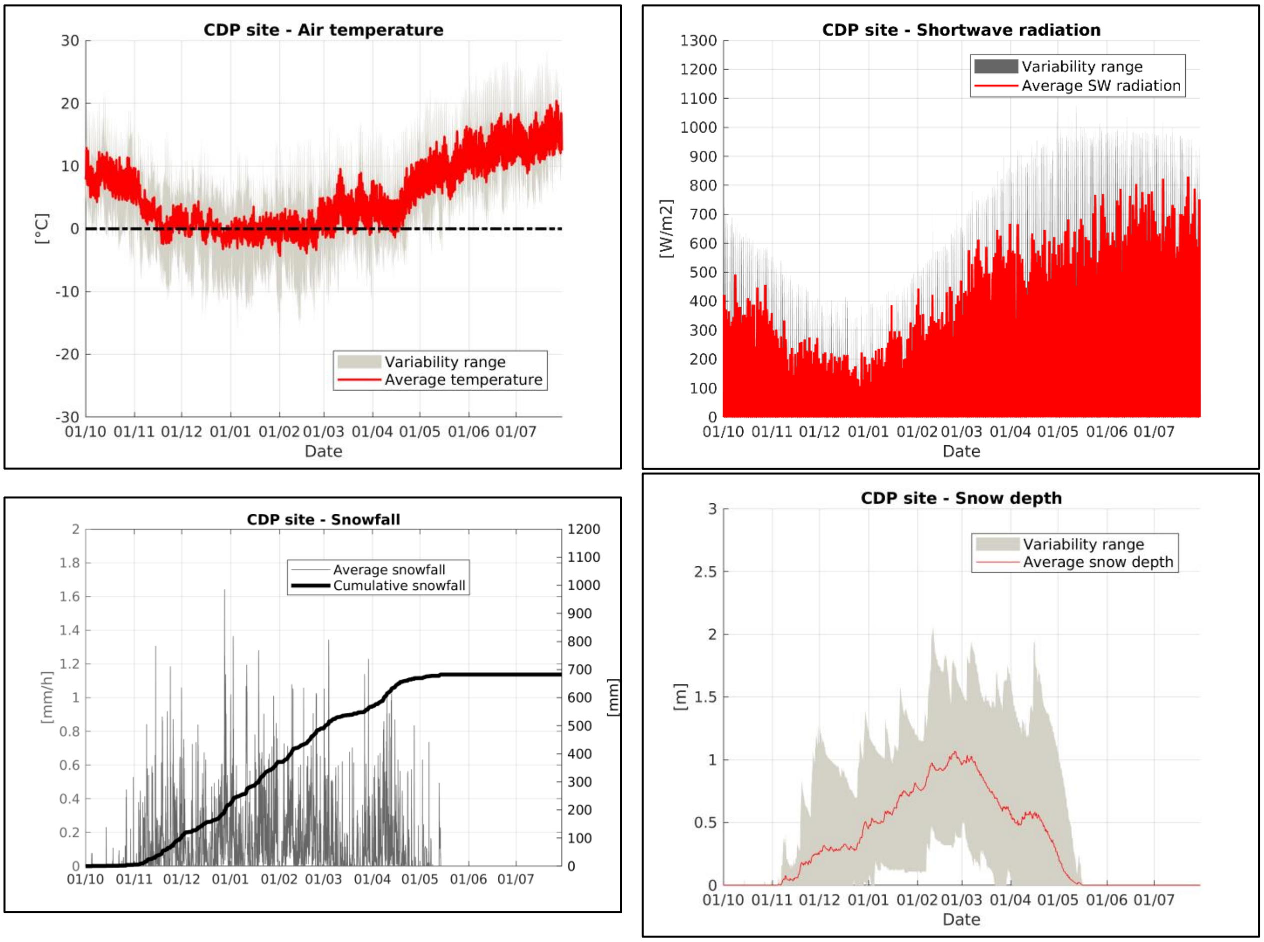

Figure 3.4: *Meteorological characterization of CDP site – From the top-left (clockwise): Air temperature, shortwave radiation, snowfall and snow depth throughout 18-years average snow season (early October – late July).*

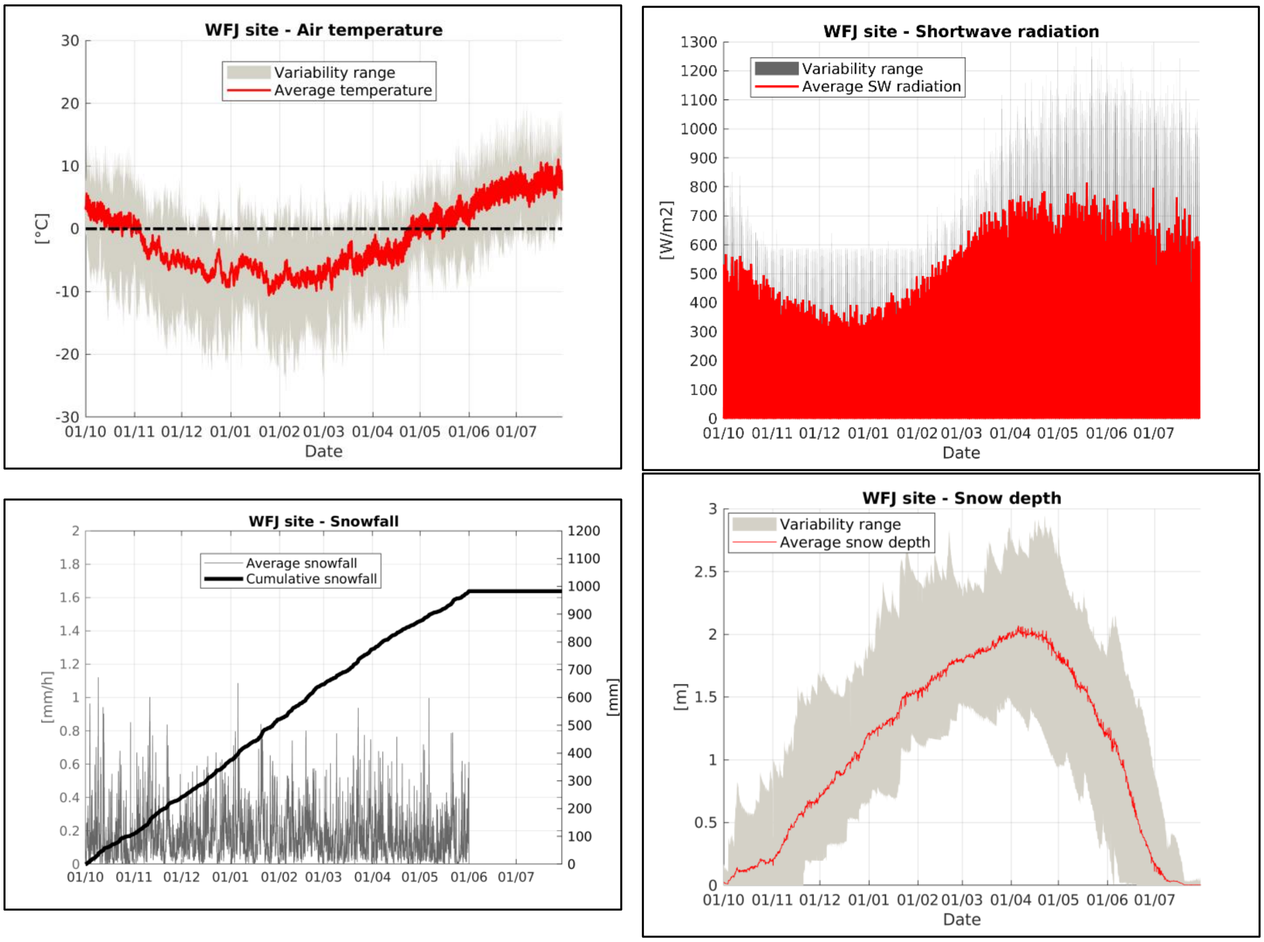

Figure 3.5: *Meteorological characterization of WFJ site – From the top-left (clockwise): Air temperature, shortwave radiation, snowfall and snow depth throughout 19-years average snow season (early October – late July).*

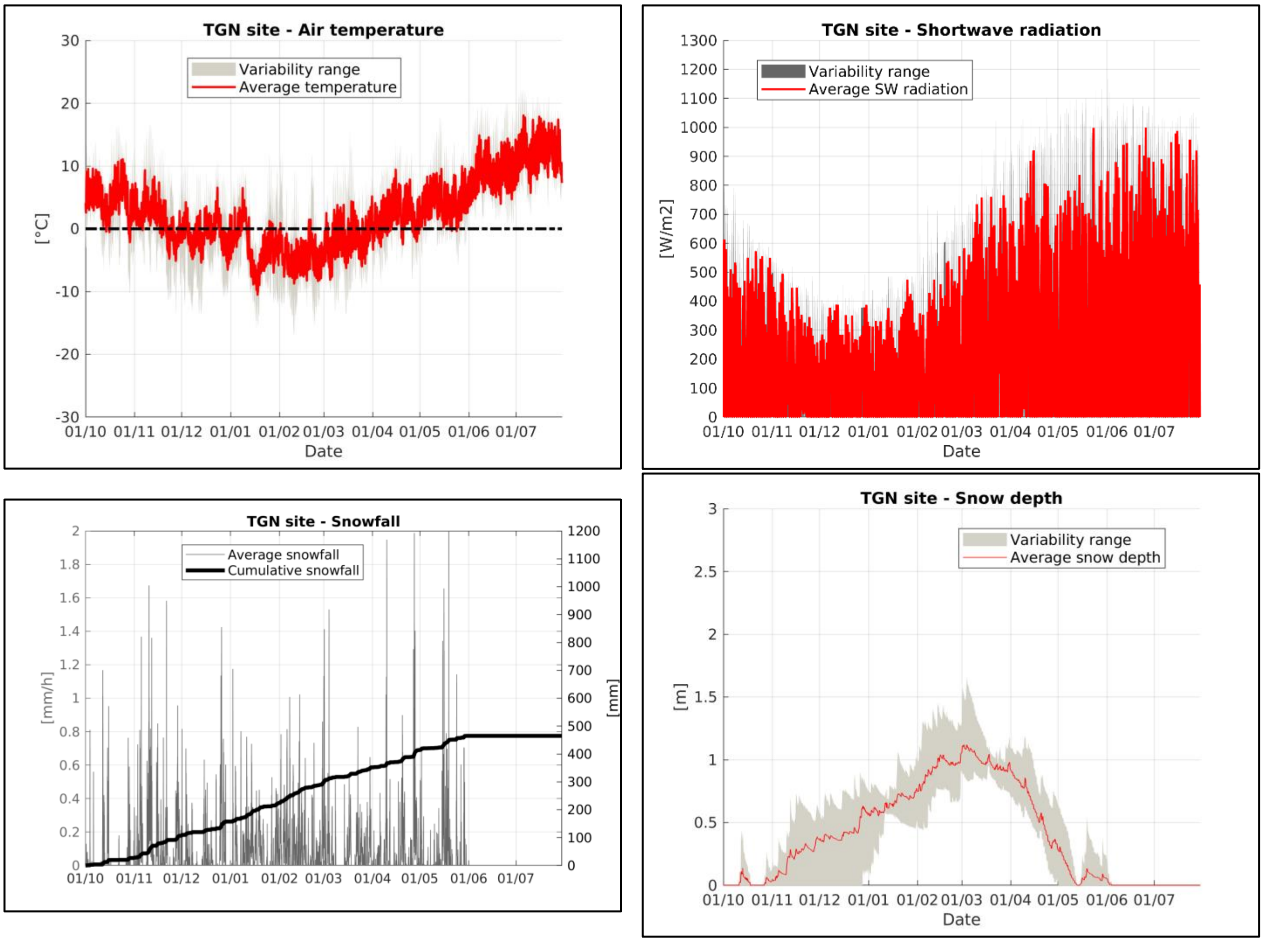

Figure 3.6: *Meteorological characterization of TGN site – From the top-left (clockwise): Air temperature, shortwave radiation, snowfall and snow depth throughout 4-years average snow season (early October – mid-June).*

3.3 Snow observational data

When modelling the snowpack dynamics, a dataset of observations of snow-related quantities is needed to properly assess the accuracy of simulations. However, it is noteworthy to consider that the observations, as well as model predictions, are affected by some degree of uncertainty, mainly tied to instrumental errors.

As previously explained, several advantages result from testing the modelling system at experimental sites. Firstly, at these sites in-situ observations of several variables of interest are largely available, and furthermore they are extensively checked and reliably adjusted. Secondly, the measurements are generally carried out under optimal conditions with a resulting low impact of local features generally affecting the recording procedure (e.g. wind-induced snow drifting).

3.3.1 Quality check of snow depth measures

One of the most interesting variables is the snow depth, whose observations allow to assess how the model succeeds in catching the snowpack accumulation- and ablation dynamics. A preliminary quality check of the observational data has enabled to detect spurious measurements affecting the time series of snow depths at the Italian and Swiss sites, especially during the transition periods (early winter, late melting period) (Figure 3.7). According to the snow seasonality and local features, these are likely to be misleading measurements of grass. With the aim of not inconsistently removing actual snow measurements, the estimated snowfall rates have been used to better highlight the spurious measures. Thus, the time series have been accordingly revised in order to avoid false snow detection.

While the CDP station provides continuous snow depth observations throughout the whole dataset period, at WFJ site automatic snow depth measurements have been available since the winter 1999/2000. Therefore, in order to be able to properly perform the forthcoming analysis, the Swiss dataset has been limited starting from the snow season 1999/2000 (Table 3.2).

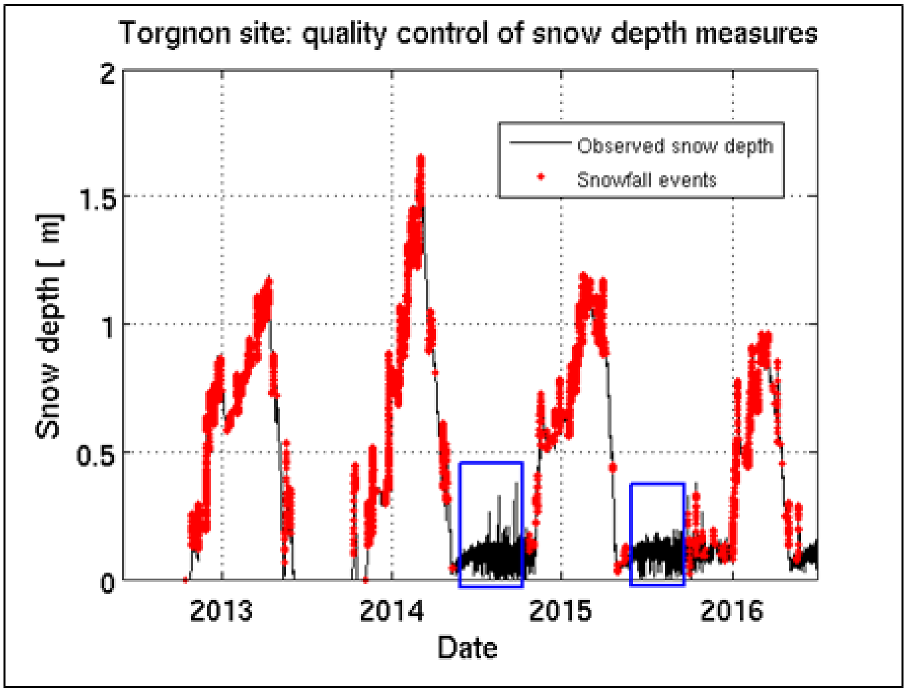

Figure 3.7: *Quality check of the snow depth time series – TGN site. Grass detection is highlighted in blue.*

3.3.2 SWE in-situ observations

From a hydrological point of view, one of the most important variables is the SWE. Even though direct measurements of this variables are widely lacking, the experimental sites are one of the main sources of consistent in-situ SWE measures. Daily automatic measures are provided by the CDP station since the winter season 2001/2002. In light of the ruling importance of this variable to assess the model performances from a hydrological standpoint, the dataset of this station is accordingly reduced starting from this snow season (Table 3.2)

Site	**Dataset size**	**Snow seasons**
CDP	10-years	2001/02, … , 2010/11
WFJ	16-years	1999/2000, … , 2014/15
TGN	4-years	2012/13, … , 2015/16

Table 3.2: *Snow datasets resulting from the quality check.*

With the aim of better investigating the reliability of the observational data, a further analysis has been carried out at CDP site. Indeed, since measurements of both snowfall rates and SWE are available, their consistency has been analysed. This qualitative study has relied on the assumption that positive increases of SWE mainly result from snowfall events (besides possible snowmelt percolation). Thus, the seasonal cumulative SWE value has been compared year-by-year with the cumulative value of snowfall rates (Figure 3.8). The two observed time series revealed a satisfying consistency, both in terms of correlation and mean error.

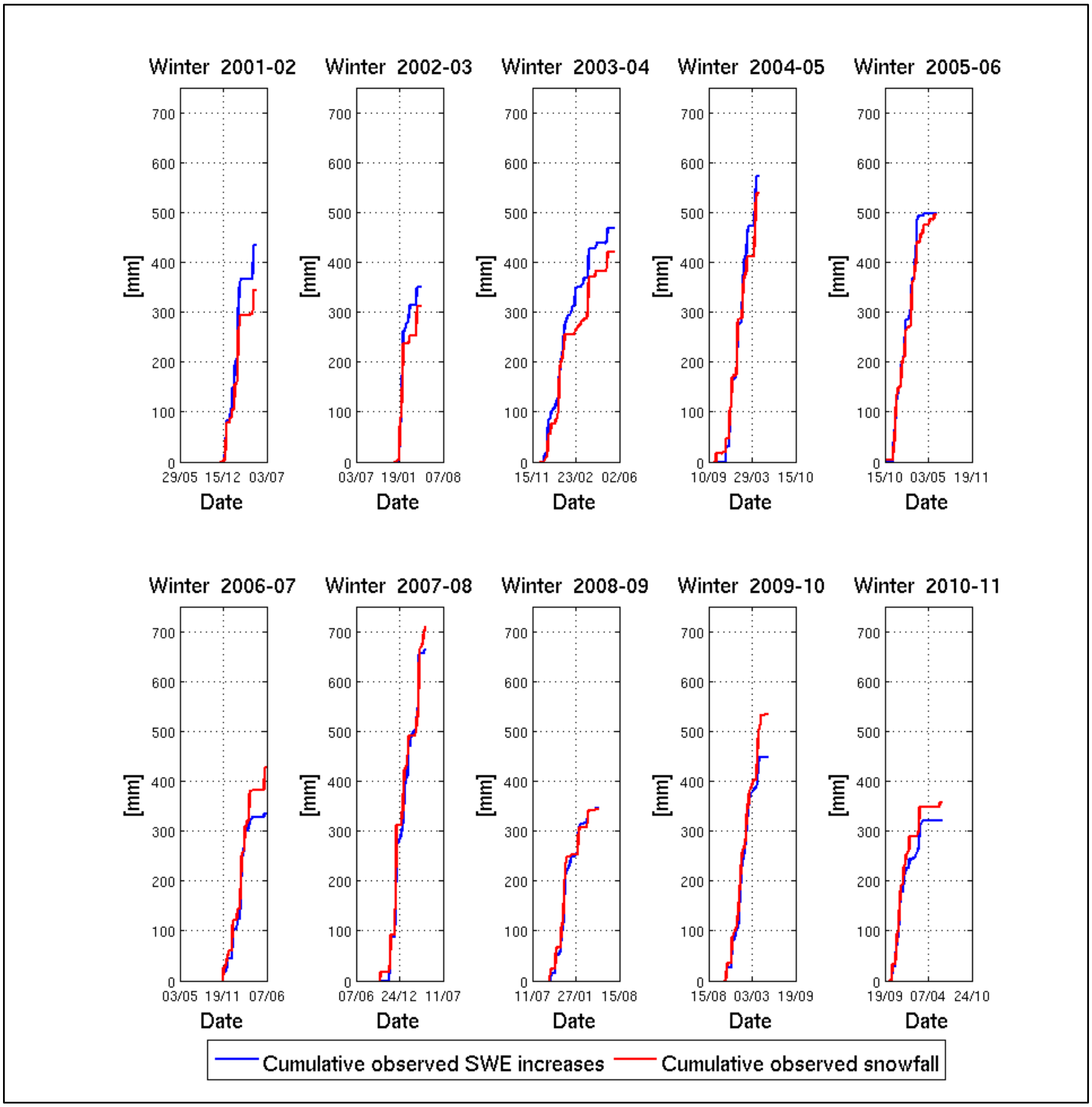

Figure 3.8: *Consistency control between SWE and snowfall observations – CdP site.*

With a lower measurement frequency, at WFJ SWE observations are available every two weeks over the whole dataset period. Unlike these two pilot sites, the TGN station does not continuously supplies SWE measurements throughout the whole 4-years dataset period. In-situ 6-hrs SWE measurements have been automatically recorded during two snow seasons, 2013/2014 and 2015/2016. In order to be able to properly use these measures within the simulations analyses on seasonal/annual scale, the raw observational data have been smoothed from possible inconsistent oscillations and anomalies (e.g. rain-on-snow events) through their daily average.

3.3.3 Indirect estimation of snow-related quantities

Even though an exhaustive knowledge of snow density is needed to properly define the snowpack state and its dynamics, direct continuous observations of snow density are generally dramatically lacking. An exception is the TGN site, where biweekly manual measurements provide useful information throughout the whole dataset period.

However, thanks to the linking relation among snow depth, SWE and snow density, observations of at least two of these mass-related variables are enough to estimate the third one, whose consistency has been qualitative assessed. For instance, when direct measures of both SWE and snow depth are available ($SWE_{direct}\ [mm], SD_{direct}[m]$), the snow density ($\rho_{indirect}\ [kg/m^3]$) can be easily derived according to the formula:

$$\rho_{indirect} = \frac{SWE_{direct}}{SD_{direct}} \tag{3.3}$$

Vice versa, SWE can be indirectly estimated whenever an observation of the snow density is available, if a snow depth measurement is provided.

According to this approach, at both the Swiss and the French sites bi-weekly and daily snow density measurements have been derived, respectively. Possible inconsistencies of the resulting values have been removed through a threshold-based control discarding all the snow densities higher than 550 kg/m^3. At TGN daily snow densities have been indirectly estimated during the two winter seasons when SWE measures are available (i.e. snow seasons 2013/2014 and 2015/2016). Conversely, bi-weekly SWE estimates have been derived during the other two snow seasons, when only manual snow densities measurements are otherwise supplied. Because the two sensors measuring snow depth and SWE can be not located exactly at the same point, however, possible inconsistencies can arise due to the spatial variability in snow cover, especially under shallow snow conditions (Essery et al., 2013; Lafaysse et al., 2017). The resulting time series of snow depth, SWE and snow density are shown below for the French (Figure 3.9), the Swiss (Figure 3.10), and the Italian (Figure 3.11) sites.

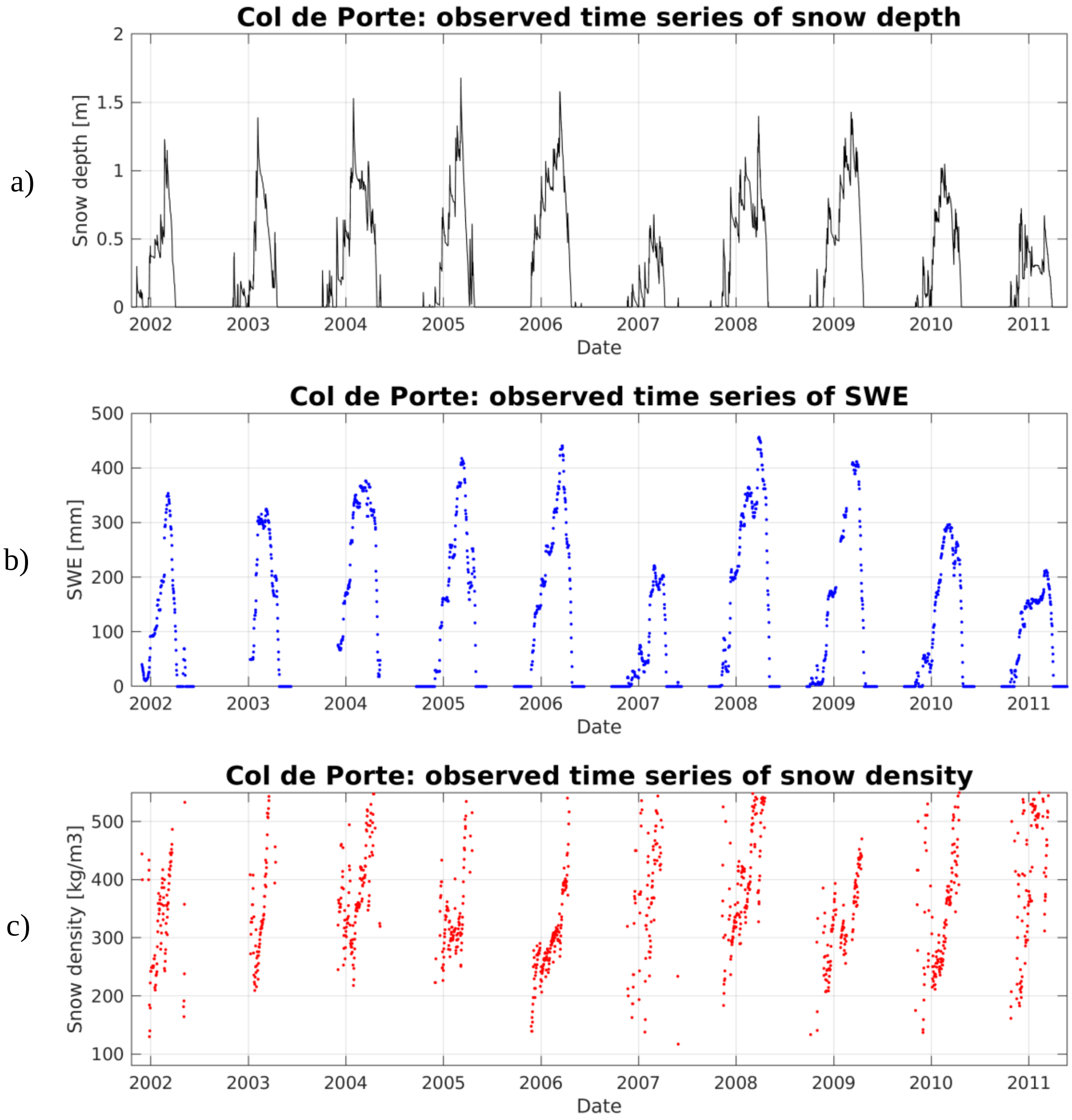

Figure 3.9: *In-situ observations of hourly snow depth (a), daily SWE (b), and indirect daily estimates of snow density (c) – CDP site.*

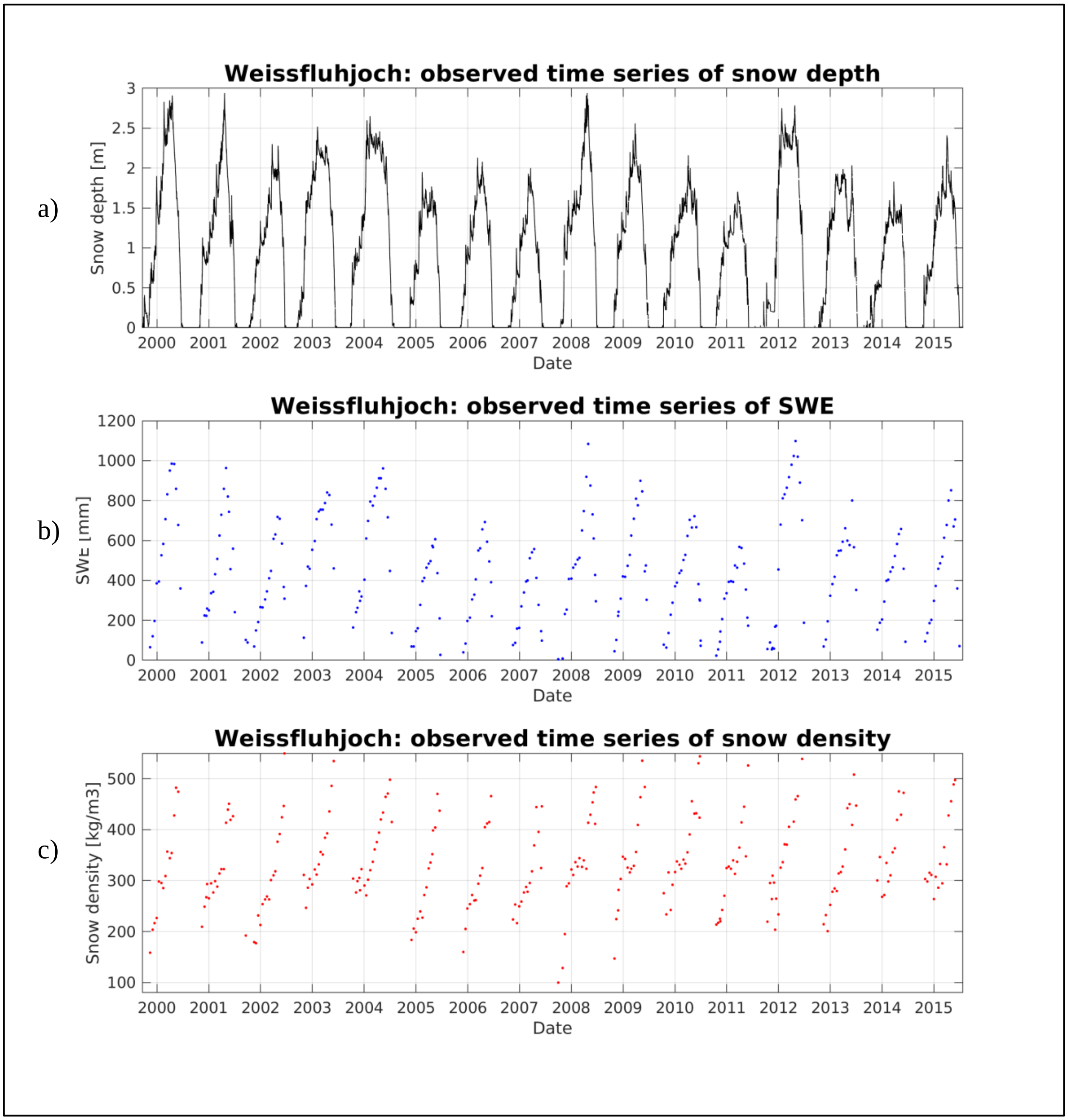

Figure 3.10: *In-situ observations of hourly snow depth (a), bi-weekly SWE (b), and indirect bi-weekly estimates of snow density (c) – WFJ site.*

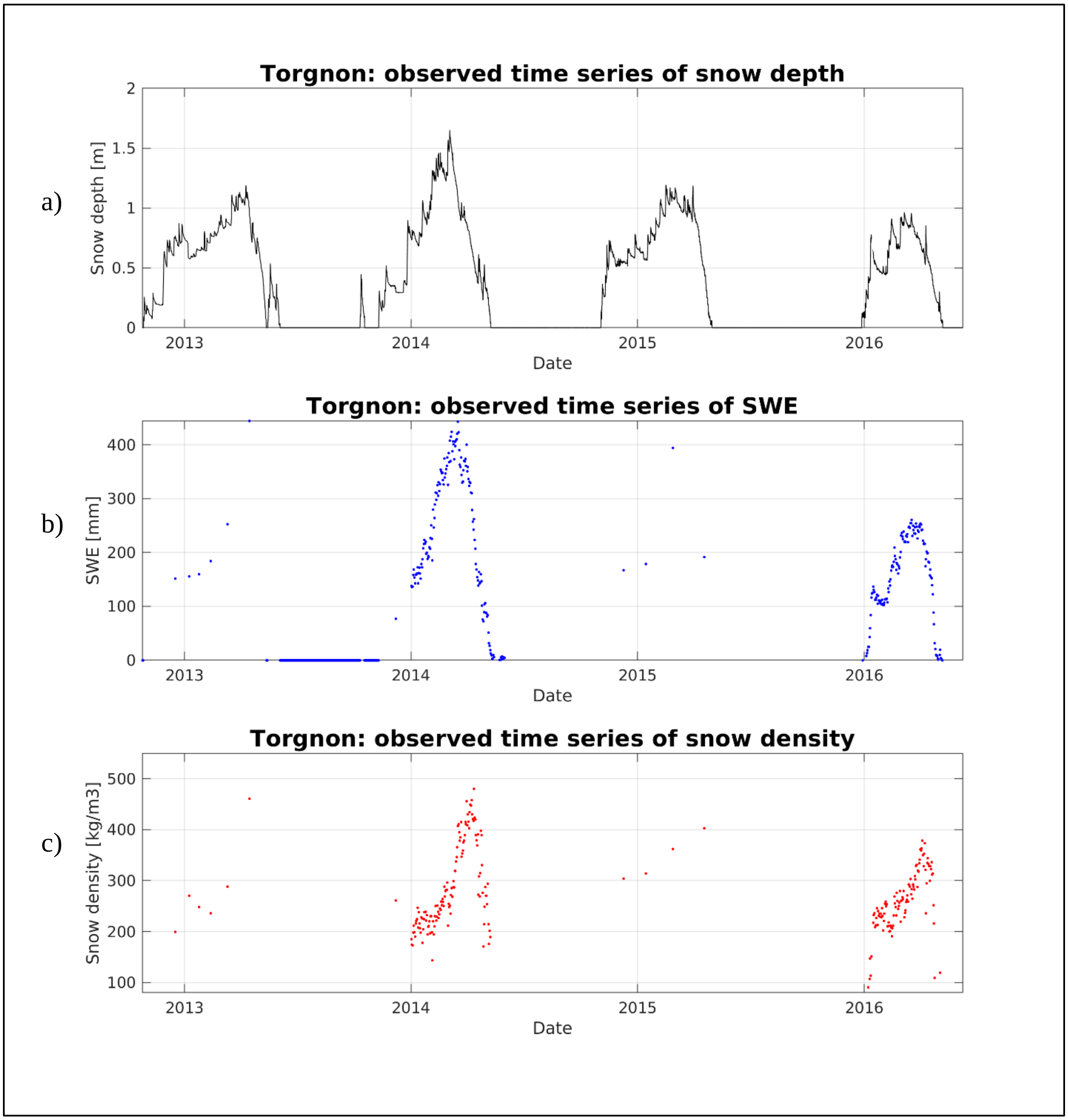

Figure 3.11: *In-situ observations of 30-min snow depth (a), daily SWE (b, II and IV snow seasons), bi-weekly snow density (c), and indirect estimates of bi-weekly SWE (b), daily snow density (c, II and IV snow seasons) – TGN site.*

Several other snow-related variables of interest are available at the pilot sites, namely the snow surface temperature and albedo, snowmelt runoff, and soil temperatures. As regards the surface albedo, it is noteworthy to underline that observations of this variable at the TGN site are available only in the years 2012 and 2013.

CHAPTER 4

Multilayer snowpack dynamics model

The multilayer snowpack model has been designed to be suited to its coupling with DA schemes for real-time applications. The snow model relies on a mass- and energy-balance scheme allowing to reproduce some of the main physical processes occurring within the snowpack (i.e. accumulation, density dynamics, melting, sublimation, radiative balance, heat and mass exchanges).

4.1 Snow multilayer mass- and energy-balance model

From a hydrological standpoint, the most relevant quantities to be predicted are the SWE and the snowmelt. The evolution of snow microstructure, snowpack stratification, and snow metamorphism are ruling processes of critical importance for the avalanches forecasting (Bartelt and Lehning, 2002; Vionnet et al., 2012). However, these snow dynamics are of less interest in most hydrological applications and thus they are here neglected.

Since the aim is to develop a snow model suitable to be coupled with multivariate DA schemes, the degree of model complexity is limited in order to facilitate the assimilation procedure while maintaining a fundamental physical consistency (Slater and Clark, 2006; Magnusson et al. 2014). This purpose leads to some model simplifications of both snowpack scheme and physics (liquid water storage and refreezing process are not included). The introduction of a finer snow layering scheme, with respect to the simple discretization described below, would add a further challenge in the assimilation of observed data through DA techniques involving state-averaging operations. Indeed, the implementation of a multivariate DA scheme would be much more demanding since a higher number of layers (i.e. increased state size) entails larger computational requirements.

The multilayer scheme consists of a 2-layers discretization for snowpack and 2-layers for soil (Figure 4.1). The scheme has a seasonally variable number of layers ranging from a minimum of two, in snow free condition, up to a maximum of four layers, in presence of snow cover. This dynamic layering scheme is adopted with the aim of solving the model energy balance in both snowy and snowless conditions without relying on a ‘model switching’ algorithm. Both snow and soil upper layers are much thinner than the underlying ones so that the top layer temperature can be considered as an acceptable approximation of the skin temperature, whose measures can be more efficiently assimilated. The model is driven by meteorological data, namely air temperature, wind velocity, relative air humidity, precipitation and incident shortwave radiation, to provide a complete estimate of snowpack state in an explicit surface energy balance framework. Model state consists of snow surface temperature $(T_s\,, [°C])$, snow temperature at the interface between the two snow layers $(T_m\,, [°C])$, surface soil temperature $(T_0\,, [°C])$, deep soil temperature $(T_d\,, [°C])$, snow water equivalent and snow density of top $(W_s\,, [mm];\ \rho_s\,, [kg/m^3])$ and bottom $(W_m\,, [mm];\ \rho_m\,, [kg/m^3])$ snow layers, surface albedo$(\alpha, [-])$.

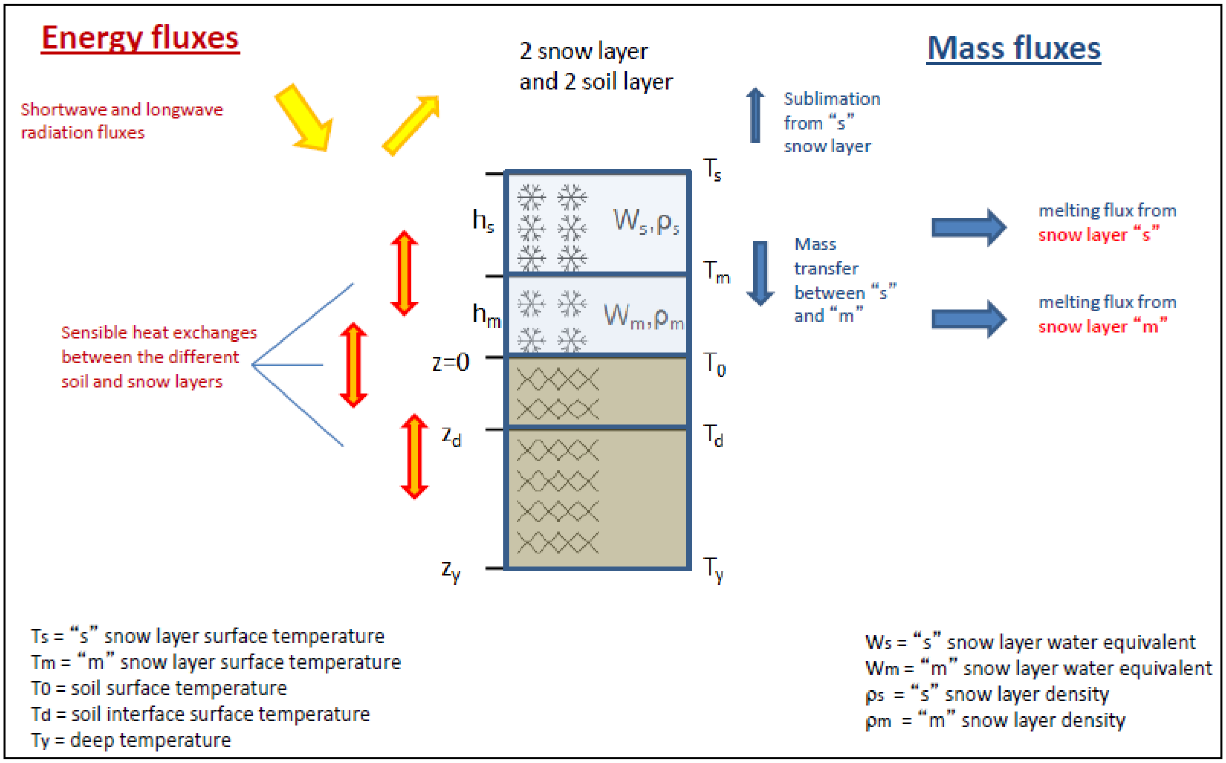

Figure 4.1: *Scheme of the multilayer snowpack model - Energy and mass fluxes between adjoining layers and atmosphere are shown.*

The thicknesses of soil layers are fixed through reference depths at 30 cm and 2 m (z_d and z_y). Snow layers vary their thickness (h_s and h_m) according to the snow dynamics (i.e. snowfalls, sublimation, density changes, and snow melting) without any constraining limit. Deep soil temperature (T_y) is the model boundary condition. Temperatures (T_s, T_m, T_0, T_d) are defined as average temperatures of the control volumes shown in Figure 4.2. The top and bottom boundaries of each volume are set in the middle of the thickness of the two corresponding consecutive layers.

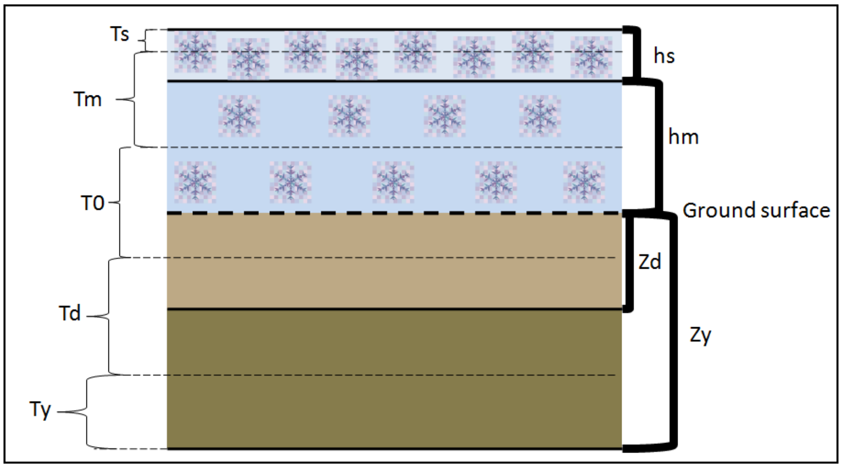

Figure 4.2*: Scheme of the snow energy-balance model - Control volumes and model layers.*

4.2. Model snow physics parameterizations

The snow model solves both energy and mass balances with an integration time step of 15 minutes. The model parameterizations of the main processes occurring within the snowpack are described below.

4.2.1 Mass balance

Snow mass balance equations evaluate SWE of each snow layer accounting for snowfalls (*Sf*), sublimation process (*subl*), melting rates of both the two snow layers (M_s and M_m) and mass transfer between them (*D*). Since neither the liquid storage nor the refreezing process is included within the snowpack model, meltwater is assumed to drain directly as surface runoff (no infiltration into the soil).

$$W_s(t) = W_s(t-1) + Sf - M_s - subl - D \tag{4.1}$$

$$W_m(t) = W_m(t-1) + D - M_m - subl \tag{4.2}$$

$$D = \frac{1}{X} W_s \, dt \tag{4.3}$$

The mass transfer from the snow surface layer downward is empirically parameterized as a function of the SWE and a temporal scale of the process (X). This parameter has been defined through several tests at different measurements sites in order to obtain a constant value allowing to maintain a thin snow surface layer. From a physical point of view, this parameterization can be assumed to contribute to the gravitational snowpack settling thanks to a consistent update of the snow density of both the snow layers.

4.2.2 Density

Snow density is updated according to the parameterization proposed by Anderson (1976) (Sect. 2.3.1, *Snow compaction*). As previously explained, this formulation considers both the compaction and the destructive thermal metamorphism. Snow compaction is evaluated as the ratio between the weight of the overlying snow and a viscosity coefficient, which stands for the snow resistance to a certain pressure and evaluated as an exponential function of snow temperature and density (Mellor, 1964; Kojima, 1967). Thermal metamorphism is estimated as a function of snow temperature and density. The influence of settling is higher in new snow layers (50-150 [kg/m^3]) up to a density value of 250 [kg/m^3]. In case of snowfall, snow density of the upper layer is evaluated as a weighted average between its current value and the fresh snow density (Sect. 2.3.1, *Fresh snow density*). Fresh snow density is evaluated according to the air temperature (Hedstrom and Pomeroy, 1998).

4.2.3 Energy balance

The model evaluates the net heat fluxes in each layer and the conductive heat fluxes between adjoining layers according to Fourier law. The surface heat flux ($\vec{G}$) is estimated by considering the resulting net shortwave and longwave radiations $\left(\vec{R}_{Sw,net}\,,\vec{R}_{Lw,net}\right)$, sensible $\left(\vec{H}\right)$ and latent $\left(\overrightarrow{LS}\right)$ heat fluxes, the advection heat flux $\left(\vec{Q}_{mix}\right)$ due to liquid precipitation:

$$\vec{G} = \vec{R}_{Sw,net} + \vec{R}_{Lw,net} + \vec{H} + \overrightarrow{LS} + \vec{Q}_{mix} \qquad [4.4]$$

Both the incoming (positive) and outgoing (negative) longwave radiation components are estimated through the Stephan-Boltzmann law, as a function of the surface temperature (i.e. the temperature of snow/soil depending on the presence/absence of snow cover) and the air temperature, respectively. While the surface emissivities are considered as constant values, the air emissivity varies over time according to both wind speed and air temperature.

The heat flux from liquid precipitation across the snowpack surface is a function of rain emissivity (ε_p), the surface specific heat (C_s), the amount of rain (P_l) and the temperature gradient:

$$Q_{mix} = \frac{\varepsilon_p C_s P_l \left(T_a - T_{sup}\right)}{dt} \quad [4.5]$$

The net shortwave radiation $\left(R_{Sw,net}\right)$ is evaluated as a fraction of the incident solar radiation $\left(R_{Sw,inc}\right)$, as a function of the surface albedo:

$$R_{Sw,net} = (1 - \alpha) \cdot R_{Sw,inc} \quad [4.6]$$

The penetration of shortwave radiation into the snowpack is estimated after Anderson (1976). According to this formulation, solar radiation decays exponentially as a function of snow depth

$$R_{Sw\downarrow} = R_{Sw,net} \cdot \exp(-\nu \cdot z) \quad [4.7]$$

where $R_{Sw\downarrow}$ is the fraction of solar radiation penetrated within the snowpack; ν is the extinction coefficient, set equal to 0.2 cm^{-1} (constant value); z is the penetration depth $[cm]$.

4.2.4 Surface albedo

In snow cover condition, the surface albedo is updated through the empirical parameterization proposed by Douville et al. (1995). The albedo is predicted as a prognostic variable, whose dynamics are described by a linear decay over time under cold snow conditions and an exponential decay in the presence of melting snow. When a snowfall event occurs, the albedo is consistently updated as a function of the snowfall rate (Sect. 2.3.1, *Snow albedo*).

4.2.5 Turbulent fluxes

Sensible and latent heat fluxes are evaluated following the bulk formulation:

$$H = c_p \rho_a C_H V \left(T_{sup} - T_a\right) \quad \text{Sensible heat flux} \quad [4.8]$$

$$LS = L_H \rho_a C_H V (q_{sup} - q_a) \quad \text{Latent heat flux} \quad [4.9]$$

Heat exchanges are proportional to the temperature (for *H*) and mixing ratio (for *LS*) gradients between the surface (T_{sup} and q_{sup}) and atmosphere (T_a and q_a). Turbulent fluxes are also function of air specific heat (c_p), latent heat (L_H) of sublimation (of vaporization when no snow cover is present), air density (ρ_a), wind velocity, and the turbulent transfer coefficient (C_H). This latter coefficient depends on the neutral conditions coefficient (C_{HN}), evaluated as a function of the surface roughness (z_0), and the atmospheric stability (ψ_{stab}) :

$$C_H = \mathrm{C_{HN}}\psi_{stab} \qquad [4.10]$$

The atmospheric stability is evaluated as a function of the Richardson Bulk number, which depends on potential temperatures of both air and interface surface between soil/snow and atmosphere and wind velocity, following the empirical scheme of Caparrini et al. (2004).

4.2.6 Heat fluxes

Temperature variation in time (ΔT_i) and snow melting rate (M_i) of each i-th layer are evaluated as a function of the net heat flux at its surface (Q_{Ti}), resulting from the balance of conductive fluxes among layers and the contribution of the penetration of solar radiation:

$$\Delta T_i = \frac{Q_{Ti}}{h_i \rho_i C_i}\,dt \qquad \text{If } T_i > T_{melt} \rightarrow M_i = \frac{Q_{Ti\_melt}}{L_m}\,dt \qquad [4.11a, b]$$

where C_i is the specific heat of the i-th layer. When the resulting temperature of the layer (T_i) exceeds the melting temperature (T_{melt} = 0°C), melting occurs in the corresponding control volume according to the equation [4.11b], where L_m is the melting latent heat.

4.3 Model calibration

The snowpack model has been calibrated at the three experimental sites in order to define the values of the model parameters allowing the best possible simulations under different meteorological conditions.

4.3.1 Sensitivity analysis of model parameters

A sensitivity analysis has allowed to select the parameters exerting the most influence on model simulations. This preliminary study has been carried out by making the parameters vary within proper ranges and analysing the impact of their variation on the resulting model predictions. Parameters ranges have been estimated in order to both avoid model numerical instabilities and comply with possible physical constraints (Table 4.1). Two model parameters have been selected, namely snow roughness (z_0) and snow viscosity (η_0).

The first parameter is used to evaluate the turbulent heat transfer coefficient (Sect. 4.2.5), thus it mainly affects the intensity of the turbulent heat fluxes, with a prominent impact on the snowpack internal energy balance and the resulting melting fluxes. The second parameter (see *Snow compaction,* Sect. 2.3.1) is one of the main ruling snow properties contributing to the snow density evolution.

Parameters			**Ranges**
Snow roughness	z_0	[mm]	$[0.001 - 0.05]$
Snow viscosity	η_0	[kg/ms]	$[7 \cdot 10^7 - 10^{12}]$

Table 4.1: *Model calibration – Parameters ranges.*

4.3.2 Calibration strategy and procedure

The calibration has been carried out through the commonly used split-sample calibration-validation procedure (Klemeš, 1986). According to this approach, the dataset of each snow experimental site has been randomly split into two sub-datasets designed to be used within the calibration and the validation procedure, respectively, both relying on 15-years datasets of observational data (Table 4.2). This choice has been largely supported by the stability of the climatic conditions between the two sub-periods of each dataset.

CALIBRATION	**Col de Porte**	2001/02	2005/06	2006/07	2007/08	2009/10			
	Weissfluhjoch	2000/01	2002/03	2003/04	2010/11	2011/12	2012/13	2013/14	2014/15
	Torgnon	2013/14	2014/15						
VALIDATION	**Col de Porte**	2002/03	2003/04	2004/05	2008/09	2010/11			
	Weissfluhjoch	1999/00	2001/02	2004/05	2005/06	2006/07	2007/08	2008/09	2009/10
	Torgnon	2012/13	2015/16						

Table 4.2: *Calibration and validation datasets.*

The Kling-Gupta Efficiency (*KGE*) criterion (Gupta et al., 2009) has been used as objective function. The *KGE* coefficient has been evaluated as:

$$KGE = 1 - \sqrt{(r-1)^2 + (a-1)^2 + (b-1)^2} \qquad [4.12]$$

where:

- *r* is the linear correlation coefficient between simulated and observed values;
- *a* is the ratio of the standard deviation of simulated values to the standard deviation of the observed ones, i.e. an estimate of the relative variability between simulated and observed quantities;

- *b* is the ratio of the mean of simulated values to the mean of observed ones, i.e. a measure of the overall bias.

The objective function (Eq. 4.12) has been evaluated by considering all the available snow-related observations supplied by each measurement station (i.e. snow surface temperature, SWE, snow depth, albedo, snow density).

The optimal *KGE* value is ideally equal to 1. Because the main aim is to succeed in well catching the observed values (theoretically, r=1, a=1, b=1), the maximization of the *KGE* index allows to minimize the Euclidian distance from the desired optimal point.

The model calibration is performed by a two-step optimization procedure:

1) Pre-filtering search in the parameters space;
2) Iterative local optimization.

Within the first phase, random combinations of parameters have been tested by making them vary within their ranges and evaluating the resulting values of the objective function.

Starting from the best parameters combinations provided by the pre-filtering search, namely those guaranteeing the highest values of the objective function, an iterative local optimization has been applied to search for local *KGE* optima over the calibration period. A constrained nonlinear optimization algorithm (Interior-point Algorithm) (Wächter and Biegler, 2006) has been implemented to define the best parameters set.

Finally, the calibrated parameters have been tested throughout the validation period. Table 4.3 shows the values of the model parameters resulting from the calibration process.

Parameters		**Calibrated values**
Snow roughness	[mm]	0.0226
Snow viscosity	[kg/ms]	10^8

Table 4.3: *Model calibration – Calibrated values of the model parameters.*

4.4 Open loop simulations

The snowpack model has been tested at each experimental site. Since the system solves both mass- and energy- balances with an integration time step of 15 minutes, the observed meteorological forcings have been accordingly downscaled.

The following Sections show the Open Loop (OL) simulations of snow mass- and energy-related variables, with the aim of assessing the model predictions resulting from the deterministic control run, which does not consider the assimilation of snow-related data (no DA scheme included).

4.4.1 Snow mass-related variables

By solving the snowpack mass balance, the model supplies simulations of SWE and snow density of each snow layer. The combination of these simulated quantities provides information on the snowpack total SWE, average density, and snow depth (Sect. 2.4; Jonas et al., 2009).

To properly neglect the period when no snow cover is present, the time series are limited starting from October up to after the average melt-out date. Within this selected period zero values of snow depth and SWE have been considered in order to assess the model reliability in simulating the formation and disappearance of the snowpack.

Figures 4.3a, b and c show the time series over the full dataset period of each measurement station, namely over both the calibration and the validation periods. When assessing the accuracy of model predictions, it is noteworthy to consider that in most cases the snow density observations are indirect estimates derived from the observations of snow depth and SWE in-situ measurements (Sect. 3.3.3).

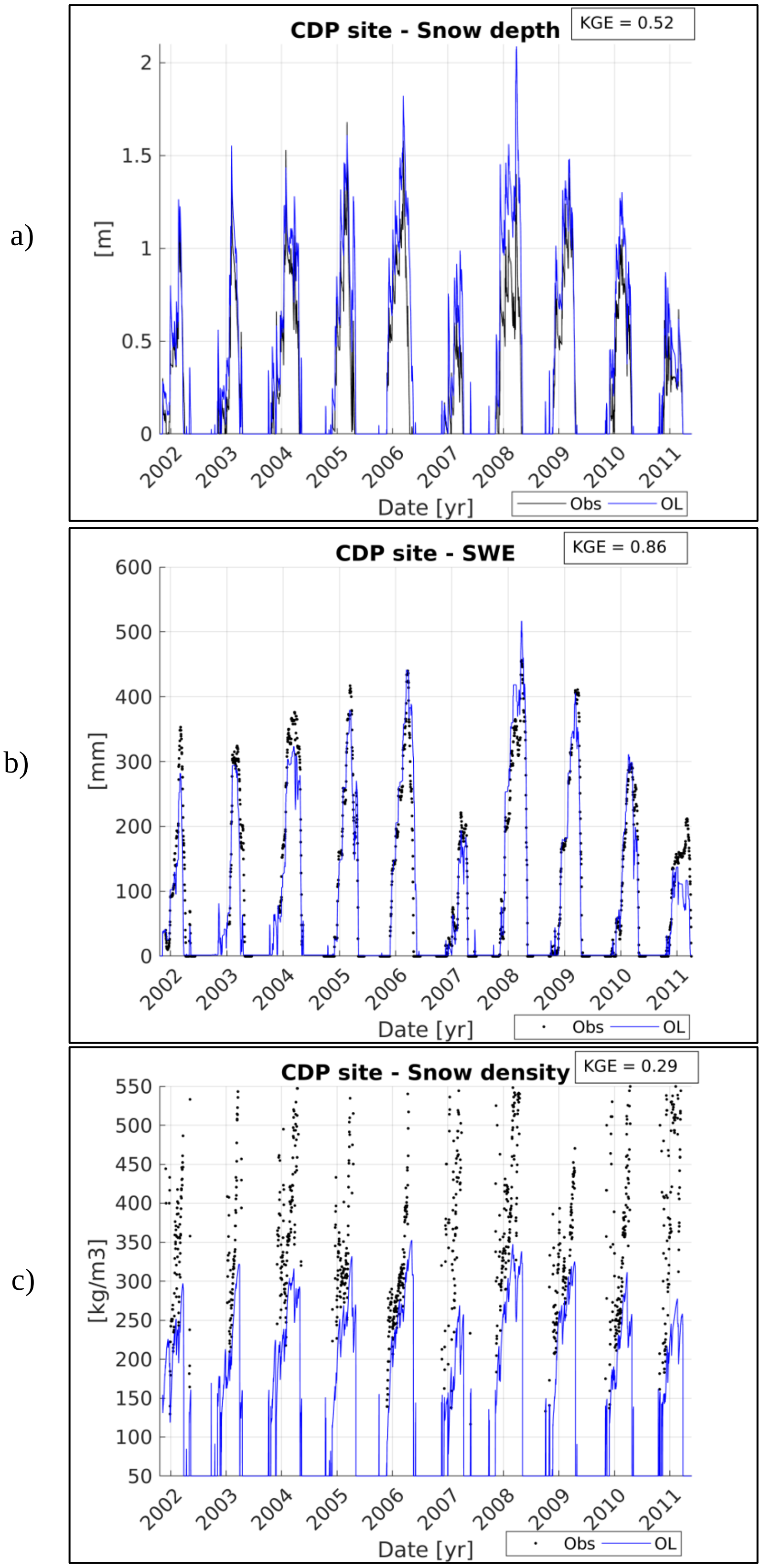

Figure 4.3a: *Seasonal OL snow mass-related simulations of (a) snow depth, (b) SWE, and (c) snow density – CDP site. The KGE indices are indicated in the upper right.*

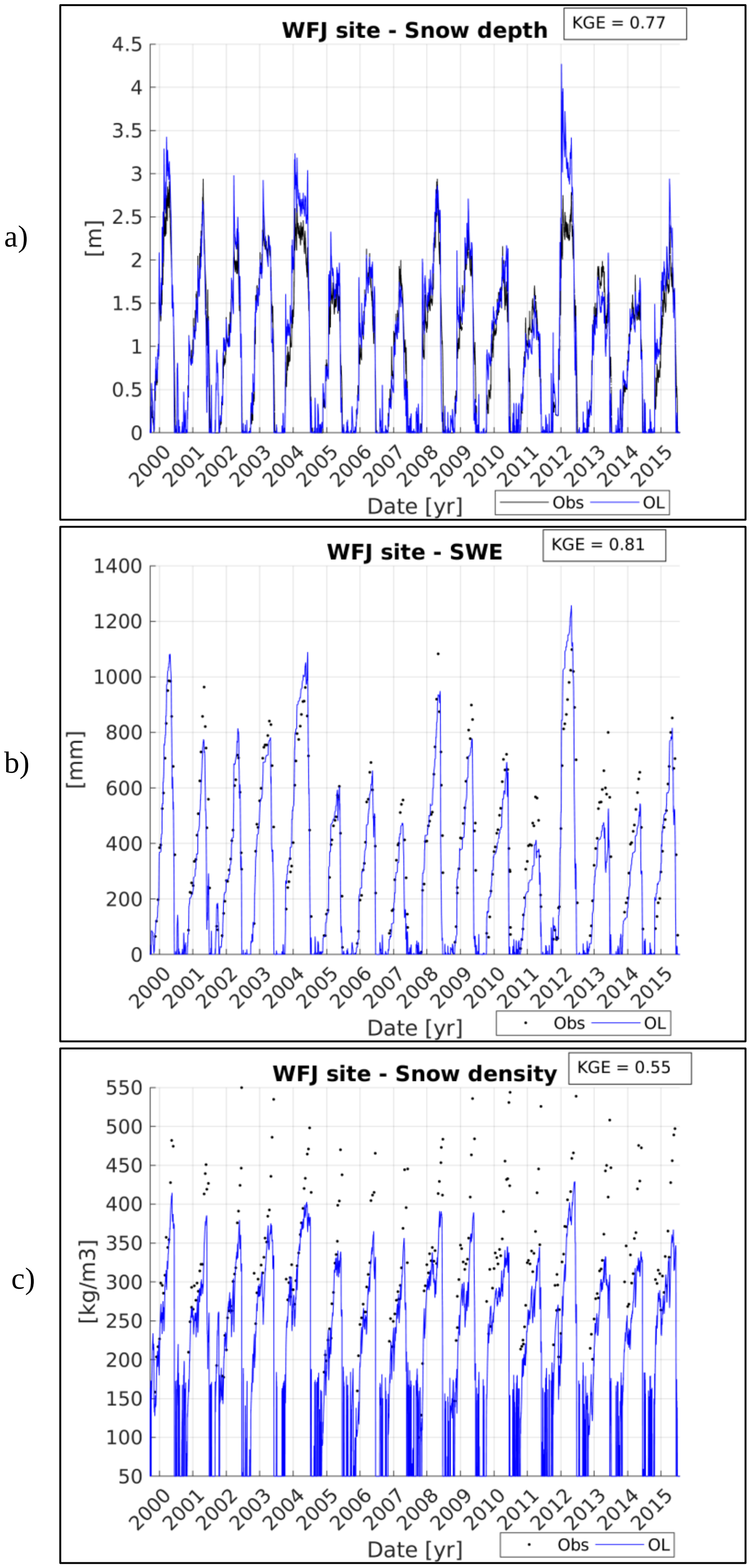

Figure 4.3b: *Seasonal OL snow mass-related simulations of (a) snow depth, (b) SWE, and (c) snow density – WFJ site. The KGE indices are indicated in the upper right.*

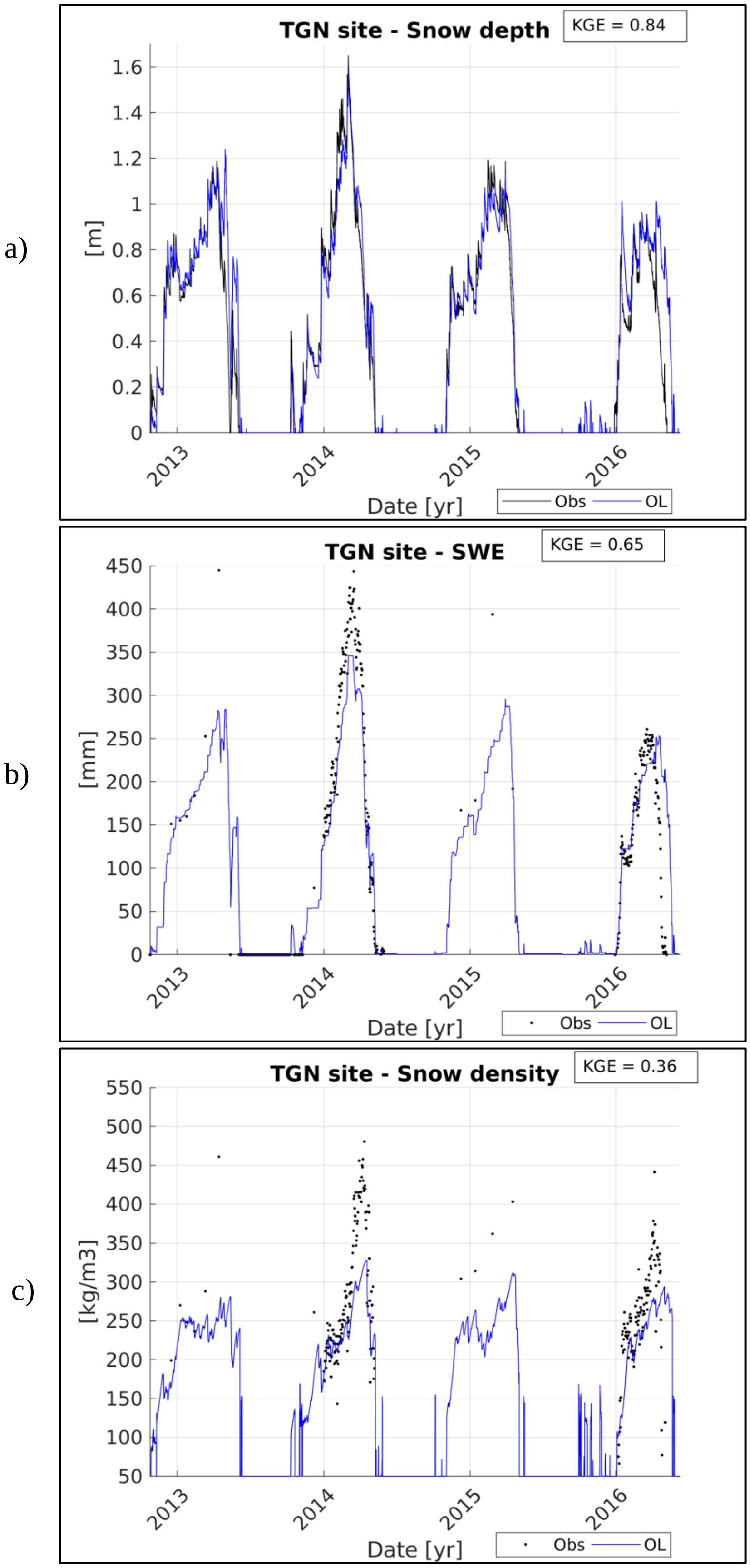

Figure 4.3c: *Seasonal OL snow mass-related simulations of (a) snow depth, (b) SWE, and (c) snow density – TGN site. The KGE indices are indicated in the upper right.*

The model succeeds in well representing the snow depth dynamics at CDP site, especially the melting timing. The accumulation period, instead, is mainly affected by the overestimation of snowfall events. This issue results from a systematic underestimation of the new snow density at this experimental site, where the higher average air temperature at its lower altitude (1350 m a.s.l.), with respect to the other two stations, impacts the estimation of the snowfall density. More generally, the model reveals a significant underestimation bias affecting the snow density simulations, which do not properly catch the snowpack settling process. As consequence, the snow ripening peaks range around 300 kg/m^3, without never exceeding 350 kg/m^3 (KGE = 0.29). Conversely, the SWE evolution is strongly consistent with the daily ground-based measurements, as proven by the considerably high KGE value of 0.86, with exception of the winter season 2010/2011, when a prominent underestimation is observed. Despite of the satisfying quality of the SWE predictions, the bias affecting the snow density dynamics hinders the accuracy of the snow depth simulations, with a resulting KGE index equal to 0.52.

With respect to the French station, at the Swiss site the model better represents the snowpack settling, with resulting higher density peaks of ripe snow ranging between 350 and 400 kg/m^3. As consequence, here the KGE of the snow density simulations reaches the value of 0.55, allowing a higher accuracy of the snow depth predictions (KGE = 0.77), for almost equivalent quality of the SWE predictions (KGE = 0.81). Nevertheless, also at WFJ the snow accumulation is overestimated due to sporadic inaccurate estimates of the new snow density, as observed throughout the winter seasons 2003-2004 and 2011-2012. Consistently with CDP, the timing of the melting dynamics is generally well represented.

At TGN the overestimation of the snowfall events is less significant, thus the snow accumulation is more consistently simulated. On the other hand, a clearly detectable delay of the melt-out date is observed for the snow seasons 2012-2013 and 2015-2016. However, the overall accuracy of the snow depth simulations is characterized through a high KGE value of 0.84. Once again, the underestimation bias of the snow density recurs, with peaks generally no higher than 300 kg/m^3 (KGE = 0.36). Throughout the winter seasons 2012-2013 and 2014-2015 the SWE predictions are consistent with the bi-weekly in-situ observations, except for the peaks observations before the beginning of the melting periods, when significant underestimations are measured. While a slight SWE underestimation is observed for the snow season 2013-2014, the delay in snow melting during the last winter 2015-2016 is prominent also in terms of SWE.

Lastly it is noteworthy to observe that at the Swiss and Italian sites, during the early winters spurious snowfall events are generated through the algorithm defining the precipitation phase (Froidurot et al., 2014). Indeed, while at CDP the precipitation phase is extensively assessed and provided within the dataset (Sect. 3.1.1; Lafaysse et al., 2017), at WFJ and TGN this quantity is empirically evaluated as a function of air temperature and relative humidity.

4.4.2 Snow energy-related variables

The accuracy of surface temperature and albedo simulations is assessed in order to investigate how the model succeeds in solving the snowpack energy balance. Consistently with the previous evaluation of the mass-related variables, the analysis period of albedo dynamics is limited throughout the snow seasons. Conversely, since at WFJ and TGN sites measurements of the surface temperature are provided over the whole dataset periods, the simulations of this variable are continuously analysed even in snowless conditions to extensively assess the model performances when no snow cover is present. Because ground-based observations of the surface temperature at CDP are supplied only during the snow seasons, the analysis is actually focused on the snow surface temperature.

Figures 4.4a, b and c show the time series of these energy-related state variables at the experimental sites.

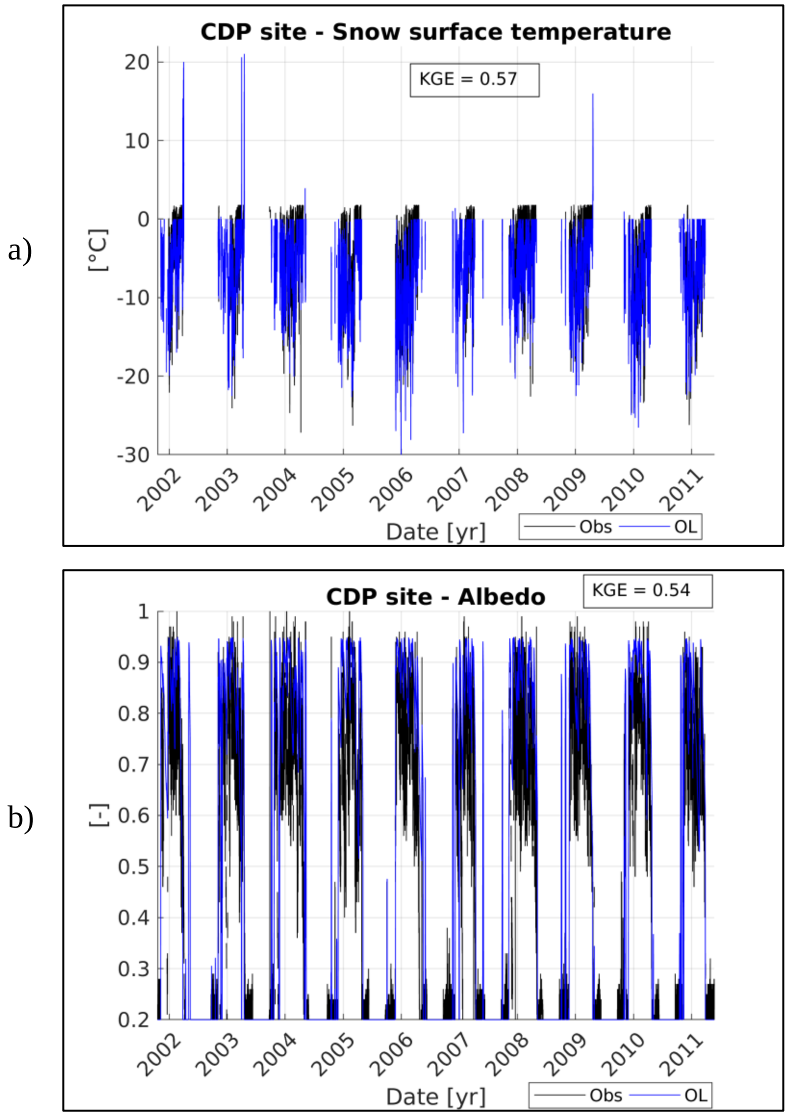

Figure 4.4a: *Seasonal OL energy-related simulations of (a) snow surface temperature and (b) albedo – CDP site. The KGE indices are indicated in the upper right.*

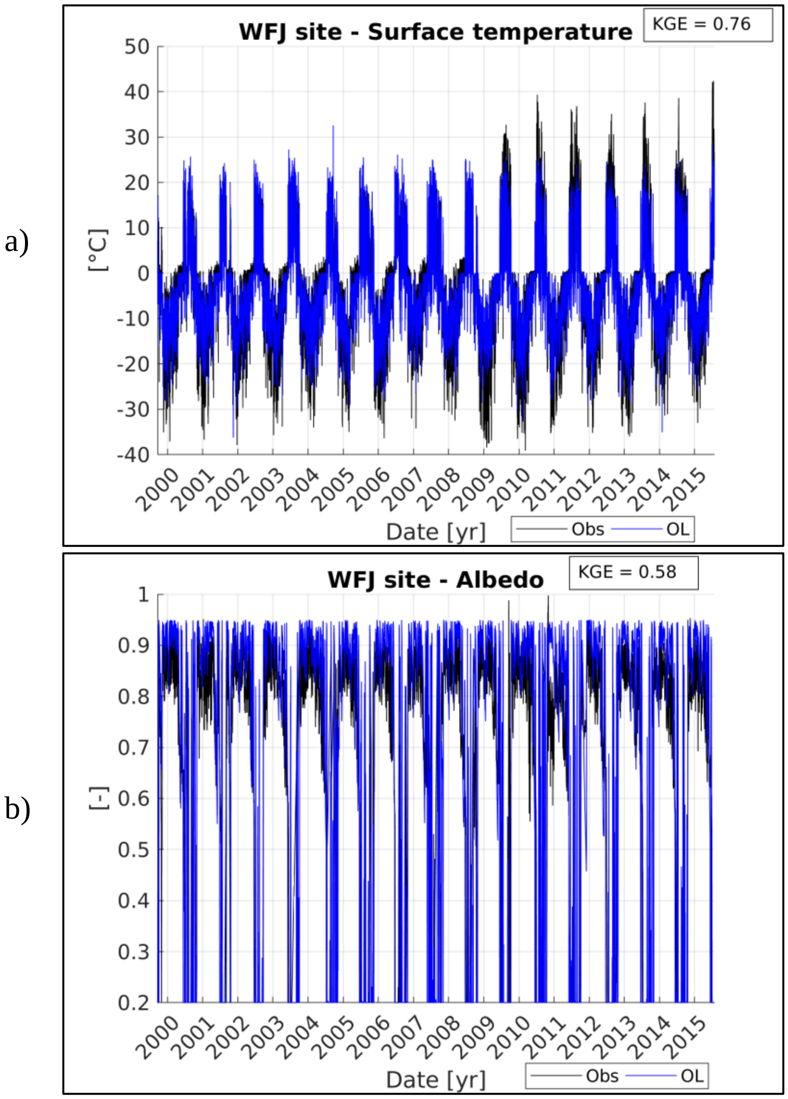

Figure 4.4b: *Seasonal OL energy-related simulations of (a) snow surface temperature and (b) albedo – WFJ site. The KGE indices are indicated in the upper right.*

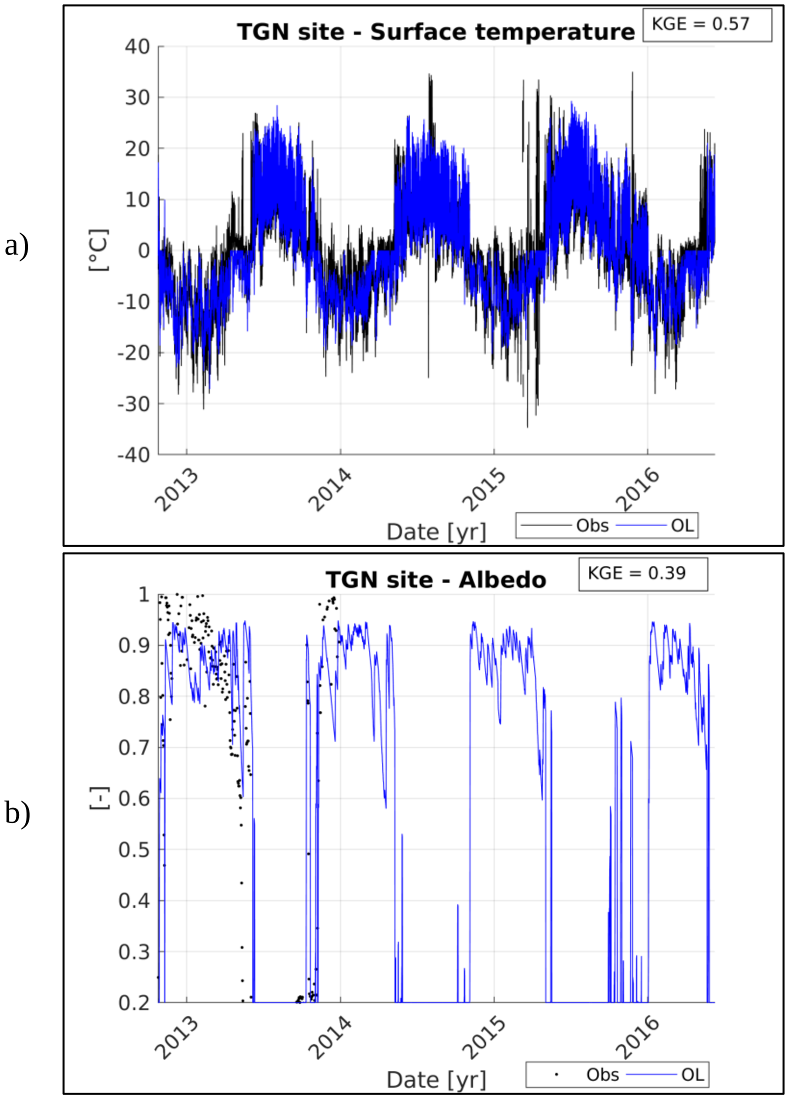

Figure 4.4c: *Seasonal OL energy-related simulations of (a) snow surface temperature and (b) albedo – TGN site. The KGE indices are indicated in the upper right.*

At the French site, the simulations of snow surface temperature are generally consistent with the in-situ measurements. However, even though the model well succeeds in representing the daily thermal cycle, it fails in reproducing the size of the temperature range. Indeed, the simulations reveal an underestimation of the diurnal peaks and a significant overestimation of the nocturnal ones. In spite of a generally satisfying positive correlation between the observed and modelled dynamics of the surface temperature, the model predictions are affected by a significant bias (*KGE* = 0.57). The same limitation recurs also at the other two experimental sites, where the surface temperature simulations are continuously analysed, instead. At the Swiss station, the *KGE* reaches a higher value of 0.76, while at the Italian site the *KGE* index drops to 0.57.

Consistently with the surface temperature simulations, the albedo dynamics are properly correlated with the in-situ measurements, even though they do not manage to well represent the size of the updates resulting from the snowpack evolution (e.g. snowfall and melting events). In the wintertime, the albedo simulations range is generally limited between 0.8 and 1, with resulting *KGE* indices around 0.5 at CDP and WFJ sites. On the other hand, at the Italian site the albedo predictions of the snow season 2012-2013 reveals a lower *KGE* value of 0.39, mainly due to the poor model capacity to catch the evolution of this energy-related state variable.

Tables 4.4a, b and c list the seasonal accuracy of the simulations of the analysed mass- and energy-related variables. Two statistical indices have been introduced in order to specifically assess both the correlation of the simulated time series and the error affecting their dynamics with respect to the in-situ observations. The selected statistical metrics are:

$$RMSE = \sqrt{\frac{1}{N}\sum_{k=1}^{N}(Obs_k - Exp_k)^2}$$

Root Mean Square Error (*RMSE*) [4.13]

$$R = \frac{cov(Obs, Exp)}{\sigma_{obs} \cdot \sigma_{exp}}$$

Correlation coefficient (*R*) [4.14]

Winter seasons	SD [m]		SWE [mm]		ρ_{snow} [kg/m^3]		T_{surf} [°C]		α [-]	
	RMSE	*R*	*RMSE*	*R*	*RMSE*	*R*	*RMSE*	*R*	*RMSE*	*R*
2001/2002	**0.14**	**0.92**	**70.5**	**0.84**	**116**	**0.78**	**3.44**	**0.79**	**0.15**	**0.76**
2002/2003	0.08	0.98	103.1	0.83	149.4	0.55	3.76	0.77	0.16	0.57
2003/2004	0.2	0.94	44.9	0.98	140.7	0.57	3.51	0.76	0.17	0.54
2004/2005	0.33	0.88	24.2	0.98	116.5	0.52	4.25	0.79	0.16	0.63
2005/2006	**0.34**	**0.85**	**55.6**	**0.92**	**68.63**	**0.87**	**5.67**	**0.72**	**0.17**	**0.73**
2006/2007	**0.27**	**0.86**	**20.8**	**0.99**	**213.2**	**0.57**	**3.98**	**0.73**	**0.19**	**0.64**
2007/2008	**0.52**	**0.93**	**52.7**	**0.99**	**145**	**0.68**	**3.76**	**0.73**	**0.18**	**0.61**
2008/2009	0.18	0.96	44.1	0.95	92.1	0.78	3.88	0.75	0.13	0.77
2009/2010	**0.25**	**0.98**	**31.2**	**0.95**	**150.4**	**0.43**	**4.41**	**0.79**	**0.16**	**0.56**
2010/2011	0.14	0.90	55.8	0.74	219	0.77	3.28	0.79	0.13	0.55

Table 4.4a: *OL simulations – Seasonal scores (RMSE and R) of snow depth (SD), SWE, snow density (ρ_{snow}), surface temperature (T_{surf}), and albedo (α) simulations – CDP site. Calibration winter seasons are highlighted in bold.*

Winter seasons	SD [m]		SWE [mm]		ρ_{snow} [kg/m^3]		T_{surf} [°C]		α [-]	
	RMSE	*R*	*RMSE*	*R*	*RMSE*	*R*	*RMSE*	*R*	*RMSE*	*R*
1999/2000	0.31	0.98	111	0.95	44.9	0.97	4.72	0.84	0.11	0.74
2000/2001	**0.22**	**0.96**	**159.4**	**0.91**	**64.1**	**0.81**	**4.52**	**0.77**	**0.13**	**0.59**
2001/2002	0.22	0.98	70	0.96	70	0.83	5.63	0.76	0.11	0.79
2002/2003	**0.18**	**0.97**	**126**	**0.88**	**71.5**	**0.75**	**4.52**	**0.75**	**0.10**	**0.71**
2003/2004	**0.48**	**0.95**	**111.2**	**0.97**	**68.5**	**0.68**	**3.97**	**0.79**	**0.11**	**0.61**
2004/2005	0.24	0.98	73.5	0.94	66	0.85	5.16	0.81	0.13	0.64
2005/2006	0.23	0.94	79.6	0.94	60.7	0.92	5.47	0.84	0.12	0.70
2006/2007	0.14	0.98	106.3	0.91	92.9	0.44	3.53	0.83	0.08	0.61
2007/2008	0.36	0.92	181	0.82	113.9	0.44	4.67	0.77	0.16	0.67
2008/2009	0.30	0.90	168.3	0.86	87.3	0.91	6.43	0.83	0.10	0.74
2009/2010	0.29	0.86	135	0.86	152.5	-0.03	5.64	0.84	0.12	0.80
2010/2011	**0.18**	**0.96**	**105.6**	**0.98**	**101**	**0.68**	**4.52**	**0.85**	**0.13**	**0.56**
2011/2012	**0.68**	**0.96**	**182.9**	**0.93**	**81.5**	**0.77**	**4.54**	**0.82**	**0.12**	**0.76**
2012/2013	**0.22**	**0.96**	**185**	**0.87**	**112.6**	**0.63**	**4.67**	**0.84**	**0.12**	**0.79**
2013/2014	**0.13**	**0.97**	**97.6**	**0.98**	**93.2**	**0.89**	**4.26**	**0.80**	**0.11**	**0.72**
2014/2015	**0.33**	**0.90**	**122.6**	**0.87**	**76.7**	**0.86**	**4.26**	**0.82**	**0.13**	**0.69**

Table 4.4b: *OL simulations – Seasonal scores (RMSE and R) of snow depth (SD), SWE, snow density (ρ_{snow}), surface temperature (T_{surf}), and albedo (α) simulations – WFJ site. Calibration winter seasons are highlighted in bold.*

Winter seasons	SD [m]		SWE [mm]		ρ_{snow} [kg/m^3]		T_{surf} [°C]		α [-]	
	RMSE	*R*	*RMSE*	*R*	*RMSE*	*R*	*RMSE*	*R*	*RMSE*	*R*
2012/2013	0.17	0.86	69.7	0.96	84.9	0.67	4.90	0.80	0.14	0.47
2013/2014	**0.10**	**0.97**	**43**	**0.98**	**62.8**	**0.89**	**4.43**	**0.68**	**-**	**-**
2014/2015	**0.07**	**0.96**	**77.1**	**0.88**	**86**	**0.71**	**5.60**	**0.64**	**-**	**-**
2015/2016	0.25	0.66	71.9	0.55	91.2	0.37	3.82	0.81	-	-

Table 4.4c: *OL simulations – Seasonal scores (RMSE and R) of snow depth (SD), SWE, snow density (ρ_{snow}), surface temperature (T_{surf}), and albedo (α) simulations – TGN site. Calibration winter seasons are highlighted in bold.*

Ground temperature simulations

The comprehensive datasets supplied by the measurement stations provide observations of ground temperature at different depths (Sect. 3.1). Since the model deep soil temperature (T_d) is representative of soil layer from a depth of 15 cm, this state variable is assumed to be the most suited reference quantity subject to the snow thermal insulation, according to the design of the model vertical snowpack scheme. Figure 4.5 shows the simulations of the ground temperature compared to the in-situ measurements at 20- and 10-cm depth at the French and Italian stations, respectively, and just below the ground surface at WFJ.

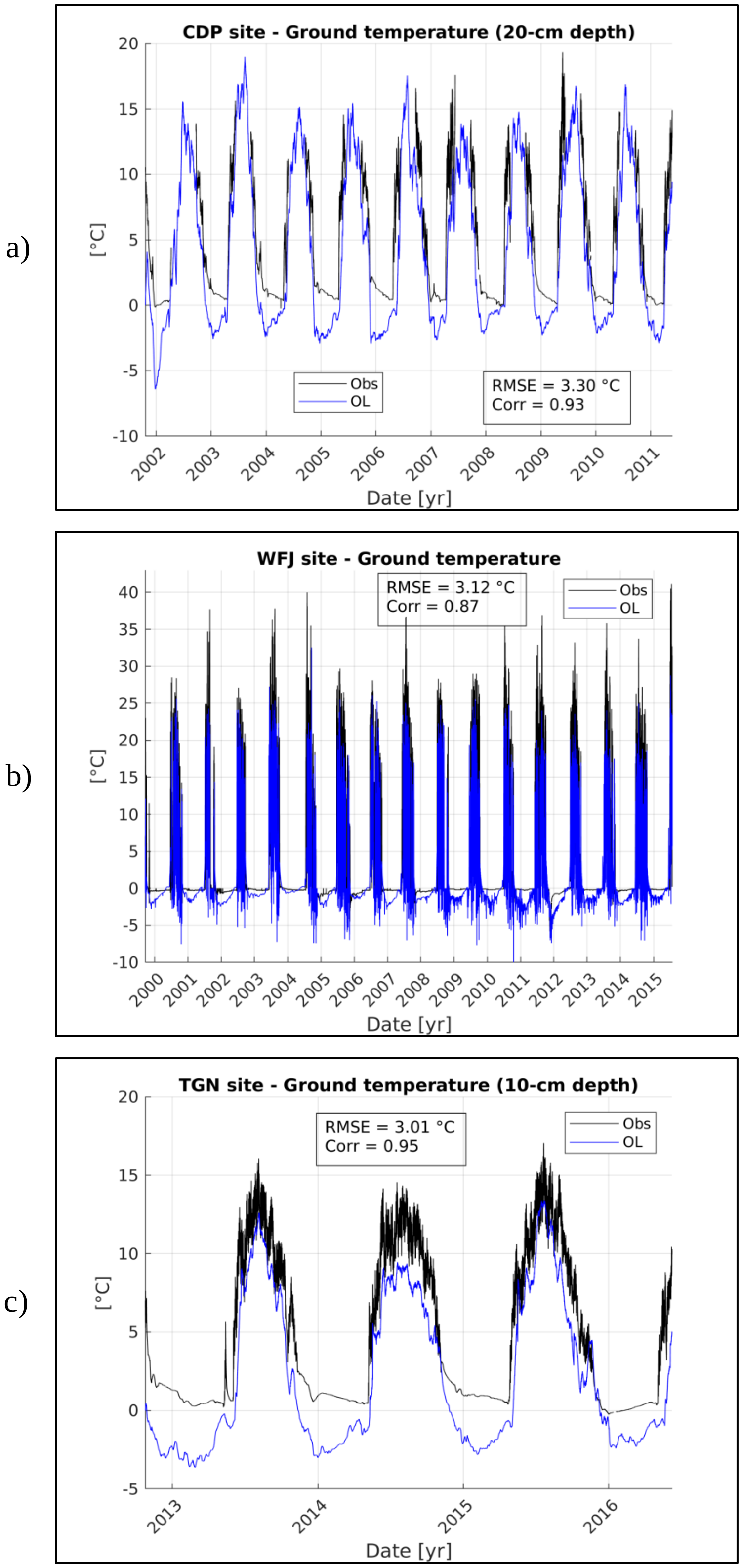

Figure 4.5: *Seasonal OL simulations of (a) ground temperature at 20-cm depth at CDP site, (b) soil temperature, just below the ground surface, at WFJ site, and (c) ground temperature at 10-cm depth at TGN site.*

At CDP site, the in-situ measurements of 20-cm depth ground temperature are limited to the winter seasons. While no significant bias is observed during both early winter and melting periods, the model simulations underestimate the ground temperature throughout the snow seasons. When assessing this bias, it is noteworthy to consider that T_d is the average temperature of a thick ground layer starting at a depth of 15 cm (Figure 4.2), and therefore it is affected by an average effect of the snow thermal insulation, which is necessarily less effective than the actual insulation at 20-cm depth. In spite of a significant *RMSE* of about 3°C, the time series are strongly correlated.

The Swiss and Italian stations supply observations of ground temperature throughout the whole datasets period. With the aim of assessing the simulations in snowy and snowless conditions, Table 4.5 shows the statistical scores evaluating snowy and snowless periods, separately. In the presence of snow cover, *RMSE* values are generally lower than in snowless conditions, even though with lower positive correlations. On the other hand, when no snow cover is present, *RMSE* values increase above 3°C at the Italian site and even close to 5°C at WFJ, but with significantly higher correlations.

The lower *RMSE* value of the ground simulations in presence of snow cover is mainly due to the narrowed size of the deep ground temperature range, instead of a higher capacity of the model in reproducing this variable in snowy conditions, as proven by the lower values of the correlation coefficient. Indeed, consistently with the result at CDP, the model does not succeed in properly simulating the snowpack insulating effect. However, it is noteworthy that the simulations are representative of average temperatures hardly comparable with the in-situ measurements, which are sampled at specific depths. Conversely, the wider scale of the daily thermal cycle in snowless conditions entails higher *RMSE* values due to the under- and overestimation of the temperature peaks, as previously discussed. Nevertheless, the model better succeeds in representing the dynamics of the ground temperature, with resulting higher correlations.

Ground temperature [°C]				
	WFJ site		TGN site	
	RMSE	*R*	*RMSE*	*R*
Snowy condition	2.00	0.62	2.86	0.54
Snowless condition	4.95	0.85	3.17	0.89

Table 4.5: *OL simulations of ground temperature – Statistical scores during snowy and snowless periods at WFJ and TGN sites.*

4.4.3 Snow melting fluxes

As previously explained, according to the purpose application of coupling the snow model with an assimilation algorithm, the degree of detail of the model snowpack physics is accordingly limited in order to lighten the system scheme by still maintaining the physical consistency. One of the main approximations concerns the liquid water storage, which is neglected, as well the refreezing of meltwater. As a consequence, the snow mass is reduced by the meltwater resulting from the dynamics of the snowpack thermal state, which is assumed to drain as surface runoff.

Therefore, the model snow melting is hardly comparable against in-situ local runoff observations due to the lack of the physical representation of the main processes involved within the snowpack hydrological balance. Nevertheless, even though the model is unlikely to well catch the runoff volumes, it is noteworthy to assess the consistency between the model melting fluxes and the observed runoff trends.

The French and Swiss stations supply snowmelt runoff data estimated through lysimeters of a surface area of 5 m^2, with hourly and 10-min measurement frequency, respectively (Sect. 3.1).

With the aim of smoothing possible inconsistencies affecting the melting simulations due to the model physical limitations, the comparative analysis has been performed at monthly scale by averaging both the observed and simulated time series, as shown in Figure 4.6.

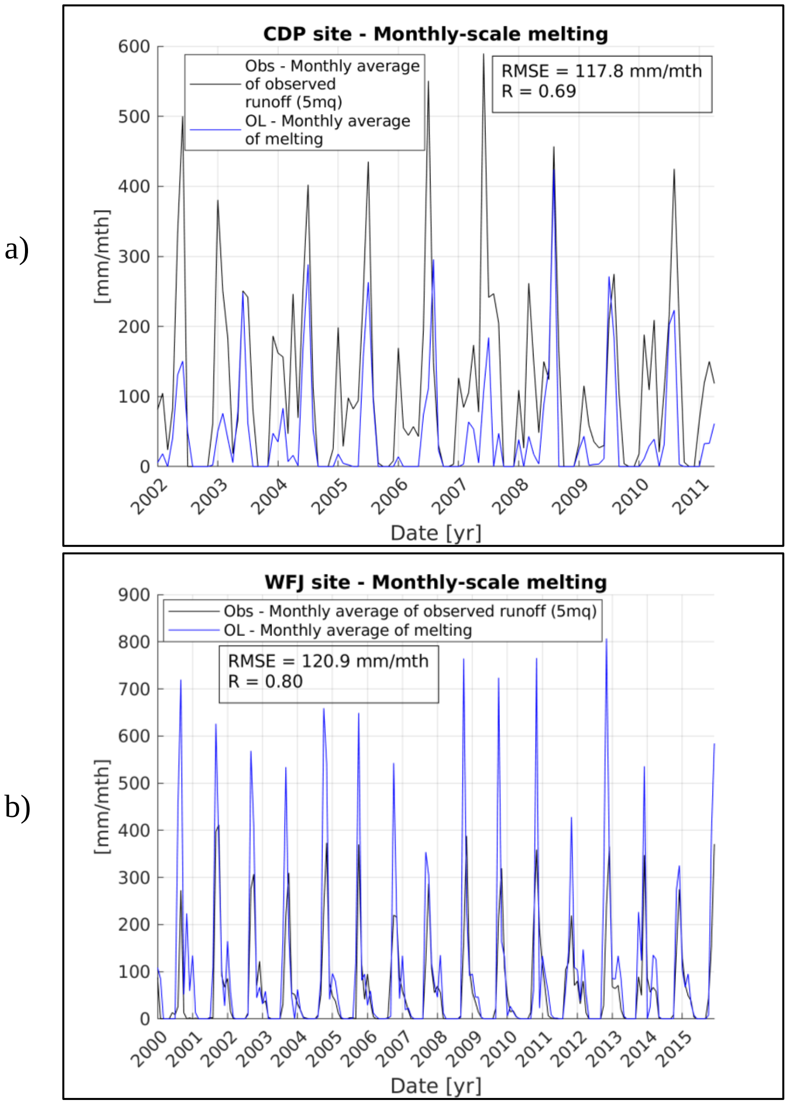

Figure 4.6: *Seasonal OL of model monthly-average simulations of snow melting compared with in-situ runoff measures over a surface area of 5* m^2 *at (a) CDP and (b) WFJ sites. RMSE and R indices are provided.*

With respect to the French site, at WFJ the simulations are strongly correlated with the runoff measurements (*R* = 0.8). Although the model well succeeds in representing the dynamics, the melting volumes are generally overestimated with respect to the observations. This bias is supposed to mainly result from the direct release of the meltwater, according to the model physical scheme. In reality, instead, the meltwater is actually retained within the snowpack, due to infiltration, storage, and refreezing processes.

Conversely, at CDP the melting simulations are less correlated (*R* = 0.8), even though with an almost equivalent bias volume. The poorer consistency can be mainly ascribable to the more complex dynamics occurring within the snowpack at the lower altitude of this site. Because the air temperature frequently rises to over 0°C (around snow melting point) during the wintertime, possible melting and refreezing events are likely to occur more frequently with respect to the Swiss site.

In order to further investigate the melting simulations at CDP, the daily SWE measurements available at this site have been used to derive melting estimations assumed to be more consistent with the model predictions. The main assumption considers the decreases in the observed SWE amount as representative of melting events. Of course, it is noteworthy to highlight that this hypothesis can entail misleading considerations, since it does not take into account possible sublimation events. Nevertheless, this comparison aims at a qualitative assessment of the consistency between the cumulative time series, rather than an analysis of the resulting melting volumes.

Figure 4.7 presents the cumulative trends of the daily-averaged melting rates throughout the whole dataset period.

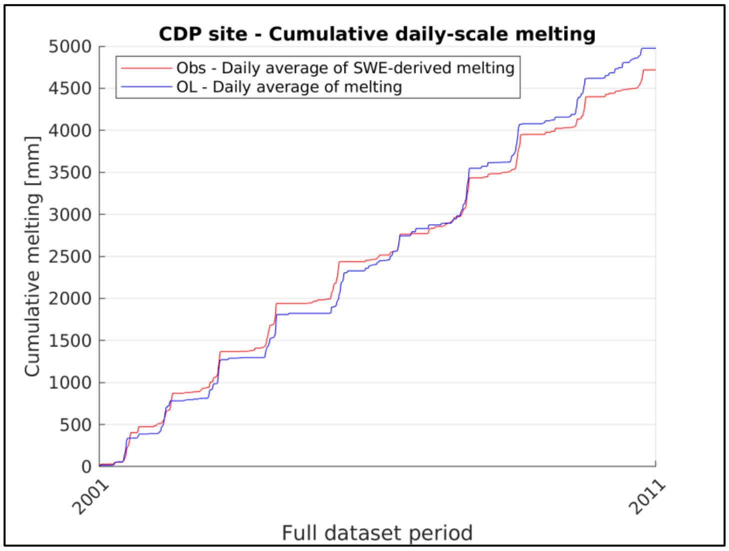

Figure 4.7: *Consistency analysis between cumulative time series of daily melting provided by model simulations and derived from SWE in-situ observations, at daily scale – CDP site.*

Although the analysis relies on an inaccurate assumption, the cumulative melting rates are strongly consistent with each other, with an overall overestimation of the model simulations of about 5% with respect to the derived observations.

4.4.4 Turbulent and ground heat fluxes

The Italian measurement station provides observations of ground and turbulent (i.e. latent and sensible) heat fluxes with a measurement frequency of 30 minutes throughout the whole dataset (i.e. snowy and snowless periods). Because the model explicitly simulates these heat fluxes by solving the snowpack energy balance, a comparative analysis has been carried out with the aim of assessing the consistency of the model predictions with the in-situ measurements. Figure 4.8 shows the scatterplots between the model heat fluxes and the heat-related observations.

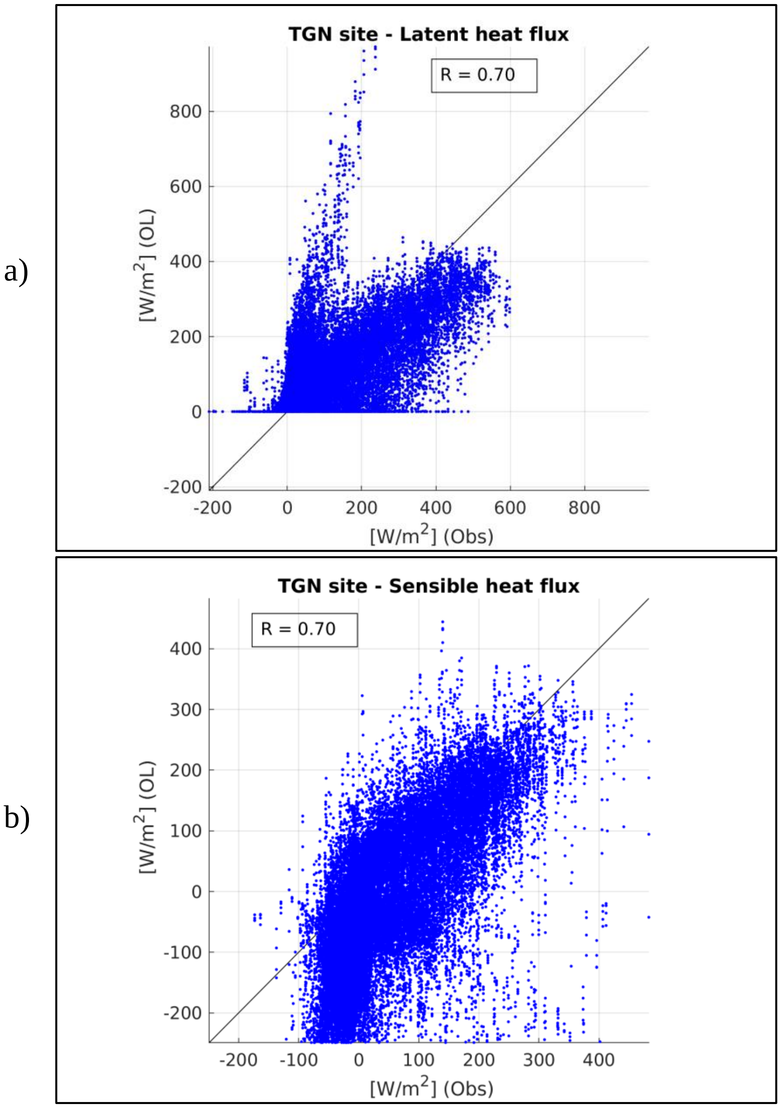

c)

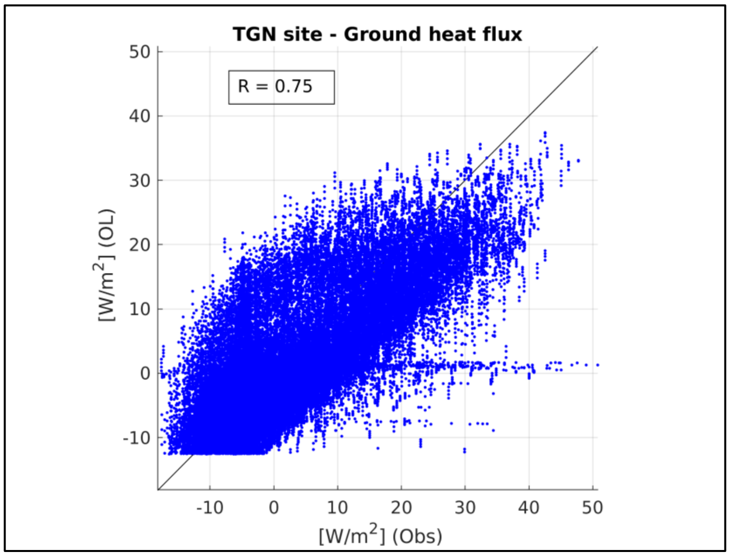

Figure 4.8: *Scatterplots between OL simulations of (a) latent, (b) sensible, and (c) ground heat fluxes and 30-min in-situ measurements – TGN site. The correlation coefficients R are indicated.*

The simulations of heat fluxes are generally well correlated with the observations, as proven by the highly positive correlation values.

When assessing the model latent heat, it is noteworthy to consider that the latent heat is transferred by vapor exchange between the snowpack and atmosphere due to phase change of water (i.e. condensation, evaporation, melt, freezing, sublimation). This quantity is positive when heat is supplied to the snowpack (e.g. sublimation and melting events), and negative if heat fluxes are released from the snowpack to the atmosphere (e.g. refreezing process). Since the model does not simulate deposition, condensation, and freezing processes, it necessarily overestimates the observed negative values, which are sporadic during the snow seasons, however. Nevertheless, the simulations turn out to overestimate the observed lower positive latent heat (i.e. in wintertime) and underestimate the more intense fluxes (i.e. in snowless conditions).

The sensible heat fluxes result from the transfer of thermal energy driven by temperature gradients between the snowpack surface and the atmosphere. According to the sign of the temperature difference, this convective transfer can be headed to or from the snowpack. In springtime, when air temperatures largely exceed the snow surface ones, melting snowpacks gain high sensible heat fluxes (positive quantity). Conversely, during winter or at night during the melt season, the snowpack can be warmer than air with a resulting loss of energy (negative quantity). While the model predictions generally underestimate the negative sensible heat fluxes, namely during the winter seasons, in melting periods and in snowless conditions the simulated and observed time series are better correlated.

With respect to the other two variables, the ground heat fluxes are generally more consistent with the in-situ observations, with a resulting correlation coefficient equal to 0.75.

With the aim of extensively assessing the reliability of the model simulations, the time series of the daily average heat fluxes have been analysed (Figure 4.9). The choice of averaging the fluxes is assumed to smooth possible inconsistencies affecting the model energy balance.

The daily average latent heat simulations reveal a lower correlation equal to 0.57 with respect to the previous evaluation, with prominent over- and underestimation in snowy and snowless conditions, respectively.

Even though the simulated time series of daily sensible heat fluxes are more correlated with the in-situ observations (R = 0.81), they are affected by a significant underestimation bias in wintertime, mainly ascribable to the poor accuracy of the snowpack surface temperature predictions.

During snow seasons, the model ground heat fluxes have more oscillating trends due to the limited model capacity to properly reproduce the snow thermal insulating effect, as indicated by the lower correlation equal to 0.68.

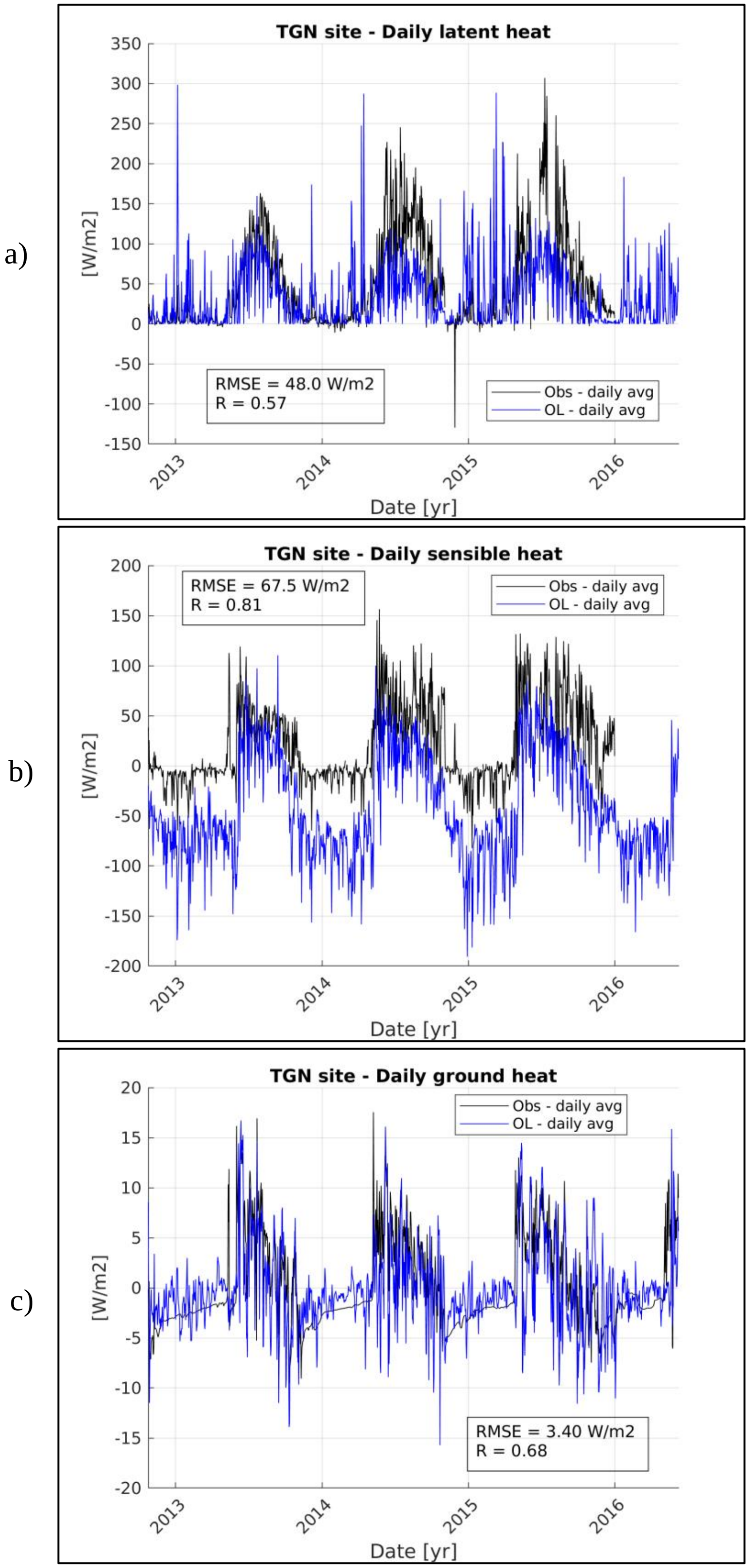

Figure 4.9: *OL simulations of daily average (a) latent, (b) sensible, and (c) ground heat fluxes – TGN site. RMSE and R values are indicated.*

CHAPTER 5
Data assimilation techniques

Data Assimilation (DA) provides a theoretical framework and practical methodologies for addressing constrained estimation problems. The main purpose is the merging of measurements and model predictions under the assumption that both supply useful information on the system state. With the aim of obtaining a statistically optimal and dynamically consistent estimate of the evolving system state, all the sources of information are properly weighted according to their degrees of uncertainty to obtain a combined estimate with the desired statistical properties (e.g. unbiased, minimum variance).

The observations, namely ground-based and remotely-sensed data, are characterized by different spatial and temporal resolutions and they generally suffer from several measurement errors (Sects 2.4, 2.5). When dealing with remotely-sensed data it is noteworthy also to consider that they are indirect retrievals of the variables of interest (e.g. electromagnetic radiation is used to indirectly estimate land surface physical properties) and thus significantly affected by uncertainty.

Even though models are simplified depictions of real systems, they rely on strong physical constraints (e.g. conservation of mass and energy balances), which limit the degrees of freedom in interpreting the observed data. Moreover, the dynamical and spatial dependencies within a model can be used to retrieve information wherever no observation is available. However, models are affected by uncertainties as well, and they generally strongly depend on the optimal estimation of ruling parameters. DA methods involve all the procedures necessary to systematically take into account spatial and temporal variability of observational and model errors.

Two main DA approaches can be implemented. Sequential assimilation uses observations, as soon as they are available, to iteratively update and reinitialize the model state before the integration continues forward in time. Non-sequential assimilation uses all the available observations up to the current assimilation time step to correct the system state and obtain the best overall fit of the state variables to the observational data.

A further distinction can be made between intermittent techniques processing the observations in small batches, or methods considering longer observational periods with a resulting analysis state smoother in time. Compromises between these approaches are also possible.

5.1 State of art

Meteorology and oceanography pioneered DA systems with the aim of enhancing short term forecasts. Conversely, the initial lack of large domain observations prevented a fast development of DA schemes for hydrological applications (Walker et al. 2003). Recently, a widespread interest aims at introducing assimilation schemes within the land-atmosphere interaction research field. Several DA techniques have been developed, differing in numerical cost, optimality and suitability for real-time applications. In the framework of snow modelling, the sequential DA approach is widely used, since it allows to readily process the observational data as they become available and sequentially update the model snowpack state.

The most basic technique is the Direct Insertion (DI). This method promotes the simple replacement of forecast predictions with observations, whenever they are available, within the model simulations. This means that according to this approach model predictions are completely unreliable and observations are considered as ground truth. By simply inserting the observations, which are notoriously imperfect, a possible significant bias can be introduced and an unbalanced state estimate can occur, with a resulting model shock. This technique has been tested in several studies. Liston et al. (1999) tested DI method to assimilate observed snow spatial pattern into an atmospheric model. Despite several limitations, this DA approach effectively made the modelled snow pattern more consistent with observations, although system deficiencies in simulating sub-grid snow distribution required the implementation of a snow sub-model accounting for air temperature and precipitation variability. Rodell and Houser (2004) employed the same simple technique to assimilate MODIS SCA observations for the updating of snow-water storage into a Land Surface Model (LSM). Every time step when some discrepancy was detected between model predictions and MODIS observations, SWE simulations were adjusted by either removing the simulated snow or adding a thin layer to neglect spurious information. When comparing these simulations with the outputs of a (not updated) control run, the assimilation of snow data proved to generally ensure more accurate snow coverage. Malik et al. (2012) applied the DI technique to assimilate snow albedo observed by MODIS sensor into a LSM, whose simulations of fluxes and snow properties, with and without the assimilation of observations, were evaluated against in-situ measurements of snow albedo, upward shortwave radiation and snow depth. Even though a mean error reduction was not always evident because of the limited impact of snow albedo updates beyond snowfall events, the assimilation scheme demonstrated to enhance the model simulations, especially for the simulated upward shortwave radiation.

An improved version of the DI scheme is the Optimal Interpolation (OI) technique. Whenever observations are available and assimilated, model predictions are adjusted according to an a priori error structure of both observations and model estimates, which are supposed to be constant throughout the simulation. Brasnett (1999) employed the OI method to assimilate snow depth observations into a simple snow dynamics model to obtain an operational real-time analysis of snow depth status. The verification of the analysis snow depths allowed to understand that they generally turned out to be more accurate than climatological estimates. More recently, Liston and Hiemstra (2008) applied OI approaches to assimilate synthetic ground- and satellite-based snow data within a snow model by constraining its predictions with their discrepancies with observations. Since these corrections could be applied retroactively to improve the simulation fields before each assimilation time step, this technique resulted to be suitable for reanalysis applications. The implementation of these schemes improved the modelled SWE distributions, with a more realistic spatial heterogeneity against the observations.

More advanced is the Cressman scheme (Cressman, 1959), accounting for an empirically chosen weighting function in terms of influence radius, which sets the interval within each observation is used to update the model. Observations included within the influence radius are weighted according to their distances to the model grid points. For more than 20 years Cressman scheme has been operatively employed for the assimilation of SYNOP (surface synoptic observations) data in ERA-Interim, a global atmospheric reanalysis produced by the European Centre for Medium-Range Weather Forecasts (ECMWF) (Dee et al. 2011). Even though the corresponding MODIS image supported the results of the updated Cressman analysis for the cloud-free regions (Drusch et al. 2004), the comparison between the operational product and the satellite-derived snow cover enabled to identify several deficiencies in areas with intermittent and/or patchy snow cover and regions with a low density of observations (Balsamo et al. 2015).

Similarly to the Cressman scheme, the Nudging method (or Newtonian relaxation) (Stauffer and Seaman, 1990) allows to take into account the observational uncertainty, which is a priori defined. According to this DA technique, a correction term is added to the prognostic model equations with the aim of gradually relaxing the predictions towards observations. The resulting nudging term is proportional to the discrepancy between model predictions and observations. Boni et al. (2010) implemented a nudging scheme to update a prior SWE estimates at watershed scale. Daily assimilation of an interpolated map of snow depth measurements, opportunely merged with MODIS SCA observations, enabled to improve performances of a simple snow dynamic model.

At a higher level of complexity among the sequential DA methods, Kalman filtering enables to evaluate the optimal weighting between modelled and observed states, according to their degrees of uncertainty (Kalman, 1960; Evensen, 2003). The main feature distinguishing this approach from more static ones is the dynamic updating of the forecast error covariance during the simulation. Several techniques based on Kalman filtering have been developed.

The standard Kalman Filter (KF) (Gelb, 1974), which relies on the system linearity assumption, is based on the relative contribution of the error covariance matrices of both model predictions and observations to obtain a statistically optimal estimate for given parameters set and uncertainties. This technique applies a standard error propagation theory, which generates an analysis state by adding a correction term to the a priori state. The correction is computed as the difference between the model estimate of the system state and the observed state, both modulated through the Kalman Gain that takes into account the information supplied by both the covariance matrices.

The Extended Kalman Filter (EKF) (Miller et al. 1994) allows to deal with nonlinear dynamic systems through a linearized statistical approach. This technique relies on an adjoint and tangent linear model to propagate the error covariance matrix forward in time. Thus, this technique is able to provide only a near-optimal estimate due to the linear approximation of the model through a Taylor series expansion. Sun et al. (2004) developed a one-dimensional EKF scheme to assimilate synthetically generated SWE observations into a LSM, neglecting the update of unobserved model states. Since SWE is highly correlated with snow depth and heat content, and independent of snow density and temperature, the study demonstrated that all snowpack prognostic variables can be efficiently reproduced by only assimilating SWE satellite observations and reconstructing the other prognostic snow states by using diagnostic model variables. Dong et al. (2007) used the assimilation system developed by Sun et al. (2004) to assimilate SWE data derived from SMMR observations into a LSM by sequentially updating both the system state and the covariance estimates, as observations became available. Compared to in-situ observations, the EKF allowed improving SWE predictions. In spite of benefits in its implementation, EKF is not a widespread method in operational applications due to the requirement of a sizeable computational time. Furthermore, even though EKF-based schemes generally result to well succeed in updating model simulations, in presence of strong system nonlinearities unstable results can be attended (Moradkhani 2008).

With the aim of overcoming the inaccuracy of the linearization procedure affecting the filter performance due to possible strong model nonlinearities, the Ensemble Kalman Filter (EnKF) has been developed (Evensen, 1994). Unlike the KF and EKF schemes, this method does not require a model linearization since the error estimates are evaluated from an ensemble of possible model realizations using the Monte Carlo approach (Evensen, 2003). Moreover, this method has the further advantage of being able to handle any number of variables in the update scheme. An increasing number of studies on snow hydrology have contributed to confirm the EnKF as a well-performing technique enabling to enhance the accuracy of hydrological simulations by consistently updating model predictions through the assimilation of snow-related observations. Andreadis and Lettenmaier (2005) applied an EnKF scheme to assimilate MODIS SE and AMSR-E SWE products into a macroscale hydrologic model to update SWE predictions. The study aimed at directly updating the SWE estimates through a snow depletion curve (SDC) in order to obtain a proper observation operator. Indeed, MODIS observations only supply information about presence or absence of snow, whereas hydrological and LSMs mainly aim to simulate SWE. This issue leads to the need of a conversion from simulated SWE data and remotely-sensed SCA and vice versa through SDCs. In their study, the assimilation of snow data successfully updated SCA over the domain of interest and guaranteed an improvement of SWE estimates. In comparison to ground-based observations, a larger DA impact was observed mainly in the ablation season, less during snow accumulation period, when EnKF estimates resulted to be very close to the OL ones. By using the same DA scheme, the study attempted to evaluate the filter performance in assimilating AMSR-E SWE data, which did not provide noteworthy results, instead. This analysis enabled to better understand the importance of an accurate parameter estimation required to create the SDC, which strongly impacted the assimilation performance. Clark et al. (2006) proposed an alternative framework to assimilate synthetic remotely-sensed SCA data in hydrologic and LSMs in order to improve streamflow simulations. SCA observations were assimilated through an EnKF scheme to modify the sub-grid probability density function (pdf) of snow-related variables. The assimilation of SCA data turned out to modify both the sub-grid SWE distribution and the basin water budget. On the other hand, the accuracy of streamflows was only slightly increased, mainly because of the quite fast transition from snow covered to snow free conditions. Since the snow dynamics are basin dependent, SCA information were supposed to be most useful in basins where snow cover is ephemeral. Consistently with Andreadis and Lettenmaier (2005), errors reduction was negligible in the accumulation period. Slater and Clark (2006) implemented an EnKF and an Ensemble Square Root Kalman Filter (EnSRKF) (Whitaker and Hamill, 2002; Tippett et al. 2003) to assimilate ground-based SWE observations. This study aimed at improving the estimation of SWE initial conditions for the ultimate objective of streamflow forecasting within a distributed conceptual hydrological model. Both ensembles of model forcing and assimilated data were derived through a spatial interpolation and the error structures were evaluated through a cross validation. Several experiments enabled to demonstrate that, especially during the melt season, the combined use of model and independent observations enabled to improve the model SWE initial conditions, which lead to a better short-term streamflow forecast. Su et al. (2008) investigated the feasibility of assimilating through the EnKF approach the MODIS FSC for the optimal retrieval of continental-scale SWE within a highly complex LSM. For this purpose, they proposed a newly developed observational operator based on snowpack density. Ground-based measurements and AMSR-E estimates were used to evaluate the assimilation performance, which demonstrated the validity of the proposed method. The analysis of the spatial differences between the EnKF and OL simulations suggested that the filter more accurately simulated the seasonal variability of SWE and reduced the uncertainties associated with the large-scale simulations. Magnusson et al. (2014) analysed the potential of providing a distributed snow model with point snow observations by assimilating ground-based SWE data through an EnKF scheme to improve the simulations. They found out that the simulations resulting from the joint assimilation of snowfall and snowmelt rates outperformed the snow model predictions relying on the assimilation of SWE observations, mainly thanks to a higher flexibility in defining error statistics. More recently, Griessinger et al. (2016) investigated the benefit of assimilating SWE observations for hydrological applications in snow-dominated regions. They evaluated the sensitivity of an operational hydrological model to the external input of snowmelt data provided by a spatially distributed snow model running in different configurations. They found that the runoff predictions relying on the sequential assimilation of snow-related observations outperformed the control simulations without DA, especially at high elevations. However, no prominent effect of the assimilation of snow data was observed at low and mid-elevations in term of runoff, due to the lower contribution of snowmelt to the runoff generation. Huang et al. (2017) evaluated whether the assimilation of SWE data through an EnKF scheme can reliably enhance seasonal streamflow predictions. They extensively examined several methodological issues, namely the observation operator and the impact of varying the uncertainty of both observations and model simulations on the forecasting skill. The results generally demonstrated an improvement of discharge predictions, especially over the basins where the simulations of the hydrological model were historically poorly accurate.

Most publications about applications of EnKF-based scheme for snow modelling deal with univariate assimilation, namely the assimilation of a single data type. Relatively few studies aimed to investigate the simultaneous assimilation of observations for multiple model state variables. Durand and Margulis (2006) assimilated synthetic passive microwave observations at SSM/I and AMSR-E frequencies, and broadband albedo observations through an EnKF scheme to study the potential of remotely-sensed snow-related observations in improving SWE simulations. Durand and Margulis (2008) assimilated synthetic SWE and snow grain size data with different spatial resolutions into a LSM using an adaptive EnKF. Su et al. (2010) developed a multisensory EnKF-based DA system assimilating both Gravity Recovery and Climate Experiment (GRACE) terrestrial water storage (TWS) and MODIS FSC with respectively the Kalman Smoother scheme (EnKS) (Dunne and Entekhabi, 2005, 2006) and EnKF into a LSM. De Lannoy et al. (2012) addressed several key critical issues by investigating the potential of assimilating coarse-scale AMSR-E SWE and high-scale MODIS FSC observations into a LSM through advanced EnKF schemes. With the aim of mitigating the bias resulting from the mismatch between the remotely-sensed data and the model finer resolution, the authors innovatively tested the dynamic downscaling of AMSR-E SWE retrievals by widely assessing the impact of the scaling of the satellite observations on the assimilation procedure. Moreover, the study deeply evaluated the performance of a multiscale EnKF scheme in jointly assimilating both the retrieval data to overcome the limitations affecting each type of observation (e.g. under thin patchy snow cover and cloudy conditions).

More recently, Stigter et al. (2016) proposed a well-performing EnKF-based methodology to estimate SWE and snowmelt runoff in a Himalayan catchment. They implemented an EnKF scheme to calibrate ruling parameters of a snow model by jointly assimilating both remotely-sensed SCA observations and ground-based measures of snow depth.

Even though Kalman filtering provides a flexible framework to explicitly handle both observational and modelling uncertainties (Salamon and Feyen, 2009), some constraining assumptions hinder filter performance when dealing with highly nonlinear systems (Chen, 2003).

In order to overcome the main limiting issues affecting the EnKF technique, sequential Monte Carlo-based filtering methods for non-Gaussian, nonlinear dynamic models have been developed. These techniques, also known as Particle Filter (PF), have the main advantage of relaxing the need for the main restrictive assumptions ruling the Kalman filtering (Arulampalam et al., 2002). Thanks to their suitability to better succeed in handling systems nonlinearities, PF schemes are currently garnering a growing attention for snow modelling applications. Leisenring and Moradkhani (2011) compared the performances of common sequential EnKF-based DA methods and PF variants at assimilating synthetic SWE measurements to improve the seasonal SWE predictions and to estimate some sensitive parameters in a small-scale snowpack model. The results suggested that all the DA techniques succeeded in enhancing the SWE dynamics. Even though PF-based DA schemes generally revealed a higher accuracy, the resulting bias was comparable with the Kalman filters one. Furthermore, the results showed the potential of using an empirical cumulative distribution function to compute the particle weights, instead of a Gaussian one. Indeed, the empirical likelihood variants supplied the best predictors of model state. Dechant and Moradkhani (2011) evaluated the PF performance in assimilating remotely-sensed microwave radiance data to update the states of a snow model. The results showed that the DA scheme allowed to improve simulations of SWE as well as discharge forecasts. Thirel et al. (2013) investigated the implementation of the PF technique to assimilate MODIS SCA data into a physical distributed hydrological model, in order to improve snowmelt-related stream flow predictions. Both synthetic and real experiments showed clear improvements of model discharge simulations, especially for intermediate values of observation error. Despite of its satisfying efficiency when applied on relatively small basins, the algorithm turned out to be affected by spatial heterogeneities over larger domains. To overcome system shortcomings the authors suggested to improve the uncertainty assessment and test different importance distributions of sub-basins when evaluating the particle weights. Margulis et al. (2015) tested a newly-proposed PF approach, called particle batch smoother (PBS), to improve SWE estimates when assimilating historical Landsat-derived observations of FSC into a LSM. The study highlights that the likelihood function needed in the PBS may become more challenging to evaluate for higher dimensional measurement vectors, especially when including observations supplied by different sensors. Moreover, in order to make the PBS more robust, they suggested to use larger prior input uncertainties or different prior distributions. The same technique has been recently applied by Cortés et al. (2016). Charrois et al. (2016) investigated the performances of the Sequential Importance Resampling PF (SIR-PF) scheme in assimilating MODIS-like synthetic data of optical reflectance into a detailed multilayer snowpack model. The study assessed the impact of the assimilation, which well succeeded in reducing *RMSE* values on both snow depth and SWE with a resulting reduction of the uncertainty on the snow melt-out date. They found that the reflectance assimilation improved at most the model simulations when the observation was available after an extended period without precipitation. On the other hand, the assimilation had a low impact right after a snowfall event. Thus, they stated that the assimilation of only few observations with suitable timing can achieve the same performances of a daily reflectance assimilation. An even larger model bias reduction was achieved by updating the model assimilating synthetic snow depth observations. The assimilation of snow depths generally outperforms the reflectance assimilation, except for thin snowpacks. However, the spatial and temporal availability of in situ measurements entailed that the joined assimilation of remotely-sensed reflectance and measurements of snow depth can be the best combination to provide a significant improvement of the model simulations. Magnusson et al. (2017) applied the PF within a multilayer energy-balance snow model in order to assess the impact of the assimilation of daily snow depth measurements on the simulations of SWE and snowpack runoff. They found that DA allows the snow model simulations to closely track the observed snow depths and greatly enhances the SWE estimates, with a resulting improvement of the predicted total runoff over the whole analysis period. However, model daily runoff dynamics did not substantially benefit from the snow depths assimilation, except during the melt-out period. Furthermore, the assimilation of snow depths demonstrated to improve simulated properties of the underlying soil, especially during the spring season, mainly thanks to an enhanced melt timing. An interesting result showed that the assimilation of snow depths was more efficient when forcing the snow model with coarse resolution data (i.e., SAFRAN data, weather forecasts). For some variables, such as SWE, PF-based simulations forced with poor quality data were at times comparable to non-assimilated model outcomes driven by high quality data.

As an alternative to sequential assimilation, the variational (VAR) methods can be efficiently used in complex modelling system (Ercolani and Castelli, 2017). Instead of using only the observations available at each assimilation time step, the VAR methods simultaneously process all the observations in the assimilation window to estimate the system state and obtain the best solution to the analysis problem (Holm, 2003). Since observations from both past and future are used to update model simulations over multiple time steps, VAR assimilation results into continuous simulated time series and it is therefore referred as a smoother technique. VAR techniques can be distinguished into two main classes. The three-dimensional (i.e. space dimensions) VAR DA (3DVAR) uses one-time observations to statistically produce initial conditions through forecast fields and observational data. The four-dimensional (i.e. space and time dimensions) VAR DA (4DVAR) differs from the 3DVAR for including the dynamic evolution of the model in the assimilation (Holm, 2003). In case of reduced dimensions, terms 1DVAR or 2DVAR are used. VAR approach use optimization algorithms to minimize an objective function according to some physical constraints derived from the dynamics of the forecast model (Reichle, 2008). The objective function is defined in terms of a trade-off between the amount of noise introduced into the model and the distance between simulated and observed variables (Lee et al., 2012). The assimilation problem is therefore redefined as an iterative process aiming at minimizing the gap between observed fields and model states. Formally it is an optimisation problem with constraints that may be solved through the Lagrange multipliers technique (Bryson and Ho, 1990). Even though the VAR DA methods are generally efficient and robust even when noisy observations and models with structural errors have to be combined, the modelling framework cannot be easily modified, since any changes require the reformulation of the ajoint model, whose implementation entails an additional level of complexity (Alvarado-Monteroet al., 2017). These techniques allow to take into account nonlinear dependencies between observations and state variables without any approximation, they do not explicitly provide any estimate of predictive uncertainty, unlike the KF-based techniques. Furthermore, since VAR methods do not consider the dynamics of the second-order moment of the state variables, they are not readily suitable to probabilistic or recursive estimation (Seo et al., 2003; 2009). On the other hand, an important advantage of the VAR method is a better handling of time lags between updated quantities and observations (Lee et al., 2012).

Dumont et al. (2012) implemented a VAR DA scheme to assimilate MODIS-derived albedo observations into a snowpack model to improve the predicted annual mass balance of a glacier. The comparison with field measurements revealed the potential of the modelling system for the monitoring of the mass balance dynamics of snowpacks and glaciers.

5.2 Sequential data assimilation

As previously anticipated, DA techniques can be split into two main categories, according to the different updating process in time:

- Non-sequential (or retrospective) assimilation, which uses simultaneously all the available observations up to the analysis time step to correct the system state and obtain the best overall fit of the state variables to the observational data. This approach is particularly useful for assimilation schemes within systems where the accuracy of the initial conditions strongly impacts on its evolution (e.g. atmospheric sciences);
- Sequential assimilation, which uses all the observations up to present, as soon as they are available, to update the model state. Therefore, sequential methods are more suitable when real-time observations are available. However, sequential techniques can lead to discontinuities in the time series of the updated state (except for the 3DVAR).

Sequential DA, also known as filtering, has garnered a widespread interest since they provide a flexible framework for explicitly considering and handling different sources of uncertainty. Furthermore, sequential DA techniques guarantee the possibility of processing the observational data sequentially as it becomes available, by assuming that observations can only influence future model simulations (Leisenring and Moradkhani, 2011). Even though non-sequential methods are computationally less expensive, since they work over a given time window containing a sequence of observations, they are more apt for smoothing problems than for the assimilation of real-time data, where observations are continuously provided in time (Salomon and Feyen, 2009).

Since the main goal of this study aims at supporting the development of a snow modelling system for real-time applications, the main focus is on the sequential DA schemes, whose features well satisfy the technical requirements for operational purposes.

At first, conceptually simple DA schemes, such as DI technique, seem like attractive methods. However, their implementation within a complex, multi-layered snow model is not straightforward. Deciding how state variables should be modified based on differences in snowpack observations and implementing these changes within the model requires a complete understanding of the system (Magnusson et al., 2017). On the other hand, more advanced sequential DA methods, such as Kalman and Particle filtering, are more robust to errors in model and observational data, which are accounted for.

5.2.1 Theoretical formulation of the analysis problem

As previously explained, the main DA purpose is to characterize a system state at some future time, according to the knowledge of the initial system state. The process of approximating the true state of a physical system at a given time is called analysis, which usefully provides a depiction of the system state based on observational data and a model of the physical system, together with background information on initial and boundary conditions.

The analysis process can be considered as an optimization problem aiming at minimizing on average the difference with respect to the observational truth. The mathematical formalization of the analysis problem firstly requires the definition of the model state, the so-called *state vector* (X_t), which includes all the state variables evolving in time according to the following law:

$$X_t = M[X_{t-1}, \theta, U_t, \Omega_t] \qquad [5.1]$$

where M is the dynamic model operator, which contains the model input vector (U_t) and the vector of the time-invariant model parameters (θ). Since the model error (Ω_t) takes into account the uncertainties related to the model structure and the forcing data, it is generally state-dependent (Cohn, 1997), and thus unknown. For this reason, the model error is statistically represented as system random noise through a stochastic perturbation.

At the analysis time step, the model supplies an *a priori* or *background state*, which is an estimate of the true system state. Whenever a set of observations is available, the analysis allows to update the first guess system state by assimilating the *observation vector* (Y_t) into the model. In order to use the observational data collected in Y_t within the analysis procedure, it is necessary to make them comparable with the state variables. If each degree of freedom were observed, the observation vector could be considered as an observed state vector. However, generally fewer observations than state variables are available, so that the only proper way to relate the two vectors is through the use of a function from model state space to observation space, the so-called *observation* (or *forward*) *operator*, denoted by H. This operator collects several operators enabling to generate the so-called *model equivalents of the observations*. At the time step when observations are available, the transformation of the state to the measurement domain is given by the observation equation:

$$Y_t = H[X_t\,,\,\Psi_t] \tag{5.2}$$

where Ψ_t is the noise considering all sources of errors in observations. The observational noise is assumed to be Gaussian and independent of the model error.

When dealing with an analysis system, it is necessary to take into account the unknown uncertainties affecting the observations and the background and analysis states. Characterizing the errors of both model and observations of the system is one of the main challenging issues of the implementation of a DA scheme.

The mathematical framework of estimation theory provides the tools required to approach the problem (Moradkhani et al., 2005a). Indeed, the analysis problem can be mathematically formalized using the conditional, or Bayesian, probabilities allowing to represent each kind of uncertainty through specific probability density function (pdf) describing the errors statistics. In real applications, limited information hinders a full knowledge of the error pfds, which are generally described through their mean and covariances. Furthermore, in most cases, model background and observation errors are assumed to be independent.

In a Bayesian formulation, the solution of an analysis problem is given by the posterior probability distribution $P(X_t|D_t)$, where $D_t = \{Y_t; t = 1, \dots, t\}$ encompasses all the available observational information on the time step *t*.

Within the Bayesian framework, the prior pdf of the model state before considering the observations is denoted as $p(X_t|D_{t-1})$, i.e. the background pdf based on data-independent prior information. The resulting mathematical description of Bayes law is given as:

$$p(X_t|D_t) = \frac{p(Y_t|X_t)\,p(X_t|D_{t-1})}{p(Y_t|D_{t-1})} \tag{5.3}$$

where the denominator is the normalization factor, also denominated as predictive distribution, ensuring that the integration of $p(X_t|D_t)$ results to 1. The likelihood $p(Y_t|X_t)$ measures the likelihood of a given model state with respect to the observed one at time *t*.

The original Bayes law (Eq. 5.3) allows to estimate uncertainty through the conditional probability by using the available observational data. However, its formulation does not include information from new observations, as they become available. The flexibility required to use the new information is provided by a sequential Bayesian scheme.

5.2.2 Recursive Bayesian scheme using ensemble filtering

Due to the stochastic nature of X_t, information about the system state can be extracted at any time *t* from observations through the recursive Bayes law. Given all the available information and supposed that the posterior pdf at time *t-1* $p(X_{t-1}|D_{t-1})$ is known, using the system model it is possible to obtain the required prior pdf of the current state at the time step t $p(X_t|D_{t-1})$ in two stages: prediction and update. Assuming that X_t follows the Markov property, the Chapman-Kolmogorov equation can be used:

$$p(X_t|D_{t-1}) = \int p(X_t|X_{t-1})\, p(X_{t-1}|D_{t-1})\ dX_{t-1} \qquad [5.4]$$

In the prediction step (Eq. 5.4), the forecast pdf is obtained assuming that also the transition pdf is known. When at time *t* a measurement Y_t becomes available, it may be used to update the forecast pdf via Bayes rule:

$$p(X_t|D_t) = p(X_t|Y_t, D_{t-1}) = \frac{p(Y_t|X_t)\, p(X_t|D_{t-1})}{p(Y_t|D_{t-1})} = \frac{p(Y_t|X_t)\, p(X_t|D_{t-1})}{\int p(Y_t|X_t)\, p(X_t|D_{t-1})\, dX_t} \qquad [5.5]$$

In the update equation (Eq. 5.5), the measurement Y_t is used to update the predicted prior pdf to obtain the required posterior pdf of the state. The recurrence relation of Eqs. 5.4 and 5.5 is the formal solution to the Bayesian recursive estimation problem. The aim of the analysis is to find the maximum of the conditional pdf of the model state $p(X_t|D_t)$, given the observations.

When dealing with high dimensional problems, the main issue in using Bayes law remains in the multidimensional integration of forecast density (Eq. 5.4), which makes the closed form solution of posterior density (Eq., 5.5) practically intractable. Since both $p(X_t|D_t)$ and $p(X_t|D_{t-1})$ generally cannot be explicitly expressed through a mathematical formulation, a Monte Carlo sampling is used to explore the posterior density. Thus, the implementation of ensemble-based methods using a Monte Carlo sampling provides a practical solution to such problems.

5.3 Ensemble-based DA schemes

Since the posterior probability density cannot usually be solved analytically due to the high dimensionality and non-linearity of physical systems (Moradkhani et al., 2005b), discrete approximations are typically used, according to the Monte Carlo approach (Andreadis and Lettenmaier, 2006; Moradkhani et al., 2005a; Slater and Clark, 2006; Durand et al., 2008).

The main assumption of the ensemble-based filtering methods is the representation of the model posterior probability density through a set of independent random states, sampled directly from the model space. As new observations become available, the posterior probability density is then updated according to the Bayesian rule**.** Following the sequential Monte Carlo (SMC) approach, the ensemble of model realizations is propagated forward in time by using the updated states from the previous time step.

In hydrological applications, the most commonly used sequential ensemble-based DA techniques are the Kalman and Particle filtering, which are gaining an increasing interest. These DA schemes allow not only to iteratively update the system state by optimally combining the model predictions with observations, but also to quantify observational and modelling errors, given all the sources of uncertainty. As explained in the following, the difference between the EnKF and PF techniques lies in the method of recursively generating an approximation to the state pdf.

5.3.1 Ensemble Kalman filter

Evensen (1994) introduced the EnKF technique, relying on the Monte Carlo approach to approximate the conditional second-order moments of the variables of interest using a finite number of randomly generated model replicates. This technique requires the definition of an ensemble of model states, which are all simultaneously integrated forward in time independently of each other, using the nonlinear forward model with replicates of the system noise:

$$X_{t,i} = M\left[X_{t-1,i}, \theta, U_{t,i}, \Omega_{t,i}\right] \qquad [5.6]$$

Whenever observations are available, which are generally considered as random variables,

$$Y_{t,i} = H\left[X_{t,i}\, ,\ \Psi_{t,i}\right] \qquad [5.7]$$

an analysis procedure is performed with the aim of updating the ensemble state through an optimal weighting between simulated and observed values. Indeed, the filter allows to correct the system state towards the observational estimate according to the difference between the modelled state and the observed one, with the degree of correction determined by the levels of error associated with each. Thus, firstly the ensemble mean of model states is evaluated:

$$\overline{X_t} = \frac{1}{N}\sum_{i=1}^{N} X_{t,i} \qquad [5.8]$$

Then, the model error covariance matrix P_t is calculated as

$$P_t = \frac{1}{N-1} E_t E_t^T \qquad [5.9]$$

where E_t is the expectation of the error in every ensemble member, calculated according to:

$$E_t = \left[X_{t,i} - \overline{X_t}, \dots \dots, X_{t,N} - \overline{X_t}\right] \qquad [5.10]$$

Since the true system state is generally unknown, this procedure allows to estimate the model error covariance matrix (P_t) from the ensemble, which is dynamically updated at every assimilation time step (Evensen 1994, 2003). This is one of the main assumptions and advantages of the EnKF technique, requiring no estimation of a priori model error covariances for the analysis step (Moradkhani et al., 2005a).

The weights are defined by the Kalman Gain (*K*), which is a combination of the error covariance matrices of both model and observations, according to the following formula:

$$K_t = P_t H^T (H P_t H^T + R)^{-1} \qquad [5.11]$$

where *R* is the error covariance matrix of observations.

Lastly, the traditional update equation from the classical KF is used, with the Kalman Gain calculated from the error covariances provided by the ensemble. The ensemble states are then updated by comparing the measurements Y_t to the model estimates:

$$X_{t,i}^a = X_{t,i} + K_t\left[Y_{t,i} - \overline{H[X_t]}\right] \qquad [5.12]$$

where $X_{t,i}^a$ is the ensemble of the analysis state vectors and $Y_{t,i}$ is the generated ensemble of measurements.

As sequential ensemble-based DA technique, the EnKF scheme provides a general framework for explicitly taking into account several sources of uncertainty. However, some limiting issues hinder filter performance (Weerts and El Serafy, 2006). The major limitation is the closure of the Kalman filtering at the second-order moments in the analysis step (Moradkhani et al., 2005b). Because the state variables in stochastic-dynamic systems are modelled as random variables, subject to unknown disturbances, the conditional probability of predictions will translate, deform, and spread, and the shape of its distribution is generally difficult to track and unlikely to be Gaussian (Weerts and El Serafy, 2006; Salamon and Feyen, 2009). Therefore, in highly nonlinear systems, the first two moments of the prior density are not likely to be sufficient to properly approximate the posterior probability distribution. For such cases, an accurate estimate of the posterior probability requires the tracking of higher-order moments (Moradkhani et al., 2005b). Moreover, the EnKF is further limited to the linear updating procedure, with a significant simplification affecting the filter performance when dealing with highly nonlinear systems.

The lack of any linearity and Gaussian property constraints on the modelling system is one of the main advantages of the Particle filtering (Weerts and El Serafy, 2006), which does not require any restrictive assumption on the form of the probability distributions (Arulampalam et al., 2002).

5.3.2 Particle filter

Likewise, the EnKF technique, Particle filtering is a recursive Bayesian algorithm, whose key idea is to represent the posterior density function by a set of randomly drawn samples through a Monte Carlo approach. The main difference between the EnKF and the PF is how they recursively generate an approximation to the probability distributions of the prognostic variables (Weerts and El Serafy, 2006). The EnKF provides an analytical solution to the analysis problem (Eq. 5.5). Unfortunately, most applications are non-linear and non-Gaussian and the multidimensional integration typically makes a closed-form solution intractable. Indeed, only in some specific case (i.e. within linear systems) a sequential analysis can be carried out using the analytical form of the filter to obtain exact calculations for the posterior distributions of interest (Moradkhani et al., 2005b).

Unlike the EnKF, which simplifies the recursive estimation by assuming Gaussian distributional properties of the prognostic variables, SMC methods based on Particle filtering have the advantage of relaxing the need for restrictive assumptions regarding the form of the distributions, since the full prior density functions are used within the updating procedure. The posterior probability distributions of prognostic variables are fully represented through a number of independent random samples, called particles. As the number of particles becomes very large, the Monte Carlo characterization becomes an equivalent representation of the posterior distributions, which are approximated by discrete random measures (i.e. particles) and a set of associated weights (Arulampalam et al., 2002). In essence, stochastic model computations are performed by generating a large number of random realizations of the variables of interest, solving deterministic equations for each realization, and estimating the resulting statistical properties of the ensemble (Moradkhani et al., 2005b).

The particles are sampled to represent the posterior probability, and updated by assimilating the information contained in the newly available observations. Particles are properly weighted and propagated sequentially by the application of the Bayesian rule. The particles drawn from the posterior distribution are used to map integrals to discrete sums by the following empirical approximation of the posterior density (Arulampalam et al., 2002):

$$p(X_{0:t}|Y_{1:t}) \approx \sum_{i=1}^{N} W_t^i \delta\left(X_{0:t} - X_{0:t}^i\right) \qquad [5.13]$$

where $\left\{X_t^i, W_t^i\right\}$ denote the *i*th particle drawn from the posterior distribution and its associated weight, $\delta(\cdot)$ is the Dirac delta function. The Dirac measure is given by:

$$\delta\left(X_t^i\right) = \begin{cases} 0\ if\ X_t^i\ \in X_t \\ 1\ if\ X_t^i\ \notin X_t \end{cases} \qquad [5.14]$$

Unfortunately, it is often unfeasible to sample directly from the posterior density function, since it is unknown. However, this limitation can be overcome by sampling from a known, easy-to-sample, proposal distribution. This is the main concept of the importance sampling principle. PFs are based on the Sequential Importance Sampling (SIS) approach (Moradkhani et al., 2005b; Guingla et al., 2012), which is the recursive version of the Bayesian Importance Sampling (BIS). The more commonly used SIS principle is based on the fact that direct sampling from the posterior distribution, which is often non-Gaussian, is generally challenging (if not impossible).

In order to overcome this limitation, the samples $\left(X_t^i\right)$ are drawn from a known function, the so-called importance density (or proposal distribution) and the importance weights of the particles are defined as:

$$W_t^{i^*} \propto \frac{p\left(X_{0:t}^i|Y_{1:t}\right)}{q\left(X_{0:t}^i|Y_{1:t}\right)} \tag{5.15}$$

In order to avoid that the entire historical trajectory of particles needs to be stored, the commonly-used simplification proposed by Arulampalam et al. (2002) can be applied, which allows to modify the proposal distribution such that

$$q(X_t|X_{0:t-1},Y_{1:t}) = q(X_t|X_{t-1},Y_t) \tag{5.16}$$

Therefore, a recursive updating of the importance weights, at each iteration, is achieved according to the following formula (Arulampalam et al., 2002):

$$W_t^{i^*} \propto W_{t-1}^{i^*} \frac{p\left(Y_t|X_t^i\right)p\left(X_t^i|X_{t-1}^i\right)}{q\left(X_t^i|X_{t-1}^i,Y_t\right)} \tag{5.17}$$

Correspondingly, the filtering posterior density (Eq. 5.13) is approximated by:

$$p(X_t|Y_{1:t}) \approx \sum_{i=1}^{N} W_t^i \delta\left(X_t - X_t^i\right) \tag{5.18}$$

where W_t^i are the normalized weights given by:

$$W_t^i = \frac{W_t^{i^*}}{\sum_{i=1}^{N} W_t^{i^*}} \tag{5.19}$$

Several authors (Doucet et al., 2000; Arulampalam et al., 2002) have agreed that the choice of the proposal function is a critical design issue as it significantly impacts the filter performance. Generally, the most convenient and frequently used importance function is the transition prior, where:

$$q\left(X_t^i|X_{t-1}^i,Y_t\right) = p\left(X_t|X_{t-1}^i\right) \tag{5.20}$$

By substituting [5.20] into [5.17], the weight updating simplifies to

$$W_t^{i^*} \propto W_{t-1}^{i^*} p\left(Y_t|X_t^i\right) \tag{5.21}$$

Unlike the EnKF, the main advantage of Particle filtering is the capability of handling the propagation of non-Gaussian distributions through non-linear models. (Salamon and Feyen, 2009). Furthermore, Particle filtering performs the updating on the particles weights rather than on state variables directly, which allows to maintain the overall physical consistency of the particles.

However, since the stochastic behaviour of the system generally causes the dispersion of the particles, many of them drift from the true system state. After several iterations, only few particles are likely to have non-zero importance weights, while most of them are discarded due to their negligible probability, so that only a few particles are involved within the filtering process (Doucet, 1998). This is a well-known common issue with SIS, namely the sample degeneracy, which strongly hinders the PF performance. Degeneracy is an undesirable and unavoidable side-effect entailing that the variance of importance weights stochastically increases over time and the particles do not succeed in properly approximating the posterior distribution.

The effective sample size can be used as a measure of degeneracy. However, since the exact effective sample size cannot be computed, an estimated value is generally evaluated:

$$N_{eff} \approx \frac{1}{\sum_{i=1}^{N} W_t^i} \qquad [5.22]$$

Arulampalam et al., (2002) explained that small N_{eff} indicates severe degeneracy, and therefore it is common to set a fixed threshold N_{thresh} so that if $N_{eff} < N_{thresh}$, the effect of degeneracy needs to be reduced.

The impact of the degeneracy can be easily mitigated by increasing the number of particles, but this approach is often unfeasible due to the increase in computational demand (Salamon and Feyen, 2009). Actually, a resampling procedure is frequently introduced, since it allows to restore the sample variety without deteriorating the characterization of the posterior distribution through a Markov chain chaotic Monte Carlo (MCMC). Within the resampling step, particles having high importance weights are replicated and those with low importance weights are discarded, while the total of particles is maintained unchanged.

Several resampling schemes have been developed (Douc and Cappé, 2005), namely sampling importance resampling (Rubin, 1988; Smith and Gelfand, 1992; Gordon et al., 1993), residual resampling (MacKay, 1992; Higuchi, 1997; Liu and Chen, 1998), auxiliary sampling importance resampling (Pitt and Sphephard, 1999), minimum variance resampling (De Freitas et al., 2001), stratified resampling (Kitagawa, 1996), deterministic resampling (Kitagawa, 1996), systematic resampling (Carpenter et al., 1999) and regularization based on kernel density (Musso et al., 2001).

Sequential importance resampling

Gordon et al. (1993) proposed the Sequential Importance Resampling (SIR), which allows to avoid the sample degeneracy by introducing a resampling procedure within the SIS algorithm. The additional resampling step discards particles having a low probability while replicating those having a high importance weight. SIS and SIR PFs are very similar, with the only difference that, unlike the SIS where the resampling is carried out when degeneracy occurs, in SIR the resampling procedure is always performed at each time step, with the effective sample size remaining almost equal to the total sample size (N). The resampling algorithm maps the Dirac random measure $\left\{X_t^i, W_t^i\right\}$ (Figure 5.1b) into an equally weighted random quantity $\left\{X_t^i, 1/N\right\}$ through a uniform sampling from the discrete set $\left\{X_t^i, i = 1, \dots, N\right\}$ with probabilities $\left\{W_t^i, i = 1, \dots, N\right\}$. An empirical cumulative distribution function (cdf) is then generated based on the weights W_t^i (Figure 5.1c). By using a uniform distribution, N samples are drawn from the cdf, all of which corresponds to a certain particle index. Clearly, the greater the weight of a particle, the higher the chance of drawing that particle (Figure 5.1d). Therefore, the resulting particle set contains replications of those particles having high importance weights.

Several improvements (e.g. reduced variance, reduced number of computations) to the SIR filter algorithm have been suggested (Weerts and El Serafy, 2006). Guingla et al., (2012) stated the specific choice of the selection method among the stratified, systematic, or residual resampling does not significantly affect the performance of the SIR-PF, since all the three are designed to minimize the particle variance.

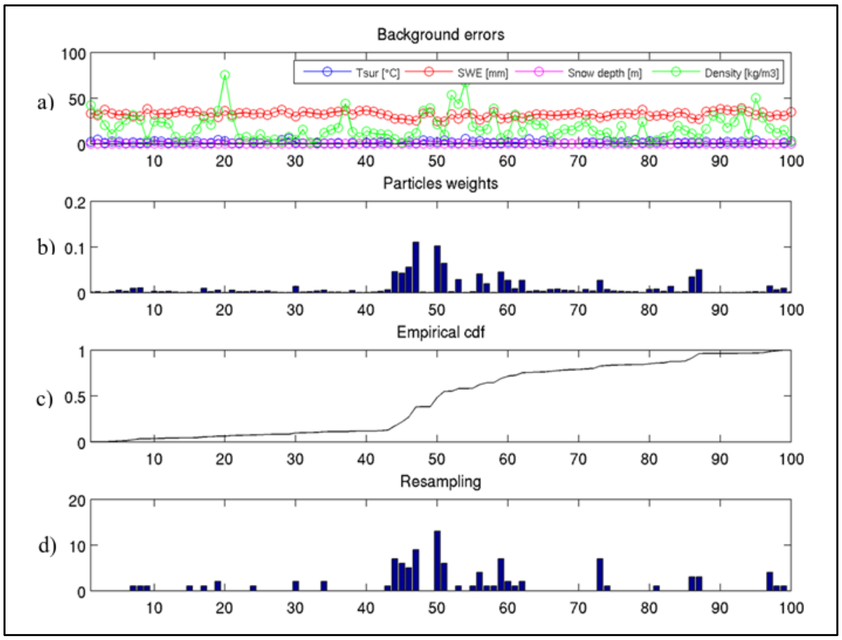

Figure 5.1: *Example of multivariate SIR-PF scheme for the assimilation of surface temperature (in blue), SWE (in red), snow depth (in magenta) and snow density (in green) observations. - (a) Open circles are the background errors of the variables of interest. (b) Importance weights as a function of the particles indices. (c) The empirical cdf of the importance weights. (d) Number of resampled particles as a function of the particles indices.*

5.4 Experimental setup

The two analysed sequential ensemble-based DA techniques have been tested and evaluated through a common methodology. The control experiments rely on an ensemble of 100 model realizations, with the aim of guaranteeing a significant sample while avoiding any computational overload. The default assimilation frequency is set at every 3 hours, in order to ensure an efficient exploitation of the ground-based observations, which are supplied with a generally high measurement frequency by the automatic stations at the analysed experimental sites (Sect. 3.1).

The multivariate DA schemes have been designed to consistently update the system state by jointly assimilating in-situ observations of surface temperature, albedo, snow depth, and SWE.

Whenever measurements of both snow depth and SWE are simultaneously available at an assimilation time step, observational information on snow density are derived and used to update the simulated values of this variable. Vice versa, at TGN site, during the winter seasons when snow density measures are provided, SWE estimates are derived and assimilated. Therefore, when assessing the filter performance, it is noteworthy that data of SWE and snow density can be indirect estimates when in-situ measurements of these snow-mass quantities are lacking (Sect. 3.3.3).

5.4.1 Observational uncertainty

According to the EnKF theory, the model error covariance matrix is diagnosed from the ensemble, which is one of the main assumptions of this DA technique. The efficiency of the analysis procedure strongly depends on the representativeness of the estimated uncertainties of both background and observations error covariances. Indeed, the ratio of the model forecast error covariance to the observation one is a key factor ruling the estimate of the updating terms.

Burgers et al. (1998) explained the effectiveness of treating the observations as random variables at the analysis time steps. That is, at each assimilation time step an ensemble of observations is generated by adding some stochastic Gaussian noise to the observed data. The perturbations are generally drawn from a normal distribution with zero mean and the observations error covariance matrix (Reichle et al., 2002a; Reichle et al., 2002b; Moradkhani et al., 2005a). According to this technique, the observations error covariances used within the evaluation of the gain matrix are estimated from the ensemble of the perturbed observations, rather than being directly used. Otherwise, the updated ensemble is likely to have a too low variance.

Whitaker and Hamill (2002) agreed that if the same observations and the same gain are used to update each ensemble member, the analysis error covariances are likely to be systematically underestimated, with a resulting degradation of subsequent analyses (filter divergence). However, they explained how the assimilation of an ensemble of perturbed observations can introduce an additional source of sampling error related to the estimation of the observations error covariances. Because of the nonlinear dependence among the analysis and background error covariances, this extra source of sampling error is likely to increase the probability of spurious estimates of the observation background error covariances with a resulting possible misestimation of the analysis error covariance. This undesirable issue is mainly due to the fact that the perturbed observations act as a source of multiplicative noise in the analysis system, since the amplitude of the noise in the analysis error covariances is proportional to the background error estimation. Kepert (2004) pointed out that the sampling error becomes even more substantial as measurements dimensionality increases, with a resulting worsening of filter performance. Increasing the ensemble size can be effective in mitigating the effect of the sampling error. However, this approach is computationally demanding.

Thus, with the dual purpose of maintaining a limited ensemble size and preventing some additional sampling errors from affecting the estimate accuracy of the analysis error covariances, the snow-related observations have been assimilated without introducing any additional noise. This choice has been further supported by the aim of testing the ensemble-based DA schemes for multivariate applications dealing with a large amount of observational data. Therefore, an a priori error covariance matrix of observations has been estimated and directly used within the evaluation of the Kalman Gain.

Stigter et al. (2017) explained that when considering the uncertainties of ground-based measurements, it is necessary to consider not only the instrumental errors, but also the errors related to the low representativeness of the point observations. Indeed, in-situ measurements do not succeed in catching the spatialized snow processes, unless with a generally high degree of uncertainty depending on the density of the monitoring network. A case in point are the snow depth measurements, which are generally affected by small errors (few centimetres), but their representativeness is often poor due to the large spatial variability of snow cover (Magnusson et al., 2017).

In this study, the observational uncertainty has been estimated according to the known instrumental errors. The representativeness error is of essential importance especially when dealing with DA applications in distributed models. Conversely, since in this study point measurements are assimilated within a one-dimensional modelling system, the observational error covariance matrix is supposed to be satisfactorily representative even though it does not take into account the representativeness uncertainty. Moreover, the observational data are supplied by experimental sites, where the in-situ measurements are extensively checked. The strategic positioning of these pilot sites in well sheltered locations from local wind patterns generally ensures a low impact of wind-induced snow drifting and also vegetation interaction. Lastly, since the main purpose is to investigate the feasibility of two different sequential ensemble-based techniques in performing multivariate DA, it is preferred to compare their performances given the same observational uncertainty. Since the representativeness errors can be affected by the local complex topography, it can be considered as site-dependent. Thus, the introduction of this type of error would add some further uncertainty in assessing the comparison results at different sites. For all these reasons, the observation error covariance matrix has been evaluated only considering the instrumental errors (Table 5.1) and it has been used within both the tested DA algorithms at all the analysed Alpine sites. Indeed, even though the stations are heterogeneously equipped, the instrumental errors of the sensors measuring a specific variable slightly differ from one other. However, as well explained in Lafaysse et al., (2017), it is important to consider that the distance of the two sensors measuring snow depth and SWE can affect the retrieval of snow density with a significant uncertainty, especially when shallow snow cover is present and during the melting period (Essery et al., 2013).

Assimilated variable	**Observational uncertainty**
Surface temperature [°C]	± 1
Snow depth [cm]	± 5
Albedo [%]	5
SWE [mm]	± 30
Snow density [kg/m^3]	± 40

Table 5.1: *Uncertainties of the assimilated measures.*

Therefore, the error covariance matrix of observations (R) is a site-independent, time-invariant diagonal matrix, since all measurement errors are assumed uncorrelated (off-diagonal null elements).

5.4.2 Evaluation metrics

The performances of the filtering techniques are assessed through their effectiveness in updating the model simulations of all the prognostic variables involved within the assimilation procedure, namely snow depth, SWE, snow density, surface temperature and albedo. In addition to the statistical metrics previously introduced in Sect. 4.4.2, namely *RMSE* and *R*, each analysis has been evaluated through the further following indices:

$$NER = \left(1 - \frac{RMSE_{Assim}}{RMSE_{OL}}\right) \cdot 100 \qquad \text{Normalized Error Reduction (NER, Chen et al., 2011)} \qquad [5.23]$$

$$Eff = \left(1 - \frac{\sum_{k=1}^{N}(Assim_k - Obs_k)^2}{\sum_{k=1}^{N}(OL_k - Obs_k)^2}\right) \cdot 100$$ Assimilation efficiency (Eff, Brocca et al., 2012) [5.24]

The scores have been evaluated throughout the whole measurements dataset supplied by each station at the original temporal resolution without considering the snowless periods.

CHAPTER 6

Multivariate Ensemble Kalman Filter scheme

==

A multivariate EnKF scheme has been developed and implemented with the aim of testing its performance in improving the snow model predictions. Even though this method is able to handle any number of variables in the updating scheme (Moradkhani et al., 2005a), when dealing with multivariate DA the implementation of an EnKF-based algorithm faces several issues.

6.1 Ensemble generation and perturbation of state variables

In an EnKF-based DA scheme, the predicted snowpack state is updated towards its observed state with a degree of correction determined by the level of error associated with each. The key feature of the EnKF is that the model error is dynamically derived from an ensemble of (typically nonlinear) model integrations. Thus, the generation of an ensemble of possible model realizations is of critical importance to ensure a well representative error covariance matrix, which strongly affects the filter performance in updating the system state.

In an ensemble modelling approach, one or more model key variables are handled as random variables, depending on which sources of uncertainty are taken into account. When considering the uncertainty of the meteorological inputs, some random noise is added to the forcing data. When aiming to consider the error affecting the simulations due to the model physics and/or the representativeness of its parameters, a stochastic perturbation of the initial conditions, key parameters or the prognostic variables is performed in order to properly represent the modelling uncertainty. The introduction of some stochastic noise affecting each ensemble member allows well diversify the model trajectories, which evolve independently with various combinations of perturbed variables. As several sources of uncertainty are involved within a modelling system, as many approaches can be adopted to generate the model ensemble. Durand and Margulis (2006) handled the precipitation input as an uncertain random variable as well as several crucial parameters. Reichle et al. (2007) considered the uncertainty related to the observed forcing fields by perturbing the input data. Furthermore, they also perturbed the state variables in order to jointly taken into account the uncertainty of the model physics and parameters. Similarly, De Lannoy et al. (2012) performed the perturbation of selected meteorological inputs and model prognostic variables through a randomly generated noise.

The uncertainty of the state variables results from all the sources of uncertainty affecting the whole modelling system. Therefore, the EnKF scheme has been here implemented by directly perturbing the model states, in order to well represent the uncertainty in the snowpack conditions. Moreover, this choice has been supported by further assumptions on the impact of the perturbations within the updating procedure.

As extensively explained in the previous Chapter, the EnKF provides an analytical solution to the analysis problem, assuming that all the involved probability distributions are Gaussian (Salamon and Feyen, 2009). Nevertheless, the strong nonlinearities in most systems hinder a proper evaluation of the posterior distributions of interest (Moradkhani et al., 2005b). Along with the unavoidable impact of the model nonlinear dynamics, it is noteworthy that the introduction of perturbations can add further sampling errors affecting the updating procedure. Moreover, it is important to consider that the Gaussian distributions of the perturbing noises are subject to unknown distortions through the model integration forward in time. All these issues are supposed to contribute in deforming the resulting distributions of the state variables, whose shapes are unlikely to be Gaussian, but instead hardly traceable. Thus, the choice of directly perturbing the prognostic variables is supposed to guarantee a sizeable model error covariance matrix while limiting possible further unknown disturbing effects of parallel perturbations on the density distributions involved within the updating procedure.

Each ensemble member has been perturbed through a stochastic noise directly added to the prognostic variables describing the system state. This approach has also allowed to prevent a too low analysis-error covariance matrix, which is likely to occur especially when the observations are not perturbed, as in this study. Indeed, an undesirable underestimation of error covariances has a larger impact on the analysis error than a commensurate overestimation (Whitaker and Hamill, 2002). Moreover, the perturbation has been extended to all the state variables with the aim of preventing inconsistencies resulting from possible imbalances within the model error covariance matrix. This expedient is of critical importance in a multivariate EnKF-based application, since a misrepresentation of the error covariance matrix can misleadingly result in high corrective terms of the well perturbed variables and negligible terms of those not perturbed, being equal observational uncertainty.

6.1.1 Gaussian perturbation of prognostic variables

The prognostic variables have been perturbed through an additive noise, which has been randomly generated by performing, for each state variable, a sampling from a multivariate Gaussian distribution characterized by a zero-mean vector and an assigned covariance matrix (COV_{pert}). The sampling has been carried out by choosing equidistant cumulated probability values, in order to guarantee null mean-valued perturbations and the sample Gaussianity, even when the sample is limited in size.

The covariance matrix has been a priori estimated in order to properly consider the different degree of uncertainty affecting each prognostic variable. The definition of cross-correlations among the perturbations of the state variables is likely to prevent possible physically inconsistent snowpack state (Reichle et al., 2007; De Lannoy et al., 2012). However, since the estimate of these a priori unknown quantities is challenging, no cross-correlation has been taken into account in order to avoid the introduction of possible spurious correlations among the state variables resulting from the perturbation procedure. Nevertheless, with the aim of preventing prominent physical inconsistencies affecting the ensemble model states, the perturbation variances have been intentionally set to low values.

The estimation of the diagonal elements has been carried out by analysing the variances of the time series of each prognostic variable at all the three analysed experimental sites throughout the whole datasets period. The resulting variance values have been then adjusted through a trial-and-error approach with the dual aim of ensuring a well representing error covariance matrix of the model ensemble (P_t) and preventing a too large ensemble spread, which is likely to lead to physically inconsistent values among the state variables.

In order to prevent the states perturbation from introducing possible physically inconsistent values of any prognostic variable, whenever this undesirable condition occurs the model ensemble is rescaled after the perturbation procedure. Indeed, the direct truncation of possible spurious values would compromise the null mean-valued perturbations. Thus, a rescaling procedure has been introduced in order to avoid the introduction of possible distortion of the perturbed ensemble while guaranteeing the model physical consistency. This contraction has been designed to preserve both the ensemble average and perturbations Gaussianity even after the ensemble limitation (Figure 6.1).

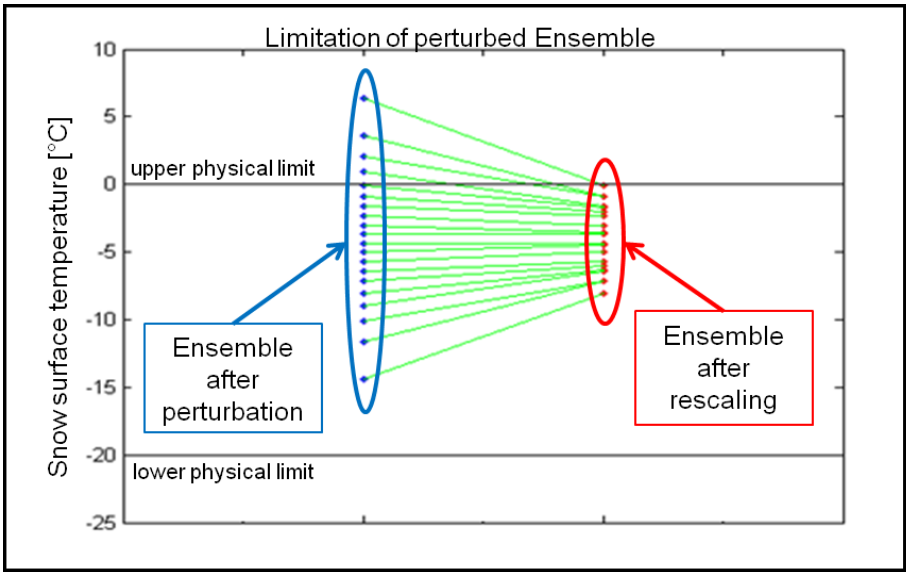

Figure 6.1: *Rescaling procedure - Limitation of the ensemble prognostic variables after the perturbation procedure.*

Whenever the rescaling procedure is applied, it unavoidably entails a decrease in the ensemble spread. The variance reduction of the model simulations can affect the updating process by leading to overly weight the predicted snowpack states and weakly assimilate the observed ones. In order to mitigate this undesired condition, the values of the model error variances (i.e. diagonal elements of the matrix P_t) resulting from the rescaling procedure are rescaled in turn. Therefore, the ensemble-based P_t-matrix is post-processed to increase its variance values proportionally to their rescaling-induced reduction. Once the diagonal matrix of error standard deviation (σ_t) is derived from the P_t-matrix, the error correlation matrix (S_t) is estimated by combining P_t- and σ_t-matrices. At this stage, the variance reduction of each state variable is evaluated by computing the ratio between the empirical variance of each state variable and its actual variance value. Once this ratio is calculated, the rescaled σ_t-matrix ($\sigma_{t,rescaled}$) is defined by multiplying each diagonal element of the σ_t-matrix by the square root of the corresponding ratio value. Lastly, the rescaled P_t-matrix is backwards obtained with the reverse approach, namely by combining S_t- and $\sigma_{t,rescaled}$-matrices, according to the following formula:

$$P_t = \mathrm{S}_t \cdot \left(\sigma_{t,rescaled} \,\mathrm{x}\, \sigma_{t,rescaled}\right) \tag{6.1}$$

6.1.2 Model physical consistency: modulating function

The implementation of the rescaling procedure of the perturbed ensemble members has entailed the definition of physically-based lower and upper limits for each state variable ($Lim_{j,INF}$, $Lim_{j,SUP}$) to ensure its consistent limitation. With the aim of properly estimating the physical ranges of state variables, they have been statistically defined through the analysis of their observed time series at the three snow experimental sites. Since the snowpack model has been designed to simulate the energy balance in both snowy and snowless conditions (Sect. 4.1), two different sets of physical limits have been required to guarantee the model consistency both in case of presence and absence of snowpack (Table 6.1).

STATE VARIABLE		$\boldsymbol{Lim_{INF}}$		$\boldsymbol{Lim_{SUP}}$	
		snowy	**snowless**	**snowy**	**snowless**
T_s	[°C]	-30	-	0	-
T_m	[°C]	-30	-	0	-
T_0	[°C]	-10	0	0	40
T_d	[°C]	-2	0	5	20
W_s	[mm]	0	-	-	-
W_m	[mm]	0	-	-	-
ρ_s	[kg/m^3]	80	-	550	-
ρ_m	[kg/m^3]	80	-	550	-
α	[-]	0.2		1	

Table 6.1: *Lower and upper limits of the state variables in snowy and snowless conditions.*

Similarly, in order to generate consistent perturbations both during and beyond the winter season (e.g. in snowless conditions the snow-related variables are not included into the model state), two different covariance matrixes have been defined for snowy and snowless conditions, respectively $(COV_{pert,snowless}\ , COV_{pert,snowy})$.

With the purpose of preventing model instabilities due to the intermittent presence of snow cover, a modulation has been introduced in order to relax the switch from snow cover to bare soil conditions, by properly setting both lower and upper physical limits of state variables $(Lim_{j,t,INF}\ , Lim_{j,t,SUP})$ and the covariance matrix used for the generation of the ensemble perturbations $\left(COV_{pert,t}\right)$. The modulation allows to well characterize the transition periods, namely the early winter and the melting season, by constraining each state variable into likely time-variant physical ranges and simulating the seasonal variability of the variance of each prognostic variable.

The modulating function (β) allows discriminating the presence or absence of snow according to both air temperature (observed) and snow mass (modelled). This approach enables to manage the transition periods: snow cover and high air temperature (melting process) and bare soil and low air temperature (early winter). The β-function is defined according to the following formulas:

$$\beta_{Ta} = \left(\gamma - \frac{\operatorname{atan}(T_a\,)}{\pi}\right) \qquad [6.2]$$

$$\beta = \beta_{Ta} + (1 - \beta_{Ta}) \cdot e^{-\left(1+\left(\frac{(W_s+W_m)-\mu}{\sigma}\right)\xi\right)^{-1/\xi}} \qquad [6.3]$$

The functional form and the parameters $(\gamma, \mu, \xi\ , \sigma)$ have been defined to centre the function on an air temperature value that could discriminate snow and no-snow conditions, assumed equal to 0°C, and asymptotically reach the desired limit values (1 for winter and 0 for summer).

Figure 6.2 shows the modulating function, which assumes values near to 0 when the air temperature is high and there is no snow cover (mainly during summer season), and near to 1 in case of snow cover and cold temperatures (winter period). In these two limit cases summer and winter physical ranges are assumed for all the state variables, respectively. The function assumes value near to 1 also when no snowpack is present, but temperatures are very low (autumn, early winter).

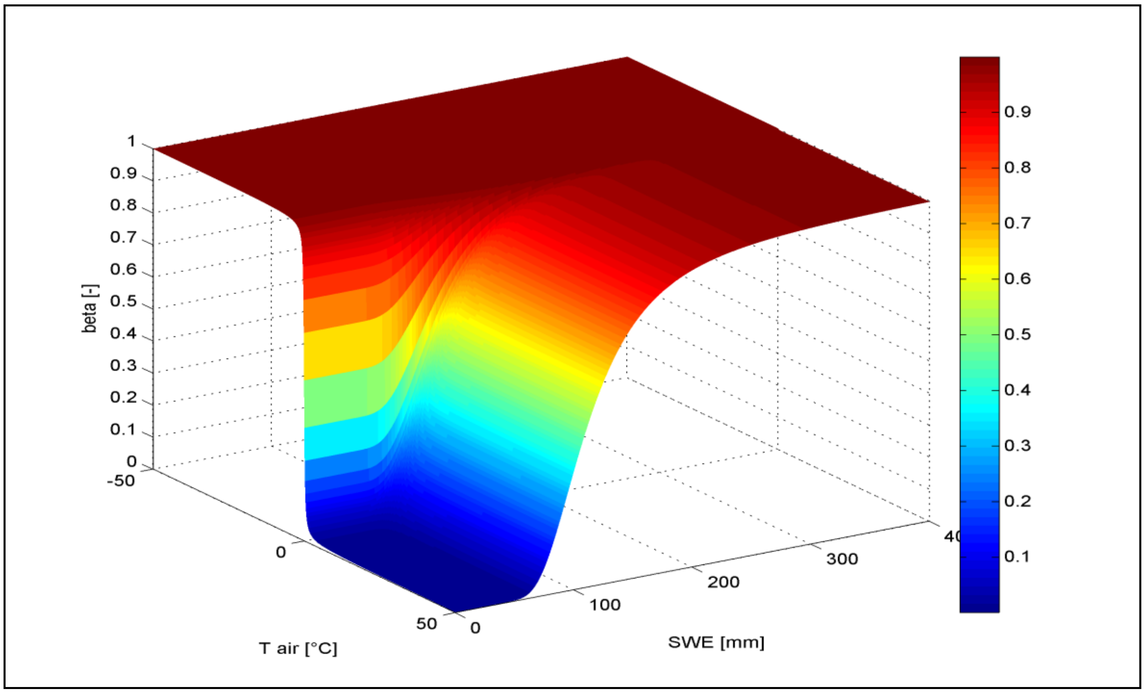

Figure 6.2: *β-modulating function.*

During transition periods β-function allows defining intermediate model run settings depending on the combination of snow and air temperature information, according to the following formulae:

$$Lim_{j,t,SUP} = \left(Lim_{j,SUP_{snowless}} \cdot (1-\beta)\right) + \left(Lim_{j,SUP_{snowy}} \cdot \beta\right) \qquad [6.4]$$

$$Lim_{j,t,INF} = \left(Lim_{j,INF_{snowless}} \cdot (1-\beta)\right) + \left(Lim_{j,INF_{snowy}} \cdot \beta\right) \qquad [6.5]$$

$$COV_{pert,t} = \left(COV_{pert,snowless} \cdot (1-\beta)\right) + \left(COV_{pert,snowy} \cdot \beta\right) \qquad [6.6]$$

6.1.3 Impact of the perturbation of state variables on ensemble simulations without DA

The aim is to verify that the stochastic noise added to the prognostic variables does not affect the model predictions on average, at any site. Therefore, the impact of the states perturbation is investigated by analysing the 100 members-ensemble simulations (Figures 6.3a, b, c), without considering the assimilation of snow data, in order to verify that no spurious trends occur with respect to the deterministic control run (i.e. OL simulations).

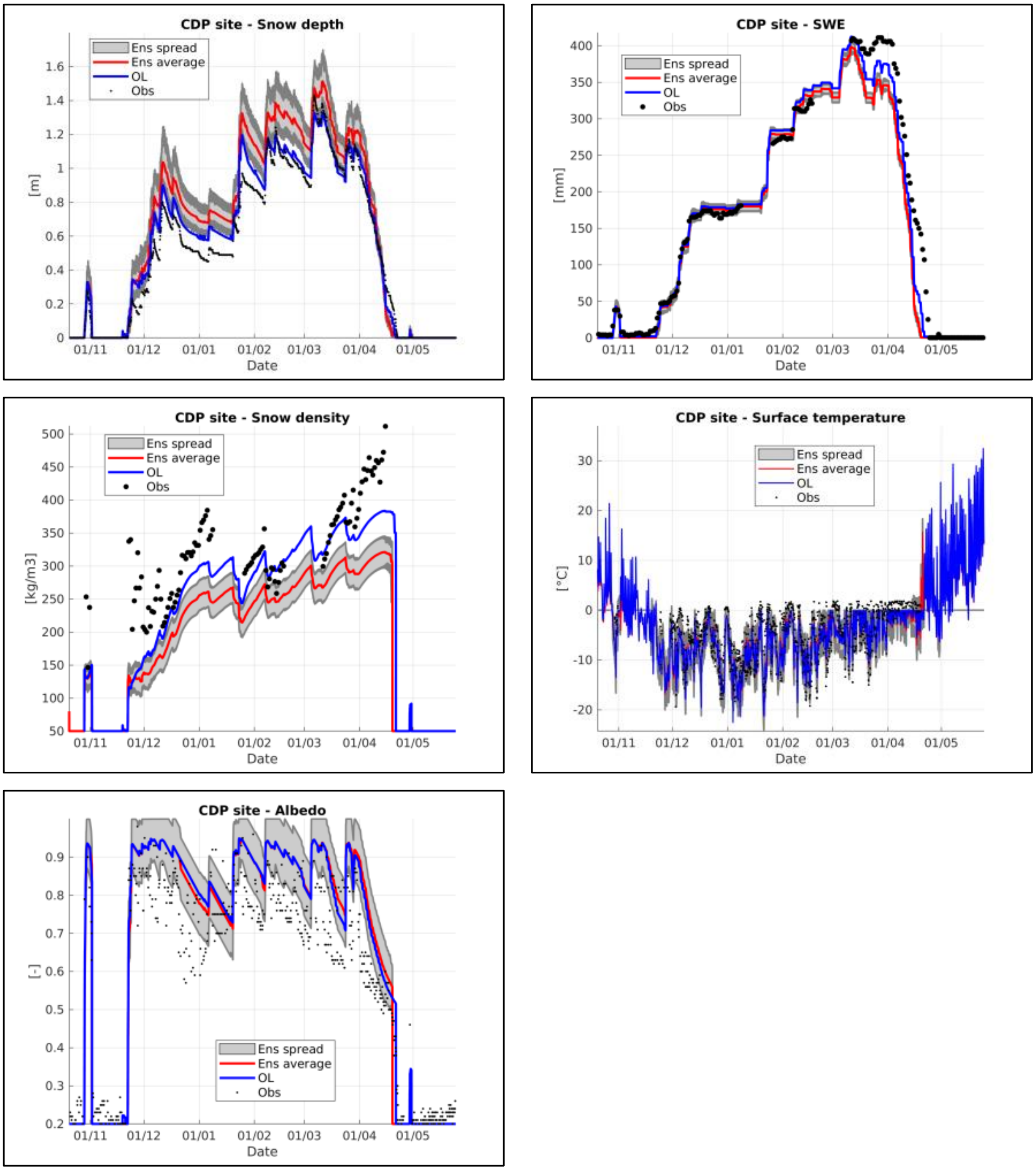

Figure 6.3a: *Perturbation of model prognostic variables - Ensemble simulations of snow depth, SWE, snow density, surface temperature and albedo – CDP site, winter season 2008-2009.*

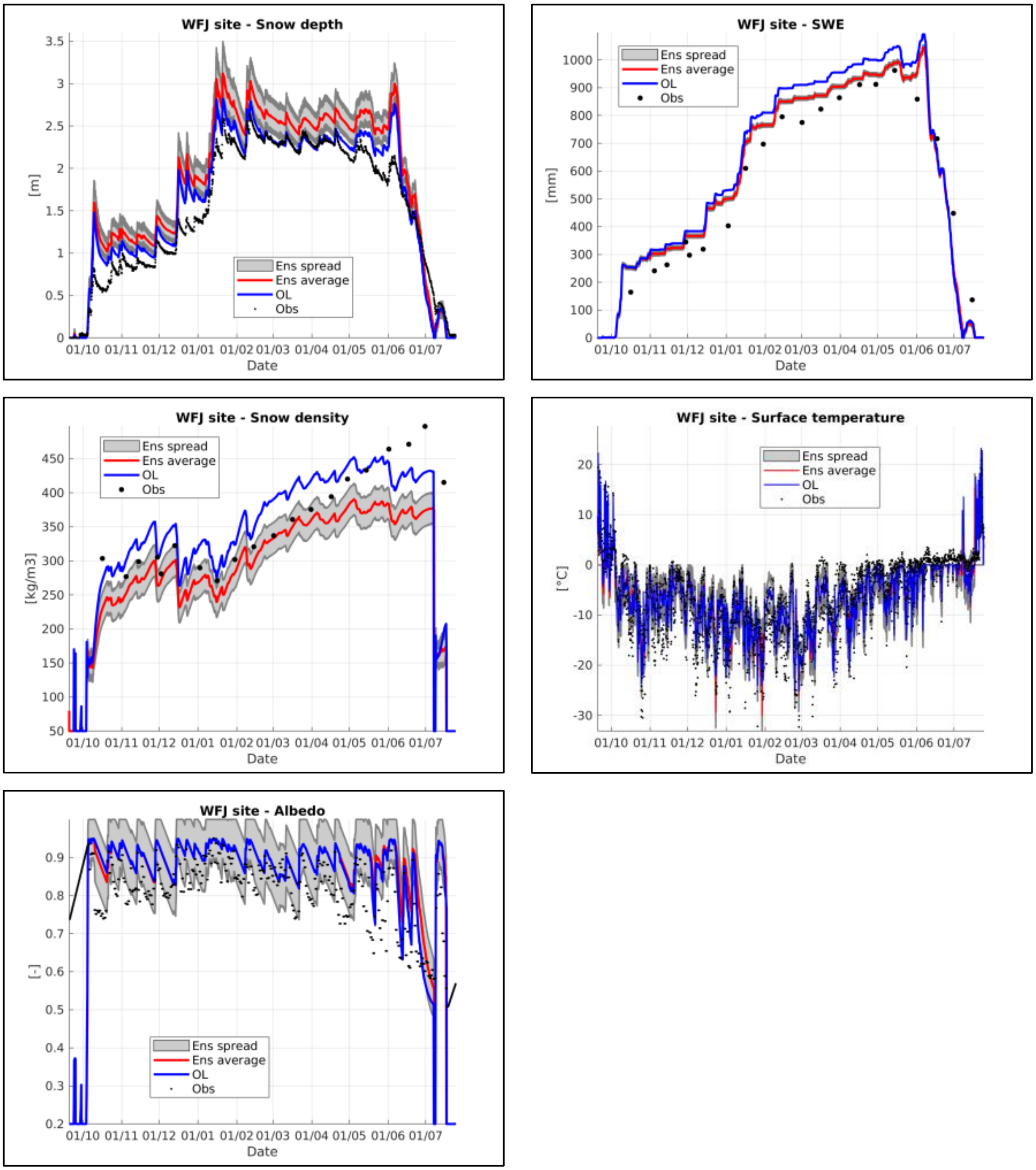

Figure 6.3b: *Perturbation of model prognostic variables - Ensemble simulations of snow depth, SWE, snow density, surface temperature and albedo – WFJ site, winter season 2003-2004.*

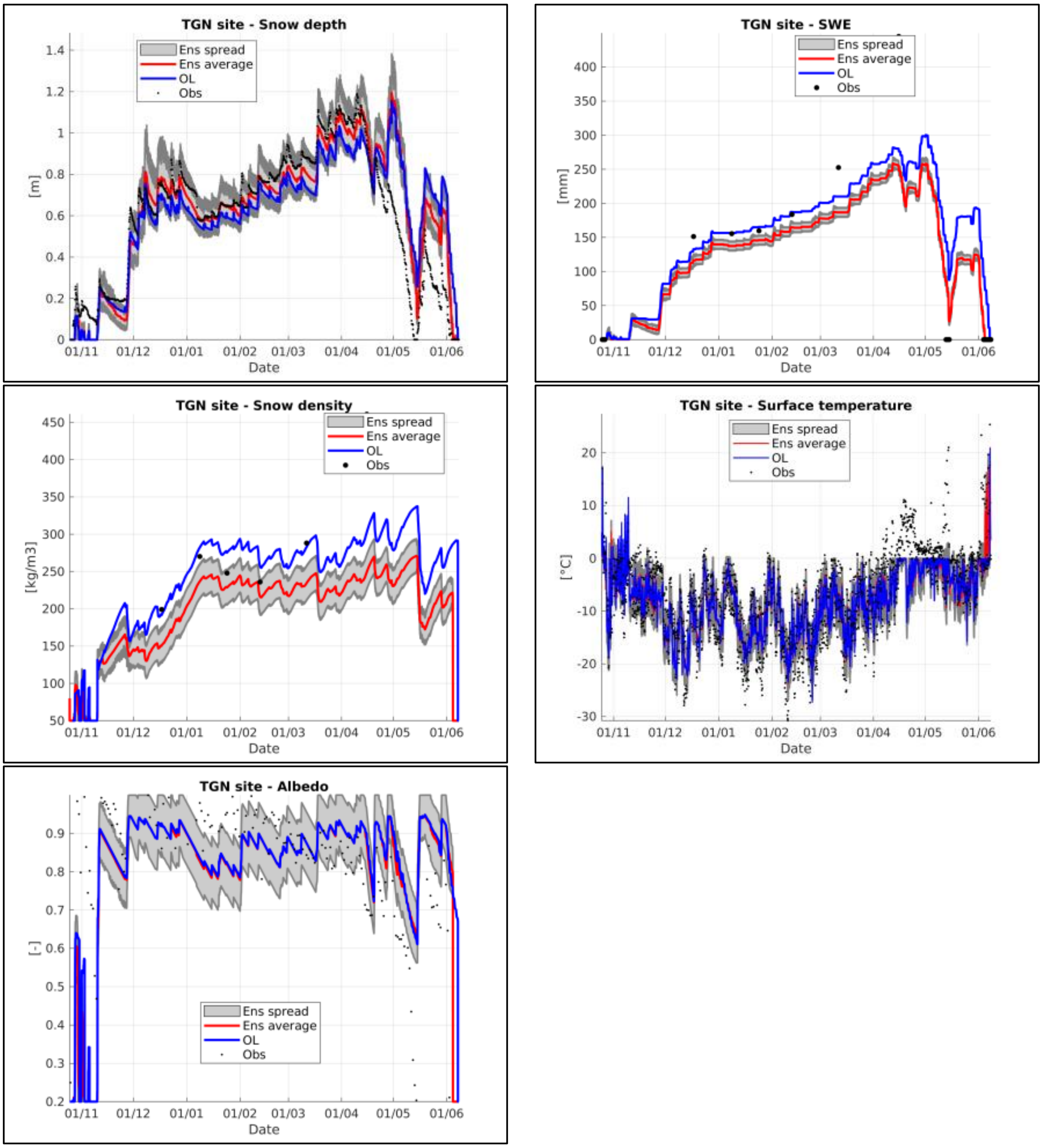

Figure 6.3c: *Perturbation of model prognostic variables - Ensemble simulations of snow depth, SWE, snow density, surface temperature and albedo – TGN site, winter season 2012-2013.*

The direct perturbation of the state variables does not result in neither divergent trend nor spurious predictions with respect to the control OL run. Nevertheless, the introduction of the stochastic noise can lead to possible over- and underestimation of the ensemble simulations, on average. The ensemble envelopes generally include the time series of the deterministic run, except for the SWE and snow density simulations, which however are not strongly affected by the perturbation procedure. Furthermore, this approach ensures a rather steady ensembles variance, with no prominent seasonality. It is noteworthy that some threshold processes involved within the snow dynamics model (e.g. disappearance of the surface snow layer; limitation of state variables within physical ranges) can result to be counter-productive in enlarging the ensembles spread.

6.2 Multivariate EnKF scheme

Several issues have been addressed within the implementation of the multivariate EnKF scheme into the snow model. Indeed, in a multivariate application the handling of the model nonlinearities becomes even more challenging and specific approaches are needed to limit the impact on the filter performance.

6.2.1 Model error covariance matrix

The correlations among state variables of a highly non-linear model may be difficult to assess through simple ensemble statistics, with possible miscorrection of model background errors, especially for those state variables which are not directly observed. In order to overcome some of these limitations and obtain an overall consistent update of the snowpack state, the model error covariance matrix has been reduced to a block-diagonal one. Two minors allow to handle the covariances among energy- and mass-related variables independently. The implementation of this solution allows updating both energy and mass balances by limiting physically incoherent corrections. Furthermore, in order to avoid possible model instabilities, any inconsistent value generated through the ensemble updating is removed by limiting each state variable into proper physical ranges. According to this approach, any outlier value is set equal to upper or lower limit of the corresponding physical range.

6.2.2 Multivariate EnKF simulations

The effectiveness of the Kalman filter is tested by assimilating in-situ snow-related measurements to update the model simulations of a 100-members ensemble. According to the experimental setup (Sect. 5.4), point ground-based observations of surface temperature, snow depth, albedo, SWE and snow density are assimilated every 3 hours.

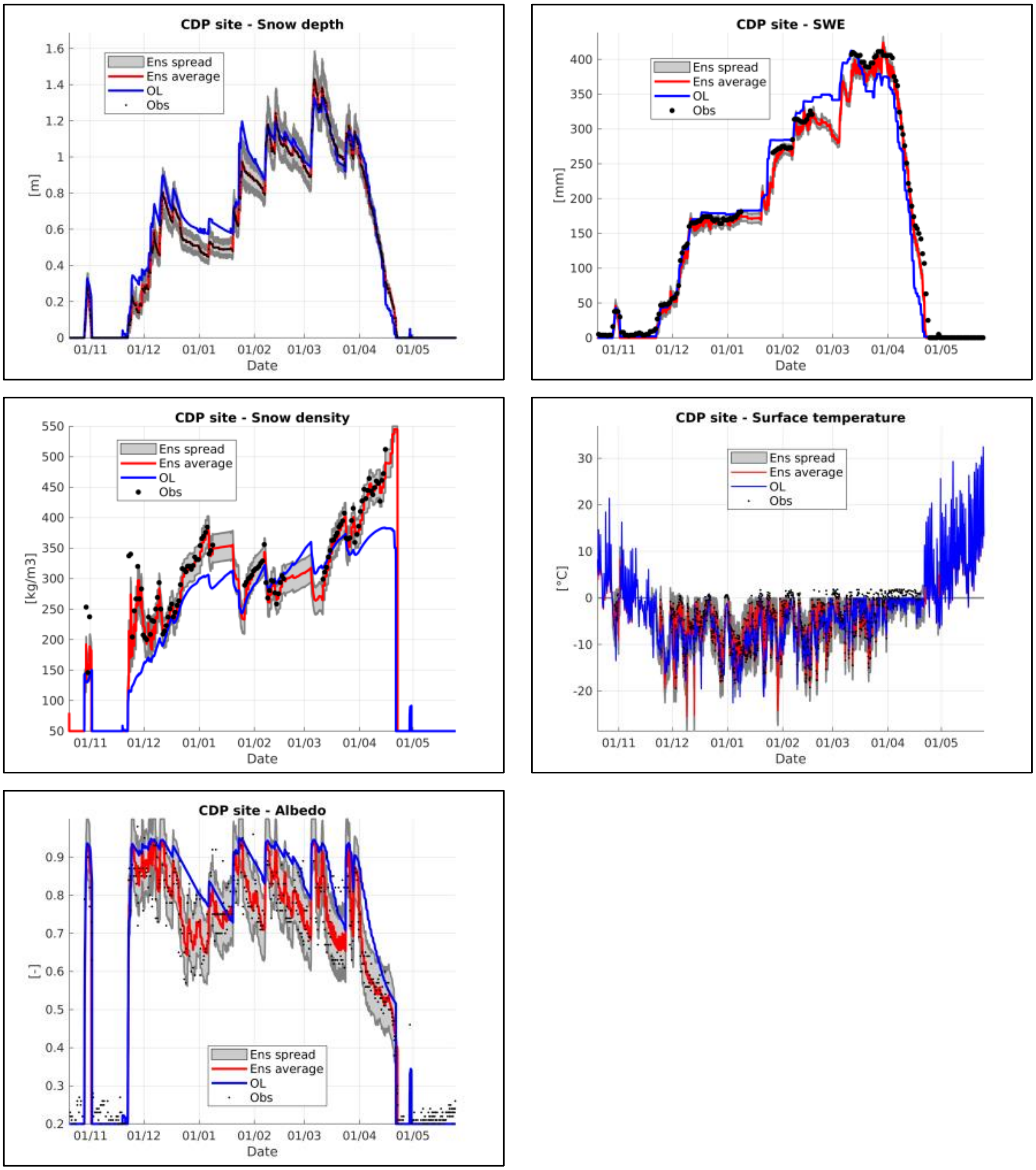

Figure 6.4a: *Multivariate EnKF simulations of snow depth, SWE, snow density, surface temperature and albedo – CDP site, winter season 2008-2009.*

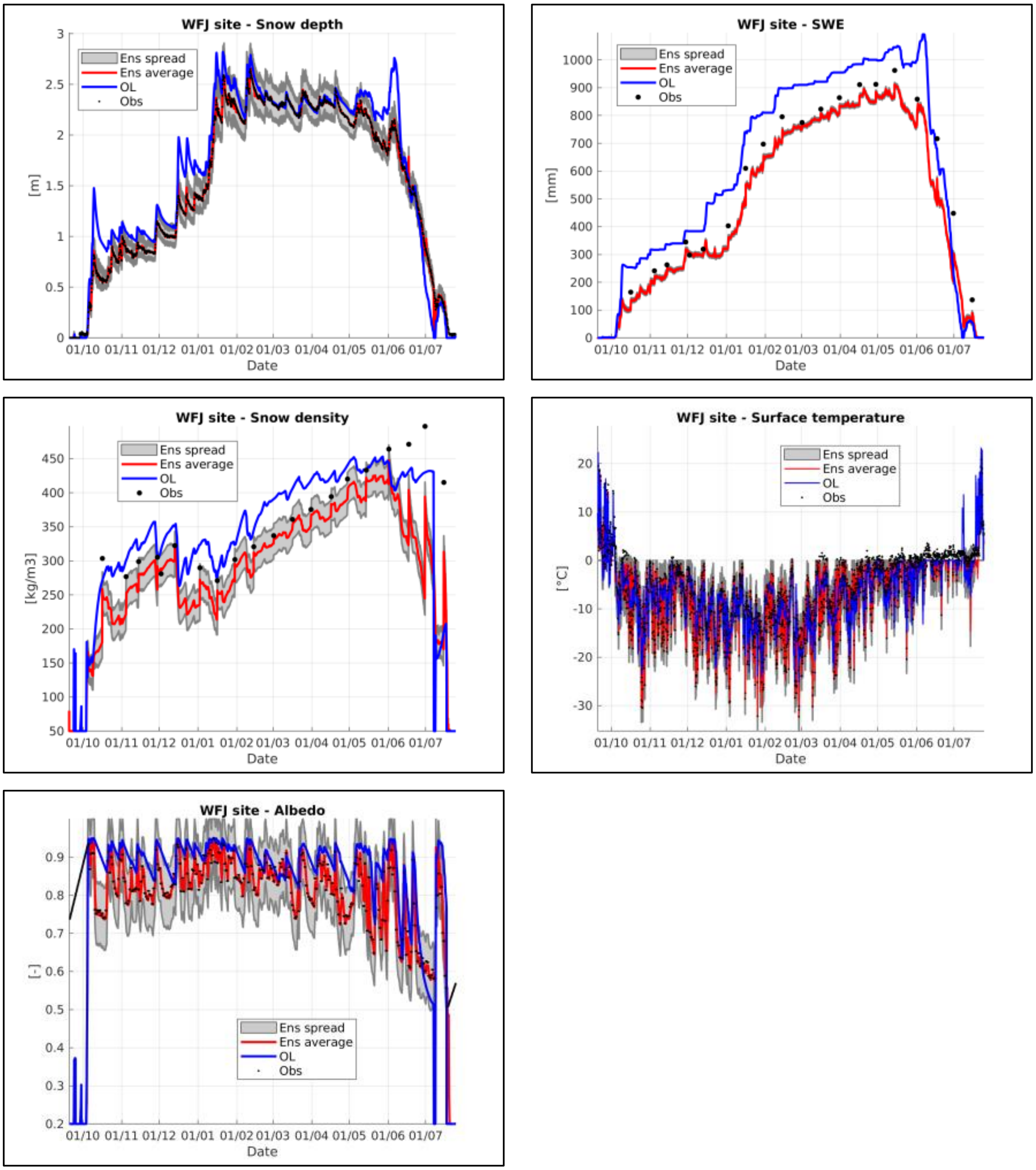

Figure 6.4b: *Multivariate EnKF simulations of snow depth, SWE, snow density, surface temperature and albedo – WFJ site, winter season 2003-2004.*

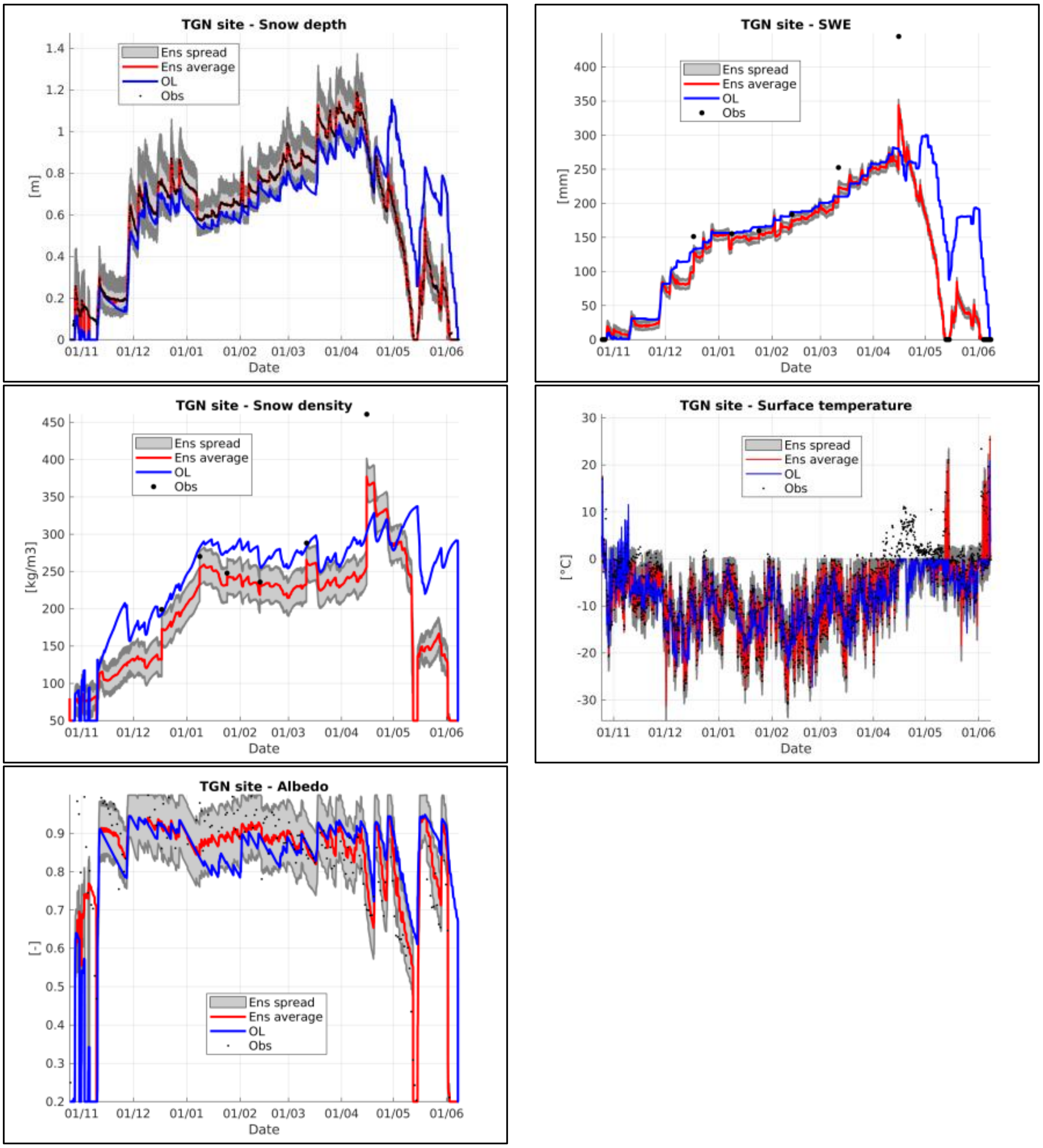

Figure 6.4c: *Multivariate EnKF simulations of snow depth, SWE, snow density, surface temperature and albedo – TGN site, winter season 2012-2013.*

Figures 6.4a, b, c show the multivariate EnKF simulations throughout one benchmark winter season at each analysed experimental site. The filter well succeeds in handling the model nonlinearities, as proved by the general improvement of the simulated snowpack dynamics. The snowfalls overestimation is significantly reduced and the model enables to better reproduce the melting timing with respect to the control run simulations. The over- and underestimation biases affecting the snow mass balance during both the accumulation and the melt-out periods are significantly decreased. Indeed, the filtering process guarantees to generally improve both the snowpack settling and ripening dynamics. At WFJ and TGN sites, the lower SWE measurement frequency entails a saw tooth pattern resulting from the model responses to the sharp filter updates between two following assimilation time steps. The daily SWE observations at the French site ensure a smoother trend thanks to more frequent filter updating calling for lower corrective terms. Accordingly, the same pattern is observed in the snow density simulations, where the system sharply tends to its previous state right after the steep stretches towards observations. Even though the deterministic simulations well get the daily thermal cycle, generally they reveal an underestimation of the diurnal surface temperature peaks and a significant overestimation of the nocturnal ones. The assimilation of temperature measurements allows to better reproduce the size of the temperature range by forcing the ensemble surface temperatures towards the observations, on average. The albedo simulations are more consistent with the observations, since they better catch both its seasonal evolution and the albedo increase whenever a snowfall event occurs. Furthermore, it is noteworthy that the filter updating does not necessarily guarantee the physical consistency among the prognostic variables describing the state of each ensemble member. The often-sharp corrective terms individually applied to each the state variable can result in a suboptimal estimate of the system state, which tends to quickly restore its previous conditions, as demonstrated by the saw tooth trend that characterizes the resulting simulations.

The resulting statistical indices (Sect. 4.4.2; Sect. 5.4.2) are shown in Figures 6.5a, b, c. The snow depth simulations get the most benefit from the filter updating thanks to the high measurement frequency and the slow dynamics of this prognostic variable. The overall snow mass balance benefits from the assimilation of snow data, as proven by the scores of the snow density and SWE simulations, except for some sporadic winter seasons at CDP site. The filter reveals a satisfying efficiency in updating the surface temperature. However, even though the filtering procedure ensures a higher consistency with the temperature measurements at each assimilation time step, the updating effect turns out not to be long-lasting. This limitation is mainly ascribable to the sharp filter sequential corrections of the surface temperature, which are likely to generate thermal conditions remarkably different from the current simulated ones. The low model thermal inertia allows the system to quickly restore its previous thermal state between two following assimilation time steps. Consistently, the albedo simulations are generally enhanced.

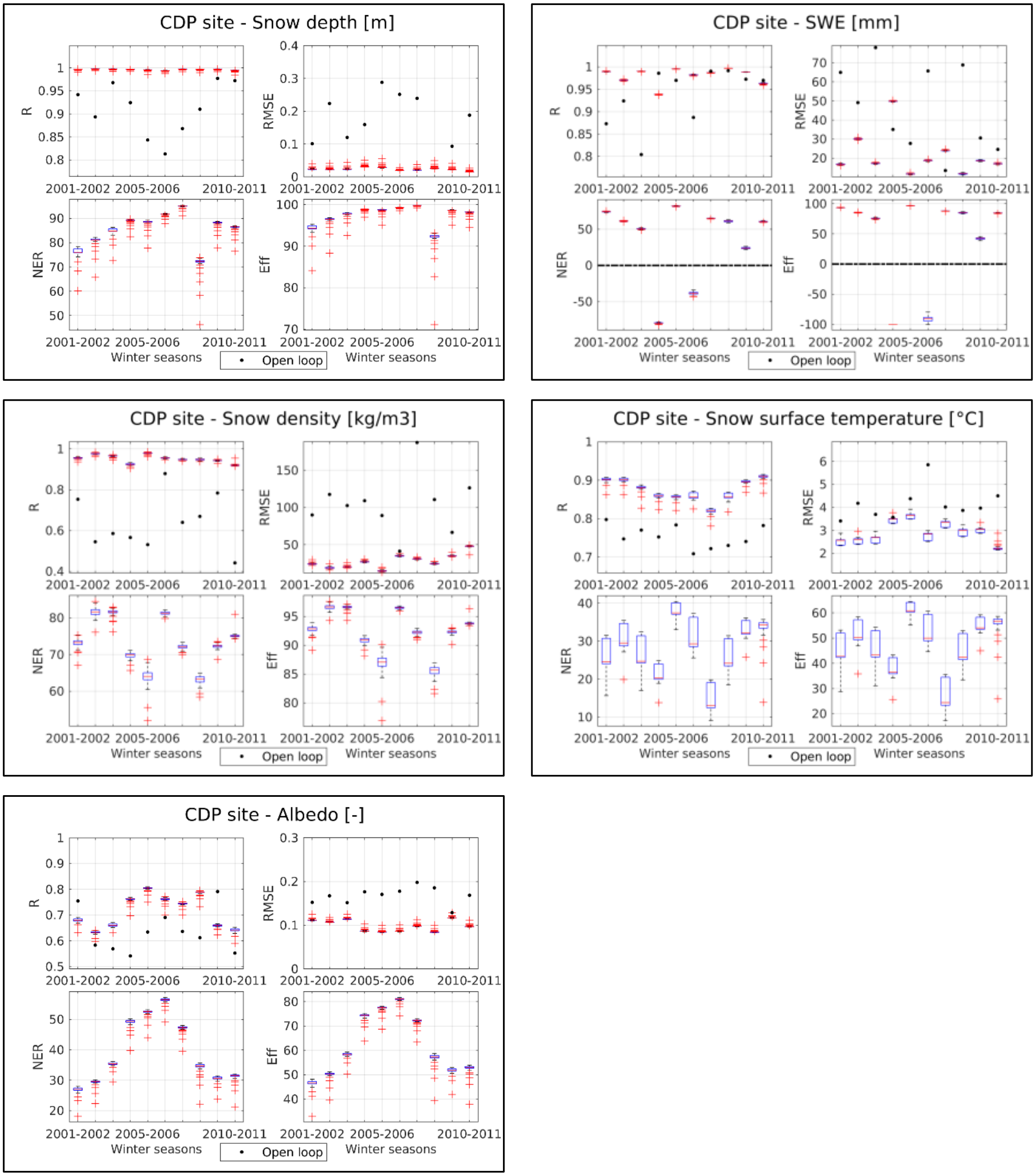

Figure 6.5a: *Multivariate EnKF scheme - Statistical scores of snow depth, SWE, snow density, surface temperature and albedo simulations - CDP site (full dataset). The bottom and top edges of each box indicate the 25th and 75th percentiles of the scores distribution of the ensemble members, respectively.*

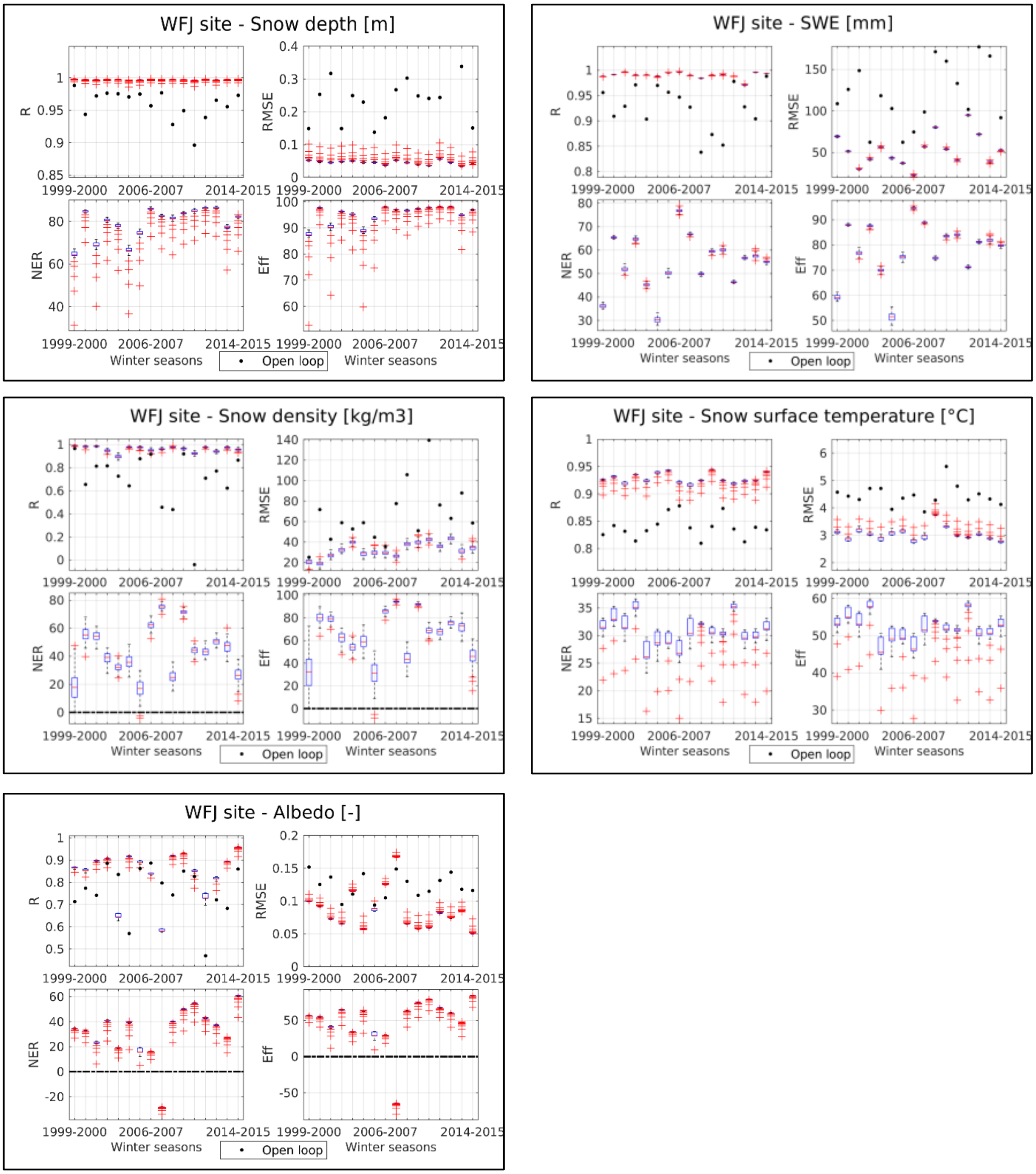

Figure 6.5b: *Multivariate EnKF scheme - Statistical scores of snow depth, SWE, snow density, surface temperature, and albedo simulations - WFJ site (full dataset).*

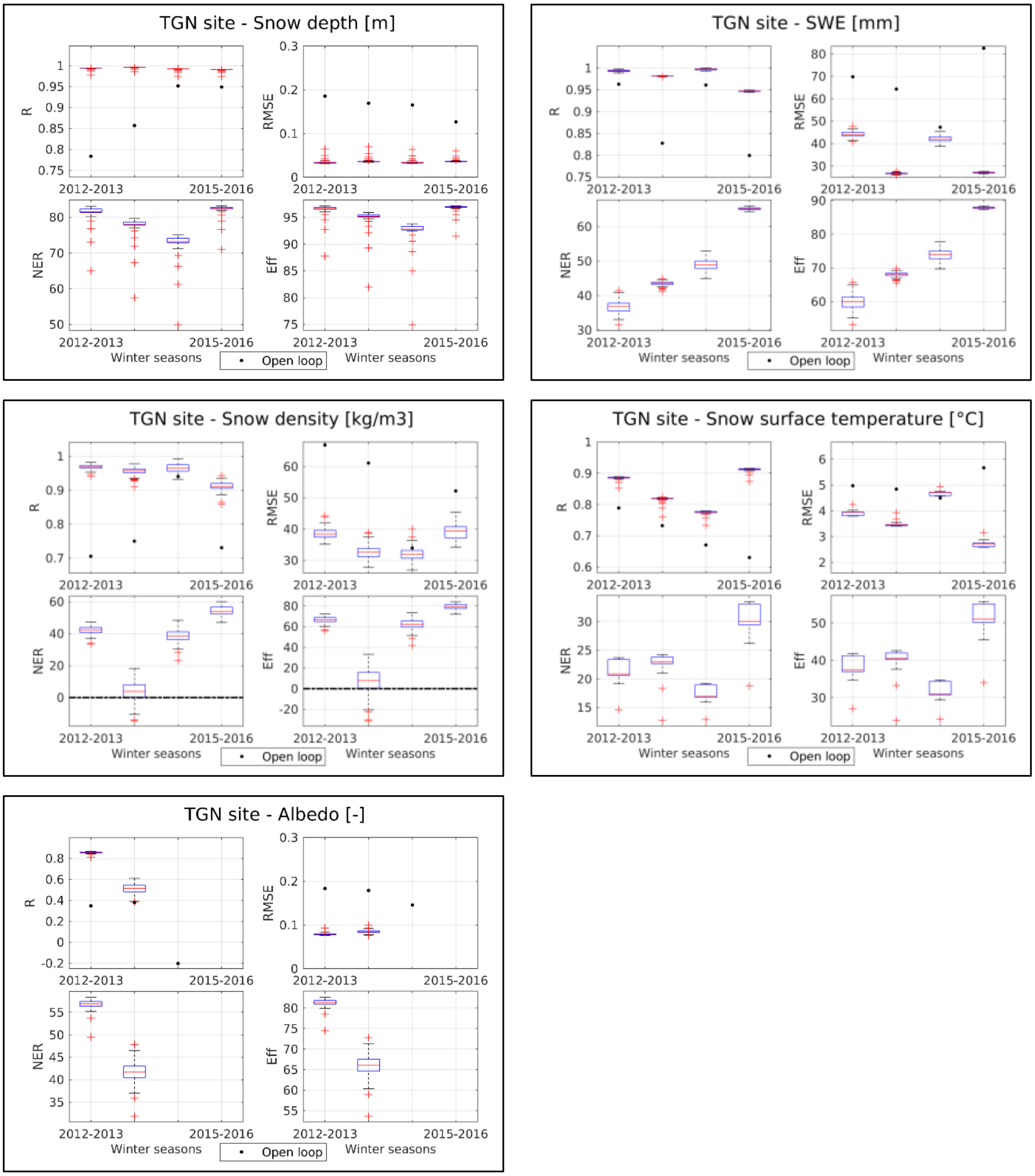

Figure 6.5c: *Multivariate EnKF scheme - Statistical scores of snow depth, SWE, snow density, surface temperature, and albedo simulations - TGN site (full dataset).*

6.3 Sensitivity experiments

With the purpose of investigating the system sensitivity to different DA settings, several experiments have been carried out. Firstly, the sensitivity to the DA frequency has been tested. Secondly, the sensitivity to the ensemble size has been evaluated by varying the number of ensemble members. Lastly, the impact of the assimilation of different observed variables has been studied by assimilating different combinations of them.

6.3.1 System sensitivity to the assimilation frequency

This first experiment has been performed by varying the assimilation frequency, for a given 100-members ensemble size. Snow data have been assimilated every 3, 6, 12, 24 hours in order to assess the impact on the filter effectiveness. Figures 6.6a, b, c show the resulting statistical scores at decreasing assimilation frequency.

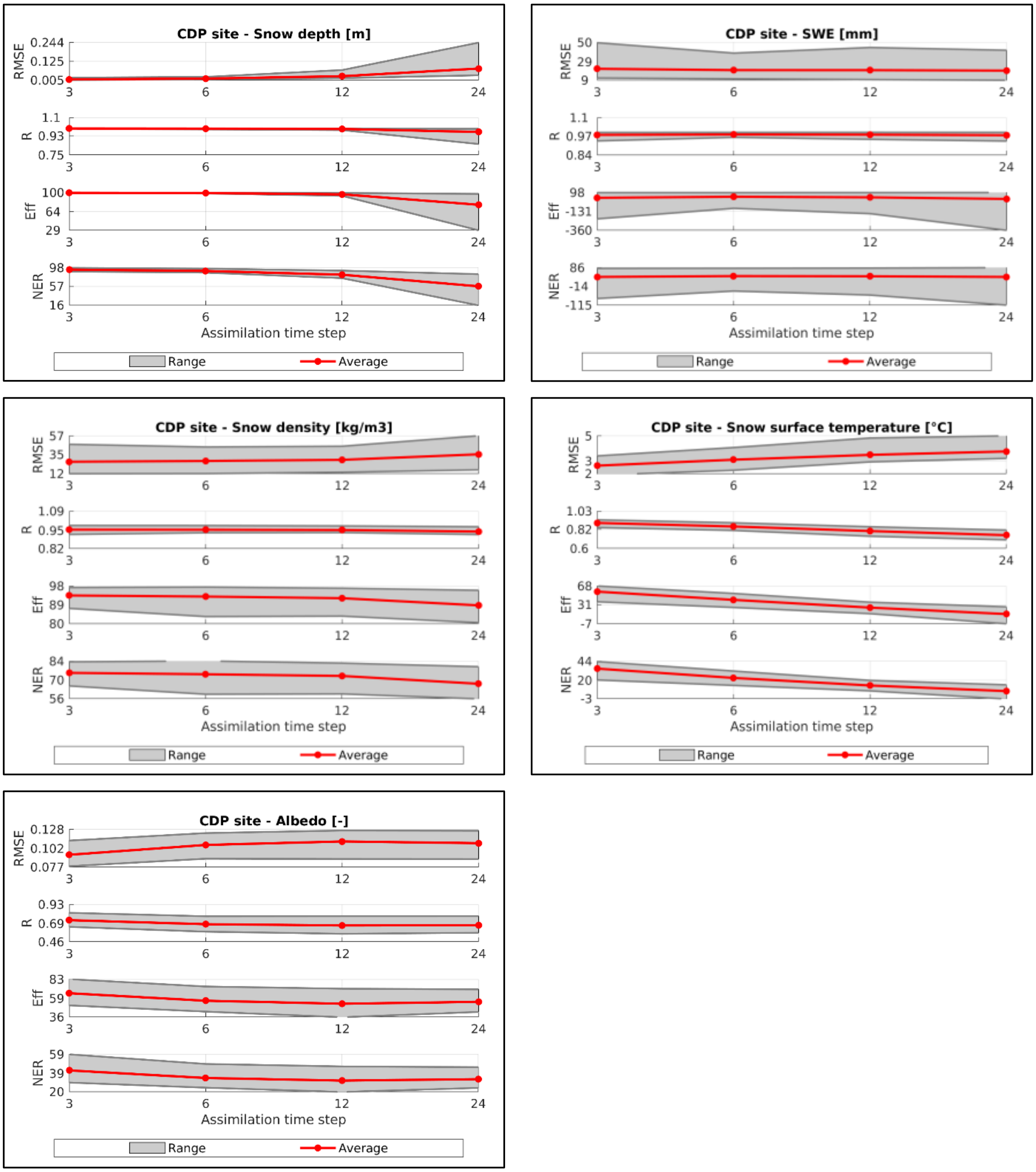

Figure 6.6a: *Multivariate EnKF scheme – System sensitivity to the assimilation frequency - Statistical scores of snow depth, SWE, snow density, surface temperature, and albedo simulations – CDP site, (full dataset). The range is evaluated across the dataset winter seasons.*

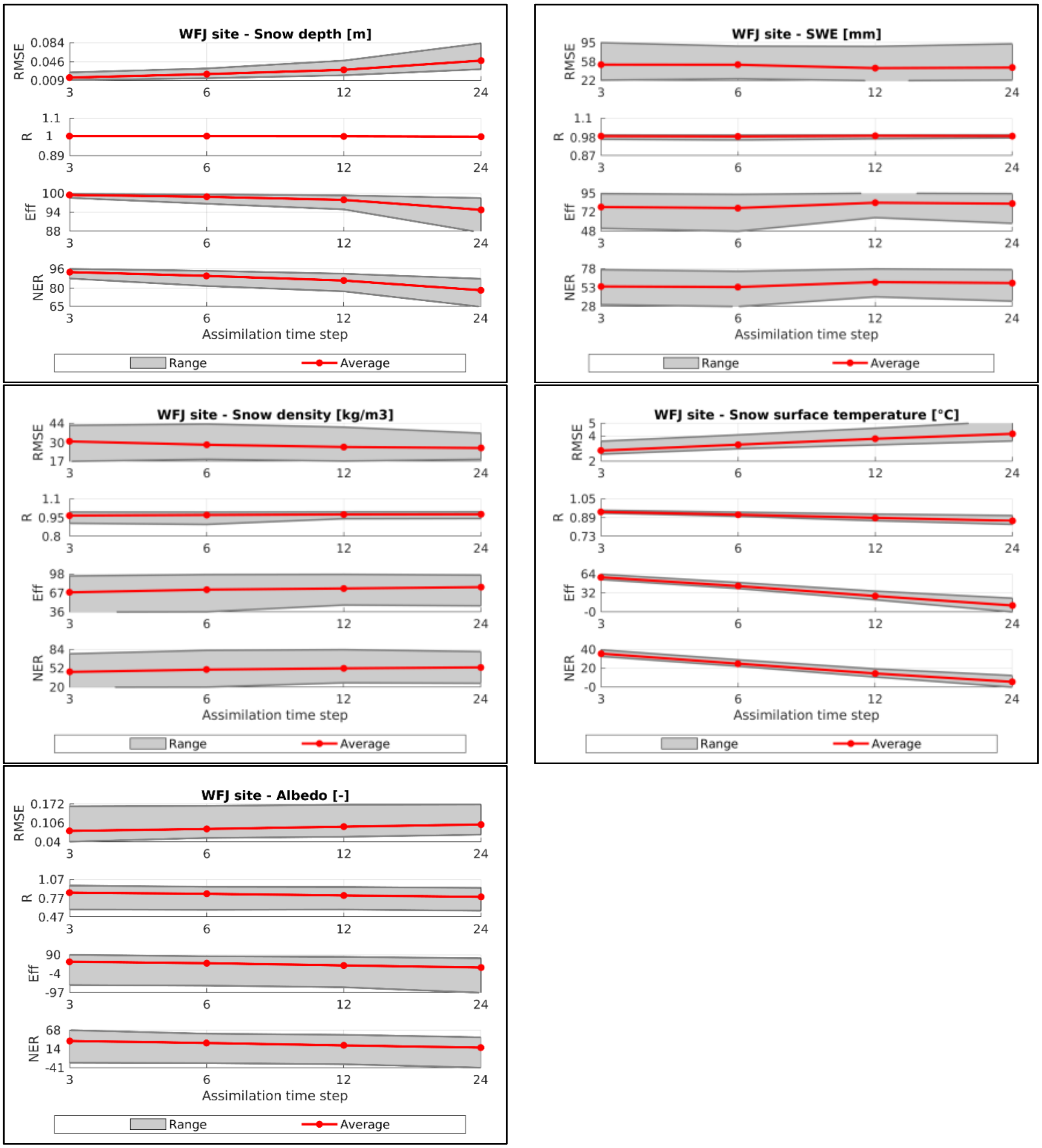

Figure 6.6b: *Multivariate EnKF scheme – System sensitivity to the assimilation frequency - Statistical scores of snow depth, SWE, snow density, surface temperature, and albedo simulations – WFJ site, (full dataset).*

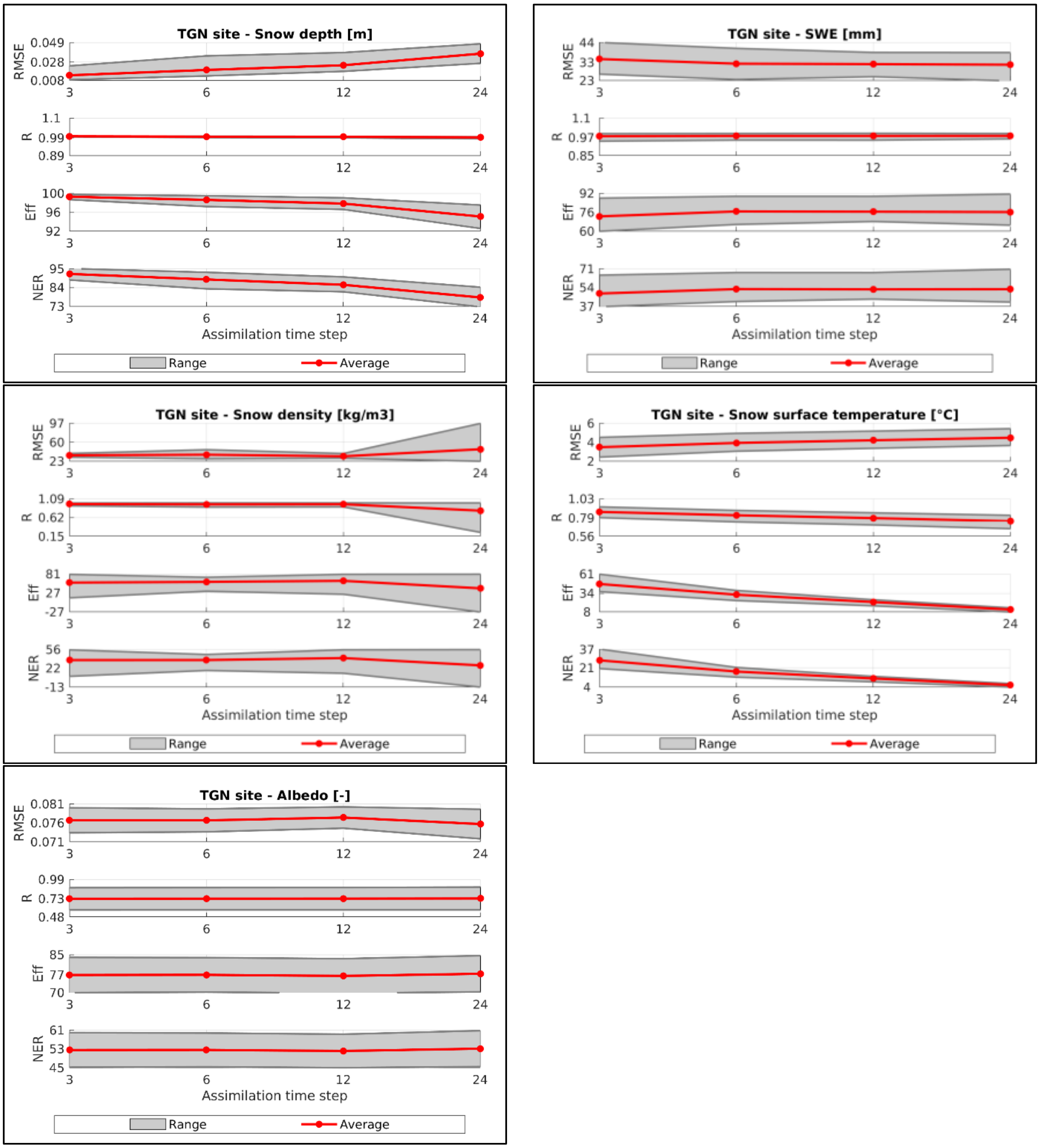

Figure 6.6c: *Multivariate EnKF scheme – System sensitivity to the assimilation frequency - Statistical scores of snow depth, SWE, snow density, surface temperature, and albedo simulations –TGN site (full dataset).*

Generally, statistical metrics reveal a foreseen worsening of the filter performance as the assimilation frequency decreases from every 3 to 24 hours.

At the French site, the decrease in the assimilation frequency does not prominently affect the snow depth predictions up to every 12 hrs. The daily assimilation entails a worsening of the average values of *Eff* and *NER*, while the other two scores show an increase in the spread of their samples. This trend is mainly due to the system sensitivity in terms of snow density, whose simulations, in turn, reveal a slight worsening of the scores as the assimilation frequency drops to every 24 hrs, except for *R* values proving a preserved satisfying positive correlation. The SWE predictions at CDP maintain the average values of the statistical scores with a decreasing assimilation frequency, while their spreads are slightly wider with the daily assimilation. With respect to CDP, at the Swiss and Italian sites the *RMSE* and *R* values of the snow depth simulations turn out to be more conservative up to every 24 hrs. Nevertheless, a higher sensitivity is detected in terms of *Eff* and *NER*, which entails a more marked progressive worsening of these metrics. At WFJ the statistical scores of snow density predictions are better preserved than at the French site. As the assimilation frequency decreases, the scores samples of the snow density simulations at TGN are generally less spread up to the 12-hrs assimilation. With the daily assimilation, sharp increases in their spreads are observed, along with a worsening of the average statistical metrics. Consistently with CDP, at Swiss and Italian sites the filter performance in updating the SWE predictions is weakly sensitive to the assimilation frequency. However, at WFJ both the simulations with 12-hrs and 24-hrs assimilation slightly outperform those with a higher assimilation frequency, mainly due to the poorer bi-weekly availability of the in-situ measurements of this variable. Similarly, at TGN a slight improvement is observed as the assimilation frequency becomes coarser than every 3 hrs, especially in term of *Eff* and *NER*.

With respect to the other analysed variables, at all the experimental sites the surface temperature simulations are generally characterized by a well-defined trend revealing a sizeable worsening of the filter performance with a decreasing assimilation frequency, which leads to statistical indices almost equivalent to the OL ones with the 24-hrs assimilation. This undesired issue is mainly due to the faster dynamic evolution of this variable, whose daily thermal cycle can make the predictions diverge from their analysis simulations between two following daily assimilation time steps. However, up to a frequency of 12 hrs the assimilation procedure well succeeds in properly updating this variable. At all the pilot sites, generally the filter performance is slightly sensitive to the assimilation frequency in terms of albedo, whose simulations are not subject to a progressive worsening of neither their average statistical indices nor the spread of their samples, up to every 24 hrs. Nevertheless, at CDP the scores get slightly worse from 3-hrs and 6-hrs assimilation frequencies, whose satisfying scores are then preserved up to the daily assimilation.

In light of these results, a useful assimilation frequency between 3 and 12 hrs can ensure a consistent update of the system state.

6.3.2 System sensitivity to the ensemble size

Alongside with the assimilation frequency, another critical parameter of the DA procedure is the ensemble size. Indeed, if the amount of model realizations is too limited, the evaluation of the model error covariance matrix could be not properly accurate. The uncertainty of this estimation decreases in a rate proportional to $1/\sqrt{N}$, with N model states (Evensen, 1994). On the other hand, if the ensemble is oversized, an excessive computational load could be required.

The system sensitivity to the ensemble size has been evaluated by varying the number of the members from 20 to 200, for a given 3-hrs assimilation frequency.

The resulting scores (Figures 6.7a, b, c) prove that the system is not markedly sensitive to the ensemble size. The increase in the ensemble size does not entail a progressive improvement of the statistical indices, whose average values have a steady trend as the number of the model realizations raises. As well, the scores spreads are not characterized through well-defined trends as a function of the ensemble size. Nevertheless, the snow depth simulations generally reveal the narrowest spreads of both *RMSE* and *R*. At CDP and TGN sites the *RMSE* values of the albedo predictions are weakly spread, as well as the *R* indices of the SWE, snow density and surface temperature at all the experimental sites.

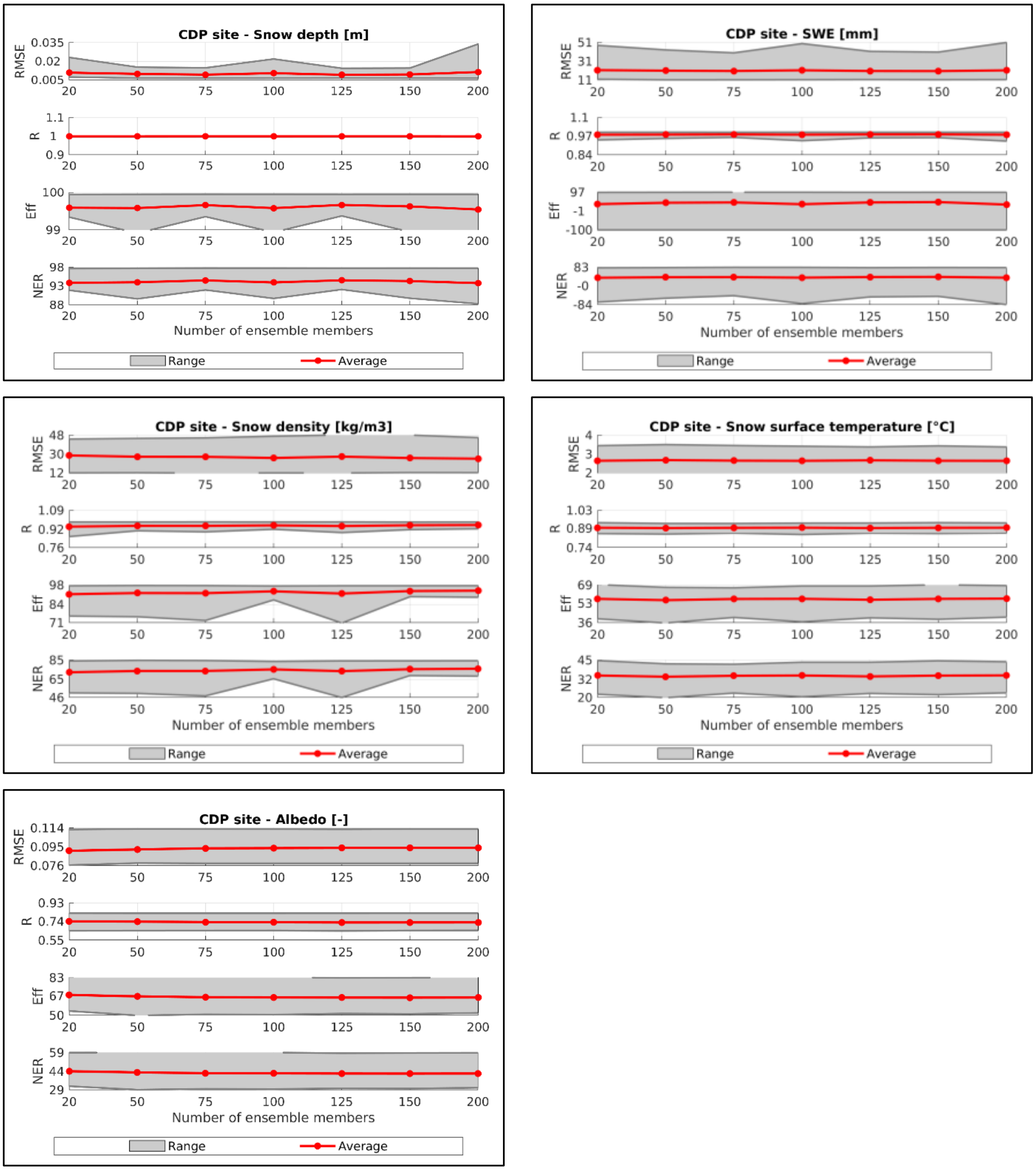

Figure 6.7a: *Multivariate EnKF scheme – System sensitivity to the ensemble size - Statistical scores of snow depth, SWE, snow density, surface temperature, and albedo simulations – CDP site (full dataset). The range is evaluated across the dataset winter seasons.*

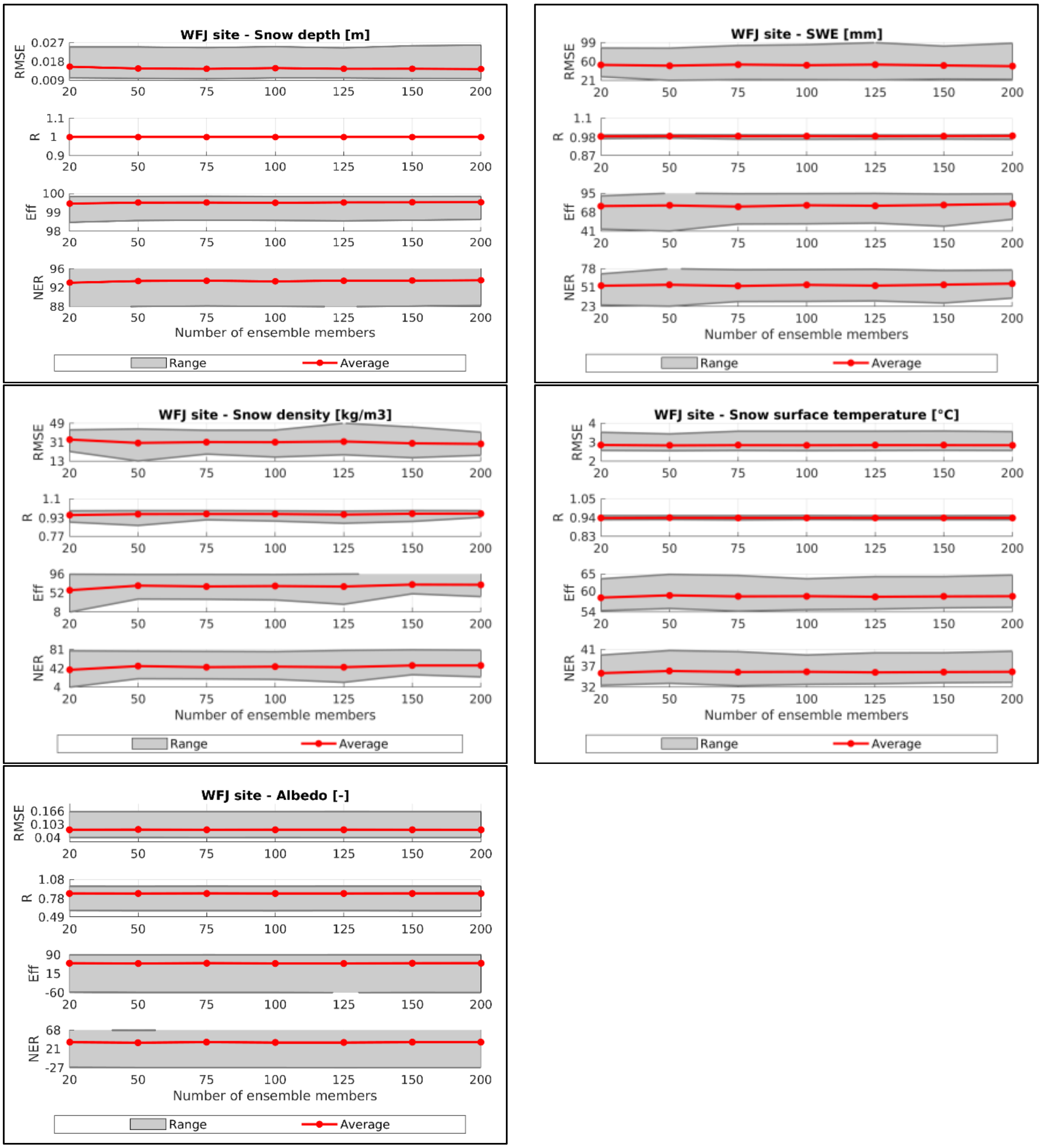

Figure 6.7b: *Multivariate EnKF scheme – System sensitivity to the ensemble size - Statistical scores of snow depth, SWE, snow density, surface temperature, and albedo simulations –WFJ site (full dataset).*

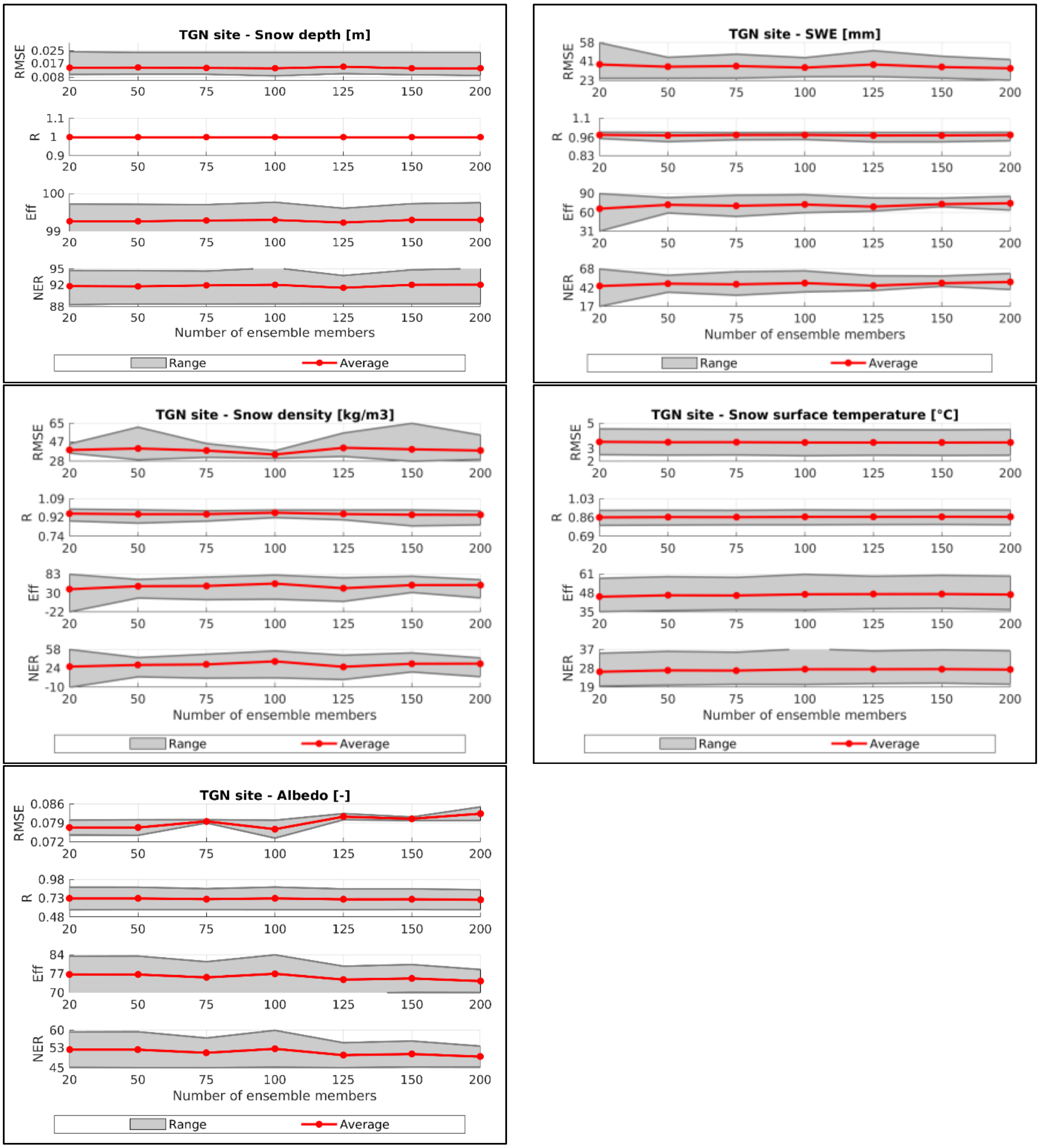

Figure 6.7c: *Multivariate EnKF scheme – System sensitivity to the ensemble size - Statistical scores of snow depth, SWE, snow density, surface temperature, and albedo simulations – TGN site (full dataset).*

6.3.3 System sensitivity to the assimilation of different variables

While keeping unchanged both the 100-members ensemble size and the 3-hrs assimilation frequency, the impact of the assimilation of different observed variables is investigated by assimilating different combinations of them:

a. Only surface temperature (T);
b. Only SWE (W);
c. Only albedo (A);
d. Only snow depth (H);
e. Surface temperature and snow depth (TH);
f. Surface temperature and albedo (TA);
g. Albedo and snow depth (AH);
h. Surface temperature and SWE (TW);
i. SWE and albedo (WA);
j. SWE and snow depth (WH);
k. Surface temperature, albedo and snow depth (TAH);
l. Surface temperature, SWE, albedo (TWA);
m. SWE, albedo and snow depth (WAH);
n. Surface temperature, SWE and snow depth (TWH).

Figures 6.8a, b, c show the performances of the multivariate EnKF scheme depending on the assimilated quantities. As expected, the simulations of each involved prognostic variable generally benefit from the assimilation of its direct observations, even when assimilated in combination with other measurements.

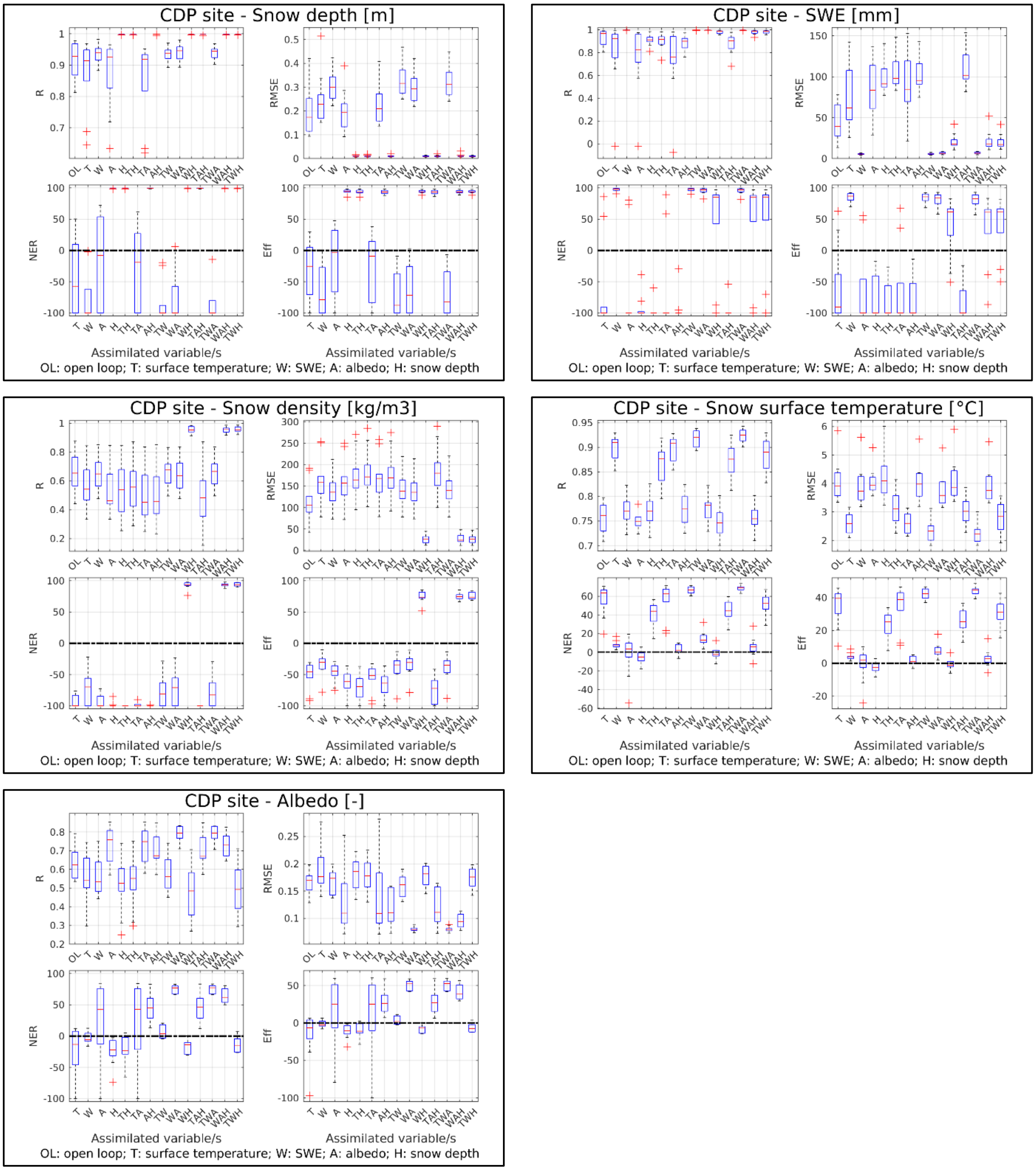

Figure 6.8a: *Multivariate EnKF scheme – System sensitivity to the assimilation of different variables - Statistical scores of snow depth, SWE, snow density, surface temperature, and albedo simulations – CDP site (full dataset). The bottom and top edges of each box indicate the 25th and 75th percentiles of the scores distribution throughout the dataset winter seasons, respectively. Reference open loop skills are reported in terms of R and RMSE values.*

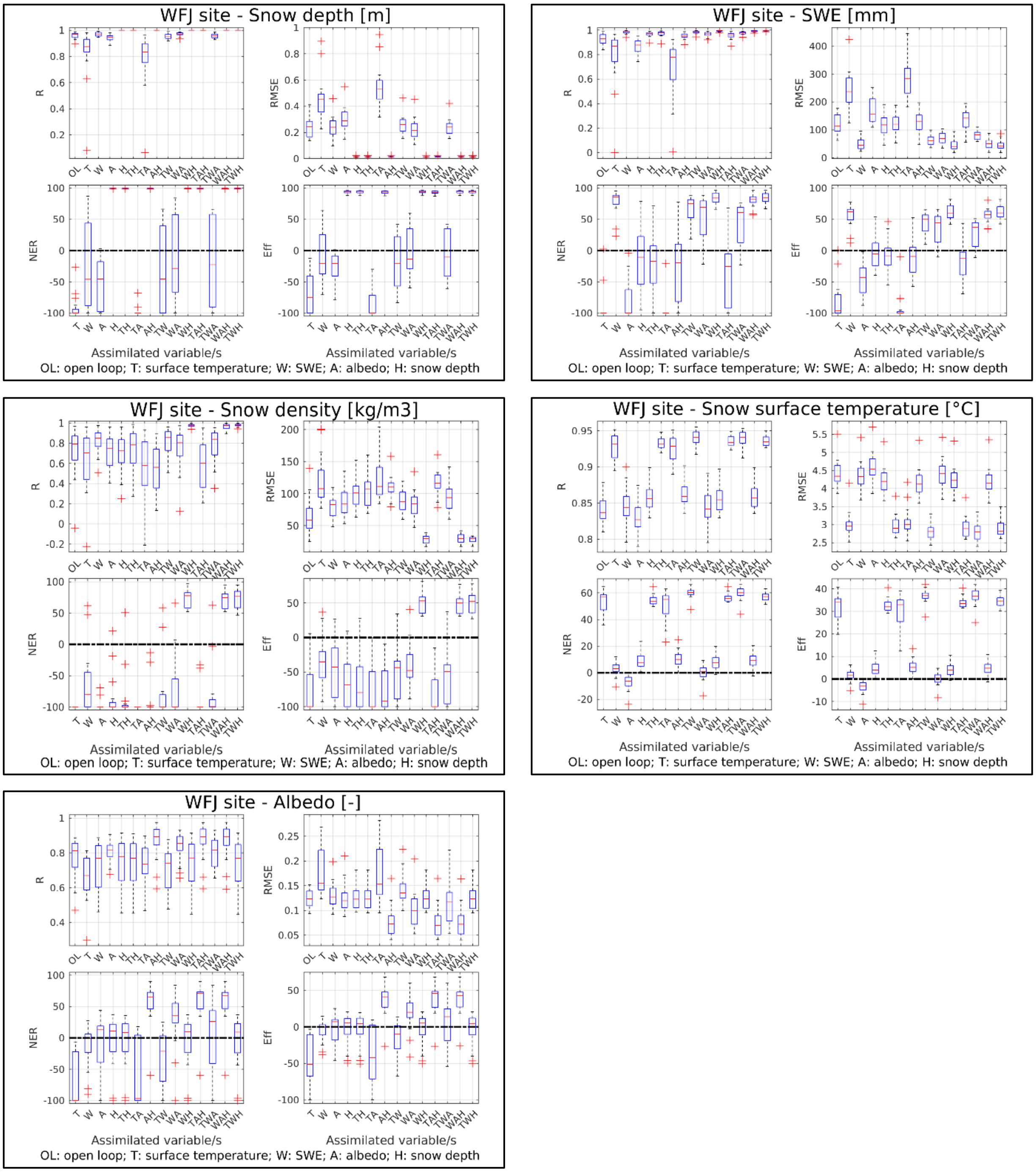

Figure 6.8b: *Multivariate EnKF scheme – System sensitivity to the assimilation of different variables - Statistical scores of snow depth, SWE, snow density, surface temperature, and albedo simulations – WFJ site (full dataset).*

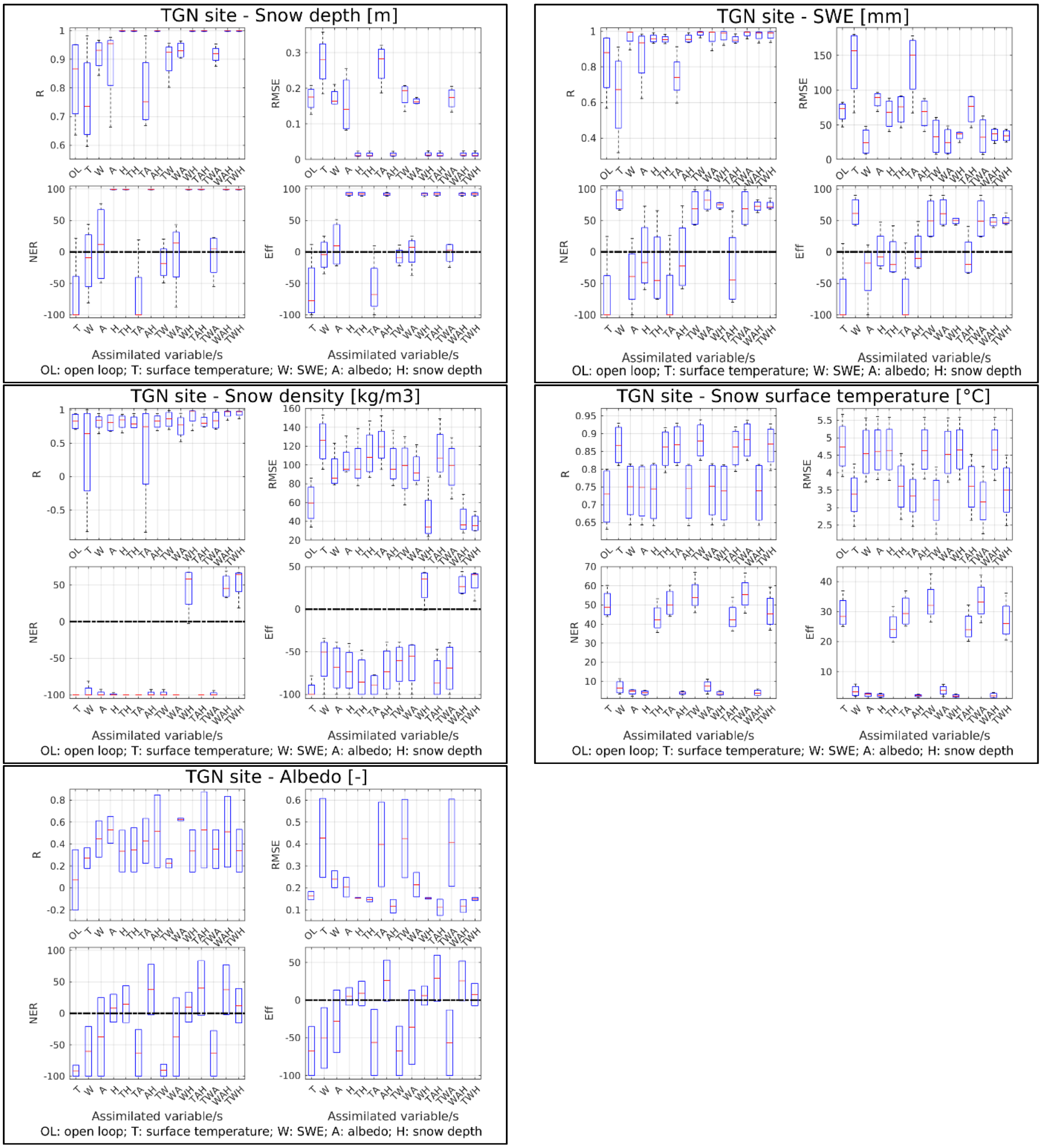

TGN site - Snow depth [m]

TGN site - SWE [mm]

TGN site - Snow density [kg/m3]

TGN site - Snow surface temperature [°C]

TGN site - Albedo [-]

Assimilated variable/s

OL: open loop; T: surface temperature; W: SWE; A: albedo; H: snow depth

Figure 6.8c: *Multivariate EnKF scheme – System sensitivity to the assimilation of different variables - Statistical scores of snow depth, SWE, snow density, surface temperature, and albedo simulations –TGN site (full dataset).*

Snow mass-related prognostic variables

To consistently update the mass balance of the system, the *W*-assimilation turns out not to be sufficient. Complementary information on snow density is needed to prevent possible misleading snow depth updates resulting from biased snow density estimates. The *T*-assimilation even entails a counter-productive impact on snow depth predictions, since the filter corrections of the thermal variable are likely to generate thermal conditions sensibly different from the current ones, which can also trigger threshold processes involved within the snow dynamics model (e.g. induced melt-out of the surface snow layer). Sharp updates of the system temperature to reduce the under- and overestimation of the diurnal and nocturnal peaks can respectively lead to possible spurious melting and refreezing events during the winter season, which result in a worsening of the modelled snowpack dynamics. Accordingly, even the combined *TW*-assimilation does not guarantee to cope with the induced melting events due to the general lack of information on snow density. Except for the TGN site, the *A*-assimilation does not result in any significant improvement of snow depth simulations, not even the joint *TWA*-assimilation.

It is noteworthy that the slight impact of the *A*-assimilation is mainly ascribed to an effect of the limitation of this quantity within proper physical ranges after the perturbation procedure (Sect. 6.1.1). Indeed, with respect to the other state variables, the albedo is limited within a more restricted range [0.2-1], which can lead to a lower error variance with a resulting less powerful weighting of its observations.

Similarly to the snow depth simulations, the assimilation of energy-related variables (*T*- and *A*-assimilation) does not result in any improvement of SWE predictions. The lack of information on snow density hinders the consistent SWE updating when snow depth measures are assimilated (*H*-assimilation). This issue can be regarded as a filter limitation in properly handling the nonlinear correlations among the variables included in the mass-related minor of the model error covariance matrix. A further evidence of this limitation is the filter updating of snow density simulations, which requires observations of at least two mass-related variables to consistently update the system state.

Energy-related prognostic variables

Except for the TGN station, where the filter succeeds in enhancing, more or less effectively, the simulations of the surface temperature, the updating of the mass balance generally slightly improves the model thermal state (e.g. *WH*-assimilation at WFJ site, *W*-assimilation at CDP station). The *A*-assimilation does not significantly affect the system temperature, whose predictions reveal around the same statistical indices of the deterministic control run. The higher frequency of the SWE measurements at CDP ensures a satisfying filter performance in updating the surface temperature through the combined *WA*-assimilation.

The albedo updating is more challenging, since even the *A*-assimilation does not always guarantee the filter effectiveness, as at WFJ site. Beyond the *TA*-assimilation, the greatest improvement results from the combined assimilation with snow mass measurements (i.e. *AH*- and *WA*-assimilations), except for TGN, where the lower frequency of the SWE estimates hinders the filter performance.

The sensitivity analysis of the system to the assimilation of different observed variables has allowed to highlight the potential of the multivariate DA scheme. The combined assimilation of both energy- and mass-related quantities turns out to be of critical importance. Indeed, the updating of the energy-related variables generally does not entail a consistent update of the system mass balance. Rather, the often-sharp filter corrections of the surface temperature result into misleading updates of the simulated snowpack dynamics. Nevertheless, it is noteworthy that the reduction of the model error covariance matrix to the energy- and mass-related minors cannot guarantee the update of the overall system when individually assimilating energy- or mass-related variables. Furthermore, observational information on at least two mass-related quantities is required to limit the effect of the nonlinear correlations among the prognostic variables on the filter updating.

In agreement with Durand and Margulis (2006), who demonstrated the benefit of jointly assimilating energy- and mass-related observations, the most effective DA configurations call for the joint *TWA*-, *WAH*-, *TWH*-assimilations, which generally ensure the largest consistent update of the system state.

CHAPTER 7

Multivariate Particle Filter scheme

A multivariate SIR-PF scheme has been developed and implemented within the snow dynamics model. The choice of this algorithm aims to avoid the sample degeneracy via resampling (Sect. 5.3.2, *Sequential Importance Resampling*). When performing a multivariate DA scheme, it is necessary to consider the different uncertainties affecting the observed variables in order to properly define the likelihood function. The likelihood function implemented within the multivariate SIR-PF scheme is a N_{obs}-dimensional normal distribution, where N_{obs} is the number of the effectively assimilated variables, changing according to the available observational dataset. The likelihood function is therefore defined as

$$p(Y_t|X_t) = N\{(Y_t - X_t^i), \mu, R\} \qquad [7.1]$$

where μ and R are respectively the null mean vector and the error covariance matrix of observations (Sect. 5.4.1) characterizing the multivariate Gaussian distribution N.

Thus, at each assimilation time step the particles importance weights are updated according to the following equation:

$$W_t^i = \frac{exp\left(-\frac{1}{2R}\left[Y_t - H\left(X_t^i\right)\right]^2\right)}{\sum_{i=1}^{N} exp\left(-\frac{1}{2R}\left[Y_t - H\left(X_t^i\right)\right]^2\right)} \qquad [7.2]$$

In view of assimilating snow observations through the SIR-PF method, an ensemble of possible realizations of the snowpack state is needed. As extensively explained in Section 6.1, the model ensemble can be generated by considering several sources of uncertainty affecting the simulations. In the multivariate EnKF-based application, the conservative approach of directly perturbing the state variables was adopted to accommodate the constraining assumptions by preventing both a too low analysis-error covariance matrix and the introduction of possible further sampling errors. Since the PF technique has the main advantage of relaxing most of the EnKF-related restrictive assumptions, the implementation of this DA scheme does not necessarily require a specific methodology to generate an ensemble of possible model realizations.

Among the several uncertainties affecting the simulations of a physical model, the meteorological forcings are generally one of the major sources of uncertainty of snow-related predictions (Raleigh et al., 2015). Therefore, an ensemble of model simulations is here generated by perturbing the model inputs, namely precipitation, air temperature and relative humidity, solar radiation, wind speed. The ensemble of perturbed inputs allows to take into account a well-representative range of weather conditions at the experimental sites, which results in an ensemble of possible snowpack states standing for the uncertainty of model predictions (Charrois et al., 2016).

7.1 Multivariate SIR-PF simulations with perturbed meteorological data

7.1.1 Generation of the perturbed meteorological input data

A meteorological ensemble of 100 members has been generated by perturbing the in-situ meteorological data with an additive stochastic noise applied at each time step. Following the methodology proposed by Magnusson et al. (2017), the random perturbations are provided through a first-order autoregressive model in order to guarantee a physical consistency and a temporal correlation of the time-variant forcings. The time evolution of the error q_t for time t in the forcing data can be represented as:

$$q_t = \gamma q_{t-1} + \sqrt{1-\gamma^2}\omega_t \qquad [7.3]$$

where ω_t is the white noise with mean equal to 0 and variance equal to 1, and γ defines the time decorrelation. The initial error (q_0) is drawn from a standard normal distribution. The parameter γ is a function of a time decorrelation length (τ), according to the following formula:

$$\gamma = 1 - \frac{\Delta t}{\tau} \qquad [7.4]$$

where Δt is the model time step, namely 15 minutes.

Then, the time series of correlated noise are shifted and scaled to obtain the desired mean and variance. The normally distributed error q_t is transformed to lognormally distributed noise l_t using the following relationship:

$$l_t = \exp(\mu + \sigma q_t) \qquad [7.5]$$

where μ is the mean and σ is the standard deviation of the associated normal distribution.

Perturbations of meteorological data are generated considering the error statistics evaluated at the CDP site (Table 7.1) (Magnusson et al., 2017), which result from the comparison between SAFRAN reanalysis data (Vidal et al., 2010) and the observations supplied by the French station (Charrois et al., 2016).

Variable		Unit	Distribution	μ	σ	τ [hr]	Lower limit	Upper limit
Air temperature	Ta	[°C]	Normal	0	0.9	4.8	-	-
Relative humidity	RH	[%]	Normal	0	8.9	8.4	0	100
Solar radiation	SW	[W/m²]	Normal	0	min(SW,109.1)	3.0	0	-
Precipitation	P	[mm]	Lognormal	-0.19	0.61	2.0	0	-
Wind speed	V	[m/s]	Lognormal	-0.14	0.53	8.2	0.5	25

Table 7.1: *Error statistics for the generation of the meteorological ensembles (Magnusson et al., 2017).*

This approach has been tested at each measurement station in order to verify that the introduction of the stochastic noise does not affect the observed inputs on average at any experimental site by avoiding possible distortions (Figures 7.2a, b, c). Indeed, the ensemble average of each meteorological variable is supposed to maintain the observed value.

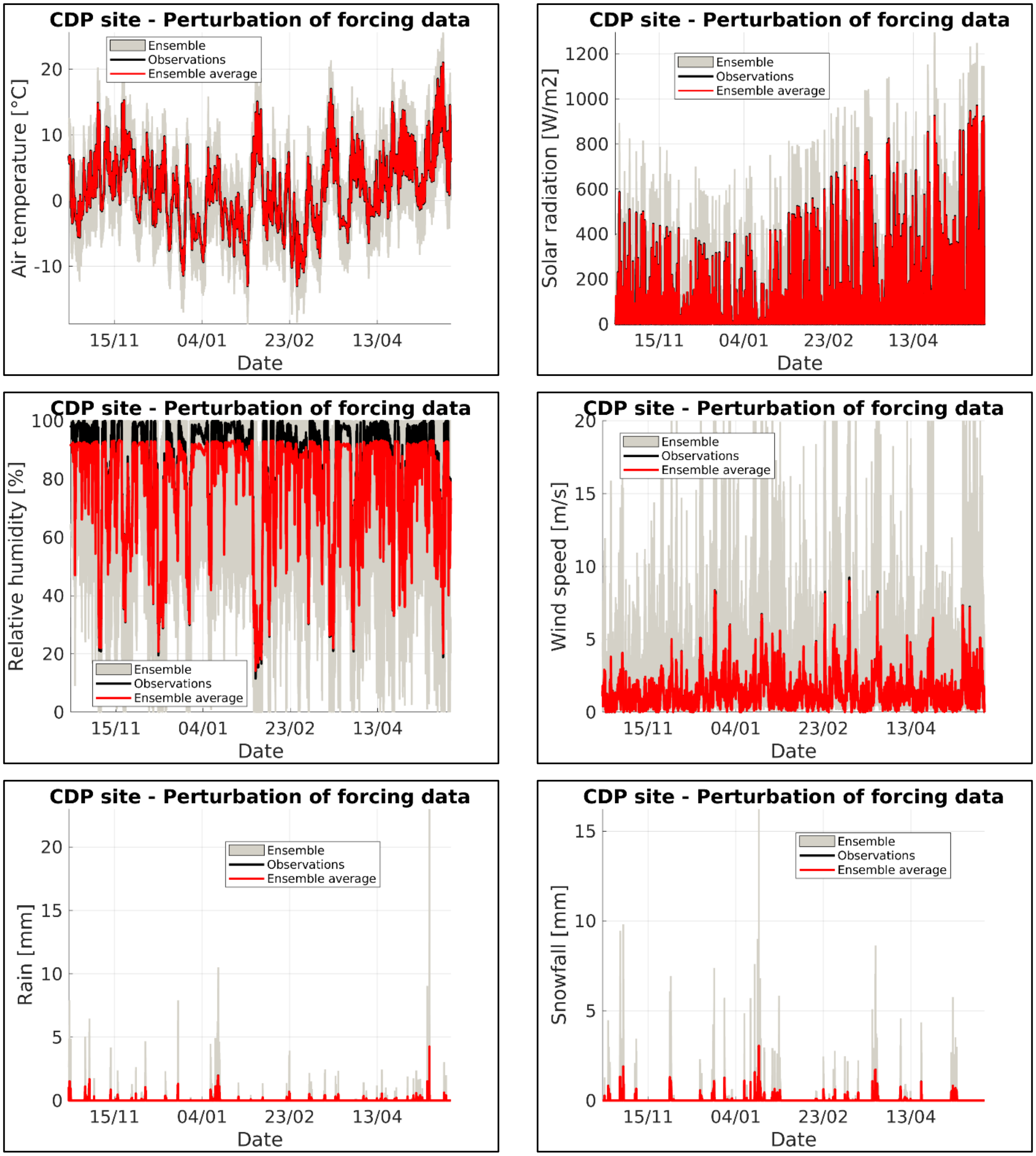

Figure 7.1a: *Ensembles of meteorological forcings – CDP site – Winter season 2003-2004. The panel shows the 100 members-ensembles of the meteorological variables: air temperature; solar radiation; air relative humidity; wind speed; rain; snowfall.*

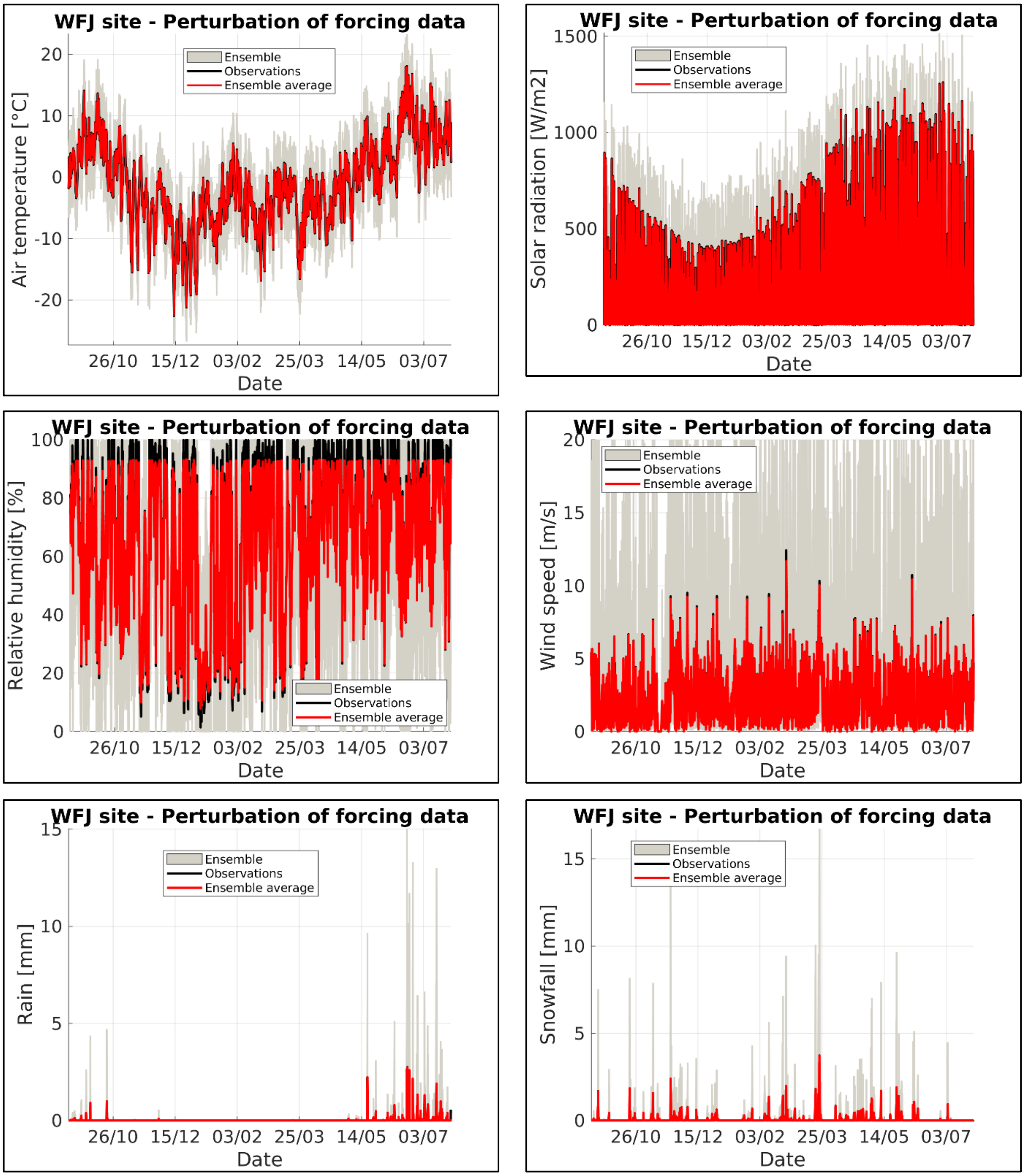

Figure 7.1b: *Ensembles of meteorological forcings – WFJ site – Winter season 2001-2002. The panel shows the 100 members-ensembles of the meteorological variables: air temperature; solar radiation; air relative humidity; wind speed; rain; snowfall.*

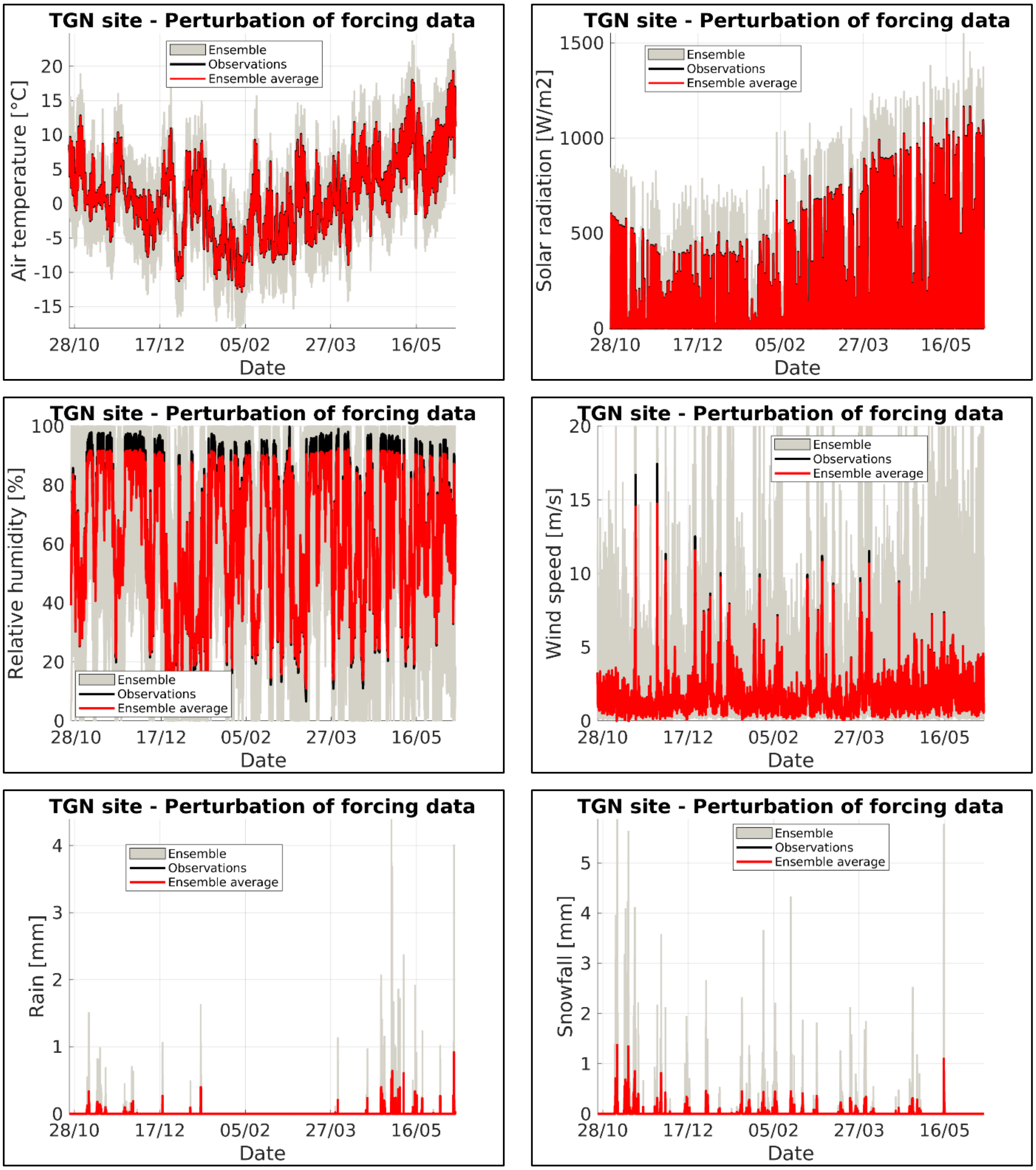

Figure 7.1c: *Ensembles of meteorological forcings – TGN site – Winter season 2014-2015. The panel shows the 100 members-ensembles of the meteorological variables: air temperature; solar radiation; air relative humidity; wind speed; rain; snowfall.*

The meteorological data are generally not substantially affected, on average, by the perturbations applied at each model time step (every 15 min). However, the limitation of the perturbed values within proper physical ranges makes the ensemble average slightly differ from the observed values, especially in terms of air relative humidity and wind speed.

Nevertheless, the main limitation of this procedure is the lack of correlations among the perturbed forcing variables, which does not ensure their physical consistency (Charrois et al., 2016). It is also noteworthy that the same error statistics specifically derived from the observations supplied by the CDP station have been used for the generation of the meteorological ensembles at all the pilot sites. As highlighted by Magnusson et al. (2017), this approach is likely to reduce the filter performances at the Italian and Swiss stations.

7.1.2 Impact of the meteorological uncertainty on ensemble simulations without DA

When considering the uncertainty of the forcing data, each ensemble model realization is forced by different meteorological conditions generating distinct snowpack states. Therefore, after verifying that the introduction of the stochastic noise does not affect the observed inputs on average, the aim is to assess the impact of the meteorological uncertainty on the ensemble snowpack simulations.

Indeed, since the strong system nonlinearities make the model response to the inputs perturbation hardly predictable and possible inconsistencies among the meteorological variables can generate unlikely system states, it is important to verify that no spurious trends occur with respect to the deterministic control run (OL simulations).

To investigate the impact of the meteorological stochastic perturbations, 100-members ensemble of snowpack simulations forced by as many different meteorological conditions have been analysed, without considering the assimilation of snow data. For the sake of concision and clarity, a representative winter season is shown for each site (Figures 7.3a, b, c).

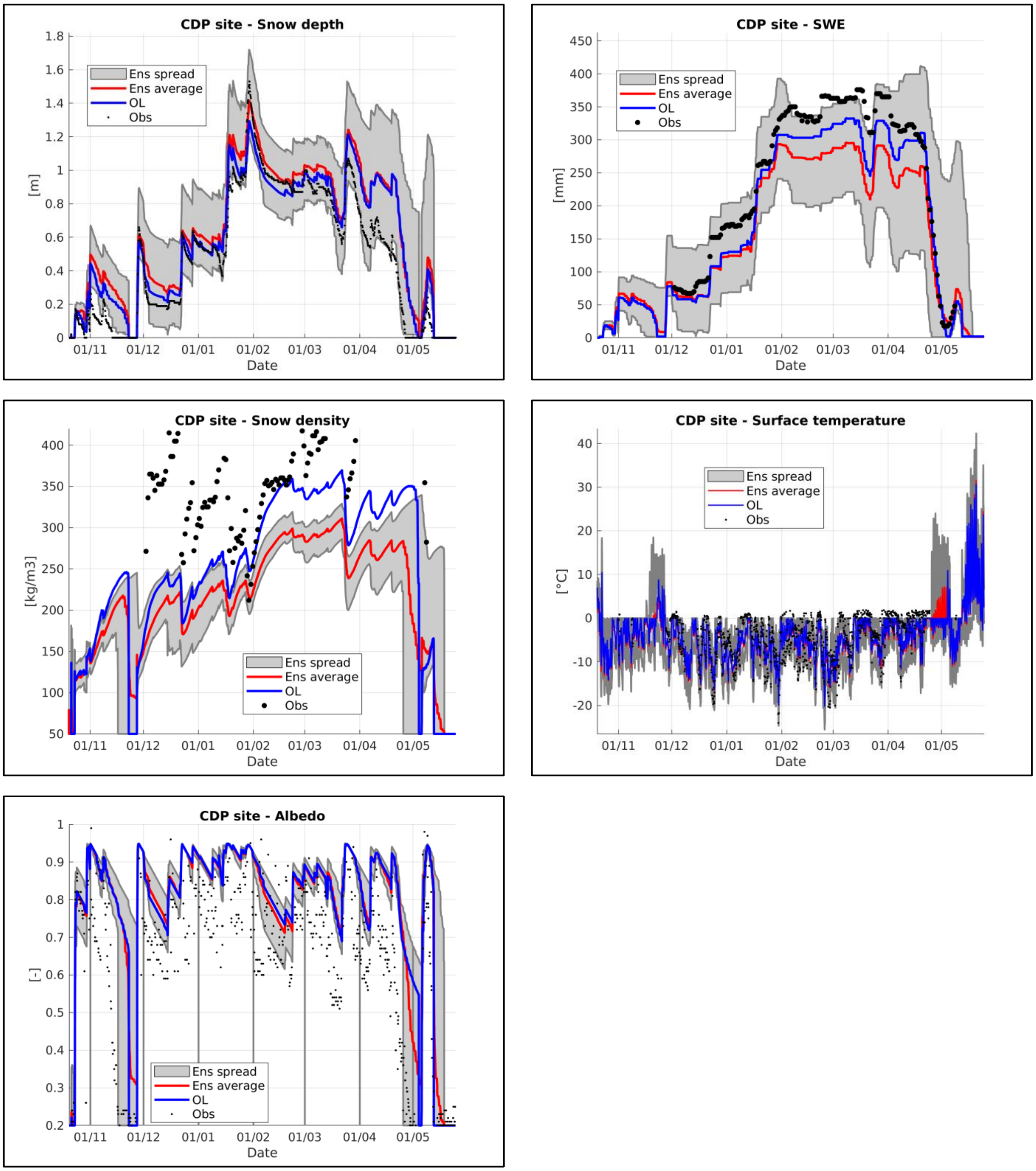

Figure 7.2a: *Impact of the meteorological uncertainty - Ensemble simulations of snow depth, SWE, snow density, surface temperature, and albedo – CDP site, winter season 2003-2004.*

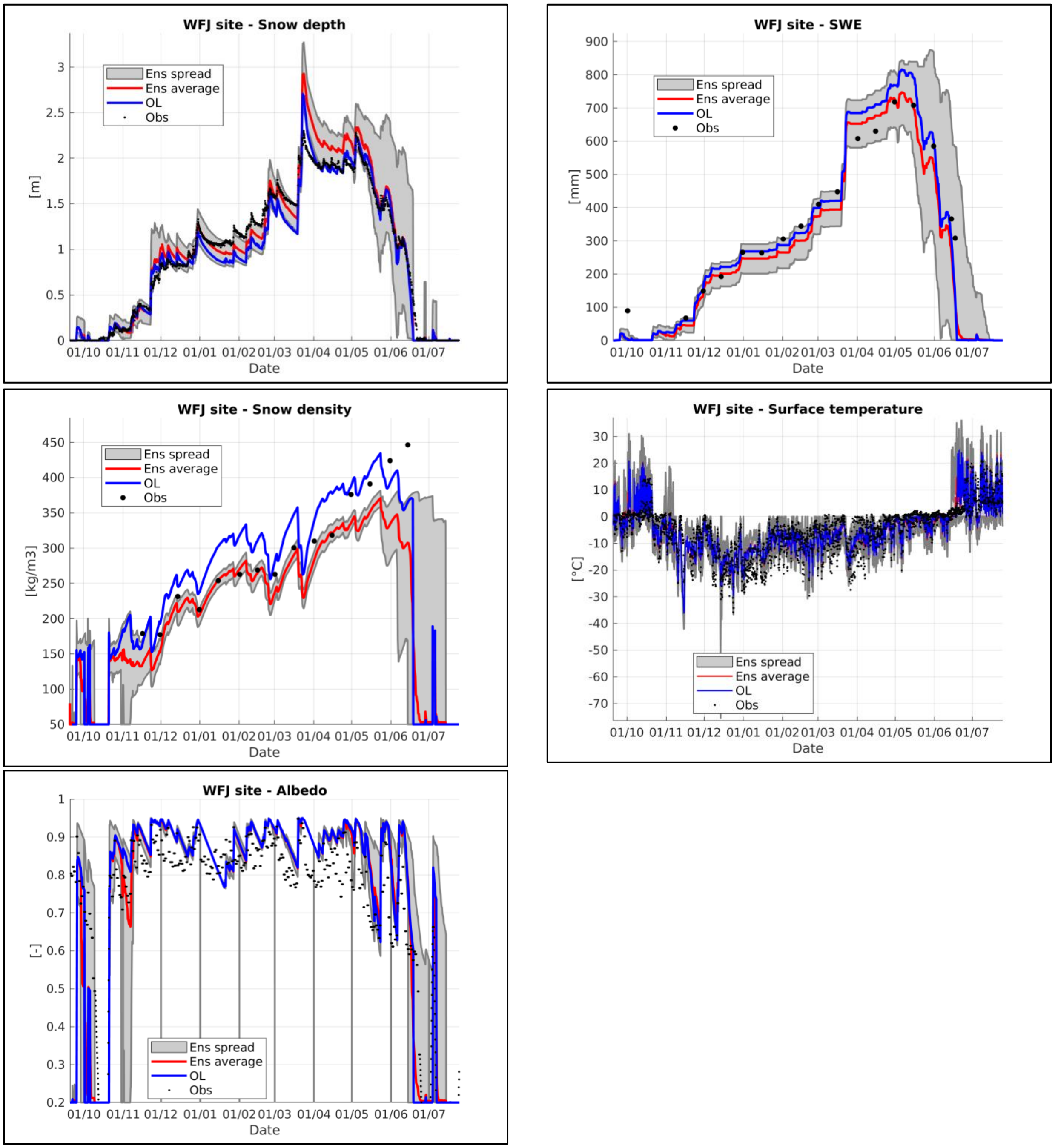

Figure 7.2b: *Impact of the meteorological uncertainty - Ensemble simulations of snow depth, SWE, snow density, surface temperature, and albedo – WFJ site, winter season 2001-2002.*

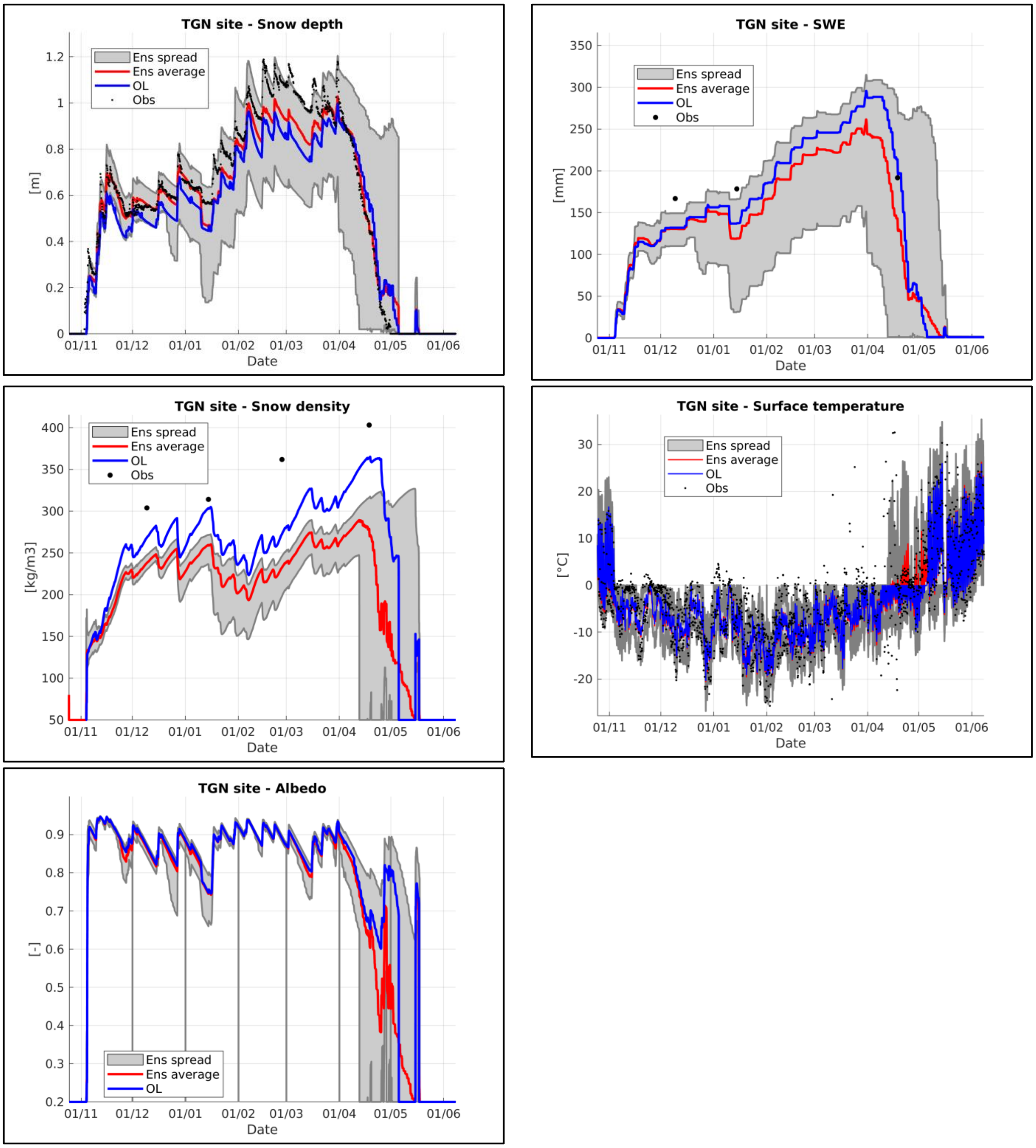

Figure 7.2c: *Impact of the meteorological uncertainty - Ensemble simulations of snow depth, SWE, snow density, surface temperature, and albedo – TGN site, winter season 2014-2015.*

The ensembles spread reveals possible over- and underestimation of the model simulations as direct consequence of the meteorological uncertainty. Nevertheless, the time series of the deterministic control run are generally included within the ensemble envelop, except for snow density, whose underestimation is increased.

With respect to the other state variables, snow density and albedo are generally less affected by the input perturbation, since their evolution indirectly depends on meteorological inputs through their physical parameterization laws. Thus, the resulting ensembles of these two state variables are often poorly spread.

The variance of the mass-related ensembles is generally the largest at the end of the winter season, when the perturbation of energy-related forcing variables (i.e. air temperature, shortwave radiation) leads to well spread melt-out scenarios resulting from the difference in melt timing (i.e. some particles have just started to melt and some others have already disappeared). During the winter season, the spread of SWE ensembles is increased whenever a snowfall event occurs due to the uncertainty in the precipitation rates allowing to provide the mass balance of each model realization with a different input of snowfall rate. Of course, sites climatology (e.g. frequency of snowfall events) strongly impacts the resulting ensemble variance.

A significant variance of the surface temperature ensembles is ensured by its high sensitivity to the inputs uncertainty, namely the perturbation of the air temperature and shortwave radiation, which directly impacts the snowpack energy balance.

However, it is important to consider that some threshold processes involved within the snow dynamics model (e.g. disappearance of the surface snow layer, limitation of state variables within physical ranges) can be counter-productive in enlarging the ensembles spread.

7.1.3 Multivariate SIR-PF simulations with perturbed input data

After generating the meteorological ensembles to obtain consistent ensemble simulations, the SIR-PF scheme has been implemented to jointly assimilate several observed snow data within the snowpack model. The aim is to assess the performances of the multivariate DA system and investigate its efficiency in updating the model state variables whenever observations are available. According to the experimental setup (Sect. 5.4), the SIR-PF scheme is designed to assimilate measures of snow surface temperature and albedo, snow depth and density, SWE every 3 hours.

The resulting statistical scores (Sect. 4.4.2; Sect. 5.4.2) (Figures 7.4a, b, c) reveal the filter effectiveness in updating snow depth simulations, whose correlation and *RMSE* values are significantly improved with respect to the control run, especially at the French and Swiss stations.

The update of model predictions of SWE and snow density is more challenging. Indeed, in most cases the assimilation of snow data actually leads to a worsening of the quality of the model simulations with respect to the deterministic control run, except for some sporadic winter seasons. Conversely, a significant improvement of SWE predictions is observed at the Swiss station, where the filter updating benefits from a larger spread of the SWE simulations ensured by a higher frequency of snowfall events, on average.

Even though the filter well succeeds in enhancing the simulations of surface temperature and albedo at CDP and WFJ sites, the snowpack thermal state at TGN is generally adversely affected by the assimilation of snow data.

The filter better succeeds in updating snow depth simulations since its effect lasts longer thanks to the slower physical dynamics of this variable, with respect to the surface temperature. Indeed, despite of the snow thermal inertia, the daily cycle of the surface temperature can weaken the updating effect within two following assimilation time steps. As snow depth, the albedo dynamics are mainly affected by snowfall events which swiftly update its state. However, since the albedo is less affected by the perturbation of the meteorological inputs, the resulting poorer ensemble spread makes its update less straightforward.

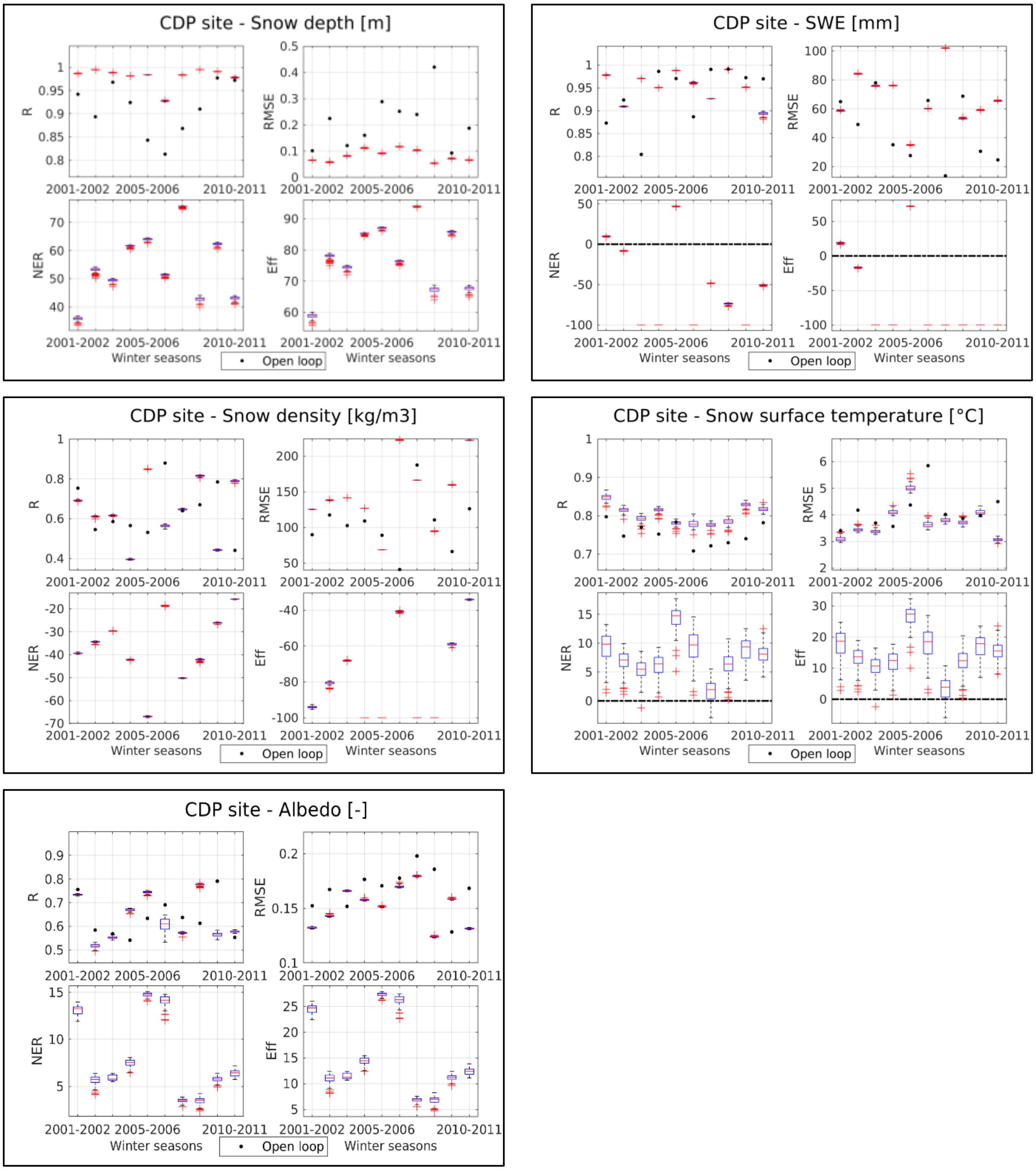

Figure 7.3a: *Multivariate DA scheme with perturbed meteorological data – Statistical scores of snow depth, SWE, snow density, surface temperature, and albedo simulations – CDP site (full dataset). The bottom and top edges of each box indicate the 25th and 75th percentiles of the scores distribution of the ensemble members, respectively.*

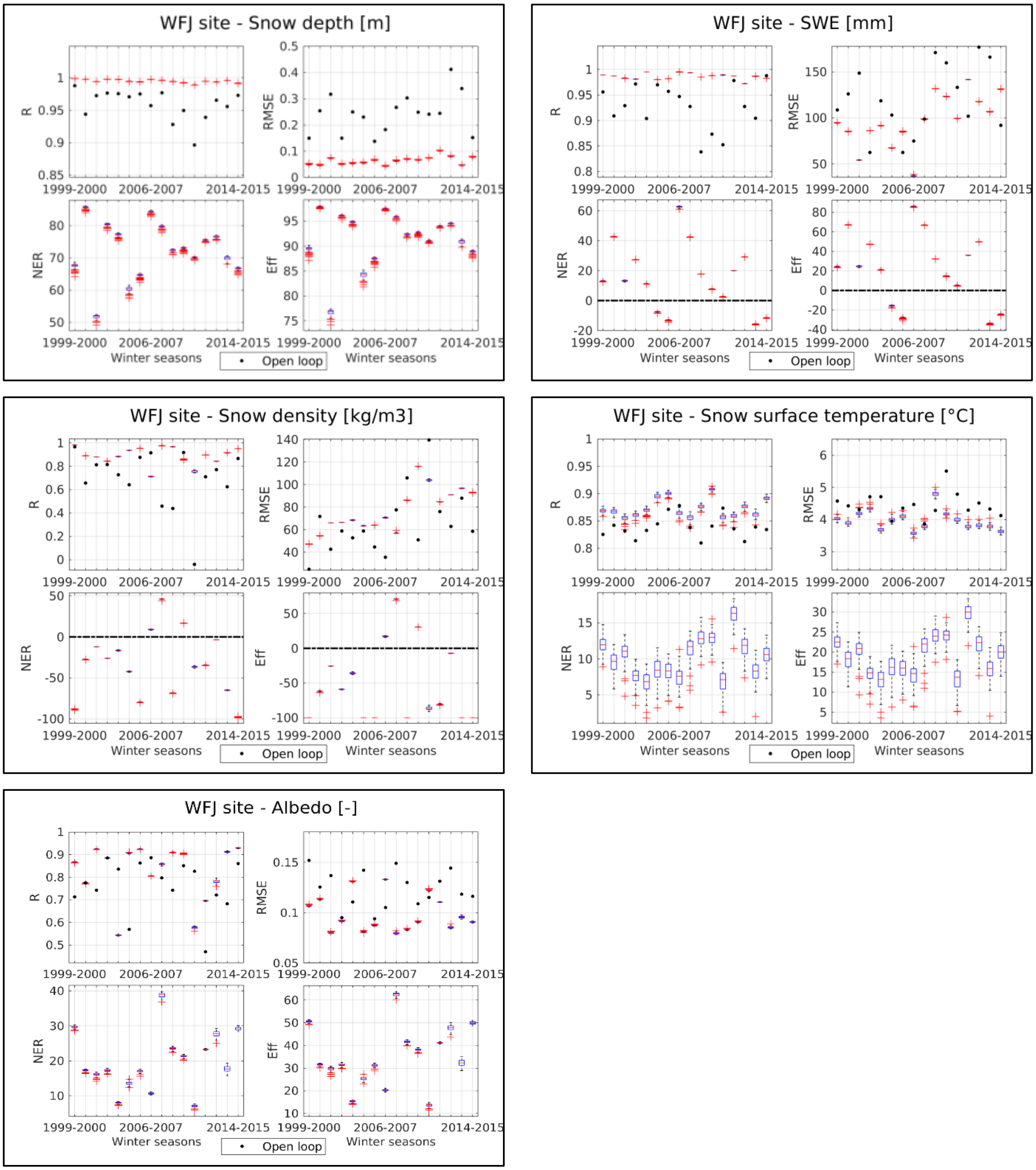

Figure 7.3b: *Multivariate DA scheme with perturbed meteorological data – Statistical scores of snow depth, SWE, snow density, surface temperature, and albedo simulations – WFJ site (full dataset).*

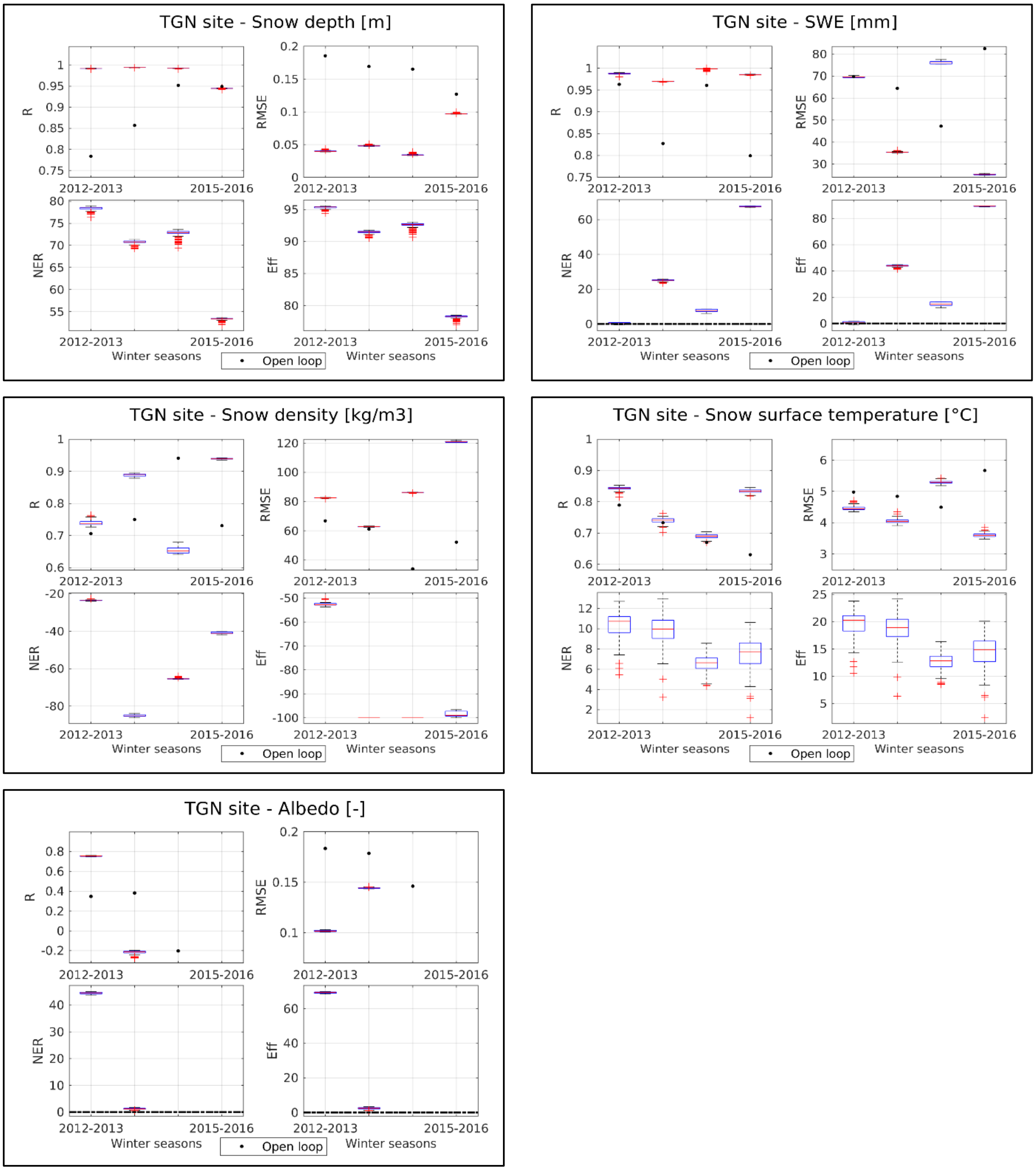

Figure 7.3c: *Multivariate DA scheme with perturbed meteorological data – Statistical scores of snow depth, SWE, snow density, surface temperature, and albedo simulations – TGN site (full dataset).*

To better understand and properly assess the results, it is important to stress some key conditions exerting the most influence on the filter effectiveness.

One of the main ruling issues is the scale of the model ensemble spread. A well-spread ensemble makes the filter efficient in weighting the particles. When the ensemble is squeezed, the resampling procedure is more challenging since all the particles are close to each other with resulting similar likelihood values. In this undesired case, the filter might not succeed in well discriminating the more likely ensemble members since they all are assigned almost the same weight. On the other hand, if the particles are well spaced, their resampling is more straightforward since each particle is properly discriminated through a specific weight proportional to its likelihood.

Alongside this issue, it is of critical importance how the particles are placed on average with respect to the observations. The most conducive condition calls for well-spread ensembles enclosing their corresponding measures. In this situation, the filter is favoured in selecting the most likely particles and properly weighting them. However, the spread of the model ensemble turns out to be the overriding condition. Indeed, even if the model predictions are significantly biased, a large ensemble spread can allow to progressively stretch the simulations towards the observed system state through subsequent proper updates.

When dealing with a multivariate DA scheme, the fulfilling of these conditions is even more challenging. In such an application, the filter is designed to select the particles best describing the observed system state with respect to all the available observations at each assimilation time step. Therefore, with respect to a univariate DA scheme, here the filtering procedure is more heavily constrained, depending on how many observations are provided.

Even though the effects of the ensemble degeneracy can be reduced through the resampling procedure, the meteorological uncertainty turns out to be not sufficient to prevent the sample impoverishment within two following assimilation time steps (e.g. SWE ensemble when no snowfall event occurs).

It is noteworthy that a decrease in the ensemble spread of just one variable can affect the overall resampling procedure. As previously explained, this limitation is even intensified by the physics of the snowpack model, whose threshold processes can weaken the effect of inputs perturbation.

Another further issue is the difference in the measurements frequency of the variables to assimilate. At each assimilation time step the Gaussian likelihood function is n-dimensional depending on the number of the observed variables. Thus, the particles weighting is carried out considering their likelihood values in relation to the available measurements at that time. This dynamic entails that the resampling procedure can be more strongly conditioned by the observations having a higher measurement frequency (e.g. hourly or sub-hourly measurements of snow depth). Thus, possible misleading updates of the variables less frequently observed can occur, since they are updated without taking into account particles likelihood with respect to their own lacking observations (e.g. daily or bi-weekly measurements of SWE). For instance, when a measure of snow depth is provided, no observational information on SWE can be retrieved unless its indirect estimate if snow density data are available. Otherwise, the filter can fail in consistently updating the overall snow mass-related state, since a lot of possible combinations of SWE and snow density can well fit the observed snowpack depth. In terms of filter efficiency, this means that when only a snow depth observation is provided the filter looks for particles having the higher likelihood with respect to this snow quantity, regardless the SWE and snow density states. Nevertheless, it is not unlike that several particles have the same likelihood because the combination of even strongly biased values of SWE and snow density can well fit the observed snow depth through offsetting effects among these variables. This is the main reason explaining the higher filter performance in terms of snow depth with respect to the SWE simulations.

The multivariate SIR-PF simulations have allowed to point out two main limitations of this application. Firstly, the ensemble spread needs to be enlarged in order to improve the filter efficiency in well weighting and resampling the ensemble particles. Moreover, the effect of the difference in measurement frequency of the assimilated variables needs to be limited in order to consistently update the snow mass balance.

7.2 Multivariate SIR-PF with perturbed model parameters

Even though the resampling procedure prevents the sample degeneracy, the perturbation of the meteorological forcing data has resulted not to be sufficient to avoid the sample impoverishment. As highlighted in the study of Moradkhani et al. (2005b), a sample impoverishment can lead to many particles having high importance weights being selected many times, with a resulting loss of diversity among the ensemble particles after the resampling step. Gordon et al., (1993) explained that this side-effect becomes prominent when the dynamical system is noise-free or has a very small noise preventing the particles from stochastically moving in space.

With the aim of overcoming the sample impoverishment, the uncertainty of model parameters has been introduced to succeed in enlarging the ensembles spread, whose size strongly impacts the filter performances. Therefore, along with the perturbation of meteorological inputs, each particle independently evolves according to its own specific set of parameters ruling the model physical dynamics, whose parameterizations remain unchanged, however.

7.2.1 Sensitivity analysis of model parameters

When considering the uncertainty of model parameters, a preliminary sensitivity analysis is of critical importance for a twofold reason. Firstly, it is intended to identify the main ruling parameters to which the model simulations are sensitive at most. Secondly, an accurate selection accordingly enables to neglect those parameters whose perturbation would uselessly demand for a larger computational requirement.

According to the results of the sensitivity analysis previously carried out within the model calibration procedure (Sect. 4.3.1), snow roughness and snow viscosity have been considered as the model parameters having the largest impact on the simulations of snowpack dynamics.

Snow roughness strongly affects the snowpack energy balance by ruling the turbulent heat fluxes. As consequence, the perturbation of this parameter mainly impacts the SWE ensembles by proving each particle with different snow melting fluxes. The effects of the perturbation of snow viscosity are prominent on the snow density evolution, especially on the snow compaction dynamics.

However, it is noteworthy that the criterion for selecting the model parameters has been mainly focused on identifying those allowing to increase the ensembles spread of the state variables more slightly affected by the meteorological uncertainty, namely SWE, snow density and surface albedo. While the two mass-related variables are strongly affected by the perturbation of snow roughness and snow viscosity, the enlargement of the spread of the albedo ensembles has required to perturb also the three parameters involved in the parameterization of this energy-related quantity (Table 7.2).

	PARAMETER		NOMINAL VALUE	RANGE
1.	Snow roughness	[mm]	0.0226	$[0.001 - 0.05]$
2.	Snow viscosity	[kg/ms]	10^8	$[7 \cdot 10^7 - 10^{12}]$
3.	Albedo parameter τ_α	[s]	10^7	$[0.52 - 1.55 \cdot 10^7]$
4.	Albedo parameter τ_m	[s]	$3.6 \cdot 10^5$	$[1.73 - 5.2 \cdot 10^5]$
5.	Albedo parameter S_0	[mm]	10	$[2 - 15]$

Table 7.2: *Sensitivity analysis – Selection of model parameters involved within the perturbation procedure.*

7.2.2 Model parameters resampling and perturbations generation

Since the introduction of stochastic noise plays a major role in reducing the effect of the sample impoverishment, the uncertainty of model parameters is supposed to significantly contribute to restore the ensembles spread between two following assimilation time steps.

Following the methodology proposed by Moradkhani et al. (2005b), the resampling procedure has been introduced both in the parameters and the state variables spaces. According to this approach, at each assimilation time step, after the particles resampling the parameters are perturbed before being used at the successive time step:

$$\theta_{t+1}^{i} = \theta_{t,resamp}^{i} + \varepsilon_t^i \qquad [7.6]$$

where θ is the parameters vector and ε is a random noise, normally distributed with zero mean and variance φVar_t^θ. Var_t^θ is the variance of parameter particles at time *t* before resampling, and φ is a tuning parameter standing for the radius around each particle being explored.

In order to avoid model instabilities due to large changes in the perturbed parameter samples and to also assure a minimum process noise by preventing the parameters variance to collapse to very small values, Var_t^θ has been restricted between upper and lower limits (Salamon and Feyen, 2009). These variance limits have been set according to the results of various tests carried out by varying them and evaluating the impact on filter performances. Unlike the study of Moradkhani et al. (2005b), who applied the dual SIR-PF scheme to estimate model parameters, in this case the main aim was to succeed in enlarging the parameters ensemble to ensure a significant particles spread. Therefore, tuning parameters have been specifically set to guarantee a significant variance of the parameters distribution. Thanks to this approach, the degeneracy of the model ensembles is avoided via resampling and the sample impoverishment is prevented through the parameters perturbation (Figure 7.4). While the uncertainty of the albedo parameters mainly results in an enlargement of the ensemble of this prognostic variable, the perturbation of snow roughness and snow viscosity strongly impacts the snowpack dynamics. Several analyses have revealed a high sensitivity of model simulations to the resampling of these mass-related parameters, especially in terms of SWE and snow density.

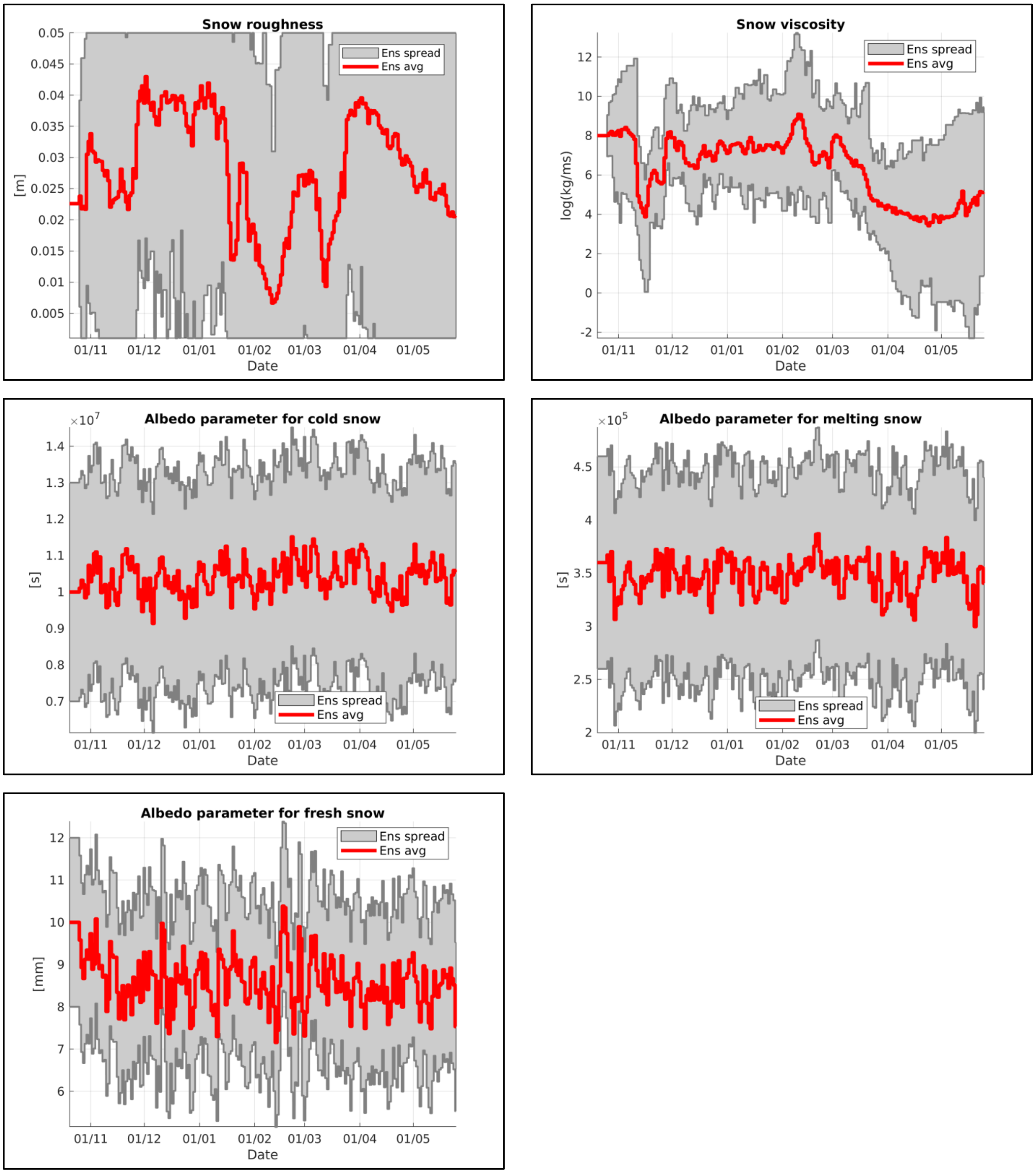

Figure 7.4: *Uncertainty of model parameters – CDP site – Winter season 2010-2011. The panel shows the ensembles seasonality of the model parameters: snow roughness, snow viscosity, the albedo parameters for cold, melting and fresh snow.*

7.2.3 Multivariate DA simulations with parameters resampling

As stated by Salamon and Feyen (2009), when dealing with parameters uncertainty it is important to consider that the model response to a change in parameters has not immediate effect on the simulated state. This issue can be overcome by giving the model a sufficiently large response time between following system updates. The assimilation frequency has been therefore reduced to every 24 hours. This choice was intended to guarantee a higher model response time to parameters change without omitting a large number of observed snow data.

Figures 7.6a, b, c show the statistical metrics of the multivariate DA simulations resulting from the implementation of the model parameters resampling. With respect to the previous analysis considering the meteorological data as the only source of uncertainty (Sect. 7.1.3), the introduction of the parameters resampling has allowed to heavily increase the filter efficiency in updating the model simulations of SWE, snow density and albedo at CDP site. It is noteworthy that the parameters resampling does not only ensure a sizeable enlargement of the ensembles spread but it also allows to better estimate the model parameters on average. Indeed, while the resampling of the state variables allows to consistently update the system state at the assimilation time step, the modelling of snowpack dynamics between two following assimilation time steps benefits from the parameters resampling, which enables to better take into account the parameters seasonality (e.g. melting period). At the French site, the daily SWE measurement frequency ensures an effective resampling of the mass-related parameters, namely snow roughness and snow viscosity. Furthermore, the joint improvement of the model simulations of snow density dynamics results in an even more satisfying filter performance in updating snow depth predictions. Conversely, the introduction of the parameters resampling does not always result in a significant improvement of SWE simulations at the Swiss station, with a further prominent worsening of the model snow density dynamics. This limitation is mainly due to the lower biweekly frequency of the SWE measurements, with respect to the French case study. At WFJ site, at the daily assimilation time steps when no SWE observation is available and no indirect estimate of snow density can be derived, the estimate of the particles likelihood cannot rely on observational information on the snow mass-related (e.g. SWE, snow density). Therefore, it is not unlikely that the resampling procedure leads to suboptimal values of the mass-related parameters. Moreover, the enlargement of the ensembles spread ensured by the parameters resampling entails a higher probability of selecting particles having SWE and snow density values even farther from the actual state with respect to the deterministic simulations of the control run, when no direct SWE observed data are provided. This thesis is supported by the results obtained at the TGN site, where the multivariate DA scheme allows to consistently update the SWE simulations when daily-averaged SWE measurements are available, namely throughout the winters 2013-14 and 2015-16. In this latter wintertime, the filter also reveals a higher efficiency in terms of snow density, with respect to the previous case. During the other two snow seasons, when biweekly SWE observations are assimilated, the filter does not succeed in improving model mass-related predictions.

The filter updating is not as effective for the simulations of surface temperature, especially at the Swiss and French sites. This suboptimal performance is mainly due to the concurrence of several factors. Firstly, the quicker dynamics of the daily thermal cycle make the temperature simulations more sensitive to the reduction in assimilation frequency, with respect to the other variables. Secondly, even though the filter succeeds in daily updating the system thermal state, the parameters values resulting from the resampling procedure do not ensure a long-lasting effect on the temperature trend between two following assimilation time steps. Indeed, since the parameters are resampled according to their representativeness at the assimilation time step, their values are not likely to be the optimal ones to well catch the sequence of diurnal and nocturnal peaks. The enlargement of the albedo ensembles, guaranteed by the parameters resampling, generally ensures a slightly higher filter performance in updating the simulations of this variable.

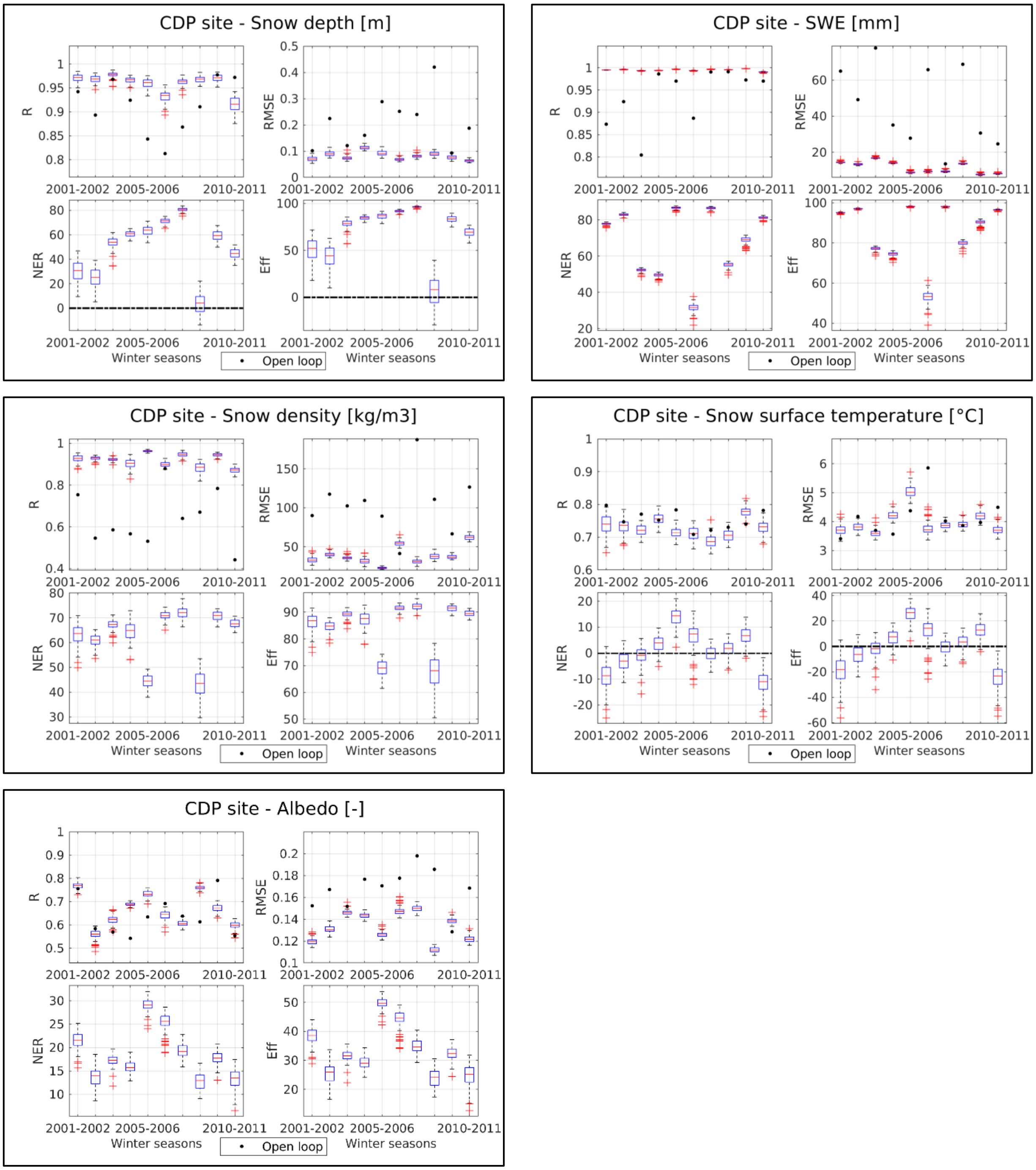

Figure 7.5a: *Multivariate DA scheme with perturbed meteorological data and model parameters resampling – Statistical scores of snow depth, SWE, snow density, surface temperature, and albedo simulations – CDP site (full dataset). The bottom and top edges of each box indicate the 25th and 75th percentiles of the scores distribution of the ensemble members, respectively.*

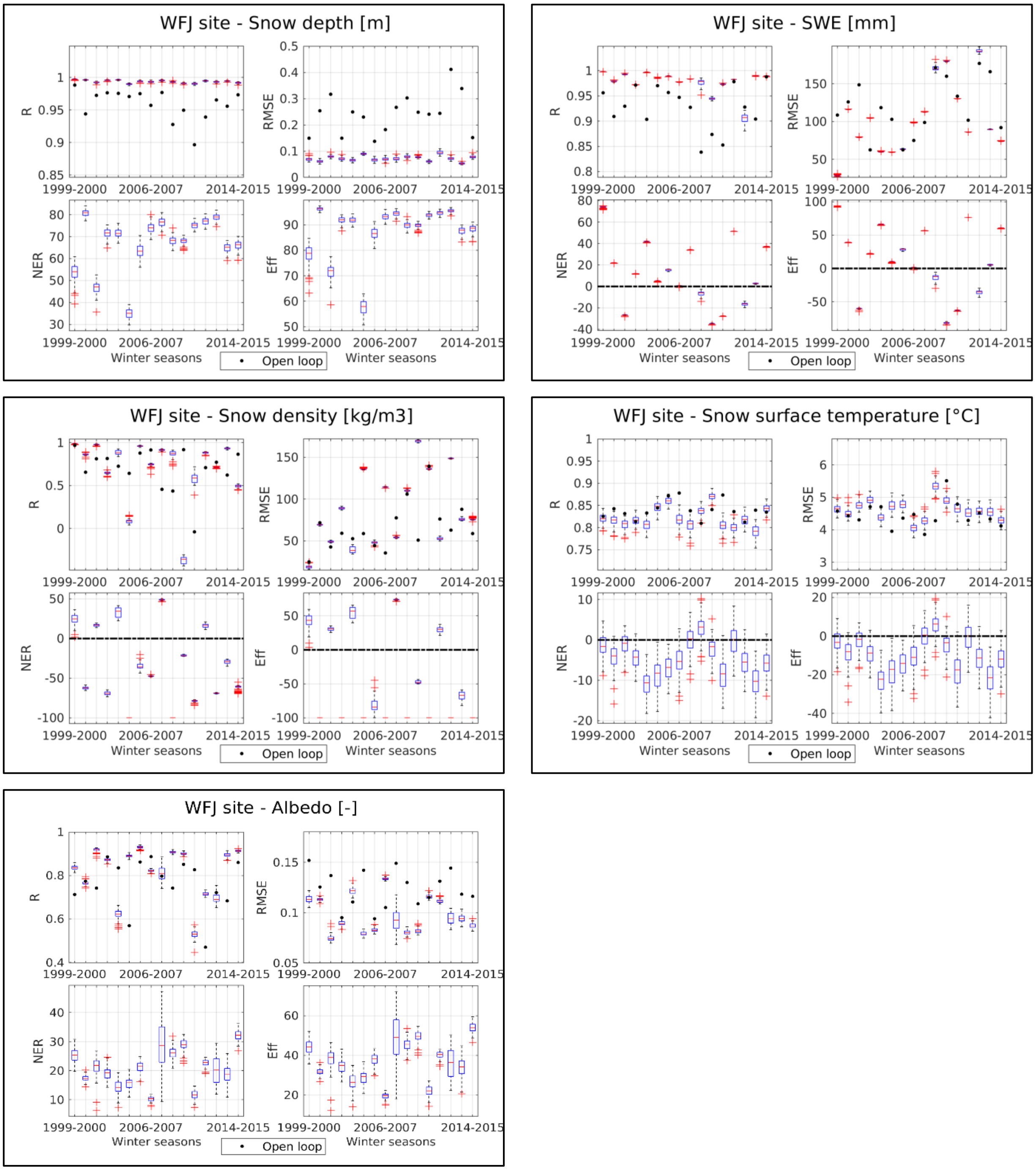

Figure 7.5b: *Multivariate DA scheme with perturbed meteorological data and model parameters resampling – Statistical scores of snow depth, SWE, snow density, surface temperature, and albedo simulations – WFJ site (full dataset).*

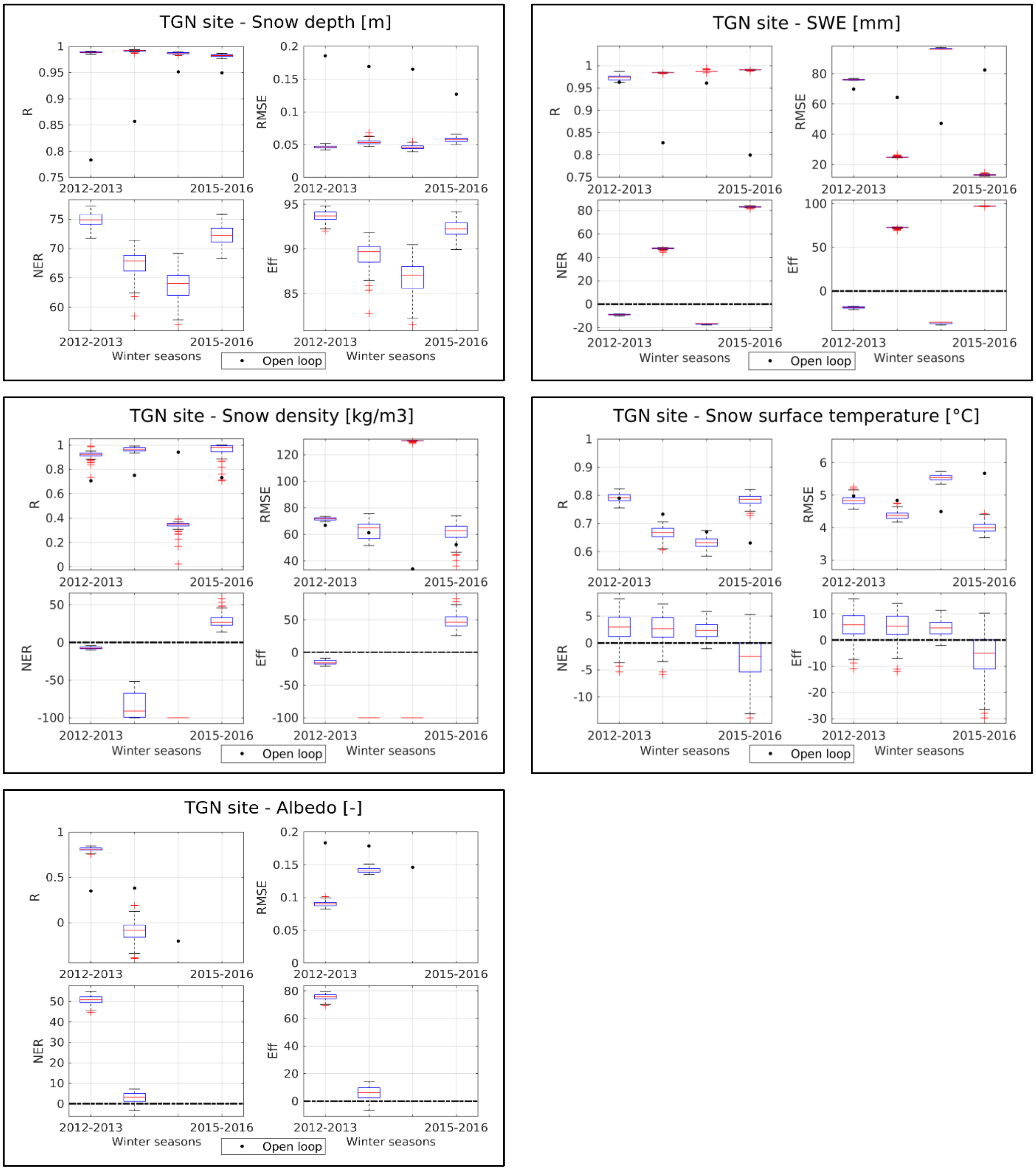

Figure 7.5c: *Multivariate DA scheme with perturbed meteorological data and model parameters resampling – Statistical scores of snow depth, SWE, snow density, surface temperature, and albedo simulations – TGN site (full dataset).*

Although the parameters resampling entails an enlargement of the ensembles spread, which is one of the constraining conditions to ensure the filter effectiveness, the quality of the multivariate DA simulations strongly depends on the reliability of the parameters resampling, which requires direct observational information to properly estimate the most likely parameters values.

7.2.4 Sensitivity of parameters resampling to the SWE measurement frequency

The Italian case study has provided evidence of the impact of the difference in SWE measurement frequency on the parameters resampling. In order to further investigate the system sensitivity, an experiment has been performed at the CDP station with the aim of assessing how the reduction from daily to biweekly SWE observed data affects the 24-hours multivariate DA simulations. Obviously, a reduction in measurement frequency is expected to limit the impact of the filter updating on the model simulations. However, when dealing with a multivariate DA scheme, the imbalance among the measurement frequency of the assimilated variables can lead to a further side-effect hindering the parameters estimate due to the largest impact of the more frequently observed variables (e.g. snow depth, surface temperature) within the particles weighting. Figure 7.6 shows the ensembles of snow viscosity and snow roughness resulting from the assimilation of daily and biweekly SWE observations throughout the winter season 2001-2002 at CDP site. A divergence between the two ensemble time series is clearly detectable on average, especially in terms of snow viscosity. The suboptimal estimate of the mass-related parameters based on biweekly SWE measurements leads to a worsening of model predictions with respect to the deterministic control run, as shown in Figure 7.7. Conversely, the filter effectiveness is not affected in terms of snow depth thanks to offsetting effects between SWE and snow density simulations.

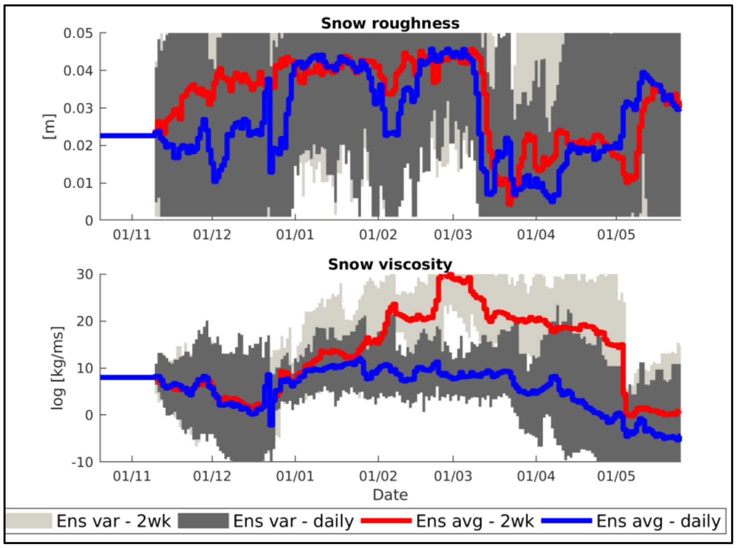

Figure 7.6: *Sensitivity analysis of the multivariate DA scheme to SWE measurement frequency at CDP site, winter season 2001/02 – Parameters ensembles: snow roughness (on top) and snow viscosity (second row) resulting from the assimilation of daily (average trend in blue) and biweekly (red) SWE observations.*

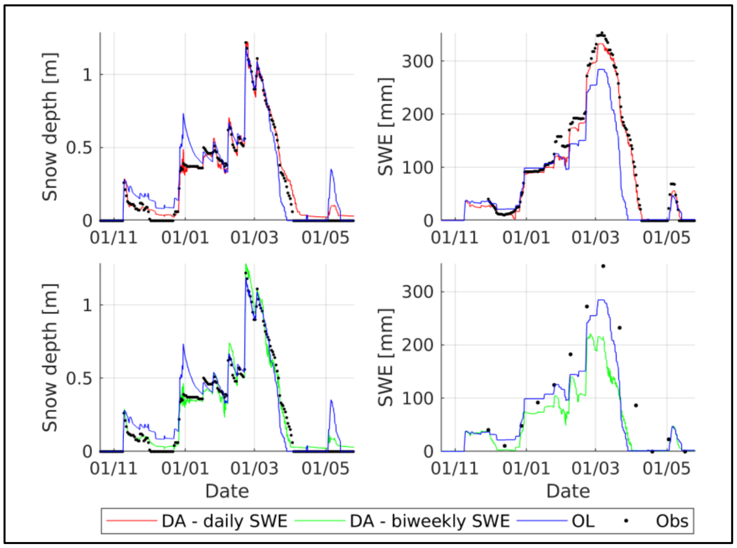

Figure 7.7: *Sensitivity analysis of the multivariate DA scheme to SWE measurement frequency at CDP site, winter season 2001/02 – Simulations of snow depth (left column) and SWE (right column) for daily (first row) and biweekly (second row) SWE measurements.*

7.3 Proxy information of snow mass-related variables

Even though the introduction of the parameters uncertainty has well succeeded in enlarging the ensembles spread, the resampling procedure of both states and parameters have turned out to be even counter-productive when it is not properly conditioned by observed data of ruling snow mass-related variables. Nevertheless, since SWE and snow density measurements are time-consuming and thus often not available for real-time applications, the aim was to reduce the system sensitivity affecting the filter performances by deriving indirect information on these snow variables.

7.3.1 Additional snow density model

Jonas et al. (2009) proposed an empirical snow density model to reliably determine indirect sampling of SWE states from snow depth measurements though a parameterization of snow density. They identified four main factors affecting the snow density: seasonality, observed snow depth, site altitude and location. These factors are used as input variables for the snow density model allowing to convert measured snow depth values into SWE ones. As is well known, at low snow depths snow density features a pronounced variability. Indeed, a shallow snow cover can range from low-density new snow in autumn to high-density slush in spring. Snow density gradually increases over the course of the winter season, and it corresponds to the increasing compaction of snow initially due to settling and later to snow cover ripening. Unlike mean snow depths, which are significantly site-dependent due to different precipitation and temperature patterns, mean snow densities only slightly differ between regions. Also the site altitude has a minor direct effect on snow density, on average. However, Jonas et al. (2009) found that the interaction between the factors altitude and season reveals an indirect effect on snow density (Mizukami and Perica, 2008). Indeed, in early winter the snow density increases with altitude, since at this time of the year only higher altitudes feature considerable snow depths. On the other hand, in late winter snow density decreases with altitude, because the melt-out progresses faster at lower altitudes.

Jonas et al. (2009) considered three altitude range classes (>2000 m, >1400 m and <2000 m, <1400 m) and 10 monthly classes within the winter season. For each class, they defined through a linear regression the two coefficients [b, a] best fitting the dataset of snow depths and snow densities measured biweekly over five decades at 37 sites throughout the Swiss Alp (Table 7.3).

MONTH	Altitudes > 2000 m [b,a]	Altitudes > 1400 m and < 2000 m [b,a]	Altitudes < 1400 m [b,a]
October	-	-	-
November	[206, 47]	[183, 35]	[149, 37]
December	[203, 52]	[190, 47]	[201, 26]
January	[206, 52]	[208, 47]	[235, 31]
February	[217, 46]	[218, 52]	[279, 9]
March	[272, 26]	[281, 52]	[333, 3]
April	[331, 9]	[354, 15]	[347, 25]
May	[378, 21]	[409, 29]	[413, 19]
June	[452, 8]	-	-
July	[470, 15]	-	-

Table 7.3: *Regression coefficients [b, a] – Jonas et al. (2009).*

An estimate of snow density (ρ_{estim}) can be evaluated as a function of the snow depth observation (SD_{obs}) according to the formula:

$$\rho_{estim} = a \cdot SD_{obs} + b \qquad [7.7]$$

where [b, a] are to be selected from the Table 7.3, according to the site altitude and the recording date. Since this is an application at single measurement sites, as first attempt the region-specific offsets are neglected. Thus, the resulting SWE estimation (SWE_{estim}) is retrieved as:

$$SWE_{estim} = SD_{obs} \cdot \rho_{estim} \qquad [7.8]$$

Both the Italian and the Swiss sites fall within the first altitude class (>2000 m).

With the aim of evaluating the reliability of the resulting estimates, a qualitative comparison analysis has been performed with respect to the observations available at the Swiss and Italian measurement sites, as shown in Figure 7.8. Once again, it is important to stress that, since no direct observations of snow density are generally available, this assessment actually compares two indirect estimates of the snow density.

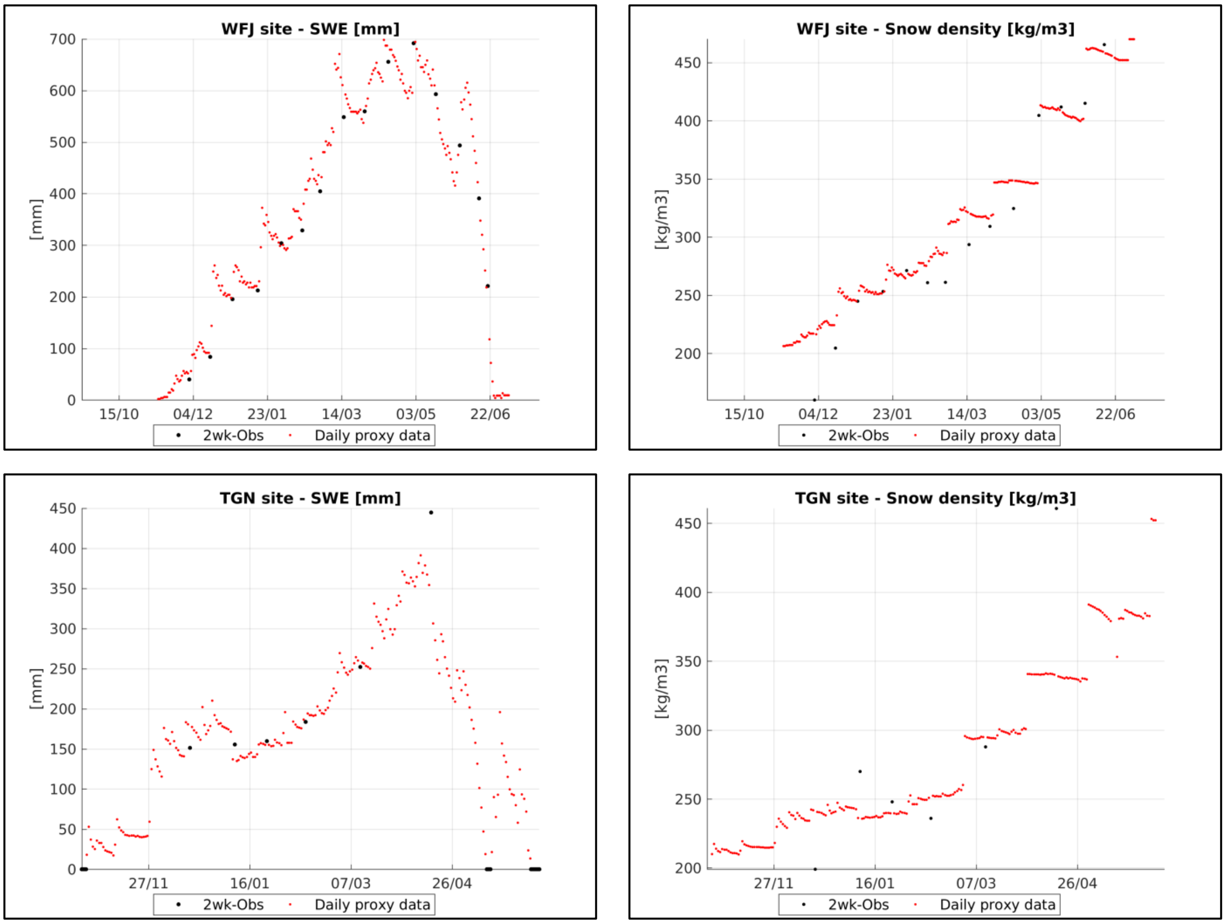

Figure 7.8: *Additional snow density model – Comparison between SWE (left column) and snow density (right column) measurements and the indirect proxy estimates - WFJ site, winter season 2005/06 (first row); TGN site, winter season 2012/13 (second row).*

Except for some sporadic winter seasons, generally the estimates of SWE and snow density well fit the observed snowpack dynamics, as demonstrated by a good agreement with the ground-based measurements.

7.3.2 Multivariate SIR-PF simulations with proxy information of snow mass-related variables

The additional snow density model has been implemented within the multivariate DA scheme in order to improve the updating of both SWE and snow density whenever no observational information on these two variables is available. This approach has enabled to evaluate particles importance weights at each assimilation time step with the support of additional estimates of these snow mass-related quantities. Therefore, the likelihood function is supposed to be more properly constrained, with a resulting lower impact of the assimilation of the more frequently observed variables within the updating procedure. The introduction of proxy information on the mass-related snow variables has allowed to significantly optimize the parameters resampling, as revealed by the outperforming statistical scores of SWE and snow density simulations, especially at WFJ site, thanks to the good correspondence between in-situ observations and indirect estimates (Figures 7.10a, b). Generally, this approach ensures a consistent improvement of the snow depth predictions, as evidence of a proper estimate of snow density, except for the winter season 1999-2000 at the WFJ site. Conversely, no prominent effects are observed in terms of surface temperature and albedo.

Of course, the impact of SWE and snow density estimates on the particles weighting procedure strongly depends on the bias affecting their values with respect to the ground-based observations. Whenever a significant bias occurs, the introduction of such estimates can be even counter-productive since their conditioning can lead to spurious updates of the system state. However, it is also noteworthy that if an estimate is significantly far from the average model ensemble, its impact on particles resampling turns out to be negligible.

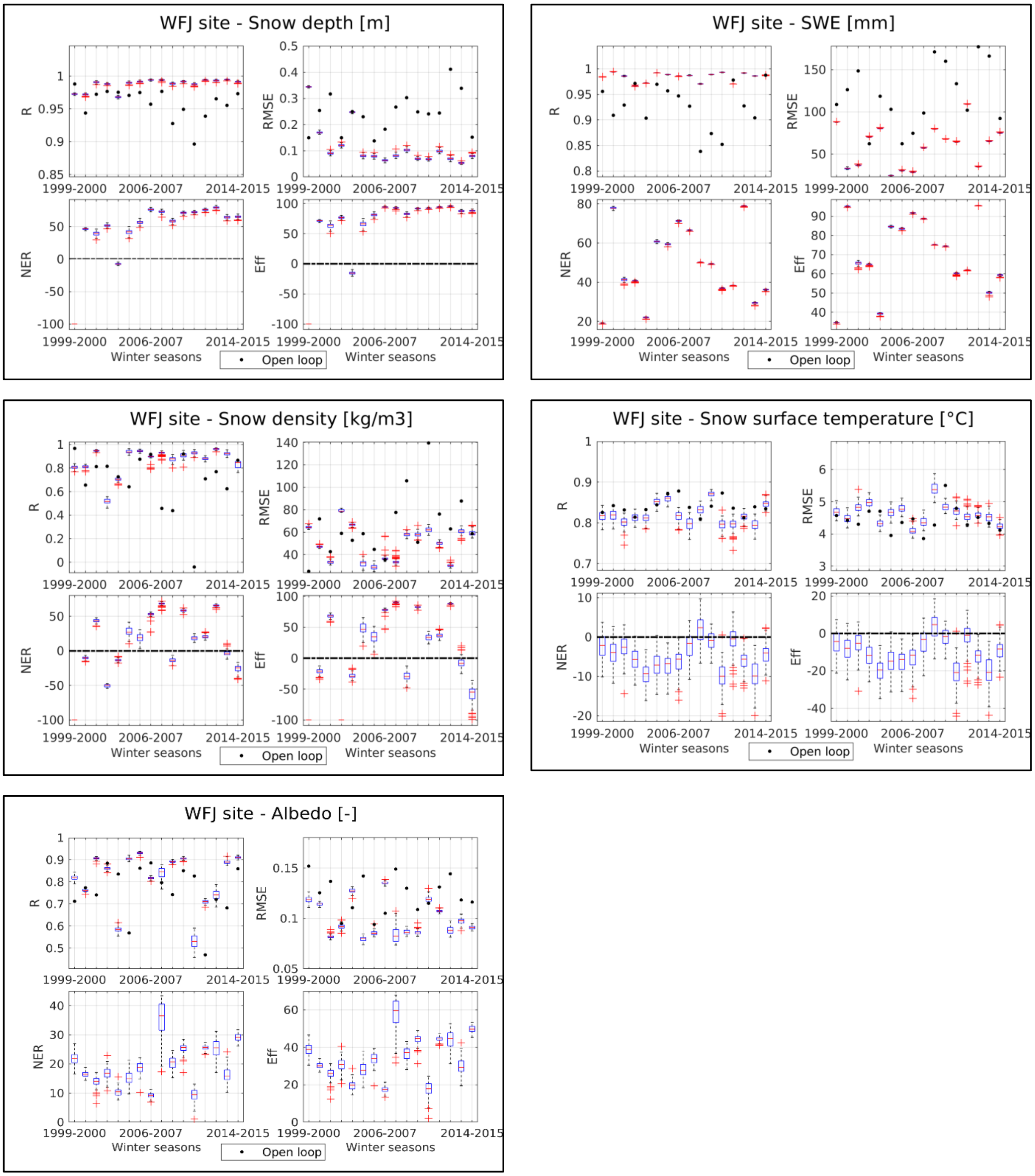

Figure 7.9a: *Multivariate DA scheme with auxiliary snow model - Statistical scores of snow depth, SWE, snow density, surface temperature, and albedo simulations – WFJ site (full dataset). The bottom and top edges of each box indicate the 25th and 75th percentiles of the scores distribution of the ensemble members, respectively.*

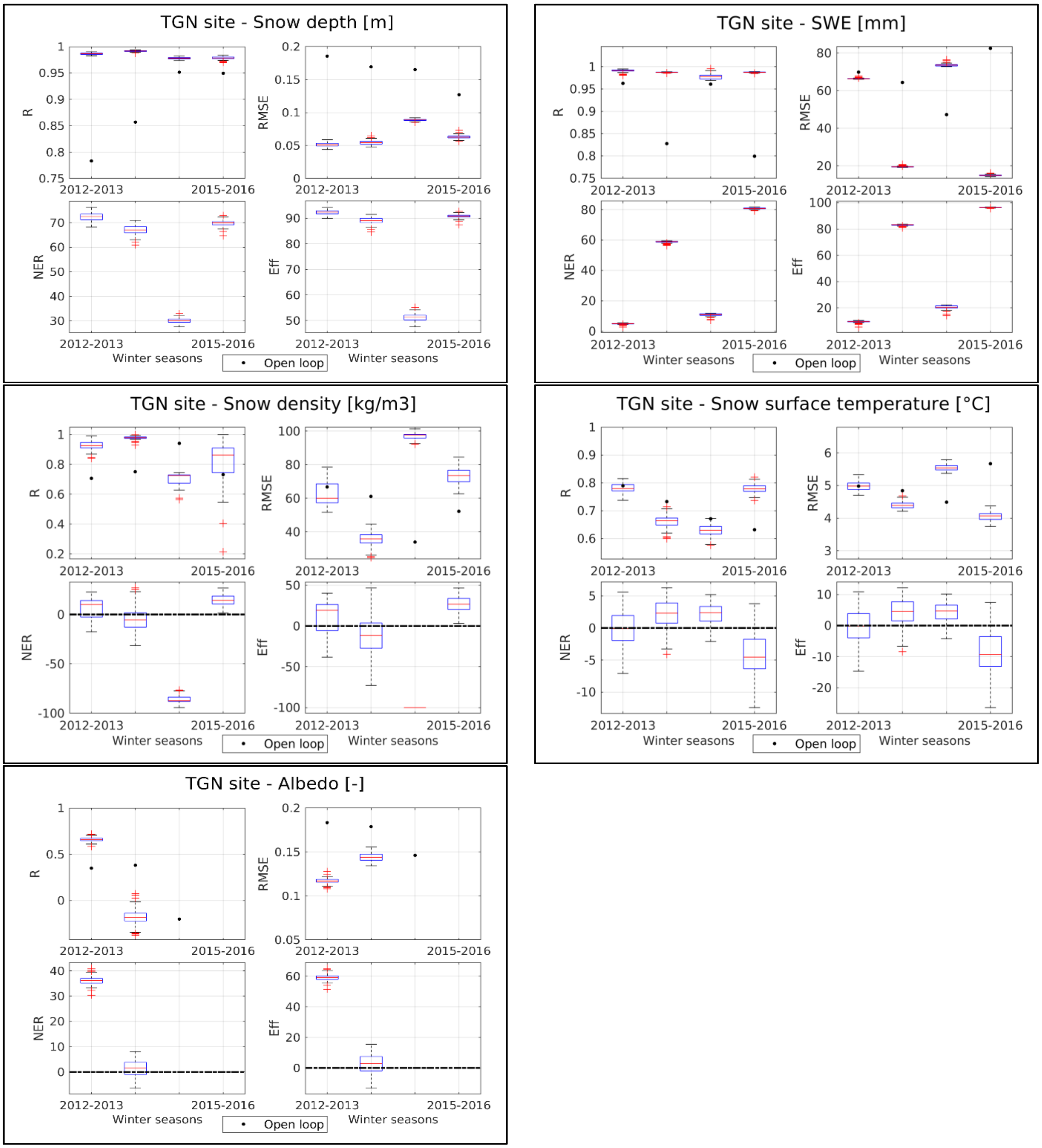

Figure 7.9b: *Multivariate DA scheme with auxiliary snow model - Statistical scores of snow depth, SWE, snow density, surface temperature, and albedo simulations – TGN site (full dataset).*

The reduction in assimilation frequency necessarily leads to omitting large quantities of observed data. With the aim of preventing this limitation, the approach proposed by Salamon and Feyen (2009) has been tested. According to this method, each particle is assigned the median of the weights evaluated at all the observation time steps within the 24-hrs response time interval. Although this approach allows to make full use of the available measurements, a more intensive use of proxy information on the snow mass-related variables has turned out to be counter-productive by sharpening the sensitivity of the filter effectiveness to the quality of estimates, with resulting heterogeneous filter performances over the analysed datasets.

CHAPTER 8

Comparative discussion on EnKF and SIR-PF schemes

==

The main goal of this Chapter is to further analyse the selected sequential ensemble-based DA techniques by comparing their performances in consistently updating the system state. The analyses are based on common DA settings, namely 24-hrs assimilation frequency and 100-members ensemble simulations.

When assessing the performance of a DA scheme, two different aspects need to be investigated. The main interest focuses on the filter effectiveness in reducing the model error at each assimilation time step. However, it is also of upmost importance to verify the impact of the filter updating on the system physics, since the analysis state can be even significantly different from the system background conditions. This key issue entails further matters to discuss addressing the physical consistency of the analysis simulations supplied by the multivariable DA scheme and how long the effect of the filter updates on model predictions lasts from the assimilation time step onwards. This last question is of critical interest with reference to forecasting applications.

8.1 Filters updating effectiveness

The purpose of this first evaluation is to assess how the filters succeed in effectively reducing the error affecting the model simulations with respect to the available observations. Indeed, because the filter aims at properly updating the model state towards the observations, the model analysis error (Err_a), that is the residual error resulting from the updating procedure, is supposed to be lower, in absolute value, than the model background error $\left(Err_{bkg}\right)$, namely the error affecting the simulations right before the assimilation is applied.

$$Err_{bkg,t_{Assim}} = Y_{t_{Assim}} - X_{bkg,t_{Assim}} \qquad [8.1]$$

$$Err_{a,t_{Assim}} = Y_{t_{Assim}} - X_{a,t_{Assim}} \qquad [8.2]$$

In order to evaluate the filters performances in reducing the model background error, they are evaluated through a newly introduced index, the updating Effectiveness $\left(EFS_{up}\right)$:

$$EFS_{up,t_{Assim}} = |Err_{bkg,t_{Assim}}| - |Err_{a,t_{Assim}}| \qquad [8.3]$$

where $Err_{bkg,\, t_{Assim}}$ and $Err_{a,t_{Assim}}$are respectively the background and analysis errors affecting the average ensemble simulations with respect to the observations available at each assimilation time step. The choice of considering the modulus of model errors ensures to prevent possible offsetting effects. It is noteworthy that the scale of this metrics also depends on the size of the model background error. Indeed, the higher the background error affecting the ensemble simulations, the greater its potential reduction through the updating process. The evaluation of the relative differences between the background and analysis errors with respect to the background one would explicitly supply this kind of information. However, when dealing with errors mostly ranging around zero, the assessment of their relative differences turns out to be challenging. Therefore, the EFS_{up} is assumed to be more suited to this purpose. According to its definition (Eq. 8.3), the larger the EFS_{up} value, the higher the filter performance. Indeed, a EFS_{up} value greater than zero is an evidence of an actual reduction of the model background error, on average. A null-valued difference between background and analysis errors reveals that the filter does not succeed in updating the system, whose state remains unchanged with respect to its previous conditions before the assimilation. At worst, a negative value of EFS_{up} warns that the filter improperly updates the system, whose analysis state is even more inconsistent with the available observations with respect to its background conditions. Figures 8.1a, b and c show the boxplots of the seasonal comparative evaluation between the filters effectiveness in updating the average ensemble simulations of each assimilated variable at the experimental sites.

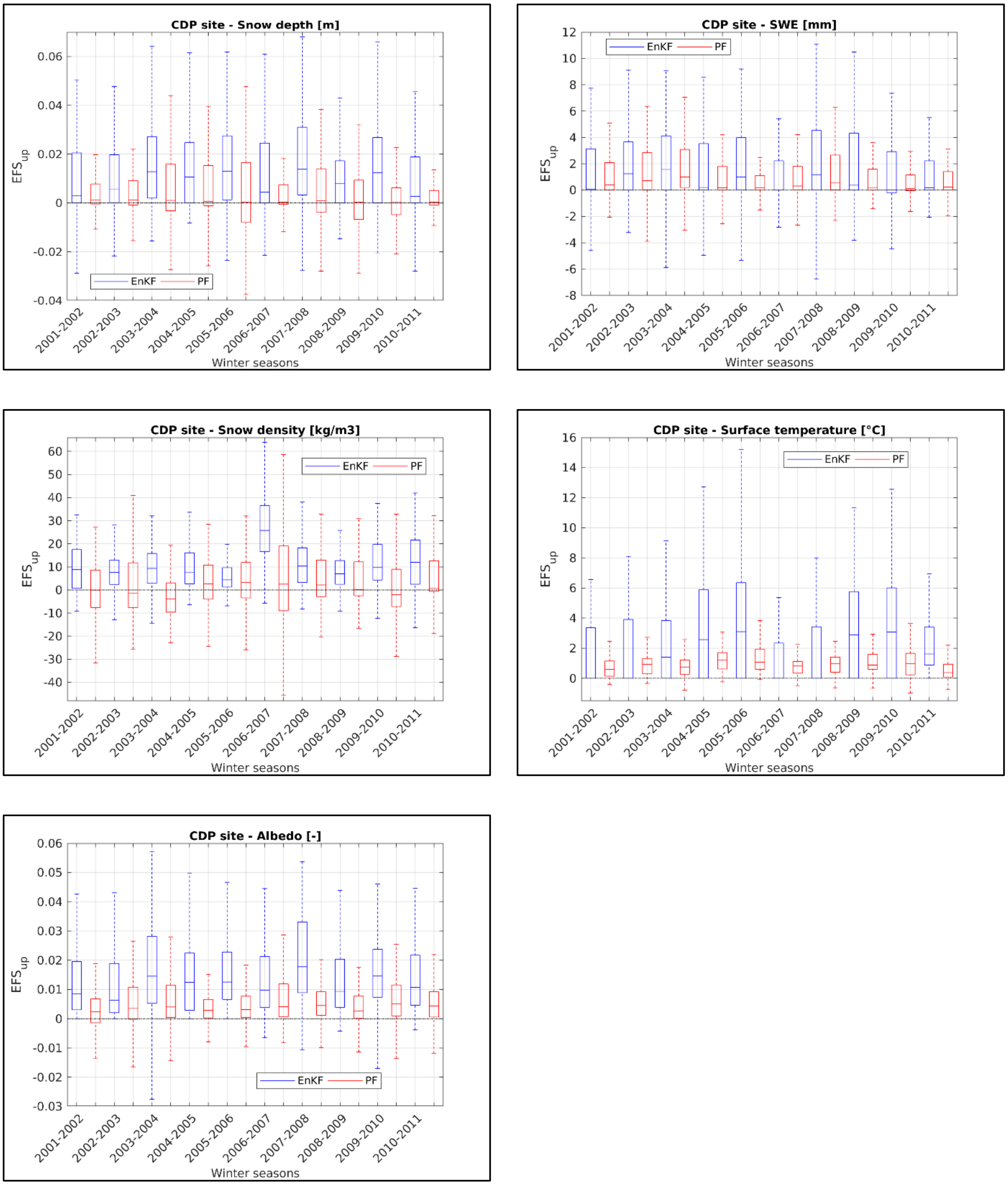

Figure 8.1a: *EnKF vs PF schemes – Filters effectiveness in updating simulations of snow depth, SWE, snow density, surface temperature, and albedo – CDP site (full dataset). The bottom and top edges of each box indicate the 25th and 75th percentiles, respectively.*

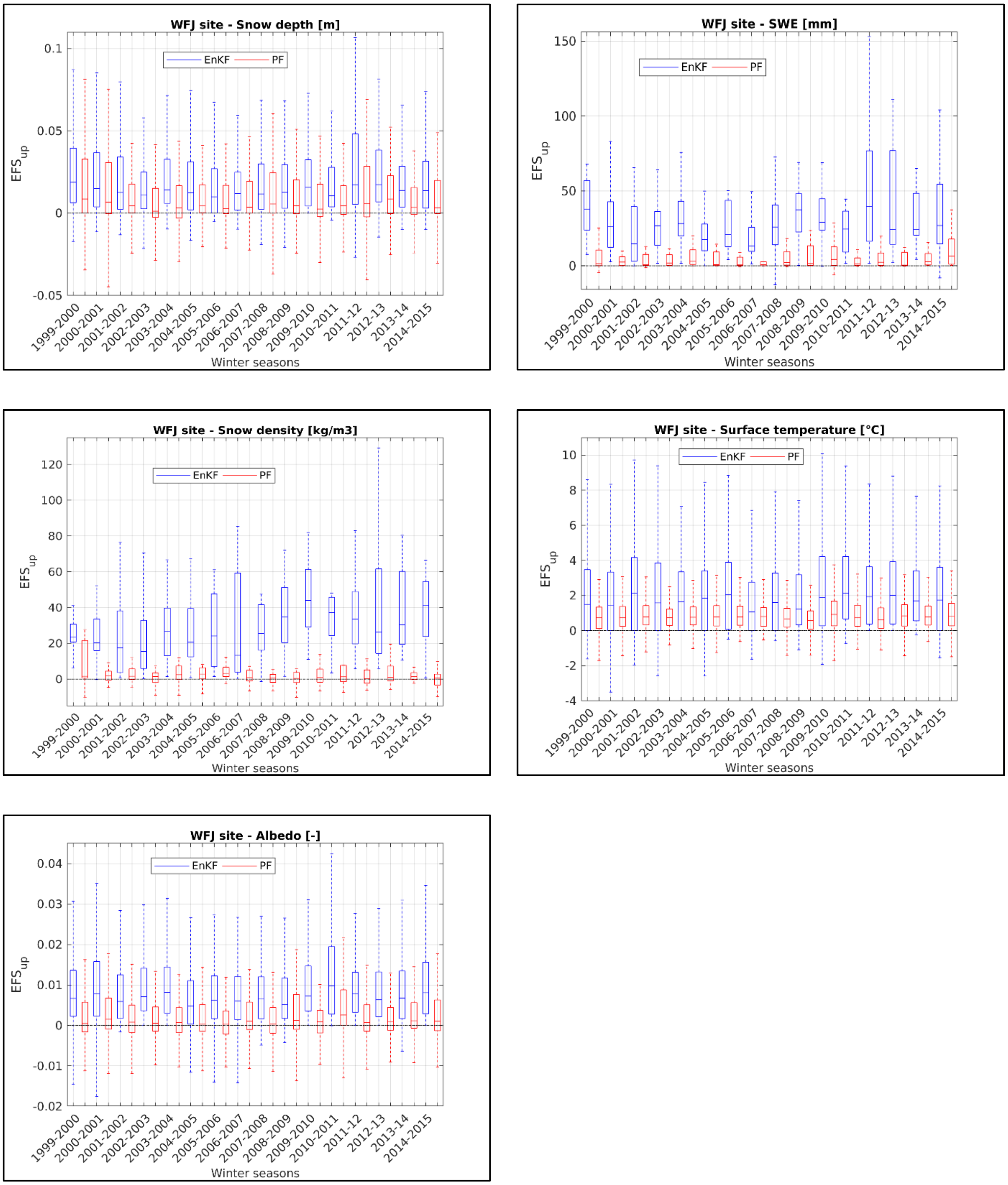

Figure 8.1b: *EnKF vs PF schemes– Filters effectiveness in updating simulations of snow depth, SWE, snow density, surface temperature, and albedo – WFJ site (full dataset).*

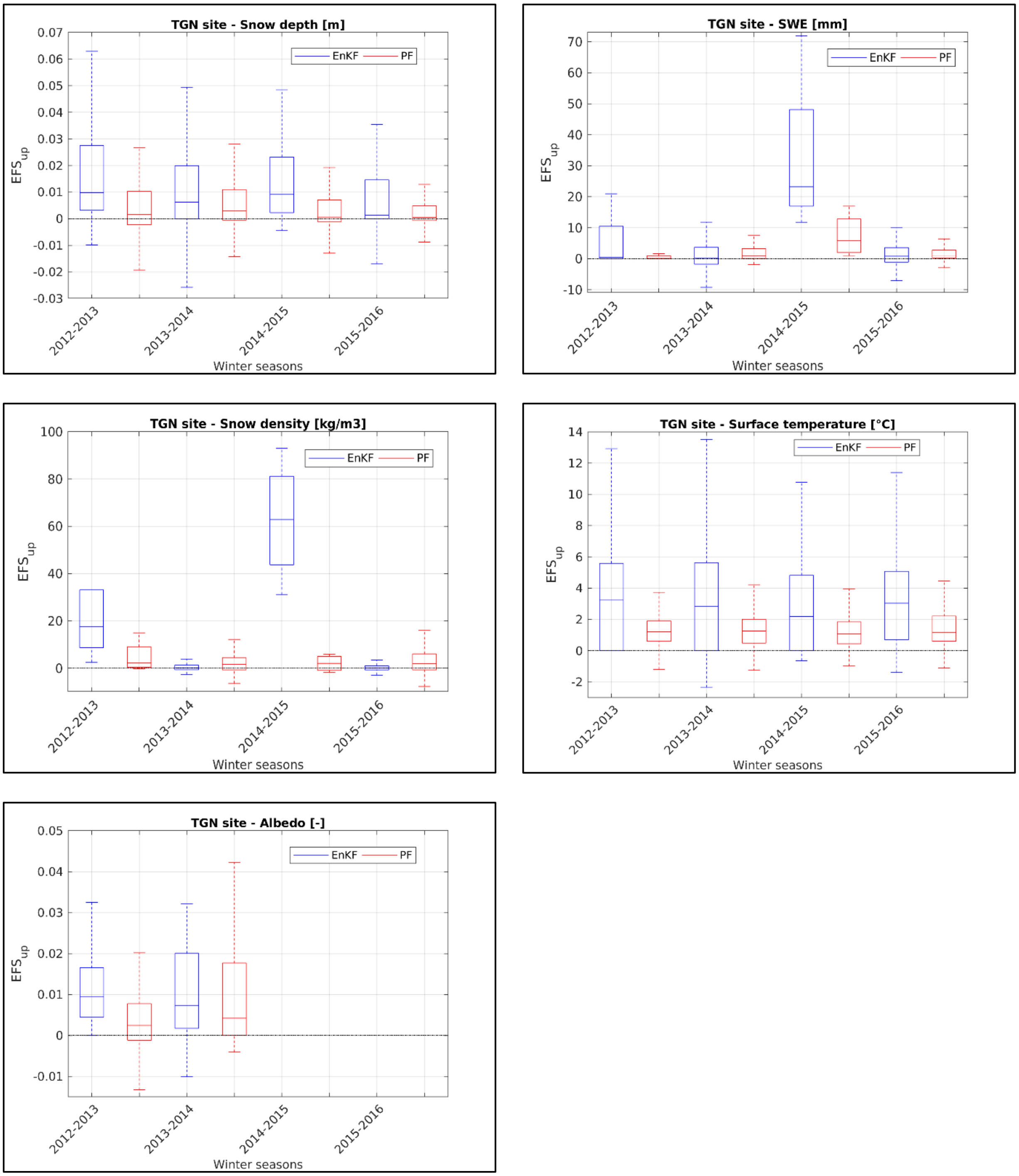

Figure 8.1c: *EnKF vs PF schemes– Filters effectiveness in updating simulations of snow depth, SWE, snow density, surface temperature, and albedo – TGN site (full dataset).*

When assessing the filter effectiveness in updating snow depth simulations at CDP site, the EnKF technique outperforms the PF scheme with median values greater than zero, revealing a satisfying filter performance, on average. On the other hand, the PF-based median values range around zero, with negative lower quartiles in most of the winter seasons, which indicate suboptimal filter updating. Even though the EnKF reveals a greater updating effectiveness also at the Swiss station, as proven by its higher median values with respect to the PF, this latter technique is here more effective with respect to the French site. Indeed, generally also the 25^{th} percentile is greater than zero, except for some sporadic snow seasons. Consistently, at TGN station, the PF discloses slightly poorer effectiveness, with both median values and lower quartiles ranging around zero. However, at this site, the two analysed DA methodologies reveal more equivalent performances with respect to the other pilot sites.

At the French site, the EnKF and PF schemes have similar performances in terms of SWE, even though the first technique is affected by a larger variance. In Switzerland, the scale of the EnKF-related EFS_{up} is significantly higher with respect to CDP. This difference in EFS_{up} scale entails a more sizeable disparity between the performances of the two DA techniques, even though the PF mostly guarantees consistent system updates (positive median values and lower quartiles). The same result is shown for the winter season 2014-2015 at TGN site, while during the other snow seasons the EnKF and PF have equivalent updating effectiveness, instead.

Consistently with SWE simulations, at WFJ site the difference in EFS_{up} scale is prominent also in terms of snow density. While the EnKF ensures to significantly reduce the model background error, generally with a sizeable variance, the PF is marked by both median values and 25^{th} percentiles ranging around zero, on average. Although more comparable performances are achieved at CDP, in terms of effectiveness the EnKF mostly outperforms the PF, whose distributions reveal negative median values for some sporadic snow seasons. At TGN site, except for the winter 2014-2015, generally the two DA schemes guarantee an almost equivalent reduction of the model background error.

The difference in scale of the filters effectiveness in updating both SWE and snow density simulations at the Swiss site is manly ascribable to the lower bi-weekly SWE measurement (and snow density estimates) frequency with respect to the higher daily frequency at CDP. At WFJ the model error resulting from the implementation of the EnKF scheme can even more quickly increase throughout the 24 hrs period between two following time steps with respect to the PF scheme. Indeed, the Kalman filtering does not benefit from the parameters resampling, which is supposed to contribute to the physical consistency of model simulations (Sect. 7.2). Of course, the larger the background error at an assimilation time step, the higher the potential filter updating effectiveness. This issue, allowing the EnKF to better succeed in sharply reducing the model error, is further supported by the consistent results at TGN site for the winter season 2014-2015, when bi-weekly SWE observations are available. Nevertheless, it is noteworthy to consider that the PF scheme is also affected by the accuracy of the estimates of the mass-related variables supplied by the additional snow density model (Sect. 7.3).

As regards to the filters updating effectiveness in terms of surface temperature, the PF shows higher performances with respect to the other analysed variables. Besides the larger variance of the EnKF-related distributions, at CDP site the PF scheme guarantees more stable performances, with both median values and lower quartiles greater than zero, unlike the EnKF, whose median values are often null-valued. Despite PF satisfying performances at the Swiss station, the Kalman filtering generally outperforms the Particle filtering in terms of EFS_{up}, consistently with the results at TGN site.

At the French snow experimental site, both the DA techniques succeed in properly updating the albedo simulations, on average, even though the medians of the EnKF-based EFS_{up} distributions are generally higher than the PF ones. The Particle filtering reveals poorer performances at WFJ, where the mostly negative values of 25th percentiles indicate suboptimal updates of this energy-related variable. Even though fewer albedo measurements are available at TGN site, the effectiveness of the two DA techniques do not show any markedly significant difference.

However, it is important to stress that a large update of the model state does not necessarily entails a positive effect between two following assimilation time steps, even though it guarantees a high effectiveness at the assimilation time steps.

8.2 The impact of filters updates on the system physical consistency

The assessment of the filters effectiveness is a useful tool to evaluate how they succeed in updating the system state at the assimilation time steps. However, this analysis is not sufficient to properly investigate the overall filters performances. In order to extensively study and compare the two selected DA schemes, it is of critical importance to analyse the effect of the filters updates on the evolution of the model analysis state.

One key factor is the size of the correction terms resulting from the updating procedure. Clearly, large correction terms ensure a significant reduction of the model background error. However, sharp corrections of some prognostic variables are likely to generate possible physical inconsistencies affecting the system state due to steep stretches towards the observations. In turn, the system can tend to restore its previous physical conditions after the assimilation time step. These dynamics can then call for further sizeable correction terms at the following assimilation step, since the system has already lost track of the previous update.

On the other hand, even though a weaker update of the state variables means a poorer filter effectiveness, it is supposed to last longer between two following assimilation time steps, according to the system inertia. Theoretically, this advantage could entail lower correction terms at the successive assimilation time steps, if the model were not affected by uncertainties. Indeed, the state of an ideal model is supposed to maintain its consistency with observations, resulting from the updating procedure, between two following assimilation time steps, aside from the observational uncertainty. Conversely, the simulations of a real system are likely to gradually diverge with respect to the ideal trend from the filter updating onwards, according to possible biases affecting its predictions. However, low background errors at the assimilation time steps, resulting from sequential minor updates, are an evidence of a proper model physical consistency. In this desired case, since the system does not significantly diverge from the analysis conditions, the state variables are likely to have a more physically consistent evolution, whose trend is not subject to unreliable sharp gradients due to the sequential updates.

With the aim of addressing this crucial issue, the two sequential DA techniques are compared by analysing the trend of the average analysis time series. Figure 8.2a, b and c show the scatterplots of the time derivatives of the multivariate DA simulations resulting from the implementation of the EnKF and PF schemes $\left(\frac{\delta X_{analysis}}{\delta t}\right)$. In blue and red are highlighted the no- and assimilation time steps, respectively.

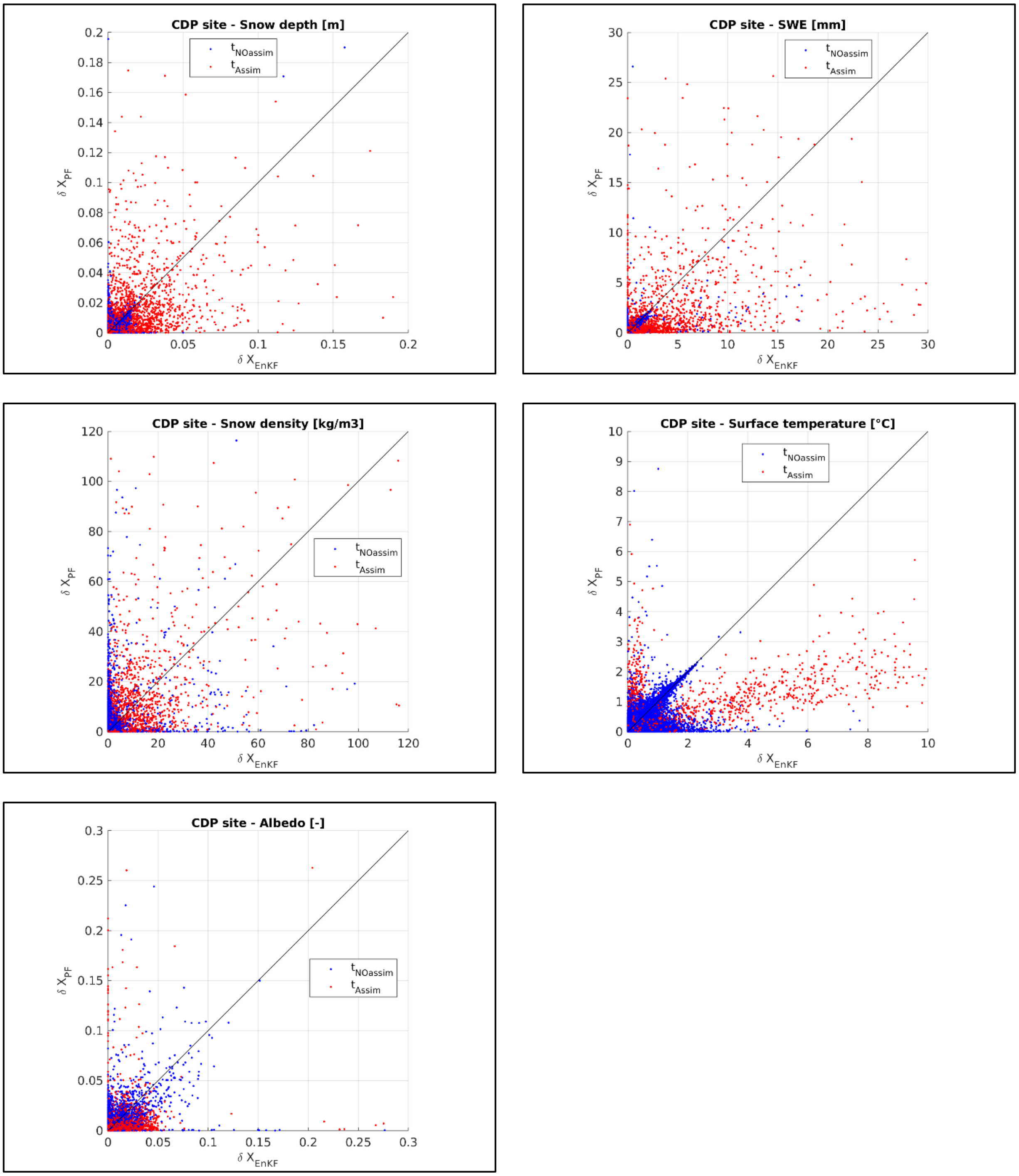

Figure 8.2a: *EnKF vs PF schemes– Scatterplot of time derivative of the multivariate DA simulations of snow depth, SWE, snow density, surface temperature, and albedo – CDP site (full dataset).*

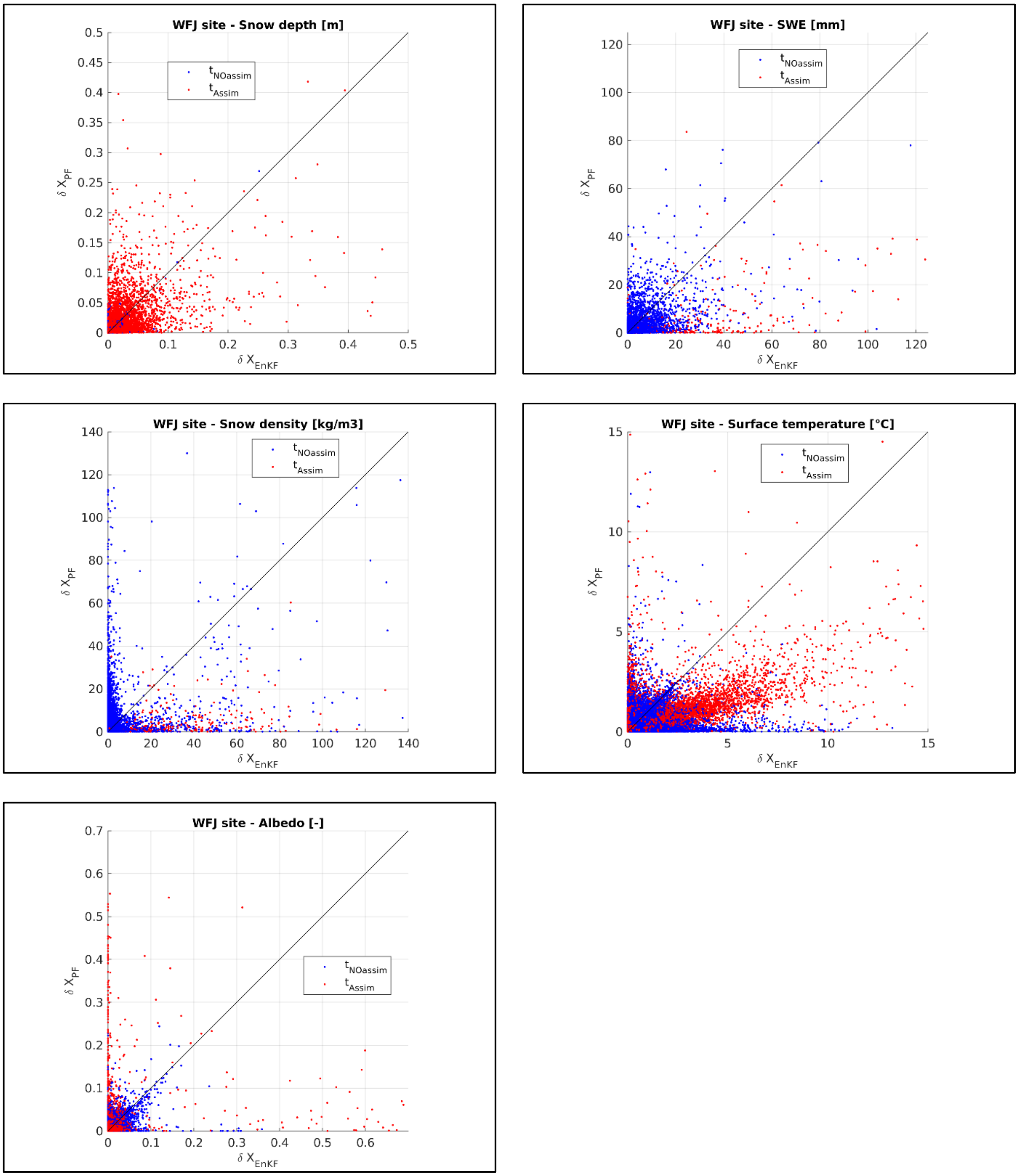

Figure 8.2b: *EnKF vs PF schemes– Scatterplot of time derivative of the multivariate DA simulations of snow depth, SWE, snow density, surface temperature, and albedo – WFJ site (full dataset).*

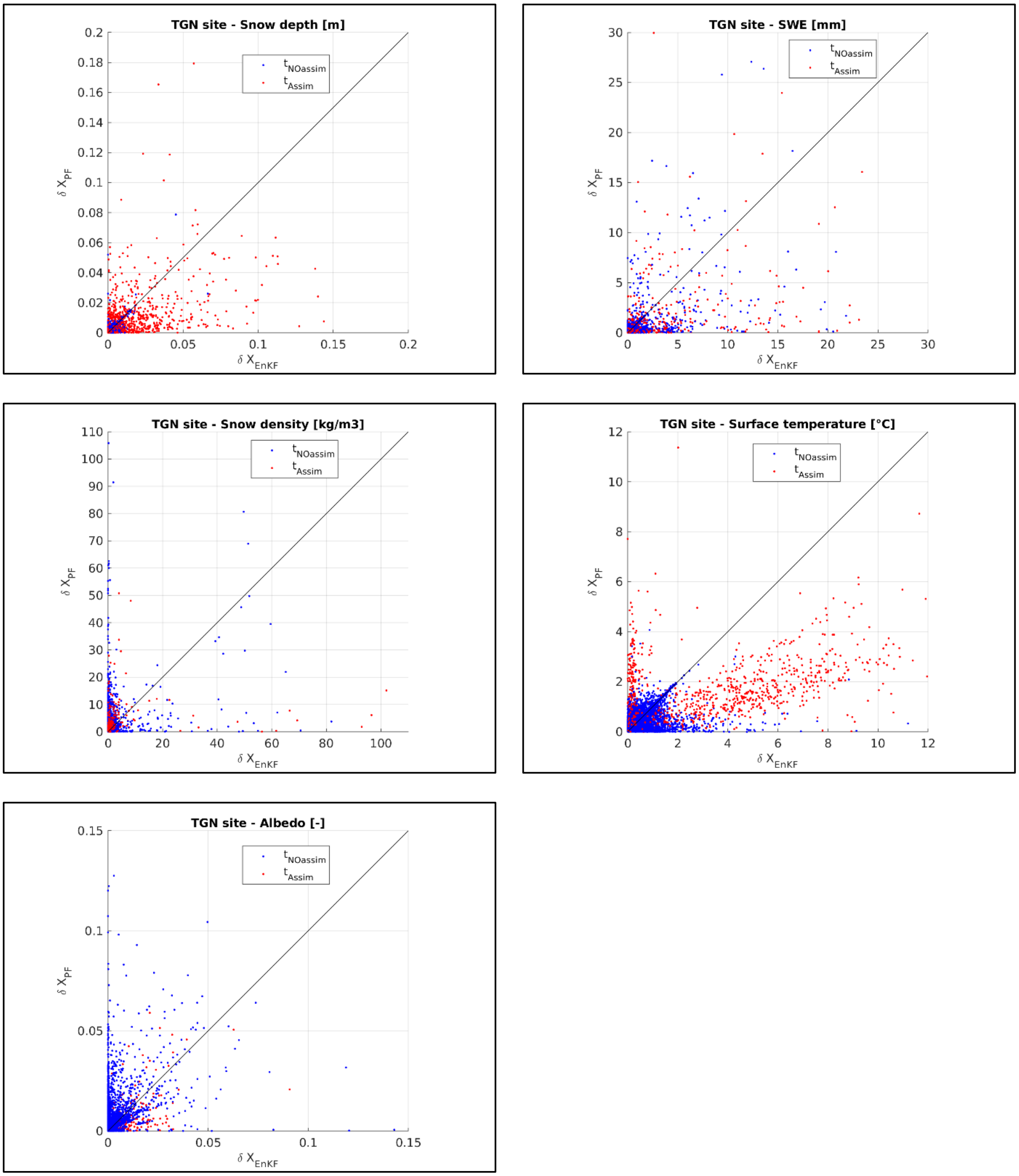

Figure 8.2c: *EnKF vs PF schemes– Scatterplot of time derivative of the multivariate DA simulations of snow depth, SWE, snow density, surface temperature, and albedo – TGN site (full dataset).*

The main interest focuses on the analysis states at the assimilation time steps (red dots), whose distributions in the graphs provide useful information for the comparative assessment of the scale of the filters updates. The surface temperature shows the most well-defined behaviour, namely the EnKF-based correction terms are typically much larger with respect to the PF ones. While this trend is not easily detectable for the snow depth simulations, the EnKF reveals generally sharper updates of SWE simulations at CDP and WFJ stations, and albedo and snow density simulations at the French and Swiss sites, respectively. Conversely, the PF updates turn out to be larger in terms of snow density and albedo at TGN and CDP pilot sites, respectively.

Furthermore, it is noteworthy that the spreads of the no-assimilation states (blue dots) result from the filters updates and how these latter impact the evolution of the system state, namely the physical dynamics between two following assimilation time steps.

Of course, a longer-lasting effect of the filters updates from an assimilation time step onwards entails a well-spread distribution of the no-assimilation states, since each DA scheme differently updates the system state. In this case, the analysis system keeps track of the filter updating, which contributes to diversify the no-assimilation states resulting from the implementation of these two DA techniques. Nevertheless, even when the system loses track of the filters updating by tending to restore its background state, the correspondence between the EnKF- and PF-based no-assimilation states is not guaranteed. Indeed, at each assimilation time step, the background conditions of both the DA runs result from the physical evolution of the system having as initial conditions the analysis conditions resulting from the previous system update, which are different between the two DA runs. This is the main reason why the no-assimilation states are generally well spread, with resulting heterogeneous distributions. The higher density of the distributions of the surface temperature no-assimilation states along the bisector is mainly justified by the fast dynamics of this variable, which allow the system to quickly restore its background thermal state, with a resulting higher correspondence between the no-assimilation states of the two DA runs.

In order to jointly take into account of both the filters effectiveness at the assimilation time steps and the scale of the resulting correction terms, a further evaluation has been performed with the aim of assessing the impact of the filters updating on the temporal evolution of the system state.

Indeed, as previously explained, a high effectiveness can be to the detriment of the physical consistency of the system state dynamics, subject to possible far-fetched discontinuities.

Figures 8.3a, b, and c present the scatterplots of the ratio between the analysis and background errors of the average ensemble simulations with respect to the observations $\left(\frac{\left|Err_{a,t_{Assim}}\right|}{\left|Err_{bkg,t_{Assim}}\right|}\right)$ against the difference between the corresponding average background and analysis ensemble states $\left(\left|X_{a,t_{Assim}} - X_{bkg,\,t_{Assim}}\right|\right)$ at each assimilation time step. This kind of graph can be somehow interpreted as a cost-benefit study, namely how large are the state updates required to attain a certain error reduction. Ideally, the most conducive condition calls for a null errors ratio, namely a zero-valued analysis error, and the lowest possible difference between the system state before and after the updating procedure. This outstanding result, ensuring an efficient model error reduction even through a minimal filter updating, can be theoretically achieved only if the model background state is not far from the observed one, namely if it succeeds in keeping track of all the previous sequential updates. To better understand the graphs shown in Figures 8.3a, b and c, it is noteworthy to consider both the x- and y-axis as extreme cases. The x-axis corresponds to the Direct Insertion DA technique (Sect. 5.1), which promotes the simple replacement of model predictions with the observations. In this case, the analysis error is null-valued, but unbalanced state estimates may occur with resulting possible model shocks. Conversely, the y-axis can be regarded as a VAR DA scheme, or a smoother DA technique, which allows to preserve the physical consistency of the system state by preventing possible discontinuities in the model trajectories.

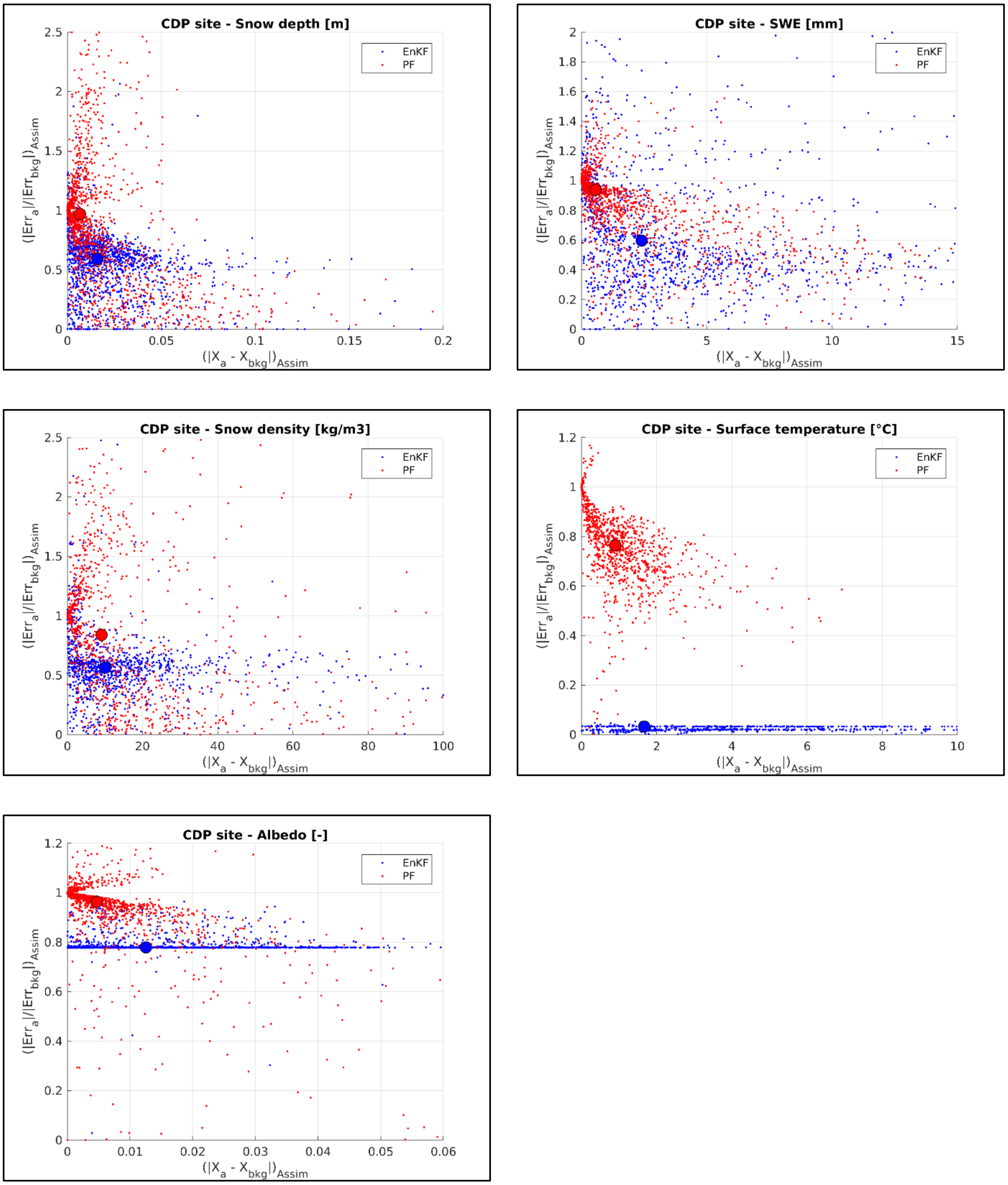

Figure 8.3a: *EnKF vs PF schemes– Scatterplot of filters performances in terms of snow depth, SWE, snow density, surface temperature, and albedo (big dots for the average performances) – Big dots are the centre points of the distributions - CDP site (full dataset).*

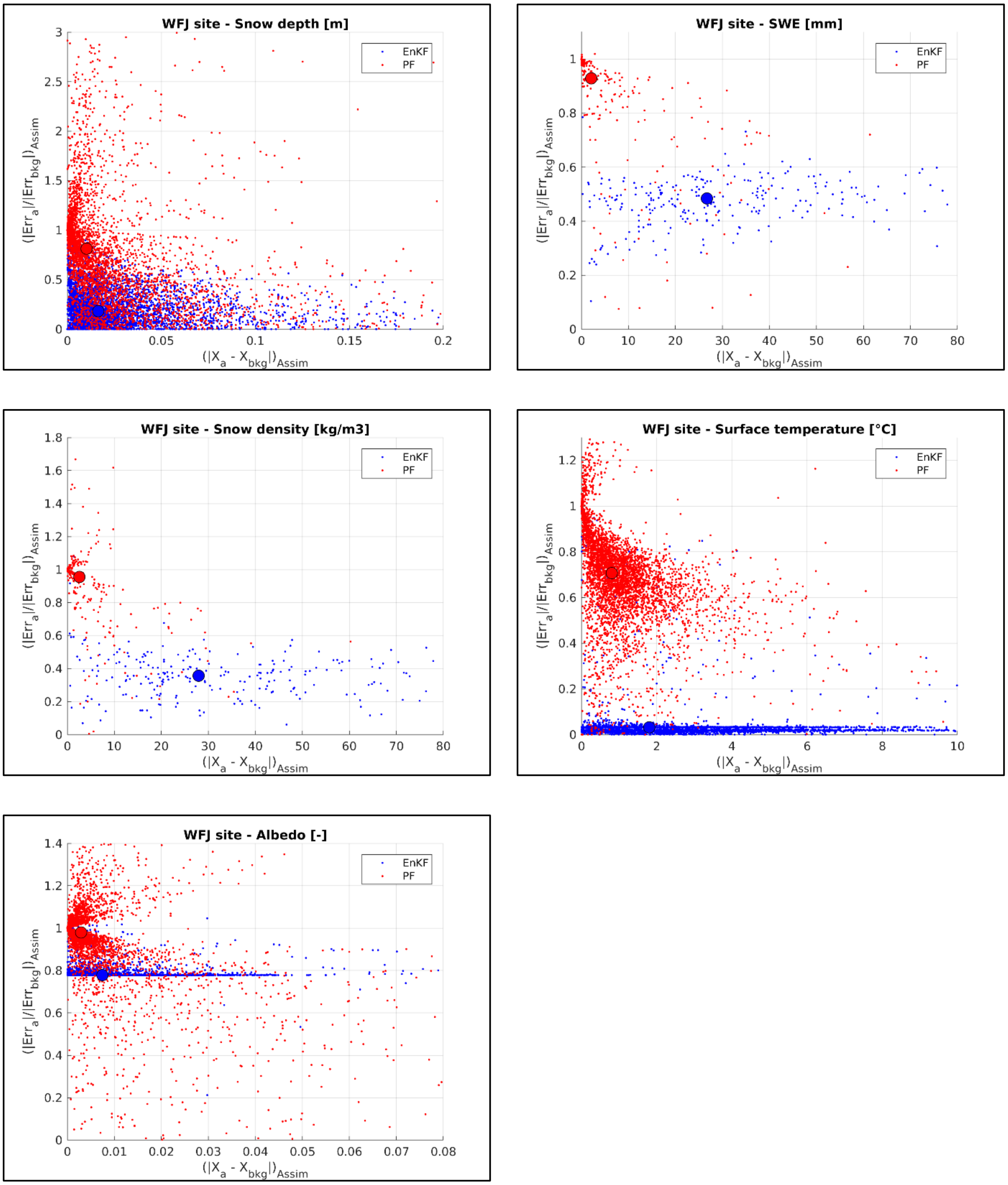

Figure 8.3b: *EnKF vs PF schemes– Scatterplot of filters performances in terms of snow depth, SWE, snow density, surface temperature, and albedo (big dots for the average performances) – WFJ site (full dataset).*

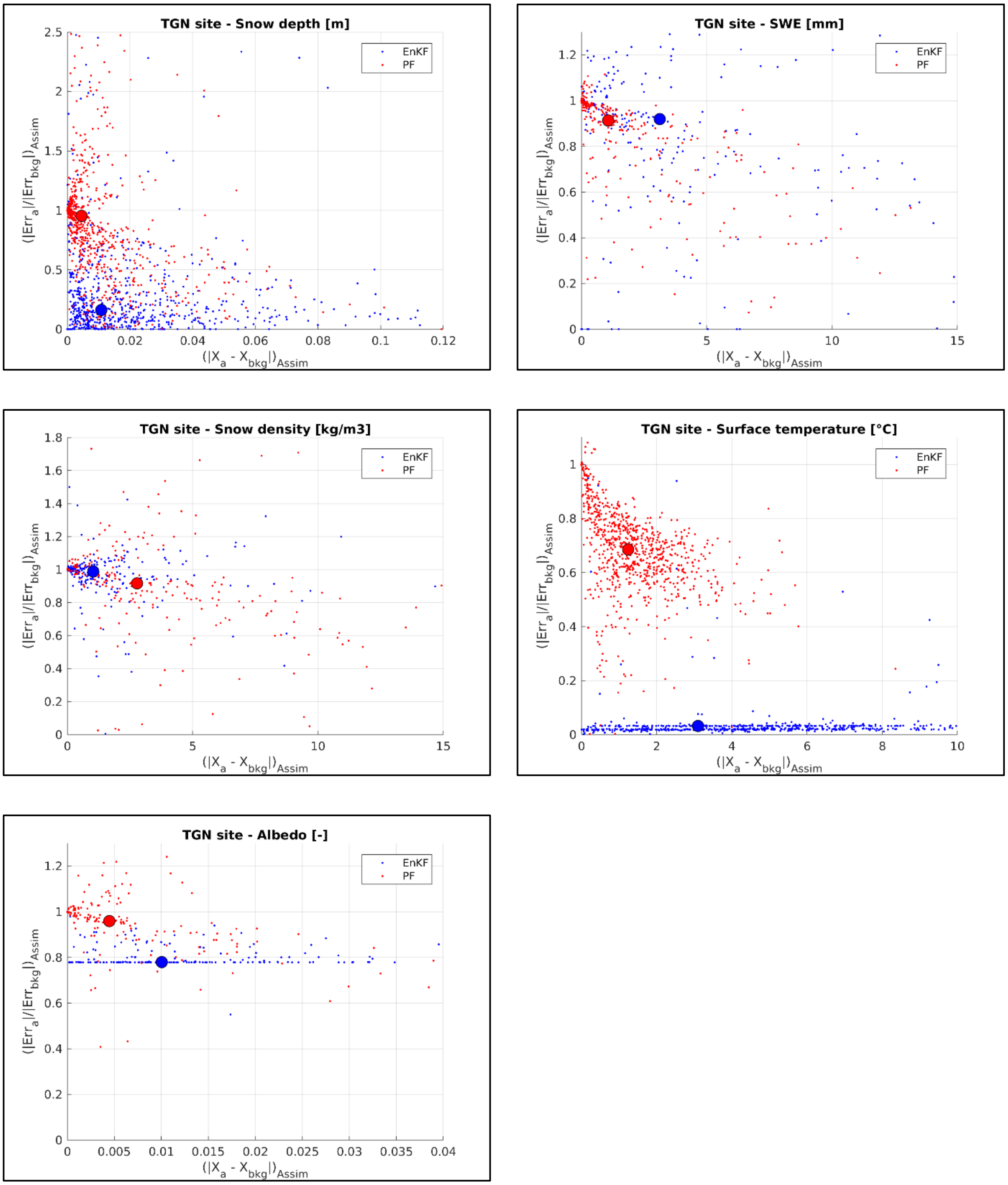

Figure 8.3c: *EnKF vs PF schemes– Scatterplot of filters performances in terms of snow depth, SWE, snow density, surface temperature, and albedo (big dots for the average performances) – TGN site (full dataset).*

According to the definition of background and analysis errors, the ratio of their absolute values is supposed to range between 0, perfect correction, and 1, when the filter does not succeed in updating the system state, at worst. Thus, both the analysed DA methodologies well succeed in properly updating the system state, since their average performances generally reveal ratio values lower than unity.

Consistently with the results of the previous evaluations, with respect to the PF technique, in most cases the EnKF scheme ensures a more effective reduction of the model background error, but through larger correction terms, especially in terms of surface temperature, snow depth and albedo.

When assessing the surface temperature, the EnKF scheme ensures an almost equivalent reduction of the background error at all the experimental sites. At TGN station, the resulting discontinuities in the analysis time series are larger (about 3°C) with respect to the other sites (less than 2°C), on average. In comparison to the EnKF technique, the PF scheme reveals a lower updating effectiveness, but it preserves a more consistent trend of the analysis simulations with average temperature leaps of around 1°C, which are slightly larger at the Italian site, as well.

The filters reveal the same difference in performances in terms of albedo. However, it is noteworthy that each DA technique guarantees almost equivalent results at all the experimental sites, in terms of both background error reduction and size of discontinuities affecting the analysis simulations of the state variables.

Consistently, the evaluation of the PF-based updating of the snow depth simulations generally reveals lower changes in the analysis snowpack thickness (around 5 mm) with respect to the EnKF technique (about 15 mm), except for the Swiss site, where the doubling of the 5-mm average value results in an even poorer updating effectiveness. On the other hand, the EnKF scheme shows a lower average reduction of the background error at the CDP site with respect to the other station, in spite of an almost equivalent average of the snow depth changes in the analysis predictions.

The filters performances in terms of SWE and snow density are more diversified. At the French site, the PF and EnKF schemes entail almost equivalent average discontinuities affecting the snow density simulations (about 10 kg/m^3), but with a resulting lower effective reduction of the background error through the PF technique. Conversely, at TGN station, the PF scheme slightly outperforms the EnKF in updating the snow density simulations, on average, even though through larger discontinuities. Furthermore, at this site the PF technique succeeds in guaranteeing the same SWE error reduction of the EnKF scheme through lower average updates.

With respect to the other two sites, at the Swiss station the two DA schemes reveal a significant difference in the size of the resulting discontinuities affecting the analysis simulations of both SWE and snow density. Indeed, while the EnKF entails average discontinuities of about 27 mm and 28 kg/m^3, respectively, those resulting from the implementation of the PF scheme are one order of magnitude lower, namely about 2 mm and 3 kg/m^3, which only allow a slight reduction of the background error.

However, once again, it is noteworthy to stress that the scale of the background error reduction strongly depends on its size.

8.3 Temporal persistence of filters updates

One of the key control factors affecting the overall performance of a DA scheme is the temporal persistence of the filter updates, namely how long the system state keeps track of the updating between two following assimilation time steps.

This factor mainly depends on how the system responds to the update of its prognostic variables. As already explained, it is important to consider that sharp corrections of the state are more likely to lead the system to restore its previous state. In turn, a low temporal persistence of the filter updates can entail steep corrections at the following assimilation time steps, since the system quickly diverges from its observed state.

In order to investigate this issue, an experiment has been performed with the aim of assessing if and how the analysis states tend to restore their background conditions from the assimilation time step onwards. Therefore, batch ensemble OL simulations (without DA) have been generated by setting their initial conditions equal to the corresponding background conditions of the ensemble multivariate DA simulations at each assimilation time step, namely every 24 hours (Figure 8.4).

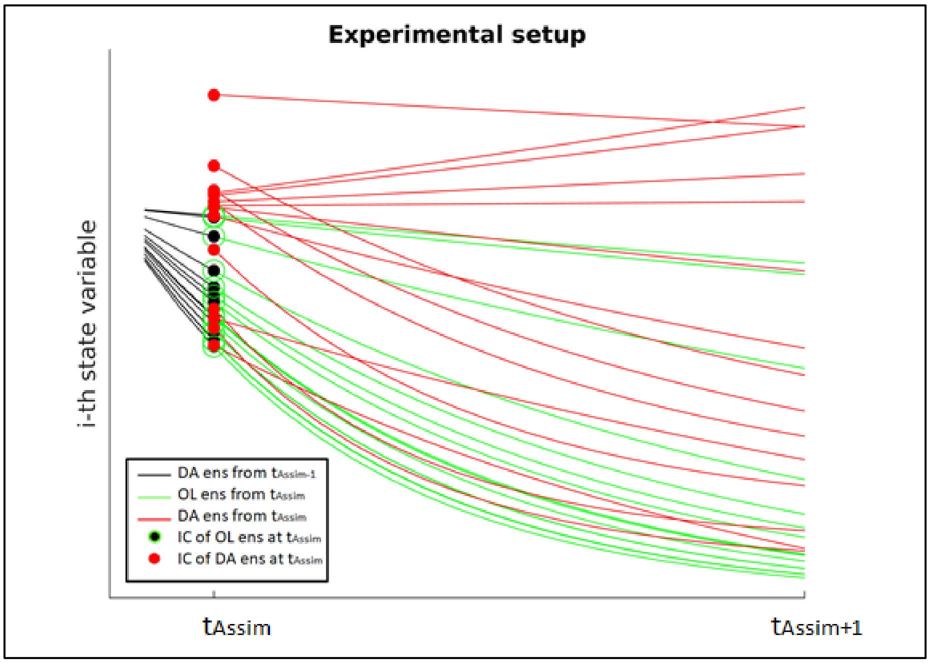

Figure 8.4: *Temporal persistence of filters updates – Experimental setup – At* t_{Assim} *the initial conditions (IC) of the OL ensemble simulations (in green) are the background conditions (black dots with green borders) of the DA ensemble simulations at* t_{Assim} *(in black); in red are the DA ensemble simulation starting at* t_{Assim} *with the analysis IC (red dots) resulting from the updating procedure.*

This experimental setup enables to properly assess the impact of the filters updating by analysing the temporal evolution of the analysis state variables with respect to the no-analysis simulations, having different initial conditions at each assimilation time step, namely background and analysis conditions for the OL ensemble and the multivariable DA simulations, respectively.

Figure 8.5a, b and c show the trend of the average differences between the ensemble background and analysis simulations supplied by the DA schemes between two following assimilation time steps $\left(\overline{X_{OL,ens} - X_{DA,ens}}\Big|_{t_{Assim+1}}^{t_{Assim}}\right)$.

Since this experiment does not address the evaluation of the filter updates, the assimilation time steps are here neglected. Furthermore, it is noteworthy to stress that this comparative study relies on differences between datasets of model simulations and no reference observational data are included. The main interest is not focused on the scales of the average differences, which depend on the size of the correction terms at each assimilation time step (Sect. 8.1). The trends of the average differences are instead of critical importance. Indeed, even though each multivariate DA and the corresponding control run are provided with different initial conditions (i.e. analysis and background conditions, respectively), they both are ruled by the same parameterization laws and meteorological inputs. Therefore, the resulting trend of their differences is mainly a consequence of the updating effect.

Assuming that a null-valued difference corresponds to the matching between the average multivariate DA and OL simulations, a convergence of the EnKF- and/or PF-based differences to zero means that the system does not succeed in keeping track of the filter updating by tending to restore its background conditions. In this undesired case, it is important to consider also the converging slope, which well represents the behaviour of the system response. Conversely, a constant average difference reveals a long-lasting effect of the system updates from the assimilation time step onwards, in full compliance with the system physics. More challenging is the assessment of the divergence from zero value of the average difference of the multivariate DA simulations, since it can be an evidence of a gradual improvement or worsening with respect to the observations. However, the purpose here is not to evaluate the updating accuracy (Sect. 6.2.2; Sect. 7.2.3; Sect., 7.3.2), but rather its temporal persistence. With the aim of taking into account the seasonality of the snowpack physics, namely the higher system inertia throughout the accumulation process (i.e. winter season), and faster dynamics over the transition periods (e.g. melting period), the evaluation has been carried out considering three main periods. The autumn period includes October and November; the winter period considers December, January, and February; the spring period encompasses March, April and May.

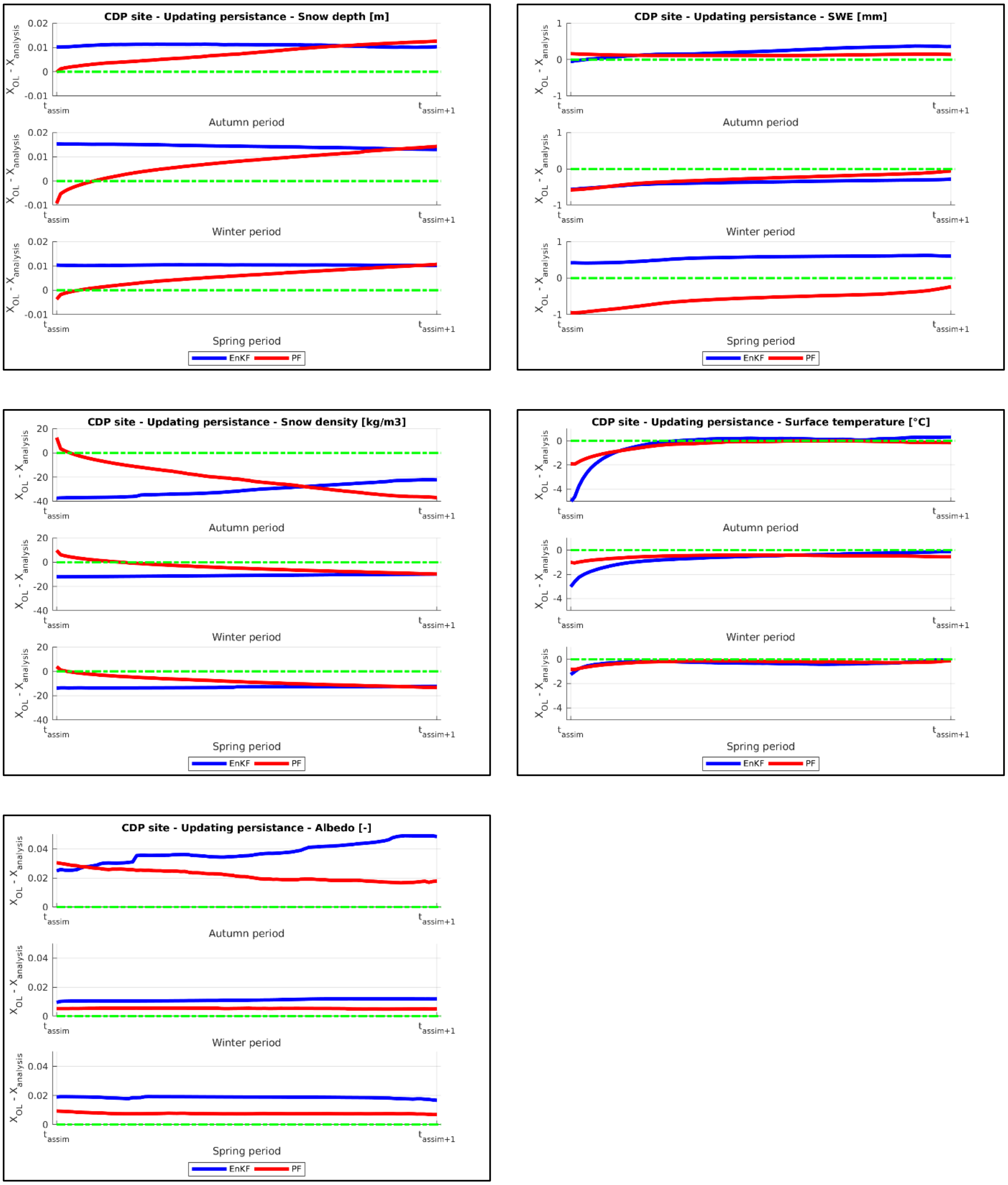

Figure 8.5a: *EnKF vs PF schemes – Seasonal temporal persistence of filters updates of snow depth, SWE, snow density, surface temperature, and albedo simulations – CDP site (full dataset).*

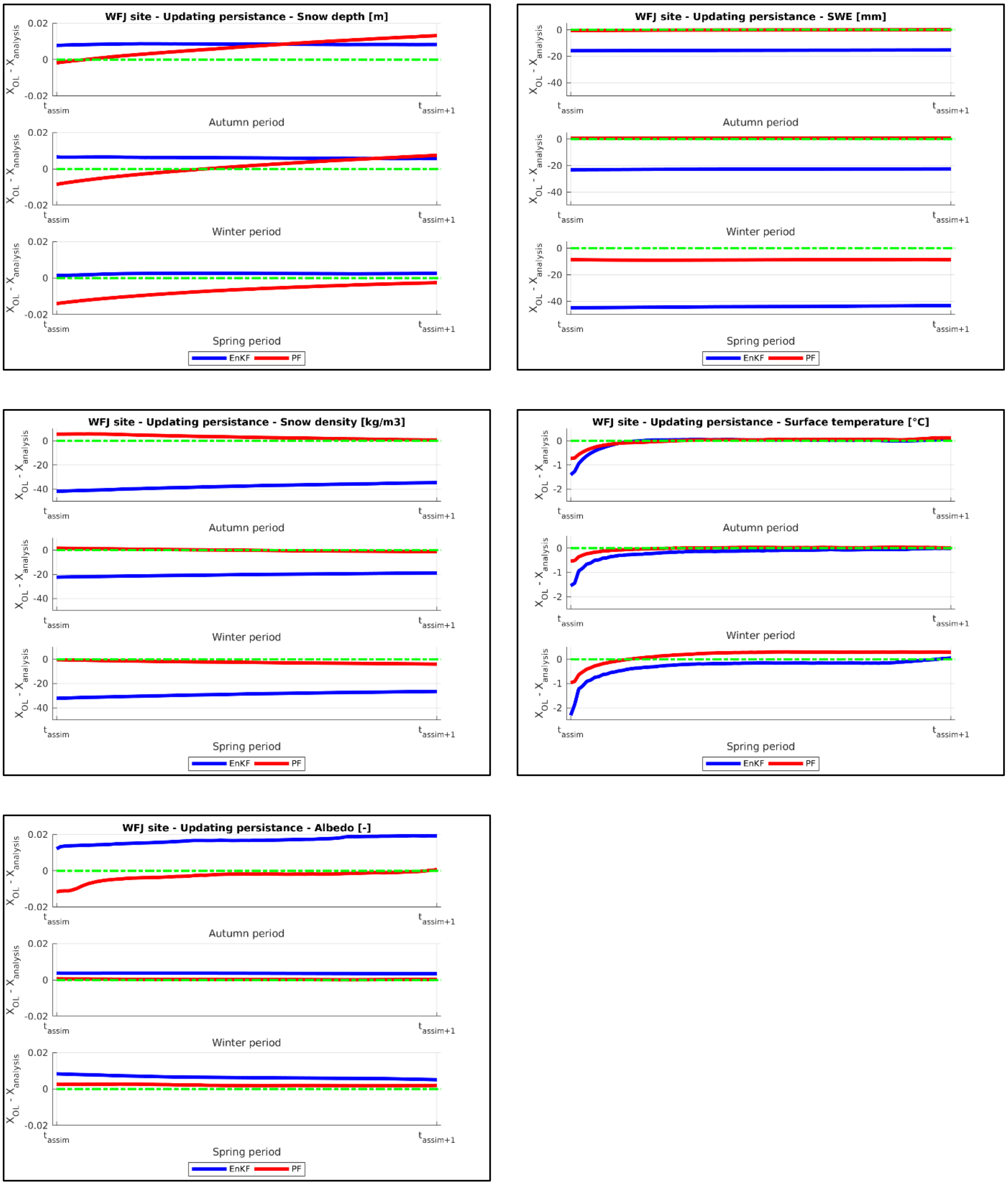

Figure 8.5b: *EnKF vs PF schemes – Seasonal temporal persistence of filters updates of snow depth, SWE, snow density, surface temperature, and albedo simulations – WFJ site (full dataset).*

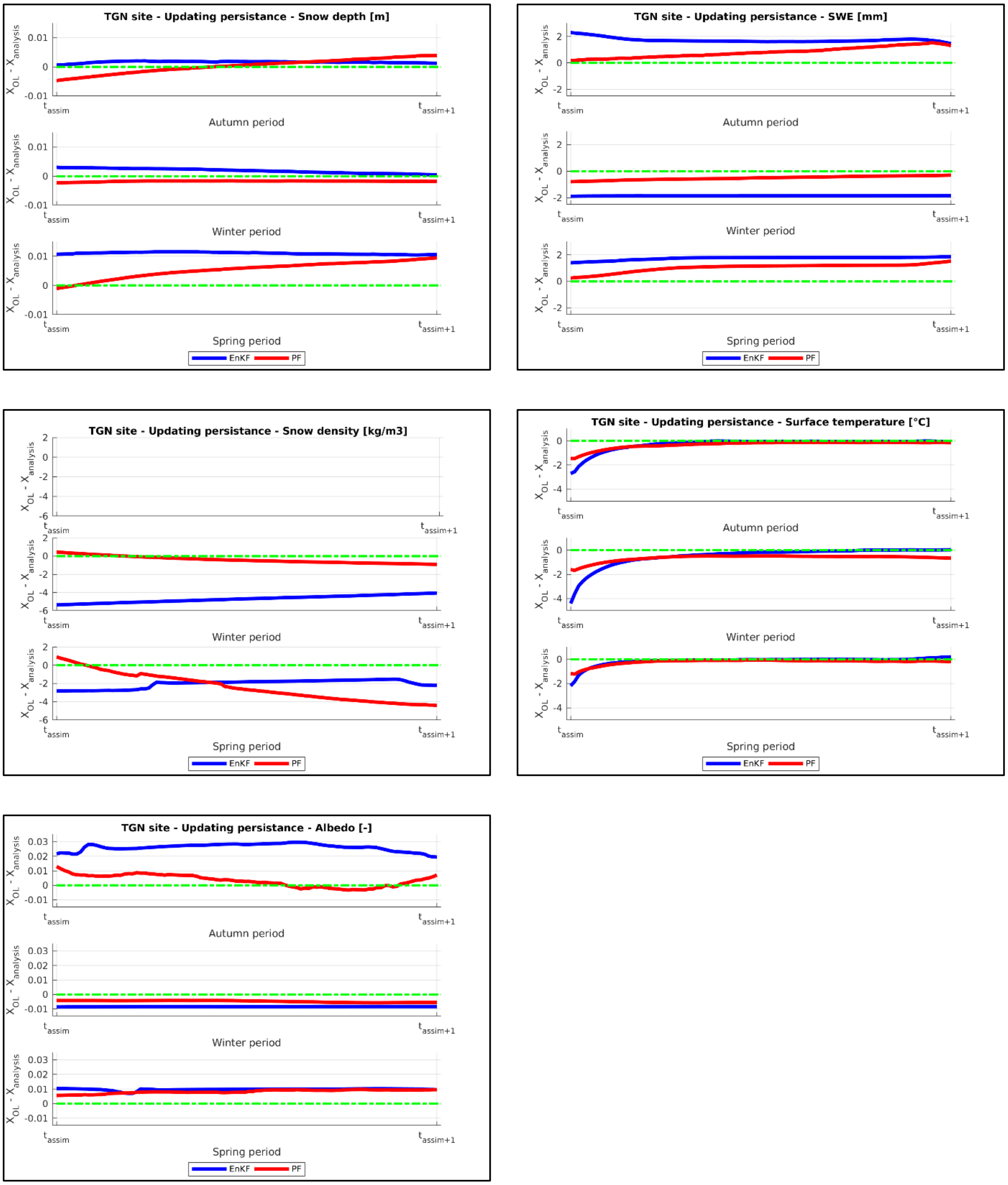

Figure 8.5c: *EnKF vs PF schemes – Seasonal temporal persistence of filters updates of snow depth, SWE, snow density, surface temperature, and albedo simulations – TGN site (full dataset).*

In most cases the constant trends of the average differences give an evidence of a proper long-lasting effect of the filters updating.

The albedo analysis simulations resulting from both the DA schemes maintain almost constant differences with respect to their average background predictions at all the experimental sites during winter and spring seasons. An exception is the autumn period, when the PF and EnKF schemes tend to slightly converge and diverge with respect to the control run, respectively. At TGN station, the more irregular trends are mainly due to the poor albedo sample including barely more than one winter season (Sect. 3.3.3).

The EnKF generally reveals the same steady trend of differences between the background and analysis snow depth simulations at all the pilot sites, except for a slight convergence during the wintertime at the Italian site. Conversely, the PF-based analysis predictions mostly disclose prominent divergent trends, except for a weak convergence to the background simulations during the springtime at the WFJ site. The divergence of the PF-based average analysis simulations can be mainly ascribable to the significantly long-lasting effect of the parameters resampling, which contributes in conditioning the snowpack dynamics, especially the evolution of the snow mass-related variables (Sect. 7.2).

Even more significant is the divergence of the PF-based average analysis simulations of snow density at the French station. The same trend recurring all the seasons suggests that the resampling procedure provides for limitations affecting the model physical representation of this variable. When assessing the convergence between the PF- and EnKF-based differences trends during both winter and spring seasons, it is noteworthy to consider that their background predictions can even significantly differ. Therefore, their convergence should be interpreted as equivalent average gaps between both the analysis simulations resulting from the two DA schemes and their corresponding background predictions, which are different from each other, however. While both PF and EnKF schemes ensure a constant tendency at WFJ station, at the Italian site the PF has a divergent trend of the differences between background and analysis simulations during the spring season (no snow density measurement is available during the autumn period). Furthermore, it is noteworthy to observe the dissimilarity in the order of magnitude of the gaps between background and analysis time series of snow density at CDP and, especially for the EnKF scheme, at WFJ with respect to the Italian site.

Consistently with the assessment on snowpack density, at the Swiss station the analysis simulations of both the DA schemes maintain constant differences with respect to their background predictions. At CDP, during the wintertime both EnKF- and PF-based analysis simulations reveal slightly convergent trends, and the second technique also during the spring season, with an even greater converging slope. On the other hand, at the Italian site, gently divergent trends characterize the PF-based analysis simulations during both autumn and spring periods. Also the evaluation of this state variable reveals different orders of magnitude among the values of the differences in simulations, especially between French and Italian sites, where the ranges are of few mm, and the Swiss station, where the EnKF-based differences even exceed 40 mm, in absolute value.

Unlike the other variables, the model response to the surface temperature updates reveals markedly well-defined features, namely the system restores its previous thermal conditions right after the assimilation time steps. Of course, the fast dynamics of the daily thermal cycle make the system response to the updates of this variable more reactive. The sharper the filter updates, the faster the convergence to the control simulations, as demonstrated by the higher EnKF converging slopes with respect PF ones, namely at TGN and CDP sites throughout the autumn and spring seasons, and at WFJ station during the springtime.

8.4 Concluding remarks

The two multivariable DA schemes have been extensively studied through several analyses with the aim of better investigating their strengths and weaknesses.

With respect to the PF technique, the EnKF scheme generally guarantees a larger reduction of the background errors affecting the model simulations at the assimilation time steps (Sect. 8.1). However, when assessing the scale of the filters updates, in most cases the EnKF-based analysis simulations are affected by steep stretches towards the observations, which do not guarantee the internal physical consistency of the state of each ensemble model realization. Indeed, at each assimilation time step the EnKF scheme applies a corrective term to each state variable according to the error with respect to its measurement. Of course, a proper estimate of the observational uncertainty is of critical importance to proper define the Kalman Gain, with the aim of avoiding far-fetched updates of state variables. Nevertheless, the evaluation of the error covariance matrix of observations is usually challenging. Furthermore, the model error covariance matrix is supposed to contribute in making the correction terms taking into account of the correlations among the state variables, whose estimate can be significantly hindered by the strong system nonlinearities, however. For these reasons, even though the EnKF proves to well succeed in updating the system state, possible sharp corrections of the prognostic variables can occur with the introduction of sporadic inconsistencies.

On the other hand, even though the PF scheme reveals a poorer updating effectiveness, on average, the physical consistency of the system analysis states is preserved through the resampling procedure. Indeed, according to the main assumption of this technique, the analysis states result from the replication of feasible model realizations (Sect. 5.3.2). Therefore, this methodology generally ensures that the actual discontinuities affecting the evolution of the state variables at each assimilation time step have a scale more compliant with the system physics (Sect. 8.2).

Even though the system response to sharp updates of the state variables is likely to aim at restoring its previous conditions, the larger average size of the EnKF-based updates does not necessarily entail a significantly poorer temporal persistence of the updating effect on the evolution of the system state variables, with respect to the PF scheme (Sect. 8.3). The temporal persistence of the filter updating turns out to be more strongly dependent on the dynamics of the physical evolution of each state variable, than on the scale of filter updates. A case in point is the assessment of the analysis simulations of the surface temperature, whose faster dynamics of the thermal cycle entail a quicker system response generally aiming at restoring its previous background conditions.

CHAPTER 9
Conclusions

==

This PhD thesis is intended to contribute to addressing critical issues for operational forecasting systems in snow-dominated regions, where the quality of hydrological predictions deeply depends on the quality of snowpack simulations, especially during the melting period.

The recent growing interest in DA techniques aiming at reducing the uncertainty of the snow model simulations has led to new challenging questions on the potential of implementing multivariate DA schemes allowing to consistently update the snowpack state through the joint assimilation of several observations. The study focuses on investigating the feasibility of a multivariate DA scheme in the framework of snowpack modelling by developing and testing the performances of two of the most commonly used sequential ensemble-based DA techniques. While the main common goal was the development of reliable and robust multivariate DA schemes relying on the EnKF and PF techniques, respectively, the implementation of these two DA methodologies has led to face different specific issues according to their main features.

The development of the EnKF scheme has entailed addressing the constraining assumptions of this technique, whose fulfilment deeply conditions the implementation strategy. Since the strong system nonlinearities not only make more challenging the meeting of the EnKF assumptions, but also proved to affect the filter updating procedure, technical solutions were needed to limit their impact on the Kalman filtering performance.

On the other hand, the impoverishment of the particles sample affecting the performance of the PF-based DA scheme was one of the main issues to deal with. Because the spread of the particles ensemble has turned out to be of critical importance to ensure a satisfying filter effectiveness, different approaches have been introduced and tested.

9.1 Main contributions and results

Along this thesis a point-scale snowpack modelling system has been tested at three Alpine experimental sites. The system consists of a multilayer energy- and mass-balance snowpack model coupled with a multivariate DA scheme. The flexible system design has allowed to test both Kalman and Particle filtering techniques, with the aim of investigating their weaknesses and strengths in jointly assimilating different observations. The main purpose was to assess their potential for being implemented in an operational hydrological forecasting chain.

9.1.1 Implementation and analysis of multivariate EnKF-based DA scheme for snow modelling

The development of a multivariate EnKF-based DA scheme has brought out several issues to face, mainly due to the constraining assumptions of this technique, which make more challenging the handling of the strong nonlinearities of the snow modelling system.

- With the aim of preventing the introduction of possible sampling errors resulting from the perturbation process and guaranteeing a well-representative model error covariance matrix, the ensemble of model realizations has been generated through the introduction of stochastic Gaussian noise directly added to the state variables. The choice of generating the perturbations by selecting equidistant cumulated probability values has proven to ensure null mean-valued perturbations and the sample Gaussianity, even when the sample is limited in size, with a significant benefit in terms of computational demand.
- In order to preserve the physical consistency of the system state, a new methodology has been proposed, which relies on a rescaling procedure of the perturbed ensemble of the

prognostic variables, combined with a modulating function. After the perturbation, the rescaling procedure ensures the removal of possible inconsistent values of any state variable without compromising the null mean-valued perturbations and their Gaussian distribution. The complementary modulating function guarantees to define time-variant physically-based ranges used within the ensembles rescaling. Because the modulating function depends on both air temperature and snow mass, it guarantees to take into account the snowpack seasonality (i.e. early winter, accumulation phase, and melting period). With the aim of considering the difference in the seasonal correlations among the state variables due to the intermittent presence of snow cover, the application of the modulating function has been extended to the covariance matrix used to generate the perturbations. This newly developed technique has revealed satisfying performance for the generation of an ensemble of model realizations by maintaining their physical consistency and without introducing any distortion, on average.

- The implementation of the multivariate EnKF scheme has required a specific approach aiming at limiting the impact of the system nonlinearities on the updating procedure, which can spuriously result in inconsistent analysis values of state variables. The reduction of the model error covariance matrix to a block-diagonal one, with two energy- and mass-related minors, has turned out to be effective in preventing the introduction of inconsistent filter updates due to possible misleading correlations resulting from its ensemble-based estimate.
- Several experiments have allowed to further investigate the sensitivity of the EnKF-based system to key DA settings. The multivariate EnKF scheme has generally revealed a low sensitivity to both the assimilation frequency and the ensemble size, which makes the design of this DA scheme promising for operational purposes. The analysis of the impact of the assimilation of different observations has confirmed the high potential of the joint assimilation of several snow-related observations allowing to consistently update both the energy- and mass balances of the system, with resulting outperforming simulations.

9.1.2 Development and testing of multivariate PF-based DA scheme for snow modelling

When implementing the multivariate PF-based DA scheme, the main challenging issue concerns the impoverishment of the particles sample. Indeed, while the sample degeneracy is limited through the resampling procedure, according to the SIR-PF technique, it is of critical importance to provide the system a significantly large noise to allow the particles moving stochastically in the model space. This essential requirement has turned out to be strongly crucial in a multivariate application, since in such an application the filtering procedure is more heavily constrained in estimating the particles likelihood. Because the PF technique allows to relax most of the EnKF-related assumptions, the need of a sizeable system noise can be met through different perturbation strategies, with the aim of ensuring a proper spread of the particles ensemble.

- The perturbation of the meteorological forcing data has turned out to be not sufficient to prevent the sample impoverishment within two following assimilation time steps. This limitation is mainly due to the threshold processes involved within the snow dynamics model, which hinder the enlargement of the ensembles spread, and the poor spread of the mass-related ensembles when no snowfall events occur.
- The introduction of the resampling of the model parameters has proven to greatly contribute in enlarging the ensembles spread through the perturbation of key parameters, with a significant improvement of the filter effectiveness in consistently updating the system state variables. However, despite the enlargement of the ensemble spread, the parameters resampling has sharpened the system sensitivity to the frequency of the assimilated observations. Indeed, to properly resample the model parameters, observations of directly related variables are needed. Otherwise, the parameters resampling can lead to suboptimal values, since it mostly relies on the observations of the more frequently measured variables.
- To overcome the generally widespread lack of ground-based snow mass-related observations, an additional snow density model has been introduced with the aim of assessing its potential in better conditioning the parameters resampling. This last system configuration relying on the perturbation of the meteorological data, the parameters resampling and the mass-related estimates supplied by the additional snow density model has revealed satisfying performance in making the simulations more consistent with the in-situ observations.

9.1.3 Comparative investigation of multivariate EnKF- and PF- based DA schemes

In their final configurations, both the analysed DA techniques generally well succeed in consistently updating the model snowpack state. As sequential ensemble-based techniques, both Kalman and Particle filtering turn out to be suited to operational applications. Indeed, sequential methodologies are particularly indicated for the assimilation of real-time data, where observations are continuously provided in time, since they allow to fully benefit from the observational information as soon as measurements are available. Moreover, because both these techniques rely on ensemble simulations, they manage to properly take into account the several sources of uncertainty involved within the assimilation procedure.

Nevertheless, an extensive comparative study has allowed to better assess their performances and the analysis time series resulting from the sequential filters updates, whose features make each DA scheme more suited to different purposes.

When comparing the two multivariate DA schemes, it is noteworthy to consider, however, that the main features and assumptions behind the analysed DA techniques have led to introduce different strategies to generate the ensembles of model realizations. Even though the differences in their implementation are supposed to condition the resulting analysis simulations, this approach was intended to address the main issues arising from different perturbation strategies and test their impact on the system simulations.

- Even though the EnKF scheme generally ensures a larger reduction of the error affecting the model predictions at the assimilation steps, the sizeable EnKF-based updates do not guarantee the internal physical consistency of the state of each model realization. By stretching the simulations towards the observations, possible sporadic inconsistencies can occur among the analysis state variables. Indeed, even though the correlations among the state variables are considered within the updating procedure through the model error covariance matrix, its ensemble-based estimate can be affected by the system nonlinearities.
- Conversely, Particle filtering ensures to preserve the physical consistency of the system analysis states thanks to the resampling procedure. Indeed, in this case, the effective filter updates result from the replication of feasible model realizations having the higher

likelihood with respect to the observations. On the other hand, the PF scheme reveals a poorer updating effectiveness, on average, which entails a lower reduction of the error affecting the model simulations.

- These differences in the filters updating result in larger discontinuities affecting the trend of the EnKF-based analysis simulations, while the smoother trend ensured by the PF technique is assumed to be more compliant with the snowpack system physics.
- The filters updating turns out to be generally effective between two following assimilation time steps. Indeed, the temporal persistence of the filters updates mainly depends on the dynamics of the physical evolution of each state variable, rather than on the scale the filters updates themselves.
- With respect to the EnKF-based simulations, Particle filtering better succeeds in more heavily conditioning the model predictions from the assimilation time step onwards. This advantage, mainly resulting from the parameters resampling, makes the PF scheme more suited to forecasting applications. Furthermore, the more physically-based trend of the PF analysis simulations is supposed to support the feasibility of including the PF-based snow module within an operational hydrological chain without introducing possible discontinuities, which are likely to lead to spurious discharge trends.
- The multivariate Kalman filtering is assumed to outperform the PF scheme for real-time analysis of the snowpack status, thanks to its higher effectiveness in updating the system state whenever observations are available.

9.2 Perspectives for future research

9.2.1 Further improvements of the modelling system

Although the snow model proves to generally succeed in catching the snowpack dynamics, several limitations persist due to two main issues. Firstly, the parameterization of the physical processes occurring within the snowpack mostly conditions the temporal evolution of the system state and impacts the accuracy of the model simulations. A case in point is the parameterization of the snow density, which results in underestimated predictions due to a misrepresentation of the snowpack settling process. With the aim of mitigating this issue, the implementation of a multiphysical ensemble-based approach would allow to better take into account the modelling uncertainty by implementing different representations of the main physical processes. Secondly, the system discretization of snowpack is another key issue of critical importance. Even though a finer layering is supposed to make the assimilation of data more challenging and demanding, the introduction of a third snow layer would improve the representation of the vertical snowpack temperature profile and therefore support the solving of the system energy balance. This approach could help in reducing the under-and overestimation of the diurnal and nocturnal peaks of the snow surface temperature.

When implementing a multivariate DA scheme, the generation of a well-representative ensemble of model realizations as well as the proper definition of the several involved sources of uncertainty are of critical importance. The direct perturbation of the state variables should be improved through an extensive study addressing the estimate of the cross-correlations within the covariance matrix used to generate the perturbations of state variables. Even though low perturbations variances are likely to not introduce any significant inconsistency among the prognostic variables, the proper estimate of the cross-correlations would significantly contribute to the physical consistency within the perturbation procedure. The representation of the meteorological uncertainty could be enhanced, in turn, by specifically deriving the site-dependent error statistics from the in-situ observations. Furthermore, the perturbation procedure would require the estimation of the correlations among forcing variables to ensure their physical consistency.

As regards the Particle filtering scheme, the potential of using empirical likelihood variants for a high-dimensional system should be extensively investigated to assess the impact of using a Gaussian distribution.

9.2.2 Development of the spatially-distributed modelling system for operational hydrological applications

In light of the high potential of the multivariate DA snowpack modelling scheme, its spatially-distributed version is currently being developed, which entails the need to address further critical issues. Firstly, the interpolation of the ground-based meteorological observations over complex orography is of key importance to provide the system with consistent forcing data, whose quality strongly impacts the simulations quality. Secondly, when dealing with the distributed system configuration, the proper estimate of the observational error becomes necessarily of even more critical relevance. In this case, the accuracy and reliability of the filter updating deeply depend on the proper definition of the spatialized error covariance matrix of observations.

The 2-D modelling system will be tested and used to assimilate also several satellite products of interest, such as MODIS SCA and snow albedo observations, Sentinel-derived SE maps (see Appendix), snow surface temperature detected by Meteosat, SWE distribution from passive microwave sensors.

The final goal aims at including the spatially-distributed snowpack model within an operational chain for hydrological forecasting in snow-dominated basins. In this application, the modelling system is supposed to provide the hydrological model with spatialized snowmelt maps contributing to the local discharge regime.

References

Albert, M., Koh, G., and Perron, F. (1999). Radar investigations of melt pathways in a natural snowpack. Hydrological processes, 13(18), 2991-3000.

Alvarado-Montero, R., Schwanenberg, D., Krahe, P., Helmke, P., & Klein, B. (2017). Multi-parametric variational data assimilation for hydrological forecasting. *Advances in Water Resources*, *110*, 182-192.

Anderson, E. A. (1976). A point of energy and mass balance model of snow cover. NOAA Tech. Rep. NWS, 19, 1-150.

Andreadis, K. M. and Lettenmaier, D. P. (2006). Assimilating remotely-sensed snow observations into a macroscale hydrology model. Advances in water resources, 29(6), 872-886.

Arslan, A. N., Tanis, C. M., Metsämäki, S., Aurela, M., Böttcher, K., Linkosalmi, M., and Peltoniemi, M. (2017). Automated Webcam Monitoring of Fractional Snow Cover in Northern Boreal Conditions. Geosciences, 7(3), 55.

Arulampalam, M. S., Maskell, S., Gordon, N., and Clapp, T. (2002). A tutorial on particle filters for online nonlinear/non-Gaussian Bayesian tracking. IEEE Transactions on signal processing, 50(2), 174-188.

Baghdadi, N., Gauthier, Y., & Bernier, M. (1997). Capability of multitemporal ERS-1 SAR data for wet-snow mapping. Remote sensing of environment, 60(2), 174-186.

Balsamo, G., Beljaars, A., Scipal, K., Viterbo, P., van den Hurk, B., Hirschi, M., and Betts, A. K. (2009). A revised hydrology for the ECMWF model: Verification from field site to terrestrial water storage and impact in the Integrated Forecast System. Journal of hydrometeorology, 10(3), 623-643.

Balsamo, G., Albergel, C., Beljaars, A., Boussetta, S., Brun, E., Cloke, H., Dee, D., Dutra, E., Muñoz-Sabater, J., Pappenberger, F., de Rosnay, P., Stockdale, T. and Vitart, F. (2015). ERA-Interim/Land: a global land surface reanalysis data set. Hydrology and Earth System Sciences, 19(1), 389-407.

Barnett, T. P., Adam, J. C., and Lettenmaier, D. P. (2005). Potential impacts of a warming climate on water availability in snow-dominated regions. Nature 438, 303e309.

Barrett, A. P. (2003). National operational hydrologic remote sensing center snow data assimilation system (SNODAS) products at NSIDC. National Snow and Ice Data Center, Cooperative Institute for Research in Environmental Sciences.

Bartelt, P., and Lehning, M. (2002). A physical SNOWPACK model for the Swiss avalanche warning: Part I: numerical model. Cold Regions Science and Technology, 35(3), 123-145.

Boni, G., Castelli, F., Gabellani, S., Machiavello, G., Rudari, R. (2010). Assimilation of MODIS snow cover and real-time snow depth point data in a snow dynamic model. In Geoscience and Remote Sensing Symposium (IGARSS), 2010 IEEE International (pp. 1788-1791). IEEE.

Boone, A., and Etchevers, P. (2001). An intercomparison of three snow schemes of varying complexity coupled to the same land surface model: Local-scale evaluation at an Alpine site. Journal of Hydrometeorology, 2(4), 374-394.

Boone, A. (2002). Description du schema de neige ISBA-ES (Explicit Snow). CNRM, Meteo France.

Boone, A., Habets, F., Noilhan, J., Clark, D., Dirmeyer, P., Fox, S., ... and Mahanama, S. (2004). The Rhone-Aggregation land surface scheme intercomparison project: An overview. Journal of Climate, 17(1), 187-208.

Bormann, K. J., Westra, S., Evans, J. P., and McCabe, M. F. (2013). Spatial and temporal variability in seasonal snow density. Journal of hydrology, 484, 63-73.

Bowling, L. C., Lettenmaier, D. P., Nijssen, B., Graham, L. P., Clark, D. B., El Maayar, M., ... and Van Den Hurk, B. (2003). Simulation of high-latitude hydrological processes in the Torne–Kalix basin: PILPS Phase 2 (e): 1: Experiment description and summary intercomparisons. Global and Planetary Change, 38(1), 1-30.

Brasnett, B. (1999). A global analysis of snow depth for numerical weather prediction. Journal of Applied Meteorology 38.6, 726-740.

Brocca, L., Moramarco, T., Melone, F., Wagner, W., Hasenauer, S., Hahn, S. (2012). Assimilation of surface-and root-zone ASCAT soil moisture products into rainfall–runoff modelling. IEEE Transactions on Geoscience and Remote Sensing, 50(7), 2542-2555.

Brodzik, M.J., Armstrong, R.A., Savoie, M. (2007). Global EASE-Grid 8-day Blended SSM/I and MODIS Snow Cover.

Brun, E., Martin, E., Simon, V., Gendre, C., Coleou, C. (1989). An energy and mass model of snow cover suitable for operational avalanche forecasting. Journal of Glaciology, 35(121), 333-342.

Brun, E., David, P., Sudul, M., and Brunot, G. (1992). A numerical model to simulate snow-cover stratigraphy for operational avalanche forecasting. Journal of Glaciology, 38(128), 13-22.

Bryson A. E. and Ho Y. C. (1990). Applied Optimal Control, Hemisphere Publishing Corporation Washington DC, USA.

Burgers, G., Jan van Leeuwen, P., and Evensen, G. (1998). Analysis scheme in the ensemble Kalman filter. Monthly weather review, 126(6), 1719-1724.

Calonne, N., Geindreau, C., Flin, F., Morin, S., Lesaffre, B., Du Roscoat, S. R., and Charrier, P. (2012). 3-D image-based numerical computations of snow permeability: links to specific surface area, density, and microstructural anisotropy. The Cryosphere, 6, 939-951.

Caparrini F., Castelli F., and Entekhabi D. (2004). Estimation of surface turbulent fluxes through assimilation of radiometric surface temperature sequences. Journal of Hydrometeorology 5.1, 145-159.

Carpenter, J., Clifford, P., and Fearnhead, P. (1999). Improved particle filter for nonlinear problems. IEE Proceedings-Radar, Sonar and Navigation, 146(1), 2-7.

Casassa, G., López, P., Pouyaud, B., and Escobar, F. (2009). Detection of changes in glacial run-off in alpine basins: examples from North America, the Alps, central Asia and the Andes. Hydrological Processes, 23(1), 31-41.

Chang, T. C., Gloersen, P., Schmugge, T., Wilheit, T. T., and Zwally, H. J. (1976). Microwave emission from snow and glacier ice. Journal of Glaciology, 16(74), 23-39.

Charrois, L., Cosme, E., Dumont, M., Lafaysse, M., Morin, S., Libois, Q., and Picard, G. (2016). On the assimilation of optical reflectances and snow depth observations into a detailed snowpack model. The Cryosphere, 10, 1021-1038.

Chen, F., Crow, W. T., Starks, P. J., Moriasi, D. N. (2011). Improving hydrologic predictions of a catchment model via assimilation of surface soil moisture. Advances in Water Resources, 34(4), 526-536.

Clark, M. P. and Hay, L. E. (2004). Use of medium-range numerical weather prediction model output to produce forecasts of streamflow. Journal of Hydrometeorology, 5(1), 15-32.

Clark, M. P., Slater, A. G., Barrett, A. P., Hay, L. E., McCabe, G. J., Rajagopalan, B., Leavesley, G. H. (2006). Assimilation of snow covered area information into hydrologic and land-surface models. Advances in water resources, 29(8), 1209-1221.

Cohn, S. E. (1997). An Introduction to Estimation Theory (Special Issue, Data Assimilation in Meteology and Oceanography: Theory and Practice). Journal of the Meteorological Society of Japan. Ser. II, 75(1B), 257-288.

Cortés, G., Girotto, M., and Margulis, S. (2016): Snow process estimation over the extratropical Andes using a data assimilation framework integrating MERRA data and Landsat imagery, Water Resour. Res., 52, 2582–2600, doi:10.1002/2015WR018376.

Cox, P. M., Betts, R. A., Bunton, C. B., Essery, R. L. H., Rowntree, P. R., and Smith, J. (1999). The impact of new land surface physics on the GCM simulation of climate and climate sensitivity. Climate Dynamics, 15(3), 183-203.

Cressman, George P. (1959). An operational objective analysis system. Mon. Wea. Rev 87.10, 367-374.

De Freitas, N., Andrieu, C., Højen-Sørensen, P., Niranjan, M. and Gee, A. (2001). Sequential Monte Carlo methods for neural networks. In Sequential Monte Carlo methods in practice (pp. 359-379). Springer New York.

De Lannoy, G.J.M., Reichle, R.H., Arsenault, K.R., Houser, P.R., Kumar, S., Verhoest, N.E.C., Pauwels, V.R.N. (2012). Multiscale assimilation of Advanced Microwave Scanning Radiometer-EOS snow water equivalent and moderate resolution imaging spectroradiometer snow cover fraction observations in northern Colorado. Water Resour. Res., 48.

Dechant, C. and Moradkhani, H. (2011): Radiance data assimilation for operational snow and streamflow forecasting. Advances in Water Resources, 34(3), 351-364.

Dee, D. P., Uppala, S. M., Simmons, A. J., Berrisford, P. Poli, P., Kobayashi, S., Andrae, U., Balmaseda, M.A., Balsamo, G., Bauer, P., Bechtold, P., Beljaars, A.C.M., van de Berg, L. Bidlot, J., Bormann, N., Delsol, C., Dragani, R., Fuentes, M., Geer, A.J., Haimberger, L., Healy, S.B., Hersbach, H., Hòlm, E.V., Isaksen, L., Kållberg, P., Köhler, M., Matricardi, M., McNally, A.P., Monge-Sanz, B.M., Morcrette, J.-J. , Park, B.-K., Peubey, C., deRosnay, P., Tavolato, C., Thépaut, J.-N., Vitart, F. (2011). The ERA-Interim reanalysis: Configuration and performance of the data assimilation system. Quarterly Journal of the royal meteorological society, 137(656), 553-597.

Derin, Y., Anagnostou, E., Berne, A., Borga, M., Boudevillain, B., Buytaert, W., ... and Lavado-Casimiro, W. (2016). Multiregional satellite precipitation products evaluation over complex terrain. Journal of Hydrometeorology, 17(6), 1817-1836.

Derksen, C., Walker, A.E. (2003). Identification of systematic bias in the cross-platform (SMMR and SMM/I) EASE-Grid brightness temperature time series. IEEE Transactions on Geoscience and Remote Sensing 41(4), 910–915.

Derksen, C., Walker, A.E., Goodison, B.E., Strapp, J.W. (2005). Integrating in situ and multiscale passive microwave data for estimation of subgrid scale snow water equivalent distribution and variability. IEEE Transactions on Geoscience and Remote Sensing 43 (5), 960–972.

Derksen, C. (2008). The contribution of AMSR-E 18.7 and 10.7 GHz measurements to improved boreal forest snow water equivalent retrievals. Remote Sensing of Environment 112, 2701–2710.

Dettinger, M. (2014). Climate change: Impacts in the third dimension. Nature Geoscience, 7(3), 166-167.

DeWalle, D. R., and Rango, A. (2008). Principles of snow hydrology. Cambridge University Press.

Dietz, A., Kuenzer, C., Gessner, U., Dech, S. (2012). Remote sensing of snow – a review of available methods. Int. J. Remote Sens. 33, 4094–4134.

Dong, J., Walker, J. P., Houser, P. R., Sun, C. (2007). Scanning multichannel microwave radiometer snow water equivalent assimilation. Journal of Geophysical Research: Atmospheres, 112(D7).

Douc, R., and Cappé, O. (2005). Comparison of resampling schemes for particle filtering. In Image and Signal Processing and Analysis, 2005. ISPA 2005. Proceedings of the 4th International Symposium on (pp. 64-69). IEEE.

Doucet, A. (1998). On sequential simulation-based methods for Bayesian filtering.

Doucet, A., Godsill, S., and Andrieu, C. (2000). On sequential Monte Carlo sampling methods for Bayesian filtering. Statistics and computing, 10(3), 197-208.

Douville, H., Royer, J. F., and Mahfouf, J. F. (1995). A new snow parameterization for the Meteo-France climate model. Climate Dynamics, 12(1), 21-35.

Dozier, J. (1989). Spectral signature of alpine snow cover from the landsat thematic mapper. Remote Sensing of Environment 28, 9–22.

Dozier, J., Bair, E., Davis, R. (2016). Estimating the spatial distribution of snow water equivalent in the world's mountains. Wiley Interdis. Rev. Water 3, 461–474.

Drusch, M., Vasiljevic, D., and Viterbo, P. (2004). ECMWF's global snow analysis: assessment and revision based on satellite observations, J. Appl. Meteorol., 43, 1282–1294.

Dumont, M., Durand, Y., Arnaud, Y. and Six, D. (2012). Variational assimilation of albedo in a snowpack model and reconstruction of the spatial mass-balance distribution of an alpine glacier. Journal of Glaciology, 58(207), 151-164.

Dunne, S., Entekhabi, D. (2005). An ensemble-based reanalysis approach to land data assimilation. Water resources research, 41(2).

Dunne, S., Entekhabi, D. (2006). Land surface state and flux estimation using the ensemble Kalman smoother during the Southern Great Plains 1997 field experiment. Water resources research, 42(1).

Durand, M., and Margulis, S. A. (2006). Feasibility test of multifrequency radiometric data assimilation to estimate snow water equivalent. Journal of Hydrometeorology, 7(3), 443-457.

Durand, M., Margulis, S.A. (2008). Effects of uncertainty magnitude and accuracy on assimilation of multiscale measurements for snowpack characterization. J. Geophys. Res. Atmos. 113, D02105.

Dutra, E., Balsamo, G., Viterbo, P., Miranda, P. M., Beljaars, A., Schär, C., and Elder, K. (2010). An improved snow scheme for the ECMWF land surface model: description and offline validation. Journal of Hydrometeorology, 11(4), 899-916.

Dutra E, Viterbo P, Miranda PMA, Balsamo G. (2011). Complexity of snow schemes in a climate model and its impact on surface energy and hydrology. Journal of Hydrometeorology.

Endrizzi, S., Gruber, S., Dall'Amico, M., Rigon, R. (2014). GEOtop 2.0: simulating the combined energy and water balance at and below the land surface accounting for soil freezing, snow cover and terrain effects. Geoscientific Model Development, 7, 2831-2857.

Ercolani, G. and Castelli, F. (2017). Variational assimilation of streamflow data in distributed flood forecasting. Water Resources Research, 53(1), 158-183.

Essery, R., Martin, E., Douville, H., Fernandez, A., and Brun, E. (1999). A comparison of four snow models using observations from an alpine site. Climate Dynamics, 15(8), 583-593.

Essery, R., and Etchevers, P. (2004). Parameter sensitivity in simulations of snowmelt. Journal of Geophysical Research: Atmospheres, 109(D20).

Essery, R., Morin, S., Lejeune, Y., and Ménard, C. B. (2013). A comparison of 1701 snow models using observations from an alpine site. Advances in Water Resources, 55, 131-148.

Etchevers, P., Martin, E., Brown, R., Fierz, C., Lejeune, Y., Bazile, E., ... and Gusev, Y. (2004). Validation of the energy budget of an alpine snowpack simulated by several snow models (SnowMIP project). Annals of Glaciology, 38(1), 150-158.

Evensen, G. (1994). Sequential data assimilation with a nonlinear quasi-geostrophic model using Monte Carlo methods to forecast error statistics. Journal of Geophysical Research: Oceans, 99(C5), 10143-10162.

Evensen, G. (2003). The ensemble Kalman filter: Theoretical formulation and practical implementation. Ocean dynamics 53.4, 343-367.

Fayad, A., Gascoin, S., Faour, G., López-Moreno, J. I., Drapeau, L., Le Page, M., and Escadafal, R. (2017). Snow hydrology in Mediterranean mountain regions: a review. Journal of Hydrology.

Feng, X., Sahoo, A., Arsenault, K., Houser, P., Luo, Y., and Troy, T. J. (2008). The impact of snow model complexity at three CLPX sites. Journal of Hydrometeorology, 9(6), 1464-1481.

Fierz, C. R. L. A., Armstrong, R. L., Durand, Y., Etchevers, P., Greene, E., McClung, D. M., ... and Sokratov, S. A. (2009). The international classification for seasonal snow on the ground (Vol. 25). Paris: UNESCO/IHP.

Filippa, G., Cremonese, E., Galvagno, M., Migliavacca, M., Di Cella, U. M., Petey, M., Siniscalco, C., 2015. Five years of phenological monitoring in a mountain grassland: inter-annual patterns and evaluation of the sampling protocol. International journal of biometeorology, 59(12), 1927-1937.

Flanner, M. G., and Zender, C. S. (2006). Linking snowpack microphysics and albedo evolution. Journal of Geophysical Research: Atmospheres, 111(D12).

Forland, E. J., Allerup, P., Dahlström, B., Elomaa, E., Jónsson, T., Madsen, H., ... and Vejen, F. (1996). Manual for operational correction of Nordic precipitation data. DNMI report, 24, 96.

Frei, A., Tedesco, M., Lee, S., Foster, J., Hall, D., Kelly, R., Robinson, D. (2012). A review of global satellite-derived snow products. Adv. Space Res. 50, 1007–1029.

Froidurot, S., Zin, I., Hingray, B., and Gautheron, A. (2014). Sensitivity of precipitation phase over the Swiss Alps to different meteorological variables. Journal of Hydrometeorology, 15(2), 685-696.

Galvagno, M., Wohlfahrt, G., Cremonese, E., Rossini, M., Colombo, R., Filippa, G., Julitta, T., Manca, G., Siniscalco, C., Migliavacca, M., Morra di Cella, U. (2013). Phenology and carbon dioxide source/sink strength of a subalpine grassland in response to an exceptionally short snow season. Environmental Research Letters, 8(2), 025008

Galvagno, M., Wohlfahrt, G., Cremonese, E., Filippa, G., Migliavacca, M., di Cella, U. M. and Van Gorsel, E. (2017). Contribution of advection to nighttime ecosystem respiration at a mountain grassland in complex terrain. Agricultural and Forest Meteorology, 237, 270-281.

Gascoin, S., Lhermitte, S., Kinnard, C., Bortels, K. and Liston, G. E. (2013). Wind effects on snow cover in Pascua-Lama, Dry Andes of Chile. Advances in Water Resources, 55, 25-39.

Gascoin, S., Hagolle, O., Huc, M., Jarlan, L., Dejoux, J.-F., Szczypta, C., Marti, R., Sánchez, R., (2015). A snow cover climatology for the Pyrenees from MODIS snow products. Hydrol. Earth Syst. Sci. 19, 2337–2351.

Gelb, A. (1974). Optimal linear filtering, in Applied Optimal Estimation, edited by A. Gelb, pp. 102– 155, MIT Press, Cambridge, Mass.

Guingla, P., Antonio, D., De Keyser, R., De Lannoy, G., Giustarini, L., Matgen, P. and Pauwels, V. (2012): The importance of parameter resampling for soil moisture data assimilation into hydrologic models using the particle filter. Hydrology and Earth System Sciences, 16(2), 375-390.

Gordon, N. J., Salmond, D. J., and Smith, A. F. (1993). Novel approach to nonlinear/non-Gaussian Bayesian state estimation. In IEE Proceedings F (Radar and Signal Processing) (Vol. 140, No. 2, pp. 107-113). IET Digital Library.

Griessinger, N., Seibert, J., Magnusson, J., Jonas, T. (2016). Assessing the benefit of snow data assimilation for runoff modelling in Alpine catchments. Hydrology and Earth System Sciences, 20(9), 3895.

Grody, N. (2008). Relationship between snow parameters and microwave satellite measurements: theory compared with AMSU observations from 23 to 150 GHz. Journal of Geophysical Research 113, D22108.

Guan, B., Waliser, D. E., Ralph, F. M., Fetzer, E. J., and Neiman, P. J. (2016). Hydrometeorological characteristics of rain-on-snow events associated with atmospheric rivers. Geophysical Research Letters, 43(6), 2964-2973.

Guingla, P., Antonio, D., De Keyser, R., De Lannoy, G., Giustarini, L., Matgen, P., and Pauwels, V. (2012). The importance of parameter resampling for soil moisture data assimilation into hydrologic models using the particle filter. Hydrology and Earth System Sciences, 16(2), 375-390.

Gupta, H. V., H. Kling, K. K. Yilmaz and G. F. Martinez (2009). "Decomposition of the mean squared error and NSE performance criteria: Implications for improving hydrological modelling." Journal of Hydrology 377(1-2): 80-91.

Hall, D.K., Kelly, R.E.J., Foster, J.L., Chang, A.T.C. (2005). Estimation of Snow Extent and Snow Properties, in: Anderson, M.G. (Ed.), Encyclopedia of Hydrological Sciences. Wiley, Berlin, pp. 811–829.

Hall, D.K., Riggs, G.A. (2007). Accuracy assessment of the MODIS snow products. Hydrological Processes 21, 1534–1547.

Harpold, A. A., Guo, Q., Molotch, N., Brooks, P. D., Bales, R., Fernandez-Diaz, J. C., ... and Flanagan, J. (2014). LiDAR-derived snowpack data sets from mixed conifer forests across the Western United States. Water Resources Research, 50(3), 2749-2755.

Hedstrom, N. R., Pomeroy, J. W. (1998). Accumulation of intercepted snow in the boreal forest: measurements and modelling. Hydrological Processes, 12, 1611-1625.

Helfrich, S.R., McNamara, D., Ramsay, B.H., Baldwin, T., Kasheta, T. (2007). Enhancements to and forthcoming developments in the Interactive Multisensor Snow and Ice Mapping System (IMS). Hydrological Processes 21, 1576–1586.

Herrero, J., Polo, M. J., Moñino, A. and Losada, M. A. (2009). An energy balance snowmelt model in a Mediterranean site. Journal of hydrology, 371(1), 98-107.

Higuchi, T. (1997). Monte Carlo filter using the genetic algorithm operators. Journal of Statistical Computation and Simulation, 59(1), 1-23.

Hinkelman, L. M., Lapo, K. E., Cristea, N. C. and Lundquist, J. D. (2015). Using CERES SYN surface irradiance data as forcing for snowmelt simulation in complex terrain. Journal of Hydrometeorology, 16(5), 2133-2152.

Hirashima, H., Yamaguchi, S., Sato, A., and Lehning, M. (2010). Numerical modelling of liquid water movement through layered snow based on new measurements of the water retention curve. Cold Regions Science and Technology, 64(2), 94-103.

Hock, R., Jansson, P., and Braun, L. N. (2005). Modelling the response of mountain glacier discharge to climate warming. In Global Change and Mountain Regions (pp. 243-252). Springer Netherlands.

Holm E. (2003). Lecture notes on assimilation algorithmes. Technical report, European Centre for Medium-Range Weather Forecasts (ECMWF), Meteorological/Training Course Lecture Series.

Huang, C., Newman, A. J., Clark, M. P., Wood, A. W., Zheng, X. (2017). Evaluation of snow data assimilation using the ensemble Kalman filter for seasonal streamflow prediction in the western United States. Hydrology and Earth System Sciences, 21(1), 635.

Hüsler, F., Jonas, T., Riffler, M., and Musial, J. P. (2014). A satellite-based snow cover climatology (1985-2011) for the European Alps derived from AVHRR data. The Cryosphere, 8(1), 73.

Jonas, T., Marty, C., and Magnusson, J. (2009). Estimating the snow water equivalent from snow depth measurements in the Swiss Alps. Journal of Hydrology, 378(1), 161-167.

Jordan, R. (1991). A one-dimensional temperature model for a snow cover: Technical documentation for SNTHERM. 89 (No. CRREL-SR-91-16). Cold Regions Research and Engineering Laboratory, Hanover, NH.

Kalman, R. E. (1960). A new approach to linear filtering and prediction problems. Journal of basic Engineering, 82(1), 35-45.

Kelly, R.E.J., Chang, A.T.C., Foster, J.L., Hall, D.K. (2004). Using remote sensing and spatial models to monitor snow depth and snow water equivalent, in: Kelly, R.E.J., Drake, N.A., Barr, S.L. (Eds.), Spatial Modelling of the Terrestrial Environment. John Wiley and Sons, Ltd., Chichester, England, pp. 5–57.

Kepert, J. D. (2004). On ensemble representation of the observation-error covariance in the Ensemble Kalman Filter. Ocean Dynamics, 54(6), 561-569.

Key, J. R., Mahoney, R., Liu, Y., Romanov, P., Tschudi, M., Appel, I., ... and Meade, P. (2013). Snow and ice products from Suomi NPP VIIRS. Journal of Geophysical Research: Atmospheres, 118(23).

Kitagawa, G. (1996). Monte Carlo filter and smoother for non-Gaussian nonlinear state space models. Journal of computational and graphical statistics, 5(1), 1-25.

Klein, A. G., and Stroeve, J. (2002). Development and validation of a snow albedo algorithm for the MODIS instrument. Annals of Glaciology, 34(1), 45-52.

Klemeš, V. (1986). "Operational testing of hydrological simulation models." Hydrological Sciences Journal/Journal des Sciences Hydrologiques 31(1): 13-24.

Koboltschnig, G. R., and Schöner, W. (2010). The relevance of glacier melt in the water cycle of the Alps: an example from Austria. Hydrology and Earth System Sciences Discussions, 7(3).

Kojima, K. (1967). Densification of seasonal snow cover. Physics of Snow and Ice: proceedings= 雪氷の物理学: 論文集, 1(2), 929-952.

Lafaysse, M., Cluzet, B., Dumont, M., Lejeune, Y., Vionnet, V., and Morin, S. (2017). A multiphysical ensemble system of numerical snow modelling. The Cryosphere, 11(3), 1173.

Langham, E. J. (1981). Physics and properties of snowcover. Pergamon Press: Toronto, Canada.

Lee, H., Seo, D. J., Liu, Y., Koren, V., McKee, P., & Corby, R. (2012). Variational assimilation of streamflow into operational distributed hydrologic models: effect of spatiotemporal scale of adjustment. Hydrology and Earth System Sciences, 16(7), 2233.

Lehning, M., Bartelt, P., Brown, B., Fierz, C., and Satyawali, P. (2002): A physical SNOWPACK model for the Swiss avalanche warning, Part II: snow microstructure, Cold Reg. Sci. Technol., 35, 147-167.

Leisenring, M. and Moradkhani, H. (2011). Snow water equivalent prediction using Bayesian data assimilation methods. Stochastic Environmental Research and Risk Assessment, 25(2), 253-270.

Li, D., Durand, M., Margulis, S. (2012). Potential for hydrologic characterization of deep mountain snowpack via passive microwave remote sensing in the Kern River basin, Sierra Nevada, USA. Remote Sens. Environ. 125, 34–48.

Liston, G. E. and Sturm, M. (1998). A snow-transport model for complex terrain. Journal of Glaciology, 44(148), 498-516.

Liston, G. E., Pielke, R. A., Greene, E. M. (1999). Improving first-order snow-related deficiencies in a regional climate model. Journal of Geophysical Research: Atmospheres, 104(D16), 19559-19567.

Liston, G. E. and Hiemstra, C. A. (2008). A simple data assimilation system for complex snow distributions (SnowAssim). Journal of Hydrometeorology, 9(5), 989-1004.

Liu, J. S. and Chen, R. (1998). Sequential Monte Carlo methods for dynamic systems. Journal of the American statistical association, 93(443), 1032-1044.

Liu, Y., Weerts, A., Clark, M., Hendricks Franssen, H. J., Kumar, S., Moradkhani, H., ... & Van Velzen, N. (2012). Advancing data assimilation in operational hydrologic forecasting: progresses, challenges, and emerging opportunities.

López-Moreno, J. I. and Nogués-Bravo, D. (2005). A generalized additive model for the spatial distribution of snowpack in the Spanish Pyrenees. Hydrological Processes, 19(16), 3167-3176.

López-Moreno, J.I., Fassnacht, S.R., Beguería, S., Latron, J., (2011). Variability of snow depth at the plot scale: implications for mean depth estimation and sampling strategies. Cryosphere 5, 617–629.

López-Moreno, J. I., Fassnacht, S. R., Heath, J. T., Musselman, K. N., Revuelto, J., Latron, J., ... and Jonas, T. (2013a). Small scale spatial variability of snow density and depth over complex alpine terrain: Implications for estimating snow water equivalent. Advances in water resources, 55, 40-52.

López-Moreno, J. I., Vicente-Serrano, S. M., Zabalza, J., Beguería, S., Lorenzo-Lacruz, J., Azorin-Molina, C., and Morán-Tejeda, E. (2013b). Hydrological response to climate variability at different time scales: A study in the Ebro basin. Journal of hydrology, 477, 175-188.

López-Moreno, J. I., Revuelto, J., Fassnacht, S. R., Azorín-Molina, C., Vicente-Serrano, S. M., Morán-Tejeda, E., and Sexstone, G. A. (2015). Snowpack variability across various spatio-temporal resolutions. Hydrological processes, 29(6), 1213-1224.

Louis, J. F. (1979). A parametric model of vertical eddy fluxes in the atmosphere. Boundary-Layer Meteorology, 17(2), 187-202.

Luce, C. H., Lopez-Burgos, V., and Holden, Z. (2014). Sensitivity of snowpack storage to precipitation and temperature using spatial and temporal analog models. Water Resources Research, 50(12), 9447-9462.

Lundquist, J. D., Dickerson-Lange, S. E., Lutz, J. A., and Cristea, N. C. (2013). Lower forest density enhances snow retention in regions with warmer winters: A global framework developed from plot-scale observations and modelling. Water Resources Research, 49(10), 6356-6370.

Lundquist, J., Wayand, N., Massmann, A., Clark, M., Lott, F., Cristea, N. (2015). Diagnosis of insidious data disasters. Water Resour. Res. 51, 3815–3827.

Lynch-Stieglitz, M. (1994). The development and validation of a simple snow model for the GISS GCM. Journal of Climate, 7(12), 1842-1855.

MacKay, D. J. (1992). A practical Bayesian framework for backpropagation networks. Neural computation, 4(3), 448-472.

Magnusson, J., Gustafsson, D., Hüsler, F., and Jonas, T. (2014). Assimilation of point SWE data into a distributed snow cover model comparing two contrasting methods. Water resources research, 50(10), 7816-7835.

Magnusson, J., Winstral, A., Stordal, A. S., Essery, R., and Jonas, T. (2017). Improving physically-based snow simulations by assimilating snow depths using the particle filter. Water Resources Research, 53(2), 1125-1143.

Malik, M. J., van der Velde, R., Vekerdy, Z., Su, Z. (2012). Assimilation of satellite-observed snow albedo in a land surface model. Journal of hydrometeorology, 13(3), 1119-1130.

Margulis, S. A., Girotto, M., Cortés, G., and Durand, M. (2015): A particle batch smoother approach to snow water equivalent estimation. Journal of Hydrometeorology, 16(4), 1752-1772.

Marks, D., Dozier, J., and Davis, R. E. (1992). Climate and energy exchange at the snow surface in the alpine region of the Sierra Nevada: 1. Meteorological measurements and monitoring. Water Resources Research, 28(11), 3029-3042.

Markus, T., Powell, D.C., Wang, J.R. (2006). Sensitivity of passive microwave snow depth retrievals to weather effects and snow evolution. IEEE Transactions on Geoscience and Remote Sensing 44 (1), 68–77.

Marshall SE, Warren SG. (1987): Parameterization of snow albedo for climate models. In: Goodison BE, Barry RG, Dozier J, editors. Large scale effects of seasonal snow cover. IAHS Publications; p. 166.

Marshall, S., and Oglesby, R. J. (1994). An improved snow hydrology for GCMs. Part 1: Snow cover fraction, albedo, grain size, and age. Climate Dynamics, 10(1), 21-37.

Matzler, C. (1994). Passive microwave signatures of landscapes in winter. Meteorological and Atmospheric Physics 54, 241–260.

Mazurkiewicz, A. B., Callery, D. G., and McDonnell, J. J. (2008). Assessing the controls of the snow energy balance and water available for runoff in a rain-on-snow environment. Journal of Hydrology, 354(1), 1-14.

Mellor, M., 1964. Properties of snow, Cold Reg. Sci. Eng. Monogr., III-A1.

Miller, R. N., Ghil, M., Gauthiez, F. (1994). Advanced data assimilation in strongly nonlinear dynamical systems. Journal of the atmospheric sciences, 51(8), 1037-1056.

Mitterer, C., Heilig, A., Schweizer, J., and Eisen, O. (2011). Upward-looking ground-penetrating radar for measuring wet-snow properties. Cold Regions Science and Technology, 69(2), 129-138.

Mizukami, N., and Perica, S. (2008). Spatiotemporal characteristics of snowpack density in the mountainous regions of the western United States. Journal of Hydrometeorology, 9(6), 1416-1426.

Molotch, N. P., Colee, M. T., Bales, R. C., and Dozier, J. (2005). Estimating the spatial distribution of snow water equivalent in an alpine basin using binary regression tree models: the impact of digital elevation data and independent variable selection. Hydrological Processes, 19(7), 1459-1479.

Molotch, N. P. (2009). Reconstructing snow water equivalent in the Rio Grande headwaters using remotely-sensed snow cover data and a spatially distributed snowmelt model. Hydrological Processes, 23(7), 1076-1089.

Molotch, N. P., and Meromy, L. (2014). Physiographic and climatic controls on snow cover persistence in the Sierra Nevada Mountains. Hydrological processes, 28(16), 4573-4586.

Montzka, C., Pauwels, V., Franssen, H. J. H., Han, X., Vereecken, H. (2012). Multivariate and multiscale data assimilation in terrestrial systems: A review. Sensors, 12(12), 16291-16333.

Moradkhani, H., Sorooshian, S., Gupta, H. V., and Houser, P. R. (2005a). Dual state–parameter estimation of hydrological models using ensemble Kalman filter. Advances in water resources, 28(2), 135-147.

Moradkhani, H., Hsu, K. L., Gupta, H., and Sorooshian, S. (2005b). Uncertainty assessment of hydrologic model states and parameters: Sequential data assimilation using the particle filter. Water resources research, 41(5).

Moradkhani, H. (2008). Hydrologic remote sensing and land surface data assimilation. Sensors, 8(5), 2986-3004.

Morin, S., Lejeune, Y., Lesaffre, B., Panel, J. M., Poncet, D., David, P., and Sudul, M. (2012). An 18-yr long (1993-2011) snow and meteorological dataset from a mid-altitude mountain site (Col de Porte, France, 1325 m alt.) for driving and evaluating snowpack models. Earth System Science Data, 4(1), 13.

Musso, C., Oudjane, N., and Le Gland, F. (2001). Improving regularised particle filters. In Sequential Monte Carlo methods in practice (pp. 247-271). Springer New York.

Nagler, T. and Rott, H. (2000). Retrieval of wet snow by means of multitemporal SAR data. IEEE Transactions on Geoscience and Remote Sensing, 38(2), 754-765.

Nagler, T., Rott, H., Ripper, E., Bippus, G. and Hetzenecker, M. (2016). Advancements for snowmelt monitoring by means of sentinel-1 SAR. Remote Sensing, 8(4), 348.

Nijssen, B., Bowling, L. C., Lettenmaier, D. P., Clark, D. B., El Maayar, M., Essery, R., ... and Jin, J. (2003). Simulation of high latitude hydrological processes in the Torne–Kalix basin: PILPS Phase 2 (e): 2: Comparison of model results with observations. Global and Planetary Change, 38(1), 31-53.

Nolin, A.W. (2004). Towards retrieval of forest cover density over snow from the Multi-angle Imaging SpectroRadiometer (MISR). Hydrological Processes 18, 3623–3636.

Nolin, A.W. Recent advances in remote sensing of seasonal snow (2010). Journal of Glaciology 56 (200), 1141–1150.

Oleson KW, et al. Technical description of the Community Land Model (CLM) (2004). NCAR Technical Note NCAR/TN-461+STR; National Center for Atmospheric Research, Boulder, CO.

Oleson, K. W., Lawrence, D. M., Gordon, B., Flanner, M. G., Kluzek, E., Peter, J., ... and Heald, C. L. (2010). Technical description of version 4.0 of the Community Land Model (CLM).

Pan, M., Sheffield, J., Wood, E. F., Mitchell, K. E., Houser, P. R., Schaake, J. C., Robock, A., Lohmann, D., Cosgrove, B., Duan, Q., Luo, L., Higgins, R.W., Pinker, R.T., Tarpley, J.D.

(2003). Snow process modelling in the North American Land Data Assimilation System (NLDAS): 2. Evaluation of model simulated snow water equivalent. Journal of Geophysical Research: Atmospheres, 108(D22).

Piazzi, G., Campo, L., Gabellani, S., Castelli, F., Cremonese, E., Morra di Cella, U., Stevenin, H., Ratto, S. M. (2018a): An EnKF-based scheme for snow multivariate data assimilation at an Alpine site.J. Hydrol. Hydromech (Accepted).

Piazzi, G., Thirel, G., Campo, L., and Gabellani, S. (2018b): A Particle Filter scheme for multivariate data assimilation into a point-scale snowpack model in Alpine environment, The Cryosphere Discuss., https://doi.org/10.5194/tc-2017-286, in review.

Pitt, M. K., and Shephard, N. (1999). Filtering via simulation: Auxiliary particle filters. Journal of the American statistical association, 94(446), 590-599.

Pulliainen, J. (2006). Mapping of snow water equivalent and snow depth in boreal and sub-Arctic zones by assimilating space-borne microwave radiometer data and ground-based observations. Remote Sensing of Environment 101 (2), 257–269.

Pulliainen, J. (2010). Overview on GlobSnow Project: key questions to be resolved (coverage, aggregation, validation, towards a future ECV), in: The 1st ESA DUE GlobSnow User Workshop, Innsbruck, Austria.

Quéno, L., Vionnet, V., Dombrowski-Etchevers, I., Lafaysse, M., Dumont, M., and Karbou, F. (2016). Snowpack modelling in the Pyrenees driven by kilometric-resolution meteorological forecasts. The Cryosphere, 10(4), 1571-1589.

Raleigh, M. S., Lundquist, J. D., and Clark, M. P. (2015). Exploring the impact of forcing error characteristics on physically-based snow simulations within a global sensitivity analysis framework. Hydrology and Earth System Sciences, 19(7), 3153-3179.

Raleigh, M., Livneh, B., Lapo, K., Lundquist, J., (2016). How does availability of meteorological forcing data impact physically-based snowpack simulations? J. Hydrometeorol. 17, 99–120.

Reichle, R. H., McLaughlin, D. B., and Entekhabi, D. (2002a). Hydrologic data assimilation with the ensemble Kalman filter. Monthly Weather Review, 130(1), 103-114.

Reichle, R. H., Walker, J. P., Koster, R. D., and Houser, P. R. (2002b). Extended versus ensemble Kalman filtering for land data assimilation. Journal of hydrometeorology, 3(6), 728-740.

Reichle, R. H., R. Koster, P. Liu, S. P. P. Mahanama, E. G. Njoku, and M. Owe (2007), Comparison and assimilation of global soil moisture retrievals from the Advanced Microwave Scanning Radiometer for the Earth Observing System (AMSR-E) and the Scanning Multichannel Microwave Radiometer (SMMR), J. Geophys. Res., 112, D09108, doi:10.1029/2006JD008033.

Reichle, R. H. (2008). Data assimilation methods in the Earth sciences. Advances in water resources, 31(11), 1411-1418.

Revuelto, J., López-Moreno, J. I., Azorin-Molina, C., and Vicente-Serrano, S. M. (2014). Topographic control of snowpack distribution in a small catchment in the central Spanish Pyrenees: intra-and inter-annual persistence. The Cryosphere, 8(5), 1989-2006.

Rice, R., Bales, R. C., Painter, T. H., and Dozier, J. (2011). Snow water equivalent along elevation gradients in the Merced and Tuolumne River basins of the Sierra Nevada. Water Resources Research, 47(8).

Riggs, G.A., Hall, D.K., Salomonson, V.V. (2006). “MODIS Snow Products Users’ Guide”.

Rigon, R., Bertoldi, G., and Over, T. M. (2006). GEOtop: A distributed hydrological model with coupled water and energy budgets. Journal of Hydrometeorology, 7(3), 371-388.

Robinson, D., Kukla, G. (1985). Maximum surface albedo of seasonally snow covered lands in the Northern Hemisphere. Journal of Climate and Applied Meteorology 24, 402–411.

Rodell, M. and Houser, P. R. (2004). Updating a land surface model with MODIS-derived snow cover. Journal of Hydrometeorology, 5(6), 1064-1075.

Rubin, D. B. (1988). Using the SIR algorithm to simulate posterior distributions. Bayesian statistics, 3, 395-402.

Rutter, N., Essery, R., Pomeroy, J., Altimir, N., Andreadis, K., Baker, I., ... and Douville, H. (2009). Evaluation of forest snow processes models (SnowMIP2). Journal of Geophysical Research: Atmospheres, 114(D6).

Salamon, P., and Feyen, L. (2009). Assessing parameter, precipitation, and predictive uncertainty in a distributed hydrological model using sequential data assimilation with the particle filter. Journal of Hydrology, 376(3), 428-442.

Salomonson, V. V., and Appel, I. (2004). Estimating fractional snow cover from MODIS using the normalized difference snow index. Remote sensing of environment, 89(3), 351-360.

Scherer, D., Hall, D.K., Hochschild, V., Konig, M., Winther, J.-G., Duguay, C.R., Pivot, F., Matzler, C., Rau, F., Seidel, K., Solberg, R., Walker, A.E. (2005). Remote Sensing of Snow. Remote Sensing in Northern Hydrology: Measuring Environmental Change, C. R. a. P. Duguay, Alain, Washington, DC. American Geophysical Union, p. 163.

Schlosser, C. A., Slater, A. G., Robock, A., Pitman, A. J., Vinnikov, K. Y., Henderson-Sellers, A., ... and Mitchell, K. (2000). Simulations of a boreal grassland hydrology at Valdai, Russia: PILPS Phase 2 (d). Monthly Weather Review, 128(2), 301-321.

Schmid, L., Heilig, A., Mitterer, C., Schweizer, J., Maurer, H., Okorn, R., and Eisen, O. (2014). Continuous snowpack monitoring using upward-looking ground-penetrating radar technology. Journal of Glaciology, 60(221), 509-525.

Schmucki, E., Marty, C., Fierz, C., and Lehning, M. (2014). Evaluation of modelled snow depth and snow water equivalent at three contrasting sites in Switzerland using SNOWPACK simulations driven by different meteorological data input. Cold Regions Science and Technology, 99, 27-37.

Schmugge, T.J., Kustas, W.P., Ritchie, J.C., Jackson, T.J., Rango, A. (2002). Remote sensing in hydrology. Advances in Water Resources 25, 1367– 1385.

Seo, D. J., Koren, V., and Cajina, N. (2003). Real-time variational assimilation of hydrologic and hydrometeorological data into operational hydrologic forecasting. Journal of Hydrometeorology, 4(3), 627-641.

Seo, D. J., Cajina, L., Corby, R., and Howieson, T. (2009). Automatic state updating for operational streamflow forecasting via variational data assimilation. Journal of hydrology, 367(3-4), 255-275.

Sevruk, B., Hertig, J. A., and Spiess, R. (1991). The effect of a precipitation gauge orifice rim on the wind field deformation as investigated in a wind tunnel. Atmospheric Environment. Part A. General Topics, 25(7), 1173-1179.

Shi, J., Xiong, C. and Jiang, L. (2016). Review of snow water equivalent microwave remote sensing. Science China Earth Sciences, 59(4), 731-745.

Slater, A. G., Pitman, A. J., and Desborough, C. E. (1998). The validation of a snow parameterization designed for use in general circulation models. International journal of climatology, 18(6), 595-617.

Slater, A. G., Schlosser, C. A., Desborough, C. E., Pitman, A. J., Henderson-Sellers, A., Robock, A., ... and Boone, A. (2001). The representation of snow in land surface schemes: Results from PILPS 2 (d). Journal of Hydrometeorology, 2(1), 7-25.

Slater, A. G. and Clark, M. P. (2006). Snow data assimilation via an ensemble Kalman filter. Journal of Hydrometeorology, 7(3), 478-493.

Smirnova, T. G., Brown, J. M., Benjamin, S. G., and Kim, D. (2000). Parameterization of cold-season processes in the maps land-surface scheme. Journal of Geophysical Research: Atmospheres, 105(D3), 4077-4086.

Smith, A. F. and Gelfand, A. E. (1992). Bayesian statistics without tears: a sampling–resampling perspective. The American Statistician, 46(2), 84-88.

Stauffer, D. R. and Seaman, N. L. (1990). Use of four-dimensional data assimilation in a limited-area mesoscale model. Part I: Experiments with synoptic-scale data. Monthly Weather Review, 118(6), 1250-1277.

Stigter, E. E., Wanders, N., Saloranta, T. M., Shea, J. M., Bierkens, M. F. P. and Immerzeel, W. W. (2017): Assimilation of snow cover and snow depth into a snow model to estimate snow water equivalent and snowmelt runoff in a Himalayan catchment, Cryosph., 1647–1664.

Stössel, F., Guala, M., Fierz, C., Manes, C., and Lehning, M. (2010). Micrometeorological and morphological observations of surface hoar dynamics on a mountain snow cover. Water Resources Research, 46(4).

Sturm, M., Holmgren, J., and Liston, G. E. (1995). A seasonal snow cover classification system for local to global applications. Journal of Climate, 8(5), 1261-1283.

Sturm, M., Taras, B., Liston, G. E., Derksen, C., Jonas, T., and Lea, J. (2010). Estimating snow water equivalent using snow depth data and climate classes. Journal of Hydrometeorology, 11(6), 1380-1394.

Su, H., Yang, Z. L., Niu, G. Y., Dickinson, R. E., 2008. Enhancing the estimation of continental-scale snow water equivalent by assimilating MODIS snow cover with the ensemble Kalman filter. Journal of Geophysical Research: Atmospheres, 113(D8).

Sun, S., Jin, J., and Xue, Y. (1999). A simple snow-atmosphere-soil transfer model. Journal of Geophysical Research: Atmospheres, 104(D16), 19587-19597.

Sun, C., Walker, J. P., Houser, P. R. (2004). A methodology for snow data assimilation in a land surface model. Journal of Geophysical Research: Atmospheres, 109(D8).

Surfleet, C. G., and Tullos, D. (2013). Variability in effect of climate change on rain-on-snow peak flow events in a temperate climate. Journal of hydrology, 479, 24-34.

Svoma, B. M. (2011). Winter climatic controls on spring snowpack density in the Western United States. Arctic, Antarctic, and Alpine Research, 43(1), 118-126.

Szczypta, C., Gascoin, S., Houet, T., Hagolle, O., Dejoux, J. F., Vigneau, C., and Fanise, P. (2015). Impact of climate and land cover changes on snow cover in a small Pyrenean catchment. Journal of Hydrology, 521, 84-99.

Tedesco, M., Kim, E.J., Gasiewski, A., Stankov, B. (2005). Analysis of multi-scale radiometric data collected during the Cold Land Processes Experiment-1 (CLPX-1). Geophysical Research Letters 32 (L18501), 4.

Tedesco, M., Kim, E.J. (2006). Inter-comparison of electromagnetic models for passive microwave remote sensing of snow. IEEE TGARS Special Issue 'IGARSS 2005' 44 (10), 2654–2666.

Thirel, G., Salamon, P., Burek, P., and Kalas, M. (2013): Assimilation of MODIS snow cover area data in a distributed hydrological model using the particle filter. Remote Sensing, 5(11), 5825-5850.

Tippett, M. K., Anderson, J. L., Bishop, C. H., Hamill, T. M., and Whitaker, J. S. (2003). Ensemble square root filters. Monthly Weather Review, 131(7), 1485-1490.

Torres, R., Snoeij, P., Geudtner, D., Bibby, D., Davidson, M., Attema, E., Potin, P., Rommen, B., Floury, N., Brown, M. et al. (2012). GMES Sentinel-1 mission. Remote Sens. Environ., 120, 9–24.

Van den Hurk, B. J. J. M., Viterbo, P., Beljaars, A. C. M., and Betts, A. K. (2000). Offline validation of the ERA40 surface scheme. ECMWF Tech. Mem, 295, 42.

Verbunt, M., Gurtz, J., Jasper, K., Lang, H., Warmerdam, P., and Zappa, M. (2003). The hydrological role of snow and glaciers in alpine river basins and their distributed modelling. Journal of hydrology, 282(1), 36-55.

Verseghy, D. L. (1991). CLASS—A Canadian land surface scheme for GCMs. I. Soil model. International Journal of Climatology, 11(2), 111-133.

Vidal, J. P., Martin, E., Franchistéguy, L., Baillon, M., and Soubeyroux, J. M. (2010). A 50-year high-resolution atmospheric reanalysis over France with the Safran system. International Journal of Climatology, 30(11), 1627-1644.

Vionnet, V., Brun, E., Morin, S., Boone, A., Faroux, S., Le Moigne, P., ... and Willemet, J. M. (2012). The detailed snowpack scheme Crocus and its implementation in SURFEX v7. 2. Geoscientific Model Development, 5, 773-791.

Vionnet, V., Martin, E., Masson, V., Guyomarc'h, G., Bouvet, F. N., Prokop, A., ... and Lac, C. (2014). Simulation of wind-induced snow transport and sublimation in alpine terrain using a fully coupled snowpack/atmosphere model. The Cryosphere, 8, p-395.

Viterbo, P., and Beljaars, A. C. (1995). An improved land surface parameterization scheme in the ECMWF model and its validation. Journal of Climate, 8(11), 2716-2748.

Viviroli, D., Weingartner, R., and Messerli, B. (2003). Assessing the hydrological significance of the world's mountains. Mountain research and Development, 23(1), 32-40.

Viviroli, D., and Weingartner, R. (2004). The hydrological significance of mountains: from regional to global scale. Hydrology and Earth System Sciences Discussions, 8(6), 1017-1030.

Viviroli, D., Dürr, H. H., Messerli, B., Meybeck, M., and Weingartner, R. (2007). Mountains of the world, water towers for humanity: Typology, mapping, and global significance. Water resources research, 43(7).

Viviroli, D., Archer, D. R., Buytaert, W., Fowler, H. J., Greenwood, G., Hamlet, A. F., ... and Lorentz, S. (2011). Climate change and mountain water resources: overview and recommendations for research, management and policy. Hydrology and Earth System Sciences, 15(2), 471-504.

Vuyovich, C., Jacobs, J., Daly, S. (2014). Comparison of passive microwave and modelled estimates of total watershed SWE in the continental United States. Water Resour. Res. 50, 9088–9102.

Wächter, A., and Biegler, L. T. (2006). On the implementation of an interior-point filter line-search algorithm for large-scale nonlinear programming. Mathematical programming, 106(1), 25-57.

Walker, J. P., Houser, P. R., and Reichle, R. H. (2003). New technologies require advances in hydrologic data assimilation. EOS, Transactions American Geophysical Union, 84(49), 545-551.

Weerts, A. H. and El Serafy, G. Y. (2006). Particle filtering and ensemble Kalman filtering for state updating with hydrological conceptual rainfall-runoff models. Water Resources Research, 42(9).

Weingartner, R., and Aschwanden, H. (1992). Discharge regime–the basis for the estimation of average flows. Hydrological Atlas of Switzerland, Plate, 5, 26.

Wever, N., Fierz, C., Mitterer, C., Hirashima, H., & Lehning, M. (2014). Solving Richards Equation for snow improves snowpack meltwater runoff estimations in detailed multi-layer snowpack model. The Cryosphere, 8(1), 257-274.

Wever, N., Schmid, L., Heilig, A., Eisen, O., Fierz, C., and Lehning, M. (2015). Verification of the multi-layer SNOWPACK model with different water transport schemes. The Cryosphere, 9(6), 2271-2293.

Whitaker, J. S., and T. M. Hamill (2002): Ensemble data assimilation without perturbed observations. Mon. Wea. Rev., submitted.

Winstral, A. and Marks, D. (2014). Long-term snow distribution observations in a mountain catchment: Assessing variability, time stability, and the representativeness of an index site. Water Resources Research, 50(1), 293-305

Wiscombe, W. J., and Warren, S. G. (1980). A model for the spectral albedo of snow. I: Pure snow. Journal of the Atmospheric Sciences, 37(12), 2712-2733.

Wood, A. W., Hopson, T., Newman, A., Brekke, L., Arnold, J., Clark, M. (2016). Quantifying streamflow forecast skill elasticity to initial condition and climate prediction skill. Journal of Hydrometeorology, 17(2), 651-668.

WSL Institute for Snow and Avalanche Research SLF (2015a): Biweekly manual snow profiles from Weissfluhjoch, Davos, Switzerland, Dataset, doi:10.16904/2.

WSL Institute for Snow and Avalanche Research SLF (2015b): Meteorological and snowpack measurements from Weissfluhjoch, Davos, Switzerland, Dataset, doi:10.16904/1.

Würzer, S., Jonas, T., Wever, N., and Lehning, M. (2016). Influence of initial snowpack properties on runoff formation during rain-on-snow events. Journal of Hydrometeorology, 17(6), 1801-1815.

Yang, Z. L., Dickinson, R. E., Robock, A., Vinnikov, K. Y. (1997). Validation of the snow submodel of the biosphere–atmosphere transfer scheme with Russian snow cover and meteorological observational data. Journal of Climate, 10(2), 353-373.

Yen, Y. C. (1981). Review of thermal properties of snow, ice and sea ice (No. CRREL-81-10). Cold Regions Research and Engineering Laboratory, Hanover, NH.

Zanotti, F., Endrizzi, S., Bertoldi, G., and Rigon, R. (2004). The GEOTOP snow module. Hydrological Processes, 18(18), 3667-3679.

Zappa, M., Pos, F., Strasser, U., Warmerdam, P., and Gurtz, J. (2003). Seasonal water balance of an Alpine catchment as evaluated by different methods for spatially distributed snowmelt modelling. Hydrology Research, 34(3), 179-202.

Zappa, M., and Kan, C. (2007). Extreme heat and runoff extremes in the Swiss Alps. Natural Hazards and Earth System Science, 7(3), 375-389.

Zhang, T. (2005). Influence of the seasonal snow cover on the ground thermal regime: An overview. Reviews of Geophysics, 43(4).

Zheng, Z., Kirchner, P. B., and Bales, R. C. (2016). Topographic and vegetation effects on snow accumulation in the southern Sierra Nevada: a statistical summary from lidar data. The Cryosphere, 10(1), 257-269.

Appendix

Comparative study of satellite snow products

Alongside the PhD research activities, a comparative study of satellite snow products has been carried out in the framework of the EUMETSAT Satellite Application Facility on support to Operational Hydrology and Water Management (H-SAF). This study aims at investigating the accuracy and reliability of H-SAF snow products H10 – Snow detection and H12 – Effective snow cover by VIS/IR radiometry by assessing their consistency with the high-resolution Sentinel-2A imagery.

Besides the interest of this survey within the H-SAF project, the analysis of remotely-sensed snow observations is of further crucial importance in view of the development of the spatially distributed snow modelling system, which is assumed to assimilate satellite snow products.

After describing the methodology used for the analysis of H-SAF H10 and H12 snow products, three case studies are described and discussed for both the H-SAF products.

A.1. Methodology

To properly compare and assess the satellite snow products, the following steps have to be taken:

1. Pre-processing of Sentinel-2 data;
2. Consistency check of satellite series over the area of interest;
3. Comparison analysis between H-SAF H10 and Sentinel-2 data series;
4. Comparison analysis between H-SAF H12 and Sentinel-2 data series.

A.1.1. Pre-processing of Sentinel-2 data

Sentinel-2 Level-1C (L1C) Top-of-Atmosphere (TOA) image data have been acquired from the Copernicus Open Access Hub (https://scihub.copernicus.eu/dhus). Once identified the region of interest, the tiles of the Level-1C product are downloaded (100x100 km2ortho-images, UTM/WGS84 projection, 500 MB). Each tile is pre-processed through the ESA Sentinel-2 Level-2A Prototype Processor, Sen2Cor (http://step.esa.int/main/third-party-plugins-2/sen2cor/), whose Scene Classification Module (L2A_SceneClass) provides a Scene Classification (SCL) map at a spatial resolution of 20m (JPEG-2000 image).

A.1.2. Consistency check of satellite series over the area of interest

First of all, the availability of the satellite products for all days of the analysis period has been checked. Moreover, a quality check of the satellite data series has been performed with the aim of preventing any possible inconsistency. Because the survey focuses on the detection of snow cover, cloud free scenes or scenes with minor cloud cover have been primarily selected (Nagler et al., 2014).

To properly perform the comparison analysis, it is important to guarantee that the satellite products have the same common image projection. Once assured a common projection, it was necessary to select both the original satellite products over the same area of interest. Since the analysis is tile-based, a H-SAF H10 maps over the geographic extension of the selected Sentinel-2 tile have been extracted from the original full H-SAF product. The selection of the data subset limited over the domain of interest has been carried out by considering the local coordinates of the tile borders, in order to guarantee the intersection of the satellite products over the Sentinel tile.

A.1.3. Comparison analysis between H-SAF H10 and Sentinel-2 data series

With the aim of using a common classification code, binary snow masks (presence/absence of snow cover) have been generated by selecting “soil” and “snow” pixels, as classified within the original satellite products, respectively (Table A.1). Moreover, to prevent possible cloud cover affecting the snow detection, cloud-contaminated pixels have been flagged and neglected within the comparison of snow maps (Crawford, 2015).

SATELLITE PRODUCT	SOIL CLASS	SNOW CLASS
H-SAF	85	0
Sentinel	5	11
Binary map	**0**	**1**

Table A.1: *Classification of “soil” and “snow” pixels.*

Because H-SAF H10 and Sentinel-2 data are differently gridded, a common map grid has been introduced. Since the comparison has been performed at the coarser spatial resolution of the H-SAF product (5 km) (Salomonson and Appel, 2004), Sentinel 20m- images have been re-aggregated at 5-km resolution.

For each 5-km grid cell, the percentage of snow cover has been determined on the basis of the Sentinel observations by counting the number of 20-m pixels covered by snow versus the total number of 20-m pixels in the coarser cell (Salomonson and Appel, 2004). This computation has led to Sentinel-based maps of FSC.

To restore binary snowy/snowless maps, each resulting Sentinel 5-km pixel has been then classified as “snow” if at least 50% of the Sentinel 20-m pixels within the coarser pixel was detected as snow cover; otherwise, the 5-km pixel has been classified as “soil” (Rittger et al., 2013; Crawford, 2015).

Sentinel-based 5-km pixels where more than the 50% of the Sentinel 20-m have been classified as “cloud” and thus neglected in order to not compromise the analysis results. Then, for each selected tile a pixel-to-pixel analysis has been performed with the aim of assessing the agreement between the analysed snow cover maps. Thus, a contingency table (Table A.2) has been evaluated:

i. HITS counter is increased if both satellite pixels values are equal to 1 (matched classification as “snow”);
ii. MISSES counter is increased if H12-pixel is equal to 0 (classified as “soil”) and Sentinel-pixel is equal to 1 (classified as “snow”);
iii. FALSE ALARMS counter is increased if H12-pixel is equal to 1 (classified as “snow”) and Sentinel-pixel is equal to 0 (classified as “soil”);
iv. CORRECT NEGATIVES counter is increased if both satellite pixels values are equal to 0 (matched classification as “soil”).

		Sentinel		
		Snow pixel = 1	**Soil pixel = 0**	
H10	**Snow pixel = 1**	**HITS**	**FALSE ALARMS**	HITS + FALSE ALARMS
	Soil pixel = 0	**MISSES**	**CORRECT NEGATIVES**	MISSES+ CORRECT NEGATIVES
		HITS + MISSES	FALSE ALARMS + CORRECT NEGATIVES	

Table A.2: *Contingency table.*

From these classification results, different scores for dichotomous statistics have been calculated. To simplify the formulae, the following notation can be considered:

- A = number of HITS
- B = number of FALSE ALARMS
- C = number of MISSES
- D = number of CORRECT NEGATIVES

Probability of detection

$$POD = \frac{A}{A+C} \qquad [A.1]$$

False alarm ratio

$$FAR = \frac{B}{A+B} \qquad [A.2]$$

Probability of false detection

$$POFD = \frac{B}{B+D} \qquad [A.3]$$

Accuracy

$$ACC = \frac{A+D}{A+B+C+D} \qquad [A.4]$$

Critical success index

$$CSI = \frac{A}{A+B+C} \qquad [A.5]$$

Heidke skill score

$$HSS = \frac{2 \cdot \ (AD - BC)}{[(A+C)\cdot(C+D)] + [(A+B)\cdot(B+D)]} \qquad [A.6]$$

A.1.4. Comparison analysis between H-SAF H12 and Sentinel-2 data series

Also in this case, a Sentinel-based binary snow mask has generated by selecting “soil” and “snow” pixels, as classified within the original satellite product (Table A.1) and cloud-contaminated pixels have been flagged and neglected.

Since the comparison has been performed at the coarser spatial resolution of the H-SAF product (2 km) (Salomonson and Appel, 2004), Sentinel 20m- images have been resampled to 2-km resolution.

For each 2-km grid cell, the percentage of snow cover has been determined on the basis of the Sentinel observations by counting the number of 20-m pixels covered by snow versus the total number of 20-m pixels in the coarser cell (Salomonson and Appel, 2004). This evaluation has led to Sentinel-based FSC maps. Each pixel of both satellite products has been assigned into a discrete 10% FSC-class covering 0-100%, with a total of 10 individual classes.

Consistently with the previous analysis, Sentinel-based 2-km pixels where more than the 50% of the Sentinel 20-m have been classified as “cloud” and thus neglected.

Then, for each selected tile a pixel-to-pixel analysis has been performed with the aim of assessing the agreement between the two satellite products.

The following statistical indices have been computed:

$$Bias = \frac{1}{N}\sum(FSC_{H12} - FSC_{S2A}) \tag{A.7}$$

$$RMSE = \sqrt{\frac{1}{N}\sum(FSC_{H12} - FSC_{S2A})^2} \tag{A.8}$$

A.2. Case studies

The methodology has been tested in three case studies over snow-dominated areas with the aim of investigating the consistency between both the H-SAF snow products and the Sentinel-2 high-resolution imagery over selected target regions: Aosta Valley (Italy) (Figure A.1), Pyrenees Mountains (Figure A.2), and Caucasus Mountains (Figure A.3).

For each target area, representative Sentinel tiles have been selected (Table A.3). The selection of tiles has targeted those both covering sizeable portions of the areas of interest and providing significant datasets over the analysis period, starting from December 2016 until the end of March 2017 (4 months).

Target area	**Selected tiles**	
	Tiles amount	**Tiles ID**
Aosta Valley	1	32TLR
Pyrenees	2	30TYN 31TCH
Caucasus	9	37TFJ 37TGH 37TGJ 38TLN 38TMN 38TNM 38TNN 38TPM 38TQL

Table A.3: *Selected tiles over the target areas.*

For each case study, a dataset has been built up by collecting all the available imagery of the selected tiles over the whole period.

Figure A.1: *Highlighted Sentinel tile 32TLR over the Aosta Valley.*

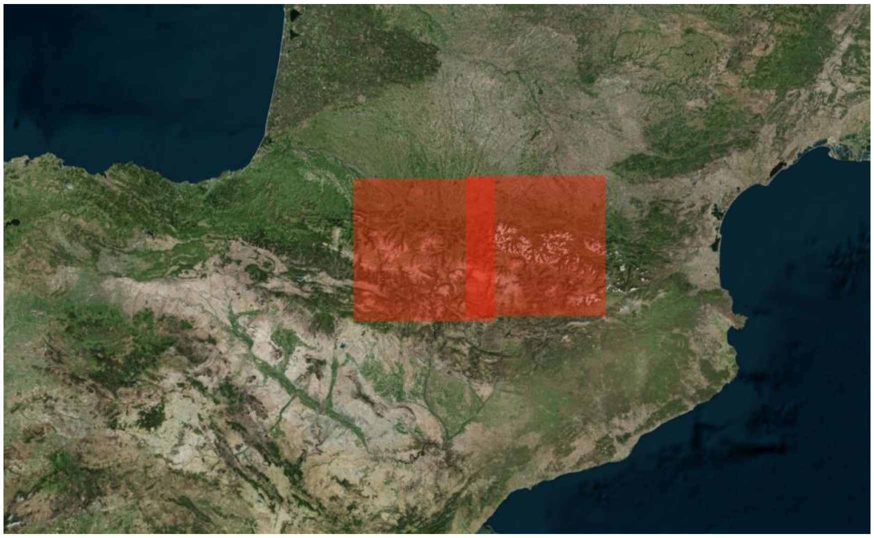

Figure A.2: *Highlighted Sentinel tiles 30TYN and 31TCH over the Pyrenees Mountains.*

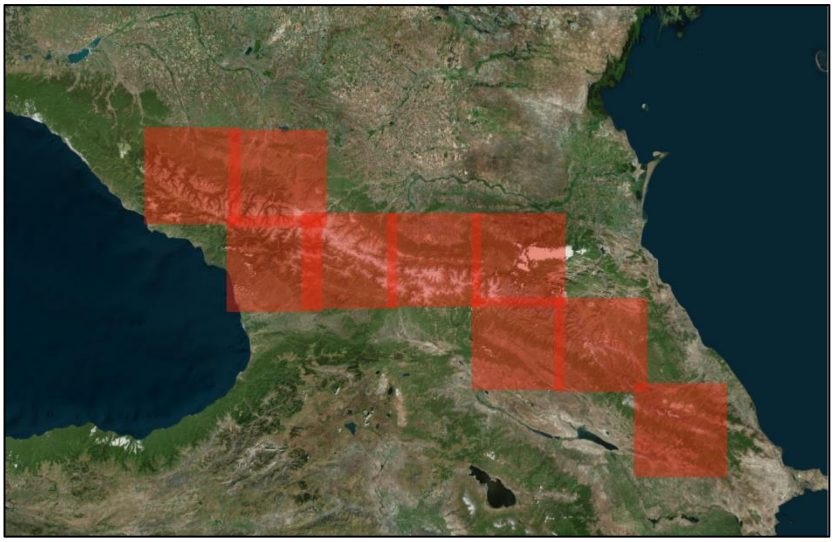

Figure A.3: *Highlighted Sentinel tiles over the Caucasus Mountains.*

Both the selected H-SAF snow products have been compared against the Sentinel-2 high resolution imagery at all the three target areas, according to the proposed methodology. The main results are hereafter shown.

A.2.1 Results of the H-SAF H10 analysis

Figures A.4 to A.6 show the distributions of the 5-km FSC pixels derived by aggregating the 20-m Sentinel ones. The results are shown for both H-SAF H10 snow- and soil-classified pixels. The two satellite products reveal a prominent agreement in detecting full snow cover (around 90%), but misclassification generally affects the products matching in classifying soil pixels.

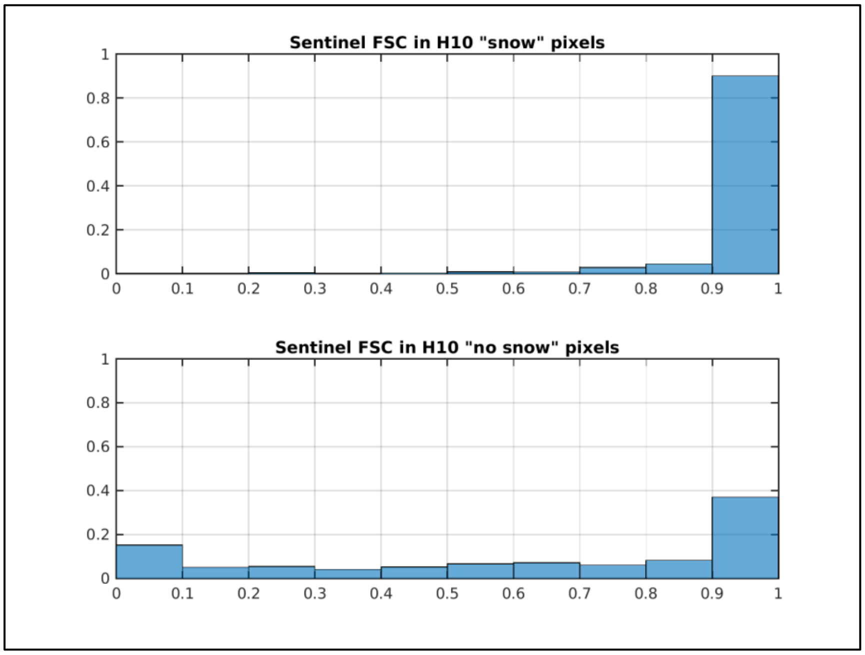

Figure A.4: *H10 vs Sentinel – Aosta Valley –Distribution of 5-km FSC pixels derived by aggregating the 20-m Sentinel pixels. The analysis results are separately shown for the 5-km H10 pixels classified as "snow" (on the top panel) and those classified as "soil" (on the bottom panel) throughout the whole analysis period.*

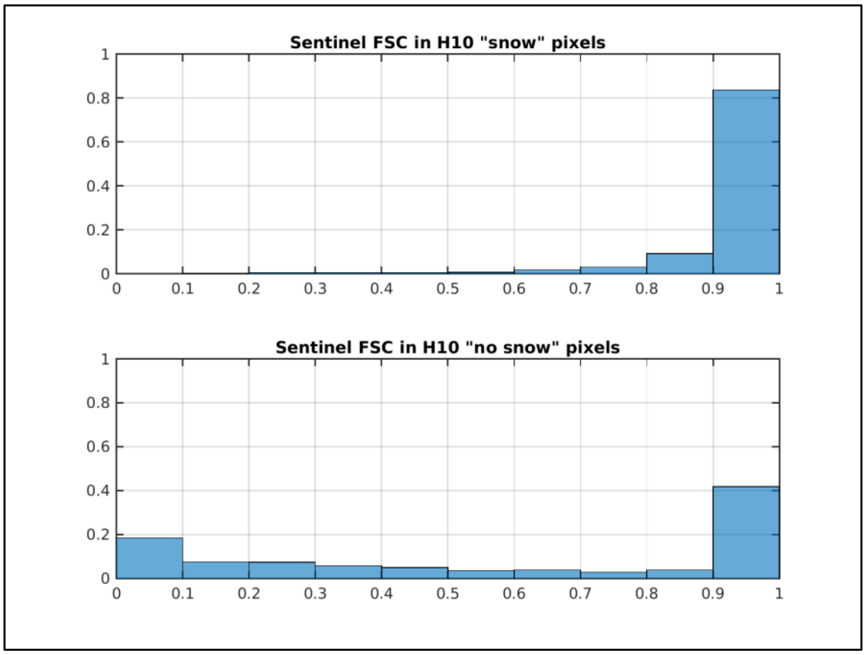

Figure A.5: *H10 vs Sentinel–2 tiles over Pyrenees Mountains – Distribution of 5-km FSC pixels derived by aggregating the 20-m Sentinel pixels. The analysis results are separately shown for the 5-km H10 pixels classified as "snow" (on the top panel) and those classified as "soil" (on the bottom panel) throughout the whole analysis period.*

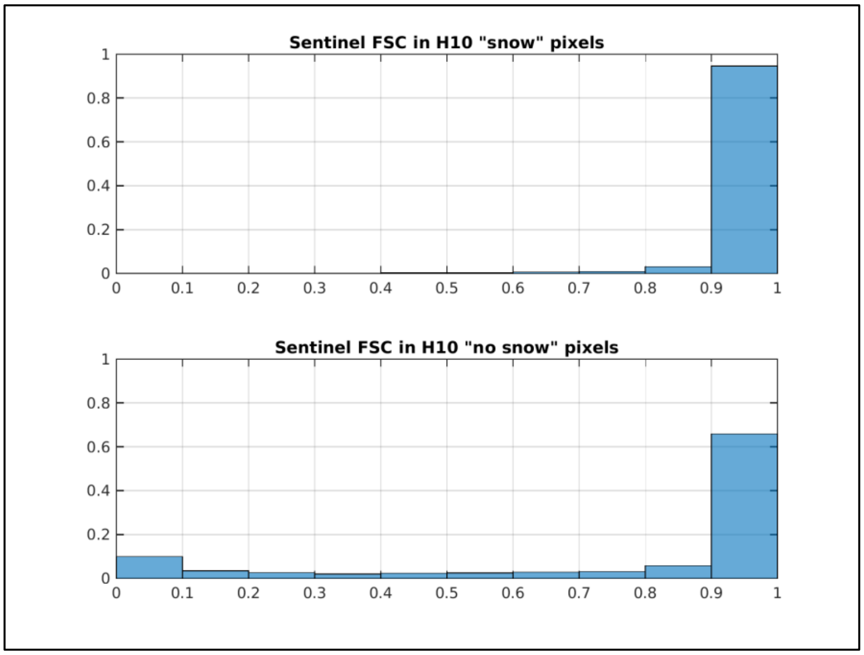

Figure A.6: *H10 vs Sentinel–9 tiles over Caucasus Mountains – Distribution of 5-km FSC pixels derived by aggregating the 20-m Sentinel pixels. The analysis results are separately shown for the 5-km H10 pixels classified as "snow" (on the top panel) and those classified as "soil" (on the bottom panel) throughout the whole analysis period.*

Figures A.7 to A.9 show the percentages of agreement between the two products in classifying “snow” and “soil” pixels. The match probabilities of each class result from the ratio of “snow” (and “soil”) H10 pixels over the amount of snow (and “soil”) Sentinel pixels. It is important to stress that Sentinel pixels have been classified as “snow” wherever the aggregation of the 20-m pixels within a H-SAF 5-km pixel was greater than 50%.

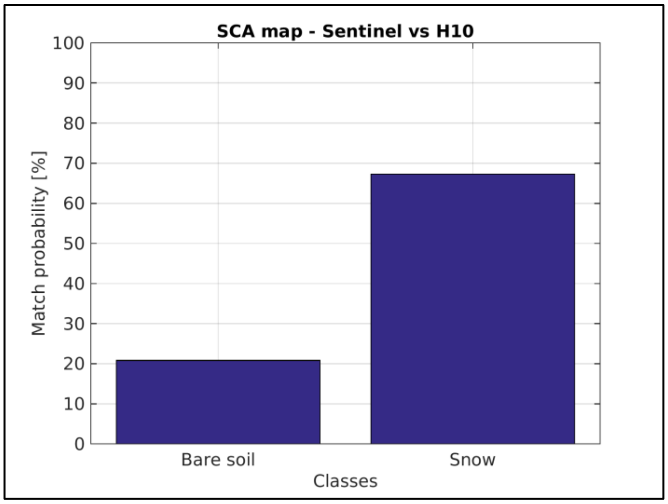

Figure A.7: *H10 vs Sentinel–Aosta Valley - Match probability in “snow” and “soil” classes throughout the whole analysis period.*

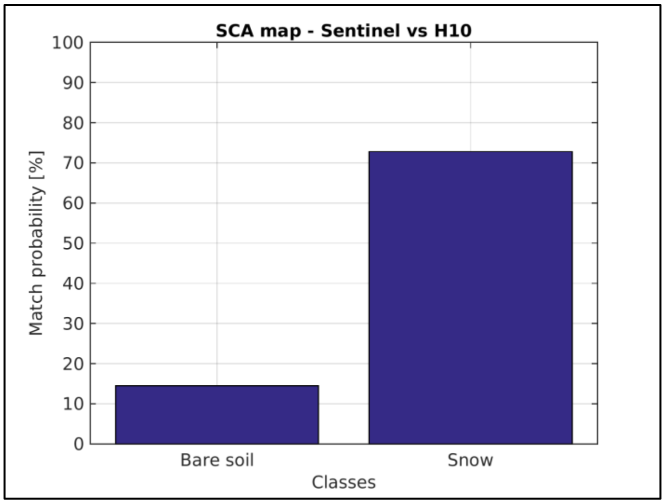

Figure A.8: *H10 vs Sentinel–2 tiles over Pyrenees Mountains - Match probability in “snow” and “soil” classes throughout the whole analysis* period.

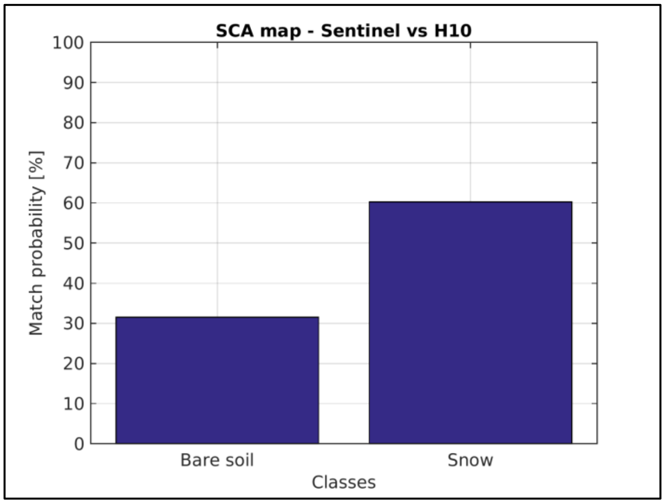

Figure A.9: *H10 vs Sentinel–9 tiles over Caucasus Mountains - Match probability in "snow" and "soil" classes throughout the whole analysis period.*

		Sentinel	
		Snow	**Bare soil**
H10	**Snow**	**0.67**	**0.006**
	Bare soil	**0.11**	**0.21**

Table A.4: *H10 vs Sentinel - Aosta Valley - Contingency table.*

		Sentinel	
		Snow	**Bare soil**
H10	**Snow**	**0.73**	**0.01**
	Bare soil	**0.11**	**0.15**

Table A.5: *H10 vs Sentinel - 2 tiles over Pyrenees Mountains - Contingency table.*

		Sentinel	
		Snow	**Bare soil**
H10	**Snow**	**0.602**	**0.004**
	Bare soil	**0.079**	**0.315**

Table A.6: *H10 vs Sentinel - 9 tiles over Caucasus Mountains - Contingency table.*

The statistical scores resulting from the analysis of the contingency matrices (Tables A.4 to A.6) are shown in Table A.7.

Scores	Aosta Valley	Pyrenees	Caucasus
POD	0.86	0.86	0.88
FAR	0.009	0.017	0.006
POFD	0.031	0.08	0.012
ACC	0.88	0.87	0.92
CSI	0.85	0.85	0.88
HSS	7.68	9.94	5.47

Table A.7: *H10 vs Sentinel–Total statistical indices throughout the whole analysis period.*

A.2.2 Results of the H-SAF H12 analysis

Figures A.10 to A.12 show the percentages of agreement in FSC and soil classifying between the two snow products. The match probabilities of each class result from the ratio of the H12 pixels within a specific class over the amount of S2A pixels of the same class, considering all the available tiles.

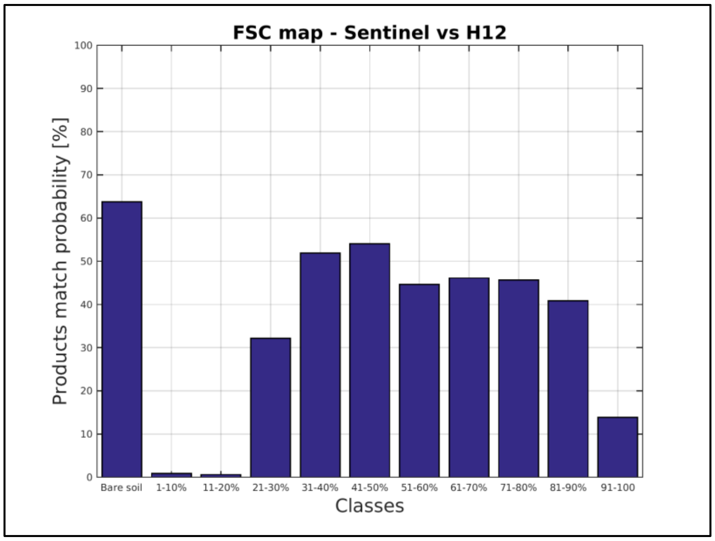

Figure A.10: *H12 vs Sentinel–Aosta Valley - Match probability in "FSC" and "bare soil" classes throughout the whole analysis period.*

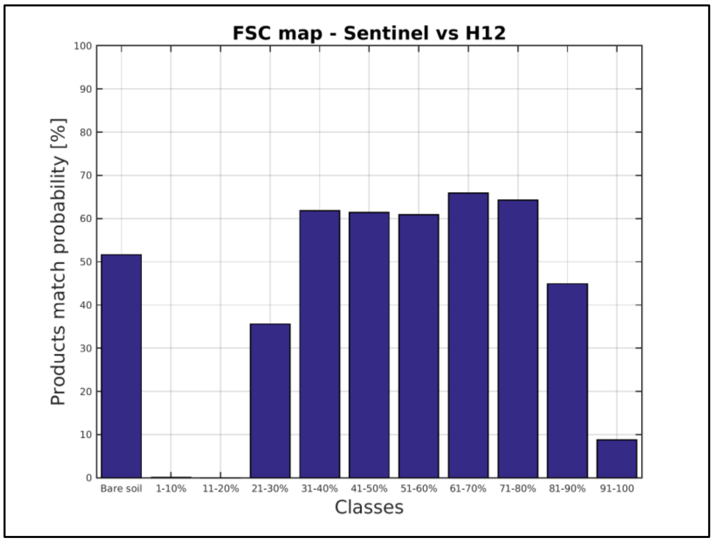

Figure A.11: *H12 vs Sentinel–2 tiles over Pyrenees Mountains - Match probability in “FSC” and “bare soil” classes throughout the whole analysis period.*

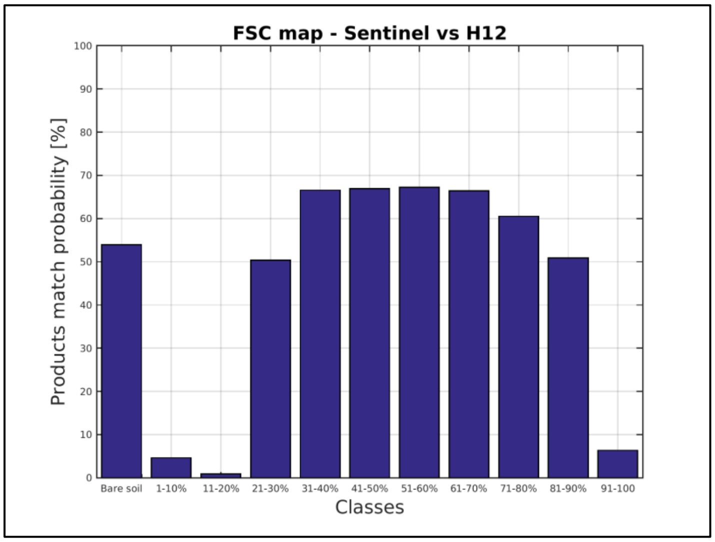

Figure A.12: *H12 vs Sentinel–9 tiles over Caucasus Mountains - Match probability in “FSC” and “bare soil” classes throughout the whole analysis period.*

The pixel-to-pixel comparison analysis between the two snow products have resulted in the statistical indices shown in the Table A.8.

Scores	Aosta Valley	Pyrenees	Caucasus
BIAS	-30.93 %	-34.75 %	-33.53 %
RMSE	45.07 %	47.42 %	46.40 %

Table A.8: *H12 vs Sentinel–Total statistical scores throughout the whole analysis period.*

Since individual pixels are often affected by some retrieval noise, the statistical metrics have been assessed also for each discrete class, whose trends are shown in the Figures A.13 to A.15.

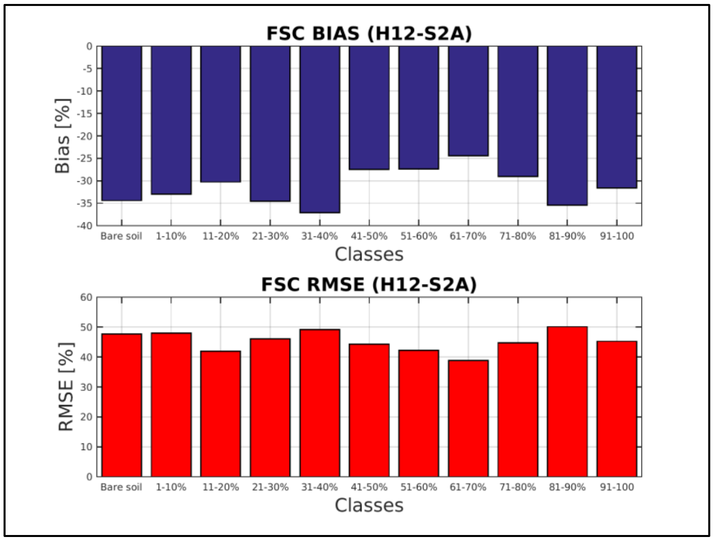

Figure A.13: *H12 vs Sentinel–Aosta Valley – Classes-based statistical scores throughout the whole analysis period.*

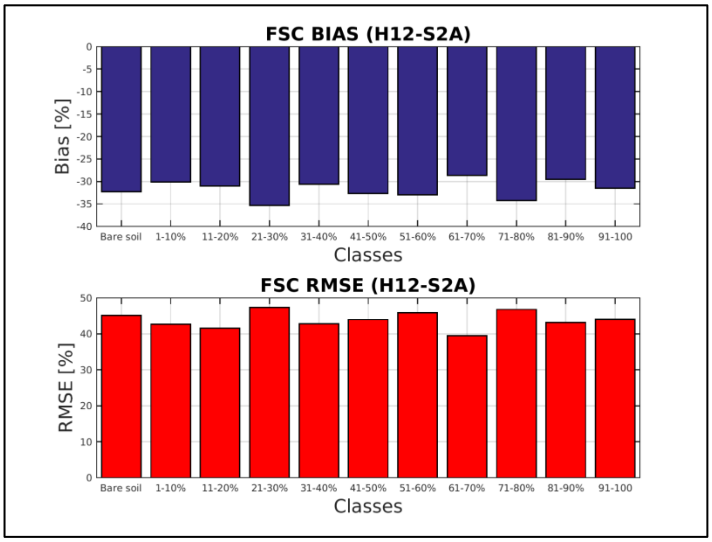

Figure A.14: *H12 vs Sentinel–2 tiles over Pyrenees Mountains – Classes-based statistical scores throughout the whole analysis period.*

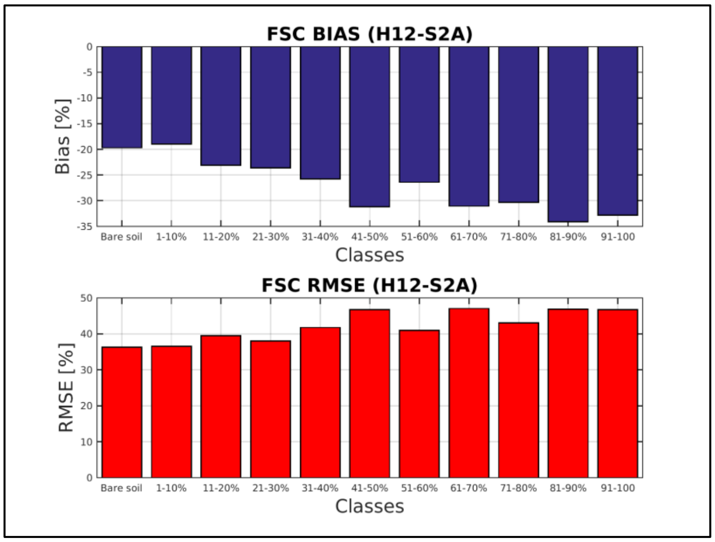

Figure A.15: *H12 vs Sentinel–9 tiles over Caucasus Mountains – Classes-based statistical scores throughout the whole analysis period.*

A.3 References

Crawford, C. J. (2015). MODIS Terra Collection 6 fractional snow cover validation in mountainous terrain during spring snowmelt using Landsat TM and ETM+. Hydrological Processes, 29(1), 128-138.

Nagler et. al (2014). REPORT ON 1st International Satellite Snow Products Intercomparison workshop (ISSPI-1).

Rittger, K., Painter, T. H., & Dozier, J. (2013). Assessment of methods for mapping snow cover from MODIS. Advances in Water Resources, 51, 367-380.

Salomonson, V. V., & Appel, I. (2004). Estimating fractional snow cover from MODIS using the normalized difference snow index. Remote sensing of environment, 89(3), 351-360.